Valerii P. Matveenko · Michael Krommer
Alexander K. Belyaev · Hans Irschik
Editors

Dynamics and Control of Advanced Structures and Machines

Contributions from the 3rd International Workshop, Perm, Russia

Springer

Dynamics and Control of Advanced Structures and Machines

Valerii P. Matveenko • Michael Krommer •
Alexander K. Belyaev • Hans Irschik
Editors

Dynamics and Control of Advanced Structures and Machines

Contributions from the 3rd International Workshop, Perm, Russia

Springer

Editors
Valerii P. Matveenko
Institute of Continuous Media Mechanics
Russian Academy of Sciences
Perm, Russia

Michael Krommer
Institute of Mechanics and Mechatronics
Vienna University of Technology
Vienna, Austria

Alexander K. Belyaev
Institute of Problems in Mech. Eng.
Russian Academy of Sciences
St. Petersburg, Russia

Hans Irschik
Institute for Technical Mechanics
Johannes Kepler University of Linz
Linz, Austria

ISBN 978-3-319-90883-0 ISBN 978-3-319-90884-7 (eBook)
https://doi.org/10.1007/978-3-319-90884-7

Library of Congress Control Number: 2018966531

This Springer imprint is published by the registered company Springer Nature Switzerland AG
The registered company address is: Gewerbestrasse 11, 6330 Cham, Switzerland

Preface

This book presents a collection of 21 contributions presented during the 3*rd International Workshop on Advanced Dynamics and Model Based Control of Structures and Machines*, which was held in September 2017 at the *Institute of Continuous Media Mechanics* of the Ural Branch of the Russian Academy of Sciences in Perm, Russia. The book contains 13 full-length papers of presentations from Russia, 3 from Austria, 3 from Japan and 2 from Taiwan.

The general goal of the workshop was to present and discuss the frontiers in the mechanics of controlled machines and structures. The workshop continued a series of international workshops: the *Japan–Austria Joint Workshop on Mechanics and Model Based Control of Smart Materials and Structures*, the *Russia–Austria Joint Workshop on Advanced Dynamics and Model Based Control of Structures and Machines* and the first two editions of the *International Workshop on Advanced Dynamics and Model Based Control of Structures and Machines*. The previous workshops took place in Linz, Austria, in September 2008 and April 2010, in St. Petersburg, Russia, in July 2012 and in Vienna, Austria, in September 2015.

As with the previous editions of this workshop, the main motivation was to proceed with and further foster the long-standing cooperation between research teams from Russia, Austria, Japan and Taiwan. The participation of a total of 39 scientists from these 4 countries led to fruitful scientific discussions among the participants, further deepening long-lasting cooperation and friendships, and to the publication of this book.

Perm, Russia — Valerii P. Matveenko
Vienna, Austria — Michael Krommer
St. Petersburg, Russia — Alexander K. Belyaev
Linz, Austria — Hans Irschik
October 2018

Acknowledgements

Support of the 3*rd International Workshop on Advanced Dynamics and Model Based Control of Structures and Machines* from the K2 area of the *Linz Center of Mechatronics GmbH* is gratefully acknowledged. This area was promoted as a K2 project with the project name *Austrian Competence Center of Mechatronics (ACCM)* in the context of *Competence Centers for Excellent Technologies (COMET)* by BMVIT, by BMWFJ and by the country Upper Austria.

The editors also wish to thank the *Institute of Continuous Media Mechanics* of the Ural Branch of the Russian Academy of Sciences as well as the *Perm National Research Polytechnic University* for hosting the workshop and Mrs. Silvia Schilgerius from Springer Nature for her support during the preparation of this book.

Contents

Measurement System of Impact Force and Specimen Deflection Based on Electromagnetic Induction Phenomena

Tadaharu Adachi, Yuto Mochizuki, and Yosuke Ishii

Abstract In this research, our measurement system based on electromagnetic induction phenomena was further improved to establish a complete system for measuring the impact force, specimen deflection, and collision velocity when a small impactor collides with a specimen. The measurement method and data analysis have been clarified to determine the impact force and specimen deflection from the measured electromotive forces induced in coils set near a specimen. The results of a rubber impact test confirmed the effectiveness of the system.

1 Introduction

The measurement of impact force [1] is important to consider the dynamic strength of several structures related to traffic accidents (automobiles, trains, airplanes) and natural disasters (debris from tornadoes, hail, lapillus, etc.). The impact force when a small impactor collides with a specimen cannot be easily measured with conventional sensors such as a load cell, accelerometer, or strain gages on the impactor due to limitations of the sensor size. Although the supporting force of a specimen can be measured as the impact force (under the assumption that the impact force is equal to the supporting force), the equilibrium of the forces is not always satisfied in the case of dynamic problems. When using other methods such as inverse analysis with dynamic response of the structure [2], it is often difficult to measure the force by virtue of the cracking or breaking of the structures. Therefore, in previous works factors such as fracture, damage, and depth of penetration have been estimated in impact tests using the impact velocity or kinetic energy of the impactor, which was determined from the impactor behavior before collision [3–9].

T. Adachi (✉) · Y. Mochizuki · Y. Ishii
Department of Mechanical Engineering, Toyohashi University of Technology, Tempaku, Toyohashi, Japan
e-mail: adachi@me.tut.ac.jp; y163191@edu.tut.ac.jp; ishii@me.tut.ac.jp

V. P. Matveenko et al. (eds.), *Dynamics and Control of Advanced Structures and Machines*, https://doi.org/10.1007/978-3-319-90884-7_1

In an earlier work, the authors proposed a system that utilizes electromagnetic induction [10] to measure impact force and specimen deflection from an electromotive force induced in coils near a specimen when a small impactor containing a magnet collides with the specimen. This method was based on earlier ones proposed by Moody et al. [11], Tansel et al. [12], and Watanabe et al. [13]. First, we proposed continuously measuring the impactor positions and velocities in the impact test from the electromotive force generated in a single coil near a specimen [14]. Although the accuracy of the electromotive force was reduced near the coil, overall effectiveness of the measured impactor behavior was demonstrated by the results of direct measurements with a high-speed camera. Second, we proposed the system for measuring impact force and specimen deflection by analyzing the electromotive force with high accuracy even near the coils using the coils connected in series [15] and quantitatively confirmed the effectiveness [16]. In this work, we further improved the system to establish a complete system for measuring the impact force, specimen deflection, and collision velocity of an impactor in impact tests.

2 Impact Testing Machine

We manufactured an impact testing machine to conduct impact tests (Fig. 1). The impactor was collided with a specimen after accelerating along the gun barrel by high-pressure air from the air chamber. The maximum air pressure was 1.0 MPa, and the length and inner diameter of the gun barrel were 0.5 m and 15 mm, respectively. A specimen was fixed circumferentially between two acrylic flanges with a circular hole 80 mm in diameter (Fig. 2) by tightening polyvinyl chloride (PVC) bolts and their nuts. Circular PVC pipes 115 mm in outer diameter were connected at both sides of the flanges to set the coils.

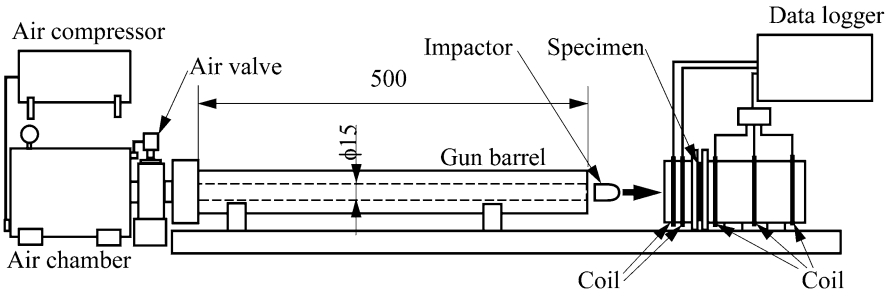

Fig. 1 Impact testing machine

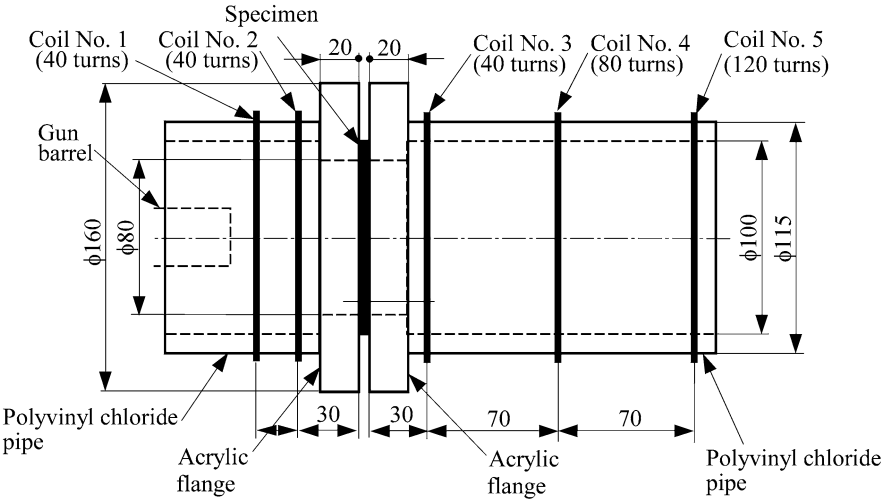

Fig. 2 Specimen support and coils

3 Coils

Two coils (No. 1 and 2) were set on the PVC pipe on the gun-barrel side to measure the electromotive forces for determining the collision velocity and initial position of the impactor (Fig. 2). Both coils had the same 40 turns. The electromotive forces induced in coils No. 1 and 2 were measured independently.

Three coils (No. 3, 4 and 5) on the PVC pipe on the back side were connected in series to measure the electromotive force for analyzing the impact force and specimen deflection. If the connected coils had the same number of turns, the electromotive force between the coils would definitely become zero, which would make it impossible to extend the measureable distance. Thus, coils No. 3, 4 and 5 had gradually increasing turn numbers (40, 80, and 120, respectively) and were used to maintain a large electromotive force and extend the measureable distance [15, 16].

Every coil was produced by wrapping 0.5 mm polyurethane-covered copper wire (2UEW-0.16, JIS C3202) around each PVC pipe. The electromotive forces induced in the coils were measured at 1 µs intervals using a data logger (GL-159 7000-U-130, Graphtec).

4 Impactor and Specimen

An impactor with a steel cone-head was manufactured to increase contact stiffness and strength at the tip of the impactor (Fig. 3). The head material did not interfere with measuring the electromotive forces in the experiment despite it being the

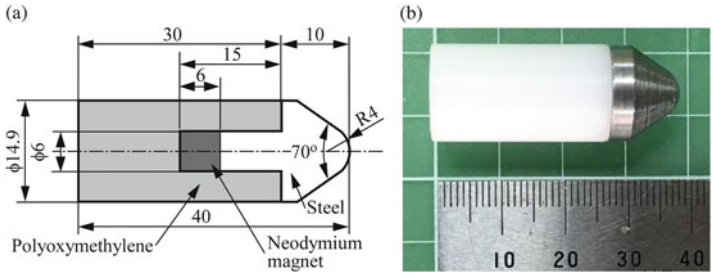

Fig. 3 Impactor. (**a**) Cross section, (**b**) Photograph

ferromagnetic. A cylindrical neodymium magnet 6 mm in diameter and length was placed at the end of the steel head. The rear part of the impactor was covered by high-density polyethylene. The length, diameter, and weight of the impactor were 36.0 mm, 14.9 mm, and 18.3 g, respectively. The impactor was launched by the testing machine at an air pressure of 0.52 MPa in the experiment.

The specimen was a sheet made of a mixture of natural and butadiene rubber filled with carbon black fillers. The thickness of the specimen was 2.3 mm. With our measurement system, specimens containing materials with the effect of a magnetic field shield cannot be measured since the magnetic field of the impactor is changed due to deformation and fracture of the specimen.

5 Data Analysis

Initial position and collision velocity were determined from the histories of the electromotive forces induced in coils No. 1 and 2 when the impactor passed through the coils before its collision with a specimen (Fig. 4). The electromotive forces become zero when the magnet in the impactor is located just at the coils No. 1 and 2, x_1 and x_2, so, the positions of the impactor, $x = x_1$ and $x = x_2$, can be identified at times $t = t_1$ and $t = t_2$. The impactor velocity before the collision, namely the collision velocity v_0, can be evaluated from the distance between the coils and the time difference $t_2 - t_1$.

The broken line in Fig. 5 shows the histories of the electromotive forces induced in coils No. 3, 4 and 5 connected in series when the impactor passed through coils at constant velocity. Because the intensity of the electromotive force in the connected coils is proportional to the impactor velocity evaluated by coils No. 1 and 2, and because its variation is solely dependent on the position of the impactor x, the electromotive force per impactor velocity was used as the reference data $e(x)$ in the analysis of the impact force and specimen deflection. The reference data can be acquired by the testing machine alone because the impactor velocity can be determined from the electromotive forces of coils No. 1 and 2 when the impactor passes through the coils without the specimen. The history of the impactor velocity

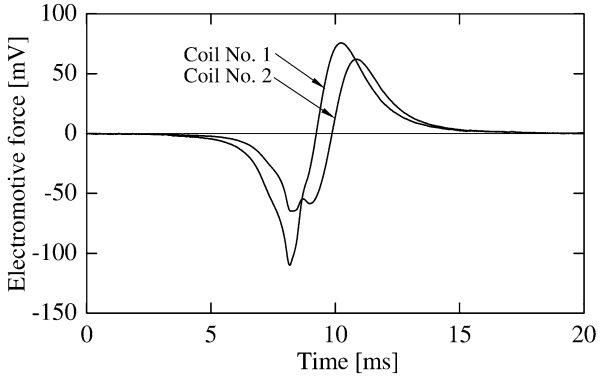

Fig. 4 Histories of electromotive forces induced in coils No. 1 and 2 when the impactor passes through coils at constant velocity

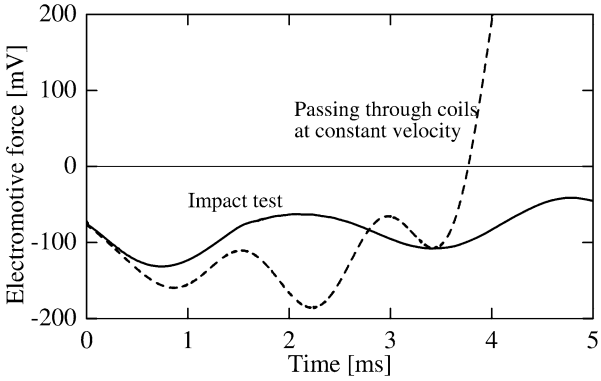

Fig. 5 Histories of electromotive forces induced in coils No. 3, 4 and 5 connected in series. Solid and broken lines respectively denote result of impact test and result when impactor passed through coils at constant velocity

in the impact test v can be evaluated with the reference data e as

$$v(t) = \frac{V(t)}{e(x)}, \quad x = x(t), \tag{1}$$

where V is the measured electromotive force induced in connected coils No. 3, 4 and 5 in series in the impact test (solid line in Fig. 5). By integrating Eq. (1) under the initial condition that $x = x_1$ or $x = x_2$ at $t = t_1$ or $t = t_2$, the impactor position can be given as

$$x(t) = x_i + \int_{t_i}^{t} v(\tau) d\tau \quad (i = 1 \text{ or } 2). \tag{2}$$

The acceleration of impactor α is determined as

$$a(t) = \frac{dv(t)}{dt}. \tag{3}$$

If the natural frequency of the impactor is sufficiently high compared to that of the specimen, the impactor behaves as a mass point. Under this condition, the impact force F can be evaluated by multiplying the acceleration by the mass of the impactor m:

$$F(t) = m\alpha(t). \tag{4}$$

Because the impactor is in contact with the specimen during the impact loading, $x(t)$ can be regarded as a specimen deformation at the collision point of the impactor.

6 Experimental Results

The impactor was collided with the rubber specimen at approximate 48 m/s and penetrated through the specimen easily, as the impactor had a steel head with high stiffness. Figure 6 shows the history of the impact velocity evaluated by Eq. (1) with the measured results in Fig. 5. The impactor velocity was found to decrease monotonically from the collision velocity, 48 to 28 m/s, and after that became constant. The constant velocity means the impactor velocity after the penetration. Figure 7 shows the histories of the impact force evaluated with Eqs. (2) and (4). The force increased at a high rate until 0.5 ms due to the collision of the impactor and then gradually increased up to 1.0 ms to initiate and extend a crack in the specimen. After that, the force decreased to zero due to the contact between the parallel side

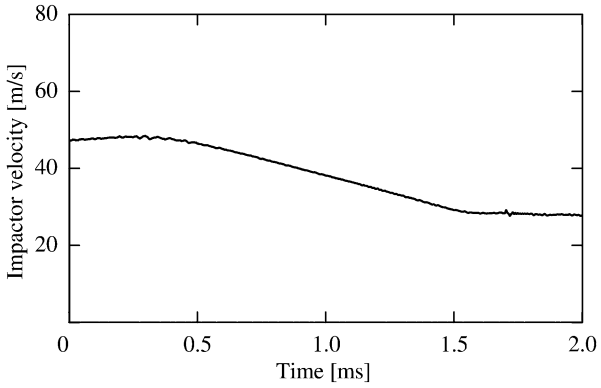

Fig. 6 History of impactor velocity

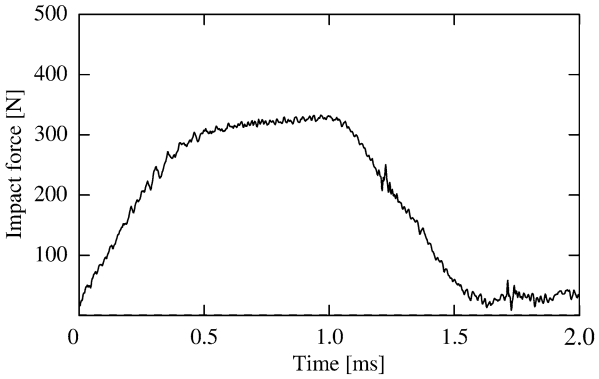

Fig. 7 History of impact force

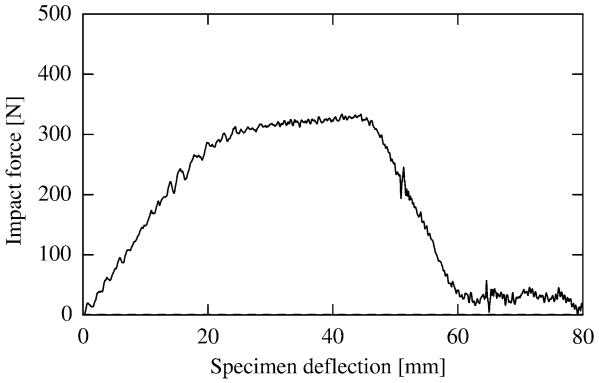

Fig. 8 Impact–specimen deflection relation

of the impactor and the hole in the specimen. Finally the impactor had completely passed through the specimen. The relation of the impact force–specimen deflection curve calculated from the data in Figs. 6 and 7 is shown in Fig. 8. To consider the energy in the experiment, external work due to the collision of the impactor W was evaluated from the relation according to

$$W(t) = \int_0^{x(t)} F(\xi) d\xi. \tag{5}$$

The kinetic energy of the impactor K was also calculated from the impactor velocity in Fig. 6 and from the impactor mass. The histories of the external work W and the total energy of the work and kinetic energy $W + K$ are shown in Fig. 9. The total energy in the collision process maintained the initial kinetic energy, although the external work increased over time. It follows from the result that the kinetic

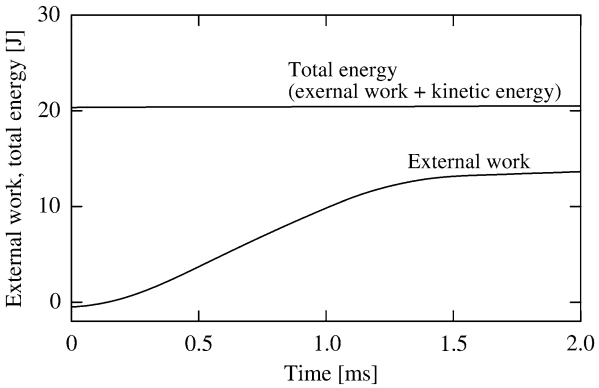

Fig. 9 Histories of external work and total energy

energy of the impactor consumed the penetration of the specimen. The above results demonstrated the effectiveness of the system quantitatively.

7 Conclusion

Our measurement system of the impact force and specimen deflection based on electromagnetic induction phenomena was further improved to establish a complete system for measuring the impact force, specimen deflection, and impactor velocity. The reference data can be acquired and the measurement of the impact force and specimen deflection can be determined by a testing machine alone, without other equipment. The effectiveness of the system was demonstrated by the experimental results of a rubber impact test. The improved system can be applied widely to impact tests for materials without magnetic shield effect to consider impact strength, penetration strength, etc.

Acknowledgements This research was supported by the Japan Society for the Promotion of Science (JSPS), KAKENHI, grant number JP17K06053.

References

1. Adachi, T., Ishii, Y.: Impact load. J. Jpn. Soc. Exp. Mech. **17**, 167–170 (2017) (in Japanese)
2. Inoue, H., Harrigan, J.J., Reid, S.R.: Review of inverse analysis for indirect measurement of impact force. Appl. Mech. Rev. **54**, 483–502 (2001)
3. Abrate, S.: Impact on Composite Structures. Cambridge University Press, Cambridge (1998)
4. Zukas, J.A., Nicholas, T., Swift, H.F., Greszczuk, L.B., Curran, D.R.: Impact Dynamics. Wiley, New York (1982)

5. Walker, J.D.: Hypervelocity penetration modeling: momentum vs. energy and energy transfer mechanism. Int. J. Impact Eng. **26**, 809–822 (2001)
6. Bourne, N.K.: On the failure and dynamic performance of materials. Exp. Mech. **52**, 153–159 (2012)
7. Warren, T.L.: The effect of target inertia on the penetration of aluminum targets by rigid ogive-nosed long rods. Int. J. Impact Eng. **91**, 6–13 (2016)
8. Antonucci, V., Caputo, F., Ferraro, P., Langella, A., Lopresto, V., Pagliarulo, V., Ricciardi, M.R., Riccio, A., Toscano, C.: Low velocity impact response of carbon fiber laminates fabricated by pulsed infusion: a review of damage investigation and semi-empirical models validation. Prog. Aerosp. Sci. **81**, 26–40 (2016)
9. Omidvar, M., Iskander, M., Bless, S.: Response of granular media to rapid penetration. Int. J. Impact Eng. **66**, 60–82 (2014)
10. Ida, K.: Engineering Electromagnetics, 3rd edn. Springer, New York (2015)
11. Moody, R.L., Konrad, C.H.: Magnetic induction system for two-stage gun projectile velocity measurements. Sandia report SAND84-0638 UC-13 (1984)
12. Tansel, I.N., Reding, B., Cooper, W.L.: Lagrangian point state estimation with optimized, redundant induction coil gages. Exp. Mech. **53**, 1065–1072 (2013)
13. Watanabe, K., Fukuma, S., Yoshisaka, T., Kobayashi, H.: Penetration velocity measurement in sands using magnet-coil gages. Appl. Mech. Mater. **566**, 371–376 (2014)
14. Adachi, T., Osada, M., Watanabe, K.: Measuring behavior of impactor penetrating through polymer sheet based on electromagnetic induction. Key Eng. Mater. **715**, 122–127 (2016)
15. Adachi, T., Matsukawa, N., Takamizo, C., Ishii, Y.: Measuring method of impact load in collision of small impactor based on electromagnetic induction. J. Jpn. Soc. Exp. Mech. **17**, 231–236 (2017) (in Japanese)
16. Adachi T., Matsukawa N., Takamizo C., Ishii Y.: New diagnostic method for evaluating penetration strength of rubber sheet by measuring electromagnetic induction. Int. J. Impact Eng. **121**, 172–179 (2018). https://doi.org/10.1016/j.ijimpeng.2018.07.002

New Cracks for Hard Contact of Lithosphere Plates with the Base

Olga M. Babeshko, Olga V. Evdokimova, and Vladimir A. Babeshko

Abstract It is being researched the existence of the hidden defects which are not visually watched in the coverings of nanomaterials in earthquake seismology and materials science. It is being developed the method of the research on such defects and coverings which are based on the topological approach. It is being adduced the analysis of the defects on the example the research on the stress–strain state of a block structure, consisting of a two-dimensional horizontal units of different types in contact with each other on the boundaries. The block structure is situated on the surface three-dimensional linearly deformable substrate and rigidly connected with it. The researching block structures are under the arbitrary harmonic outside effects. It is peculiar not only to the nanocoverings, surface reinforcement of the materials but the lithospheric plate structure, the research on which stress–strain state serves to get information about the seismic intensity of the areas. The obtained results are evidence of the fact that the hidden defects are practically new types of the cracks, additional to the cracks of Griffith–Irvine. That is, unlike crack Griffith–Irvine characterized by the roundness and smoothness of boundaries, this type of cracks includes breaks of boundaries and visually more accurately describes the boundaries of the cracks, for example, in the fragile materials such as glass.

1 Defining Equations

Consider the case of harmonic effects on the surface of the plates is rigidly coupled to the base. Then, after the reduction of the interim multiplier $e^{-i\omega t}$, equations of a boundary problem for plates can be represented as [1, 2], where the problem is

O. M. Babeshko · V. A. Babeshko (✉)
Kuban State University, Krasnodar, Russia

O. V. Evdokimova
Southern Scientific Center, Russian Academy of Science, Rostov-on-Don, Russia

V. P. Matveenko et al. (eds.), *Dynamics and Control of Advanced Structures and Machines*, https://doi.org/10.1007/978-3-319-90884-7_2

formulated and the notations are introduced, which we follow below

$$\mathbf{s}_b(x_1x_2) = \left\| \begin{matrix} -\varepsilon_{5b}s_{1b}(x_1,x_2) & 0 & 0 \\ 0 & -\varepsilon_{5b}s_{2b}(x_1,x_2) & 0 \\ 0 & 0 & \varepsilon_{53b}s_{3b}(x_1,x_2) \end{matrix} \right\|$$

$$s_{nb}(x_1,x_2) = (t_{nb} + g_{nb})$$

$$\mathbf{R}_b\left(\partial x_1, \partial x_2\right)\mathbf{u}_b = \left\| \begin{matrix} \left(\frac{\partial^2}{\partial x_1^2} + \varepsilon_{1b}\frac{\partial^2}{\partial x_2^2} + \varepsilon_{4b}\right)u_{1b} & \left(\varepsilon_{2b}\frac{\partial^2}{\partial x_1 \partial x_2}\right)u_{2b} & 0 \\ \left(\varepsilon_{2b}\frac{\partial^2}{\partial x_1 \partial x_2}\right)u_{1b} & \left(\frac{\partial^2}{\partial x_2^2} + \varepsilon_{1b}\frac{\partial^2}{\partial x_1^2} + \varepsilon_{4b}\right)u_{2b} & 0 \\ 0 & 0 & L\left(\frac{\partial}{\partial x_1}, \frac{\partial}{\partial x_2}\right)u_{3b} \end{matrix} \right\| \tag{1}$$

$$L\left(\frac{\partial}{\partial x_1}, \frac{\partial}{\partial x_2}\right)u_{3b} = \left(\frac{\partial^4}{\partial x_1^4} + 2\frac{\partial^2}{\partial x_1^2}\frac{\partial^2}{\partial x_2^2} + \frac{\partial^4}{\partial x_2^4} - \varepsilon_{43b}\right)u_{3b}$$

$$\mathbf{U}_b = \mathbf{F}\mathbf{u}_b, \quad \mathbf{G}_b = \mathbf{F}\mathbf{g}_b \quad \mathbf{T}_b = \mathbf{F}\mathbf{t}_b$$

$$\mathbf{u}_b = \{u_{1b}, u_{2b}, u_{3b}\}, \quad \mathbf{g}_b = \{g_{1b}, g_{2b}, g_{3b}\}, \quad \mathbf{t}_b = \{t_{1b}, t_{2b}, t_{3b}\}$$

Here the normal stresses t_{3b} act on the plate at the top and g_{3b} bottom.

Similarly stresses g_{1b}, g_{2b} and t_{1b}, t_{2b} act in the tangent plane, moreover, g_{2b} and t_{2b} in the direction of the normals to the edges of lithospheric plates

$$\mathbf{U}_b = \mathbf{F_2}\mathbf{u}_b, \quad \mathbf{G}_b = \mathbf{F_2}\mathbf{g}_b, \quad \mathbf{T}_b = \mathbf{F_2}\mathbf{t}_b, \quad b = \lambda, r$$

$$M_b = -D_{b1}\left(\frac{\partial^2 u_{3b}}{\partial x_2^2} + \nu_b\frac{\partial^2 u_{3b}}{\partial x_1^2}\right), \quad D_{b1} = \frac{D_b}{H^2}, \quad D_{b2} = \frac{D_b}{H^3}$$

$$Q_b = -D_{b2}\left(\frac{\partial^3 u_{3b}}{\partial x_2^3} + (2-\nu_b)\frac{\partial^3 u_{3b}}{\partial x_1^2 \partial x_2}\right), \quad u_{3b}, \quad \frac{\partial u_{3b}}{\partial x_2}$$

$$D_b = \frac{E_b h_b^3}{12\left(1-\nu_b^2\right)}, \quad \varepsilon_{53b} = \frac{\left(1-\nu_b^2\right)12^4}{E_b h_b^3} \quad \varepsilon_6^{-1} = \frac{(1-\nu)H}{\mu}$$

$$\varepsilon_{1b} = 0.5(1-\nu_b), \quad \varepsilon_{2b} = 0.5(1+\nu_b), \quad \varepsilon_{5b} = \frac{1-\nu_b^2}{E_b h_b}, \quad \varepsilon_{3b} = \frac{h_b^2}{12},$$

$$T_{x_1x_2} = \varepsilon_7 \left(\frac{\partial u_2}{\partial x_1} + \frac{\partial u_1}{\partial x_2} \right), \quad N_{x_2} = \varepsilon_8 \left(\frac{\partial u_2}{\partial x_2} + \nu \frac{\partial u_1}{\partial x_1} \right),$$

$$\varepsilon_7 = \frac{E}{2(1+\nu)H}, \quad \varepsilon_8 = \frac{E}{(1-\nu^2)H}$$

$$g_{1b} = \mu_{0b} \left(\frac{\partial u_{1b}}{\partial x_3} + \frac{\partial u_{3b}}{\partial x_1} \right), \quad g_{2b} = \mu_{0b} \left(\frac{\partial u_{2b}}{\partial x_3} + \frac{\partial u_{3b}}{\partial x_2} \right)$$

$$\mu_{0b} = \frac{\mu_b}{H}, \quad x_3 = 0, \quad \mathbf{g} = \{g_{1b}, g_{2b}\}$$

The following symbols are accepted: μ_b—shear modulus, ν_b—Poisson's ratio, E_b—Young's modulus, h_b—thickness, $\mathbf{g}_b$, $\mathbf{t}_b$—vectors of contact stresses and external horizontal, g_{1b}, g_{2b}, t_{1b}, t_{2b} and vertical, g_{3b}, t_{3b} impacts, respectively, acting at a tangent to the boundary of the base and to normal to it, in the areas Ω_b. $\mathbf{F}_2 \equiv \mathbf{F}_2(\alpha_1, \alpha_2)$, $\mathbf{F}_1 \equiv \mathbf{F}_1(\alpha_1)$—two-dimensional and one-dimensional operators of the Fourier transform, respectively. The boundary conditions described in [1, 2] are preserved here. Normals N_{x_2} and tangents $T_{x_1x_2}$ of the stress components to the median plane at the ends of the plates, and also the bending moment M_b and Q_b cutting force are determined here.

Different models may be used for the deformable base, described by the boundary value problem. These models are given by the relations

$$\mathbf{u}(x_1, x_2) = \varepsilon_6^{-1} \frac{1}{4\pi^2} \int_{-\infty}^{\infty} \int \mathbf{K}(\alpha_1, \alpha_2) \mathbf{G}(\alpha_1, \alpha_2) e^{-i\langle \alpha, x \rangle} \mathrm{d}\alpha_1 \mathrm{d}\alpha_2, \tag{2}$$

$$x \in \Omega_\lambda, \quad x \in \Omega_r, \quad x \in \Omega_\theta, \quad \langle \alpha, x \rangle = \alpha_1 x_1 + \alpha_2 x_2$$

$$\Omega_\lambda(|x_1| \le \infty;\ x_2 \le 0), \quad \Omega_r(|x_1| \le \infty;\ 0 \le x_2),$$

$$\mathbf{K} = \|K_{mn}\|, \quad m, n = 1, 2, 3,$$

$$\mathbf{K}(\alpha_1, \alpha_2) = O(A^{-1}), \quad A = \sqrt{\alpha_1^2 + \alpha_2^2} \to \infty$$

$$\varepsilon_6^{-1} = \frac{(1-\nu)H}{\mu}, \quad \mathbf{G}(\alpha_1, \alpha_2) = \mathbf{F}_2(\alpha_1, \alpha_2)\mathbf{g}$$

g—the vector of tangential and normal stresses under the plates on the boundary of the base. Some types of matrix-base $K(\alpha_1, \alpha_2)$ functions, called the symbol of the system of integral equations, are given in [3] and are given by a matrix-function

$$K(\alpha_1, \alpha_2) = \begin{Vmatrix} \alpha_1^2 M + \alpha_2^2 N & \alpha_1\alpha_2(M-N) & i\alpha_1 P \\ \alpha_1\alpha_2(M-N) & \alpha_1^2 N + \alpha_2^2 M & i\alpha_2 P \\ -i\alpha_1 P & -i\alpha_2 P & K \end{Vmatrix}$$

The matrix (1) of the boundary value problem is block-diagonal, consisting of a second-order matrix situated on the diagonal, representing a matrix operator or vector operator and a scalar operator separated on the diagonal. Since the operators are independent, this greatly facilitates the study of the boundary value problem.

2 Solution Method for the Boundary Value Problems

The boundary problems for each block of a block structure are absorbed in a topological space induced by a three-dimensional Euclidean space, after this they are reduced to functional equations by the application of the Stokes formula.

2.1 Scalar Problem

The functional equations of the scalar boundary value problem about vertical impacts may be represented in the form

$$R_b(-i\alpha_1, -i\alpha_2)U_{3b} \equiv \left[\left(\alpha_1^2 + \alpha_2^2\right)^2 - \varepsilon_{43b}\right]U_{3b} = -\int_{\partial\Omega_b} \omega_b - \varepsilon_{53b} S_{3b}(\alpha_1, \alpha_2)$$
$$S_{3b}(\alpha_1, \alpha_2) = \mathbf{F}_2(\alpha_1, \alpha_2)(t_{3b} - g_{3b}), \quad b = \lambda, r \tag{3}$$

The representation of the solution for each plate has the form

$$u_{3b} = -\mathbf{F}_2^{-1}(\alpha_1, \alpha_2)\frac{1}{\left(\alpha_1^2 + \alpha_2^2\right)^2 - \varepsilon_{43b}}\int_{\partial\Omega_b} \omega_b - \varepsilon_{53b} S_{3b}(\alpha_1, \alpha_2)$$

Here ω_b—taking part in the representation of external forms, having the form

$$\omega_b = e^{i\langle\alpha,x\rangle}\Bigg\{-\Bigg[\frac{\partial^3 u_{3b}}{\partial x_2^3} - i\alpha_2\frac{\partial^2 u_{3b}}{\partial x_2^2} - \alpha_2^2\frac{\partial u_{3b}}{\partial x_2} + i\alpha_2^3 u_{3b} + 2\frac{\partial^3 u_{3b}}{\partial x_1^2\partial x_2} - 2i\alpha_2\frac{\partial^2 u_{3b}}{\partial x_1^2}\Bigg]\mathrm{d}x_1 + \Bigg[\frac{\partial^3 u_{3b}}{\partial x_1^3} - i\alpha_1\frac{\partial^2 u_{3b}}{\partial x_1^2} - \alpha_1^2\frac{\partial u_{3b}}{\partial x_1} + i\alpha_1^3 u_{3b}\Bigg]\mathrm{d}x_2\Bigg\}, \quad b = \lambda, r$$

We can implement automorphism by calculating the Leray-residue forms, and thus obtain the pseudodifferential equations of the scalar boundary value problem. Taking into account the accepted notations, we can present pseudodifferential equations for the left plate in the form

$$\mathbf{F}_1^{-1}(\xi_1^\lambda)\Bigg\langle -\int_{\partial\Omega_\lambda}\Bigg\{i\alpha_{21-}D_{\lambda1}^{-1}M_\lambda - D_{\lambda2}^{-1}Q_\lambda - \left(\alpha_{21-}^2 + \nu_\lambda\alpha_1^2\right)\frac{\partial u_{3\lambda}}{\partial x_2} + i\alpha_{21-}\left[\alpha_{21-}^2 + (2-\nu_\lambda)\alpha_1^2\right]u_{3\lambda}\Bigg\}e^{i\alpha_1 x_1}\mathrm{d}x_1 - \varepsilon_{53\lambda}S_{3\lambda}(\alpha_1,\alpha_{21-})\Bigg\rangle = 0, \quad \xi_1^\lambda \in \partial\Omega_\lambda \tag{4}$$

$$\mathbf{F}_1^{-1}\left(\xi_1^\lambda\right)\Bigg\langle -\int_{\partial\Omega_\lambda}\Bigg\{i\alpha_{22-}D_{\lambda1}^{-1}M_\lambda - D_{\lambda2}^{-1}Q_\lambda - \left(\alpha_{22-}^2 + \nu_\lambda\alpha_1^2\right)\frac{\partial u_{3\lambda}}{\partial x_2} + i\alpha_{22-}\left[\alpha_{22-}^2 + (2-\nu_\lambda)\alpha_1^2\right]u_{3\lambda}\Bigg\}e^{i\alpha_1 x_1}\mathrm{d}x_1 + \varepsilon_{53\lambda}S_{3\lambda}(\alpha_1,\alpha_{22-})\Bigg\rangle = 0,$$

$$\alpha_{21-} = -i\sqrt{\alpha_1^2 - \sqrt{\varepsilon_{43\lambda}}}, \quad \alpha_{22-} = -i\sqrt{\alpha_1^2 + \sqrt{\varepsilon_{43\lambda}}}, \quad \xi_1^\lambda \in \partial\Omega_\lambda$$

We introduce the following notation system:

$$z_{1\lambda} = \mathbf{F}_1\frac{\partial u_\lambda}{\partial x_2}, \quad z_{2\lambda} = \mathbf{F}_1 u_\lambda, \quad z_{1r} = \mathbf{F}_1\frac{\partial u_r}{\partial x_2}, \quad z_{2r} = \mathbf{F}_1 u_r,$$

$$\mathbf{K}_\lambda = \{k_{1\lambda}, k_{2\lambda}\}, \quad \mathbf{K}_\mathbf{r} = \{k_{1r}, k_{2r}\}, \quad k_{1\lambda} = \varepsilon_{53\lambda}\mathbf{F}_2(\alpha_1,\alpha_{21-})(t_\lambda - g_\lambda),$$

$$k_{2\lambda} = \varepsilon_{53\lambda}\mathbf{F}_2(\alpha_1,\alpha_{22-})(t_\lambda - g_\lambda), \quad k_{1r} = \varepsilon_{53r}\mathbf{F}_2(\alpha_1,\alpha_{21+})(t_r - g_r),$$

$$k_{2r} = \varepsilon_{53r}\mathbf{F}_2(\alpha_1,\alpha_{22+})(t_r - g_r)$$

As a result, the pseudodifferential equations for this case may be rewritten in the form of algebraic equations

$$\mathbf{A}_\lambda \mathbf{Y}_\lambda + \mathbf{B}_\lambda \mathbf{Z}_\lambda + \mathbf{K}_\lambda = 0,$$

$$\mathbf{A}_r \mathbf{Y}_r + \mathbf{B}_r \mathbf{Z}_r + \mathbf{K}_r = 0$$

Let us consider the case when the bending moment and the cutting force are zero, that means that the plate ends are stress-free, $\mathbf{Y}_\lambda = 0$, $\mathbf{Y}_r = 0$.

The system of equations takes the form

$$\left(\alpha_{21+}^2 + \nu_r \alpha_1^2\right) z_{1r} - i\alpha_{21+}\left[\alpha_{21+}^2 + (2-\nu_r)\alpha_1^2\right] z_{2r} = -k_{1r}$$

$$\left(\alpha_{22+}^2 + \nu_r \alpha_1^2\right) z_{1r} - i\alpha_{22+}\left[\alpha_{22+}^2 + (2-\nu_r)\alpha_1^2\right] z_{2r} = -k_{2r}$$

$$\left(\alpha_{21-}^2 + \nu_\lambda \alpha_1^2\right) z_{1\lambda} - i\alpha_{21-}\left[\alpha_{21-}^2 + (2-\nu_\lambda)\alpha_1^2\right] z_{2\lambda} = -k_{1\lambda}$$

$$\left(\alpha_{22-}^2 + \nu_\lambda \alpha_1^2\right) z_{1\lambda} - i\alpha_{22-}\left[\alpha_{22-}^2 + (2-\nu_\lambda)\alpha_1^2\right] z_{2\lambda} = -k_{2\lambda}$$

The solutions of the resulting systems of equations are easily found

$$\mathbf{Z}_\lambda = -\mathbf{B}_\lambda^{-1}\mathbf{K}_\lambda, \quad \mathbf{Z}_r = -\mathbf{B}_r^{-1}\mathbf{K}_r,$$

and what is more, the determinants of the systems have the form

$$\Delta_\lambda = i\left\langle \left[\alpha_{21-}^2 + \nu_\lambda \alpha_1^2\right]^2 \alpha_{22-} - \left[\alpha_{22-}^2 + \nu_\lambda \alpha_1^2\right]^2 \alpha_{21-} \right\rangle$$

$$\Delta_r = i\left\langle \left[\alpha_{21+}^2 + \nu_r \alpha_1^2\right]^2 \alpha_{22+} - \left[\alpha_{22+}^2 + \nu_r \alpha_1^2\right]^2 \alpha_{21+} \right\rangle$$

Introducing the correlations found in the expressions for the external forms in (4) and taking $U_{31} + U_{32} = U_3$, $U_{mn}(\alpha_1, \alpha_2) = \mathbf{F}_2(\alpha_1, \alpha_2) u_{mn}$, we will have the equations placing $G_{3r} = G^+$, $G_{3\lambda} = G^-$.

$$\left[\varepsilon_{53r}\left(\alpha_1^2 + \alpha_2^2 - \varepsilon_{43r}\right)^{-2} + \varepsilon_6^{-1} K_1(\alpha_1, \alpha_2)\right] G^+(\alpha_1, \alpha_2)$$

$$= -\left[\varepsilon_{53\lambda}\left(\alpha_1^2 + \alpha_2^2 - \varepsilon_{43r}\right)^{-2} + \varepsilon_6^{-1} K_1(\alpha_1, \alpha_2)\right] G^-(\alpha_1, \alpha_2)$$

$$+\left(\alpha_1^2+\alpha_2^2-\varepsilon_{43r}\right)^{-2}\left[A_r k_{1r}+B_r k_{2r}+\varepsilon_{53r}T^{-}(\alpha_1,\alpha_2)\right]$$

$$+\left(\alpha_1^2+\alpha_2^2-\varepsilon_{43r}\right)^{-2}\left[A_\lambda k_{1\lambda}+B_\lambda k_{2\lambda}+\varepsilon_{53\lambda}T^{+}(\alpha_1,\alpha_2)\right]$$

2.2 Vector Problem

For the vector case we have

$$\mathbf{R}_b\left(\partial x_1,\partial x_2\right)\mathbf{u}_b=\left\|\begin{array}{cc}\left(\frac{\partial^2}{\partial x_1^2}+\varepsilon_{1b}\frac{\partial^2}{\partial x_2^2}+\varepsilon_{4b}\right)u_{1b} & \left(\varepsilon_{2b}\frac{\partial^2}{\partial x_1\partial x_2}\right)u_{2b}\\ \left(\varepsilon_{2b}\frac{\partial^2}{\partial x_1\partial x_2}\right)u_{1b} & \left(\frac{\partial^2}{\partial x_2^2}+\varepsilon_{1b}\frac{\partial^2}{\partial x_1^2}+\varepsilon_{4b}\right)u_{2b}\end{array}\right\|$$

The Fourier transform of the differential part of the system of equations has the form

$$-\mathbf{R}_b(-i\alpha_1,-i\alpha_2)\mathbf{U}_b=\left\|\begin{array}{cc}\left(\alpha_1^2+\varepsilon_{1b}\alpha_2^2-\varepsilon_{4b}\right)U_{1b} & \varepsilon_{2b}\alpha_1\alpha_2U_{2b}\\ \varepsilon_{2b}\alpha_1\alpha_2U_{1b} & \left(\alpha_2^2+\varepsilon_{1b}\alpha_1^2-\varepsilon_{4b}\right)U_{2b}\end{array}\right\| \tag{5}$$

$$\mathbf{U}=\mathbf{F}_2\mathbf{u},\quad \mathbf{G}=\mathbf{F}_2\mathbf{g},\quad b=1,2,\ldots,B$$

The functional equations for plates, in general, have the form [1, 2]

$$-\mathbf{R}_b(-i\alpha_{1b},-i\alpha_{2b})\mathbf{U}_b=\int_{\partial\Omega_b}\omega_b-\varepsilon_{5b}\mathbf{F}_2(\alpha_{1b},\alpha_{2b})(\mathbf{g}_b+\mathbf{t}_b), \tag{6}$$

$$\mathbf{U}_b=\{U_{1b},U_{2b}\},\quad b=1,2$$

Here $\boldsymbol{\omega}_b$—taking part in (6) a vector of external forms having the form

$$\boldsymbol{\omega}_b=\{\omega_1,\omega_2\}$$

$$\omega_{1b}=e^{i\langle\alpha,x\rangle}\left\{-\left(\varepsilon_{1b}\frac{\partial u_{1b}}{\partial x_2}+\varepsilon_{2b}\frac{\partial u_{2b}}{\partial x_1}-i\varepsilon_{1b}\alpha_{2b}u_{1b}\right)\mathrm{d}x_1\right.$$
$$\left.+\left(\frac{\partial u_{1b}}{\partial x_1}-i\alpha_{1b}u_{1b}-i\varepsilon_{2b}\alpha_{2b}u_{2b}\right)\mathrm{d}x_2\right\},$$

$$\omega_{2b} = e^{i\langle\alpha,x\rangle}\left\{ -\left(\varepsilon_{2b}\frac{\partial u_{1b}}{\partial x_1} + \frac{\partial u_{2b}}{\partial x_2} - i\alpha_{2b}u_{2b}\right)\mathrm{d}x_1 \right.$$
$$\left. + \left(\varepsilon_{1b}\frac{\partial u_{2b}}{\partial x_1} - i\varepsilon_{1b}\alpha_{1b}u_{2b} - i\varepsilon_{2b}\alpha_{2b}u_{1b}\right)\mathrm{d}x_2\right\}$$

To make calculations we receive the Wiener–Hopf functional equations of the following form:

$$MG_+ = G_- + V$$

$$\mathbf{M}\mathbf{G}_+ = \mathbf{G}_- + \mathbf{V},$$

$$M = -\left[\varepsilon_{53\lambda}\left(\alpha_1^2 + \alpha_2^2 - \varepsilon_{43r}\right)^{-2} + \varepsilon_6^{-1}K_1(\alpha_1,\alpha_2)\right]^{-1}$$
$$\times\left[\varepsilon_{53r}\left(\alpha_1^2 + \alpha_2^2 - \varepsilon_{43r}\right)^{-2} + \varepsilon_6^{-1}K_1(\alpha_1,\alpha_2)\right]$$

$$V = +\left(\alpha_1^2 + \alpha_2^2 - \varepsilon_{43r}\right)^{-2}\left[A_r k_{1r} + B_r k_{2r} + \varepsilon_{53r}T^-(\alpha_1,\alpha_2)\right]$$
$$+\left(\alpha_1^2 + \alpha_2^2 - \varepsilon_{43r}\right)^{-2}\left[A_\lambda k_{1\lambda} + B_\lambda k_{2\lambda} + \varepsilon_{53\lambda}T^+(\alpha_1,\alpha_2)\right]$$

$$\mathbf{M} = \mathbf{K_2^{-1}K_1}, \quad \mathbf{K}_1 = \varepsilon_{5r}\mathbf{R}_r^{-1} - \mathbf{K}, \quad \mathbf{K}_2 = \mathbf{K} - \varepsilon_{5\lambda}\mathbf{R}_\lambda^{-1},$$

$$\mathbf{V} = \mathbf{K}_2^{-1}\left(\mathbf{R}_\lambda^{-1}\int_{\partial\Omega_\lambda}\omega_\lambda + \mathbf{R}_r^{-1}\int_{\partial\Omega_r}\omega_r - \varepsilon_\lambda\mathbf{R}_\lambda^{-1}\mathbf{T}_\lambda - \varepsilon_r\mathbf{R}_r^{-1}\mathbf{T}_r\right)$$

When the ends of the plates fully approached each other, the contact stresses at the edges of the plates have the representation for the vertical and horizontal actions

$$\mathbf{g}_\lambda(x_1,x_2) \to \boldsymbol{\sigma}_{4\lambda}(x_1,x_2)x_2^{-1} + \boldsymbol{\sigma}_{5\lambda}(x_1,x_2)\ln|x_2| + \boldsymbol{\sigma}_{6\lambda}(x_1,x_2)\operatorname{sgn}x_2,$$
$$\mathbf{g}_r(x_1,x_2) \to \boldsymbol{\sigma}_{4r}(x_1,x_2)x_2^{-1} + \boldsymbol{\sigma}_{5r}(x_1,x_2)\ln|x_2| + \boldsymbol{\sigma}_{6r}(x_1,x_2)\operatorname{sgn}x_2 \qquad (7)$$

All vectors $\boldsymbol{\sigma}_{n\lambda}(x_1,x_2)$ and $\boldsymbol{\sigma}_{nr}(x_1,x_2)$, $n = 3,\ldots,6$ are continuous in both parameters. Taking into account the time parameter $\exp(-i\omega t)$ reduced in the solution of the harmonic boundary problem leads to the representation of the coefficients of physical stresses $\sigma_{3b}(x_1,x_2,t)$ in the case of peculiarities in the form

$$\sigma_{nb}(x_1,x_2,t) = \operatorname{Re}\sigma_{nb}(x_1,x_2)e^{-i\omega t} \equiv \operatorname{Re}\sigma_{nb}(x_1,x_2)\cos\omega t + \operatorname{Im}\sigma_{nb}(x_1,x_2)\sin\omega t$$

3 Conclusions

The resulting correlation (7) indicates that the hidden defects are actually new types of cracks, supplementing the known Griffith–Irwin cracks [4–8]. Unlike the well-known Griffith–Irwin cracks, characterized by the roundness and smoothness of the boundaries, this type of cracks contains fractures of boundaries and describes visually more accurately the boundaries of cracks, for example, in brittle materials such as glass. In this paper, this type of defects is detected in an inhomogeneous medium–formed by a block structure from a three-dimensional layer and Kirchhoff plates. The problem of the existence of such defects in homogeneous media will be the subject of the following studies.

Acknowledgements This work was realized as GZ UNC RAS, project no. 01201354241, supported by the Russian Foundation for Basic Research, projects nos (18-08-00465), (16-41-230218), (18-05-80008).

References

1. Babeshko, O.M.: Topological method in the problem of estimating of the stress concentration in faults of lithospheric plates. Ecol. Bull. Res. Cent. Black Sea Econ. Coop. **2**, 14–21 (2015) (In Russian)
2. Babeshko, V.A., Evdokimova, O.V., Babeshko, O.M.: The theory of the starting earthquake. Ecol. Bull. Res. Cent. Black Sea Econ. Coop. **1**(pt. 2), 37–80 (2016)
3. Vorovich, I.I., Babeshko, V.A.: Dynamic Mixed Problems of the Theory of Elasticity for Nonclassical Domains. Science, Moscow (1979) (In Russian)
4. Cherepanov, G.P.: Mechanics of Brittle Fracture. McGraw-Hill, New York (1979)
5. Cherepanov, G.P.: Mechanics of Destruction of Composite Materials. Science, Moscow (1983) (In Russian)
6. Irwin, G.: Fracture. In: Handbuch der Physic, bd 6. Springer, Berlin (1958)
7. Rice, J.: Mathematical analysis in the mechanics of fracture. In: Treatise on Fracture, vol. II, pp. 191–311. Academic, New York (1968)
8. Morozov, N.F.: Mathematical Questions of the Theory of Cracks. Nauka, Moscow (1984) (In Russian)

Dynamics of Contour Motion of Belt Drive by Means of Nonlinear Rod Approach

Alexander K. Belyaev, Vladimir V. Eliseev, Hans Irschik, and Evgenii A. Oborin

Abstract The contour motion of the belt drive, i.e., the motion with the constant trajectory, is addressed. The belt is considered as a closed Cosserat line whose particles have translational and rotational degrees of freedom. The problem is considered in the framework of geometrically nonlinear formulation with no restrictions on the smallness of displacements and rotations. The spatial (Eulerian) coordinate which is the arc coordinate in the actual configuration is introduced. The belt is divided into four segments: two contact segments on the pulleys and two free spans. The friction forces are assumed to obey the Coulomb law. The study is limited to the stationary case with the constant angular velocities of the pulleys and the equations in components are derived for both contact and free spans. In the contact segment two assumptions are employed to eliminate the unknown contact pressure and friction: (1) the full contact, i.e., coincidence between the pulley and the belt and (2) the stick condition, i.e., the belt velocity is related to the pulley angular velocity. A nondimensional coordinate is introduced in the segments to obtain the boundary value problem with fixed boundaries. The boundary coordinates of the contact zones are the integration constants of the derived problem along with the other constants.

The author "Vladimir V. Eliseev" was deceased on October 14, 2017.

A. K. Belyaev
Institute for Problems in Mechanical Engineering, Russian Academy of Sciences, St. Petersburg, Russia

V. V. Eliseev
Peter the Great St. Petersburg Polytechnic University, St. Petersburg, Russia

H. Irschik · E. A. Oborin (✉)
Johannes Kepler University, Linz, Austria
e-mail: evgenii.oborin@jku.at

V. P. Matveenko et al. (eds.), *Dynamics and Control of Advanced Structures and Machines*, https://doi.org/10.1007/978-3-319-90884-7_3

1 Introduction

Friction belt drives were studied extensively as they are interesting from a mechanical perspective. Until recently, one-dimensional models of extensible strings were widely used [13, 15]. However it turned out that the string model captures just a part of important effects in belt mechanics. Friction forces transmit power between the belt and the pulley. They are applied on the belt from one side and result not only in tangent forces, but also in distributed moments. The model without bending stiffness cannot describe the effects related to the moment loading. For this reason we apply the rod model accounting for the bending stiffness. In contact problems of the rod theory, the account of shear is known to be of crucial importance, cf. [2, 8]. The introduction of shear deformation causes the absence of lumped contact forces and promotes better understanding of the contact force distribution [4, 5]. Shear is also required to describe the effect of elastic microslip [3].

The goal of this study is to present a rational model of the belt as a rod with bending, extension, and shear in the steady dynamic problem, see the results of other authors on rod steady dynamics in [9, 11] which are obtained without account for shear.

2 Basic Equations

We consider the motion of a drive belt on two pulleys rotating with the angular velocities Ω_1, Ω_2 (see Fig. 1). κ_1^{-1}, κ_2^{-1} are the pulley radii; they are inverse to curvature. In the initial undeformed state the belt is a circle of radius κ_0^{-1}. Before

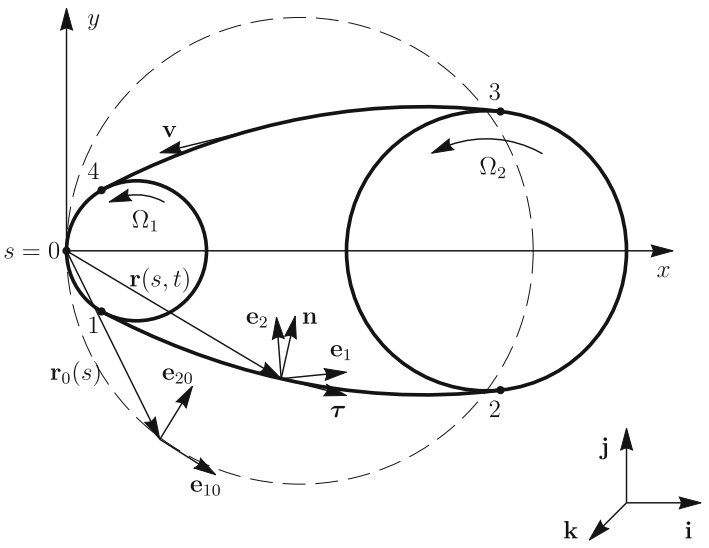

Fig. 1 Belt on pulleys

fitting the belt on the pulleys $\Delta_0 = 2\kappa_0^{-1} - \kappa_1^{-1} - \kappa_2^{-1}$ is the center distance—the pulleys are just tangent to the belt. Then the distance increases up to the value $\Delta > \Delta_0$, and the belt deforms and extends forming the contact segments on the pulleys; the stress state with forces and bending moments in the belt and the contact pressure on the pulleys arises [4, 5].

It is reasonable to formulate the corresponding model of nonlinear elastic rod as Cosserat material line [1, 7]. We introduce the material coordinate $0 < s < 2\pi/\kappa_0$ in the rod; it is the arc coordinate of the belt axis in the initial state (see Fig. 1). The position vector of a rod particle is a function of coordinate and time $\mathbf{r}(s, t)$. In the initial state

$$\mathbf{r}_0(s) = \kappa_0^{-1}\left[\mathbf{i}(1 - \cos\kappa_0 s) - \mathbf{j}\sin\kappa_0 s\right],$$

where $\mathbf{i}, \mathbf{j}$ are the unit vectors of Cartesian axes x, y (zero refers to the values in the initial state). We differentiate and obtain the tangent and normal unit vectors

$$\mathbf{r}_0' = \mathbf{i}\sin\kappa_0 s - \mathbf{j}\cos\kappa_0 s = \boldsymbol{\tau}_0 = \mathbf{e}_{10}, \quad \kappa_0^{-1}\boldsymbol{\tau}_0' = \mathbf{i}\cos\kappa_0 s + \mathbf{j}\sin\kappa_0 s = \mathbf{n}_0 = \mathbf{e}_{20}. \tag{1}$$

Particles of the Cosserat line are elementary bodies with translational and rotational degrees of freedom. Therefore we associate the directors $\mathbf{e}_1$, $\mathbf{e}_2$ with every particle, see Fig. 1. Their coincidence with the tangent and normal (as in (1)) disappears after the deformation—it is a consequence of transversal shear. The angles $\varphi(s)$, $\varphi_0(s)$ between the unit vectors $\mathbf{e}_1$, $\mathbf{e}_{10}$ and x-axis are important; their difference θ is rather more important, determines the particle rotation

$$\begin{aligned} &\mathbf{e}_1 = \mathbf{i}\cos\varphi + \mathbf{j}\sin\varphi, \quad \mathbf{e}_2 = \mathbf{k}\times\mathbf{e}_1 = -\mathbf{i}\sin\varphi + \mathbf{j}\cos\varphi; \\ &\varphi_0(s) = \kappa_0 s - \pi/2; \quad \theta(s) = \varphi - \varphi_0. \end{aligned} \tag{2}$$

The system of equations [7] of nonlinear elastic rods deforming in plane is

$$\mathbf{Q}' + \mathbf{q} = \rho\ddot{\mathbf{r}}, \quad M' + \mathbf{k}\cdot\mathbf{r}'\times\mathbf{Q} + m = 0, \quad \theta' = AM, \quad \mathbf{r}' = \mathbf{e}_1 + \mathbf{B}\cdot\mathbf{Q}. \tag{3}$$

Here $\mathbf{q}$, m are the force and moment loads distributed per unit length, ρ is the mass density per unit length, A is the bending compliance, $\mathbf{B}$ is the compliance tensor of tension and shear. Usually

$$\mathbf{B} = B_1\mathbf{e}_1\mathbf{e}_1 + B_2\mathbf{e}_2\mathbf{e}_2 \Rightarrow \mathbf{r}' = (1 + B_1 Q_1)\mathbf{e}_1 + B_2 Q_2\mathbf{e}_2. \tag{4}$$

We have two contact segments and two free spans in the belt (see the similar approach in [6]). In the free spans $\mathbf{q} = 0$, $m = 0$. In the contact segments $\mathbf{q} = -p\mathbf{n} + f\boldsymbol{\tau}$, $m = -hf/2$, where $p \geq 0$ is the contact pressure, f is the friction force, h is the belt thickness. For the driver pulley (with the angular velocity Ω_1)

there is $f > 0$ and for the driven pulley (Ω_2) $f < 0$. According to the Coulomb law we have $|f| \le \mu p$ where μ is the friction coefficient; after exceeding the boundary of this inequality the slip begins.

The point about the character of contact is of importance: is it point-wise contact or distributed. In works [4, 5] based on the exact equations of the nonlinear theory of elastic rods, it is stated that the contact is distributed.

In the present paper we consider the simplest motion of the belt, which is the contour motion [15]. It means that the spatial configuration does not change in appearance in the course of time, the belt flows along the fixed closed curve with the position vector $\mathbf{R}(\sigma)$. We take the new coordinate $\sigma \in [0, L]$ to be the arc coordinate on this curve. The boundaries of the contact segments correspond to the values $\sigma_1, \ldots, \sigma_4$, see Fig. 1; they are unknown and are subject to the determination (in contrast to the string model, they are not determined by the position of the circles tangents). The new length of belt L is also unknown. The contour motion law reads

$$\sigma = \sigma(s, t) \Leftrightarrow s = S(\sigma, t). \tag{5}$$

The inverse function S is constructed for every fixed time instance.

For the velocity and acceleration we have the well-known formulae of kinematics

$$\mathbf{v} = \dot{\mathbf{r}}(s, t) = \mathbf{R}'(\sigma)\dot{\sigma} = v\boldsymbol{\tau}, \quad \mathbf{w} = \dot{v}\boldsymbol{\tau} + \kappa v^2\mathbf{n}. \tag{6}$$

We use the formulae of differential geometry: $\mathbf{R}'(\sigma) = \boldsymbol{\tau}$, $\boldsymbol{\tau}'(\sigma) = \kappa\mathbf{n}$, where κ is the trajectory curvature. In (6) the velocity of the belt motion $v = \dot{\sigma} = \partial_t\sigma(s, t)$ appears (with the reduced notation of the partial derivative).

Below we will use also the value $D = |\mathbf{r}'| = \partial_s\sigma(s, t)$. From the equality of mixed derivatives the following is valid:

$$\partial_t D = \partial_s v. \tag{7}$$

3 Eulerian Description of Motion

Thus far we have mostly used the Lagrangian description of motion [7]. However for the contour motion the spatial (Eulerian) description is more advantageous; it has the arguments σ and t. Transition from one description to another is based on (5):

$$\begin{aligned} &u(s, t) = u(S(\sigma, t), t) \equiv \tilde{u}(\sigma, t) = \tilde{u}(\sigma(s, t), t), \\ &\partial_s u = D\partial_\sigma\tilde{u}, \quad D \equiv \partial_s\sigma = |\mathbf{r}'|, \quad \partial_t u \equiv u^\bullet = \partial_t\tilde{u} + v\partial_\sigma\tilde{u}. \end{aligned} \tag{8}$$

We introduce the material time derivative here (a bullet point in the superscript denotes it). Then in formula (6) for the tangential acceleration we have

$$w_\tau = v^\bullet = \partial_t v + v v' = \partial_t v + \partial_\sigma (v^2/2). \tag{9}$$

Besides the linear velocity v, the angular velocity ω appears in the equations

$$\omega = \theta^\bullet = (\partial_t + v\partial_\sigma)\tilde{\theta}(\sigma, t). \tag{10}$$

Because the model with shear is considered, the linear and angular velocities are independent.

We make an additional simplifying assumption: the contour motion is stationary in the same sense as in the fluid mechanics [10]: $\mathbf{v}(\sigma, t) = \mathbf{v}(\sigma)$, etc. The full list of values depending only on σ is: $\mathbf{R}$, $\mathbf{v}$, $\mathbf{Q}$, M, ω, φ, $\mathbf{B}$, $\boldsymbol{\tau}$, $\mathbf{n}$, $\mathbf{e}_1$, $\mathbf{e}_2$, $\mathbf{w}$. In particular, the values $\mathbf{r}$, θ, $\mathbf{r}_0$, φ_0, $\mathbf{e}_{10}$ are absent in this list. This brings up the question about the bending deformation and the elasticity relation which can be written as follows:

$$\theta'(s, t) = \varphi'(s, t) - \varphi_0'(s) = D\partial_\sigma \varphi - \kappa_0 = AM. \tag{11}$$

By now we have the system of ordinary differential equations (ODE) of stationary motion of the nonlinear elastic belt. Let us write it denoting the derivative with respect to σ by prime:

$$\begin{aligned} &D\mathbf{Q}' + \mathbf{q} = \rho\mathbf{w}, \quad D(M' + \mathbf{n}\cdot\mathbf{Q}) + m = 0, \quad D \equiv \sqrt{(1 + B_1 Q_1)^2 + (B_2 Q_2)^2}, \\ &D\varphi' - \kappa_0 = AM, \quad \mathbf{R}' = \boldsymbol{\tau} = D^{-1}\left[(1 + B_1 Q_1)\mathbf{e}_1 + B_2 Q_2 \mathbf{e}_2\right]. \end{aligned} \tag{12}$$

However the system (12) is not full; the equations for v, ω are missing. We deduce the equations from (7) and (10):

$$vD' = Dv' \Rightarrow v = cD, \quad c = \text{const}; \quad \omega = v\varphi' = c(AM + \kappa_0). \tag{13}$$

We use the first equation in the second one.

The system (12), (13) consists of six ODE for the unknowns Q_1, Q_2, M, φ, x, y—as the system in the "usual" nonlinear theory of rods deforming in plane [4, 5, 8]. In the free spans (see Fig. 1) the distributed load is absent, and on the pulleys it is the unknown normal pressure and friction force.

4 Contact Segment

For the case without slip, i.e., when $|f| \le \mu p$, we assume

$$v = \Omega_1 \kappa_1^{-1} + \omega h/2 \tag{14}$$

(for the left contact segment). When the limiting friction is achieved at a certain segment of belt, the tangent load becomes proportional to the normal one, as the distributed moment does. Then we need to obtain the solution again accounting for these circumstances—an iteration process is probably required. The curvature radius of the belt line is $\tilde{\kappa}^{-1} = \kappa^{-1} + h/2$. The belt coinciding with the pulley circle has the position and tangent vectors as follows:

$$\mathbf{R} = \tilde{\kappa}_1^{-1}\left[\mathbf{i}\,(1-\cos\tilde{\kappa}_1\sigma) - \mathbf{j}\sin\tilde{\kappa}_1\sigma\right], \quad \mathbf{R}' = \mathbf{i}\sin\tilde{\kappa}_1\sigma - \mathbf{j}\cos\tilde{\kappa}_1\sigma. \tag{15}$$

We note that different assumptions may be used for the present contact model.

Using the formulae (15) and elasticity relations (12), we write the projections of the tangent unit vector into the directions of unit vectors $\mathbf{e}_1$ and $\mathbf{e}_2$:

$$\mathbf{R}'\cdot\mathbf{e}_1 = (1+B_1Q_1)/D = -\sin\alpha,\ \mathbf{R}'\cdot\mathbf{e}_2 = B_2Q_2/D = -\cos\alpha,\ \alpha \equiv \varphi - \tilde{\kappa}_1\sigma. \tag{16}$$

Then similarly to the static considerations [4, 5] we may express the force component Q_2 as a function of coordinate σ, angle φ and force component Q_1 in the form:

$$Q_2 = B_2^{-1}\,(1+B_1Q_1)\cot\alpha. \tag{17}$$

For the second contact segment we express the transverse force in the same way:

$$Q_2 = B_2^{-1}\,(1+B_1Q_1)\cot\left[\varphi - \tilde{\kappa}_2\left(\sigma - \tilde{L}\right)\right]. \tag{18}$$

Here $\tilde{L}$ is the arc coordinate of the belt point lying at the rightmost point of the second pulley. In the following we focus on the first contact segment; however, in the second one the analogous equations are valid. From Eqs. (13) and (14) we obtain

$$M = -\frac{\kappa_0}{A} + \frac{2}{Ah}D - \frac{2\Omega_1}{Ah\kappa_1}c^{-1}. \tag{19}$$

This can be used to determine the friction force from the balance of moments (12)

$$f = \frac{2}{h}D(M' + Q_n) = \frac{4}{h^2A}DD' + \frac{2}{h}DQ_n. \tag{20}$$

Also we need the equation for φ' derived from (12) with the use of (19)

$$\varphi' = \frac{2}{h}\left(1 - \frac{\Omega_1}{\kappa_1}\frac{1}{cD}\right). \tag{21}$$

In the balance equations of contact segments we express Q_1, Q_2 in terms of the tangent Q_τ and normal Q_n components:

$$Q_1 = -Q_\tau \sin\alpha + Q_n \cos\alpha, \quad Q_2 = -Q_\tau \cos\alpha - Q_n \sin\alpha. \tag{22}$$

Then we rewrite Eq. (17) and Equation for D in (12)

$$Q_n = \frac{(B_1 - B_2)Q_\tau \sin 2\alpha/2 - \cos\alpha}{(1+\cos 2\alpha)(B_1 - B_2)/2 + B_2}, \quad D = -\frac{1}{\sin\alpha} - B_1 Q_\tau + B_1 Q_n \cot\alpha. \tag{23}$$

The acceleration components are

$$w_\tau = \left(\frac{v^2}{2}\right)' = \frac{c^2}{2}\left(D^2\right)' = c^2 D D'; \quad w_n = \tilde{\kappa}_1 v^2 = \tilde{\kappa}_1 c^2 D^2. \tag{24}$$

Now we write the balance of forces (12) with the use of (20) as follows:

$$Q'_\tau = \left(\tilde{\kappa}_1 - \frac{2}{h}\right) Q_n + \left(\rho c^2 - \frac{4}{h^2 A}\right) D', \quad Q'_n = -\tilde{\kappa}_1 Q_\tau + D^{-1} p + \rho \tilde{\kappa}_1 c^2 D, \tag{25}$$

where we need the derivative D'. Now we may transform the first equation of (25) into the normal form which is not stated here, because it is lengthy. Finally from the second equation of (25) we determine the contact pressure

$$p = D Q'_n + \tilde{\kappa}_1 D Q_\tau - \rho \tilde{\kappa}_1 c^2 D^2. \tag{26}$$

So, in the contact zone we have two unknown functions φ and Q_τ and one constant c determining all the remaining variables.

5 Free Span

The expression for curvature κ is cumbersome and includes the derivatives of the unknown functions under the square root. Therefore it is advisable to exclude the curvature from the system of equations. To do this we use the derivative of the tangent vector $\boldsymbol{\tau}'$ and write the acceleration vector in the form $\mathbf{w} = w_\tau \boldsymbol{\tau} + w_n \mathbf{n} = w_\tau \boldsymbol{\tau} + w_n^* \boldsymbol{\tau}'$. Exploiting the stationarity, we account for (9) and (13) and determine the acceleration components

$$w_\tau = \frac{c^2}{2}\left(D^2\right)' = c^2 \left(1 + B_1 Q_1\right) B_1 {Q_1}' + c^2 B_2^2 Q_2 {Q_2}', \quad w_n^* = v^2 = c^2 D^2. \tag{27}$$

Now we rewrite the balance equations without distributed loads and the remaining equations of system (12):

$$
\begin{aligned}
Q_1{}' &= \frac{(1-\rho c^2 B_2 D)\,Q_2\,(\kappa_0 + AM)}{D\left(1-\rho c^2 B_1 D\right)},\\
Q_2{}' &= \frac{[\rho c^2 D(1+B_1 Q_1) - Q_1](\kappa_0 + AM)}{D\left(1-\rho c^2 B_2 D\right)},\\
M' &= [(B_2 - B_1)\,Q_1 - 1]\,Q_2/D, \quad x' = [(1+B_1 Q_1)\cos\varphi - B_2 Q_2 \sin\varphi]\,/D,\\
\varphi' &= (\kappa_0 + AM)\,/D, \qquad\qquad y' = [(1+B_1 Q_1)\sin\varphi + B_2 Q_2 \cos\varphi]\,/D.
\end{aligned}
\tag{28}
$$

Now we subdivide the belt into four segments, $\sigma_4 - L \le \sigma \le \sigma_1$, $\sigma_1 \le \sigma \le \sigma_2$, $\sigma_2 \le \sigma \le \sigma_3$, and $\sigma_3 \le \sigma \le \sigma_4$. For convenience, we eventually will introduce the new nondimensional coordinate $0 \le \xi \le 1$ similarly to the previous works [4, 5, 8]. The main advantage of this transformation is dealing with the boundary value problem (BVP) with known boundaries. As a result we have 16 functions: Q_τ and φ in the contact segments; Q_1, Q_2, M, φ, x, and y in the free segments and eight constants: c from (13); four boundary arc coordinates $\sigma_1, \ldots, \sigma_4$, $\tilde{L}$, actual belt length L, and center distance Δ. The boundary conditions are the conditions of continuity in force, moment, position vector, and angle at the segment ends; altogether there are 24 conditions in components. The formulated BVP can be numerically solved, e. g. by the collocation method of Chebfun package in Matlab.

6 Conclusion

The main results of the present research are listed below:

- the drive belt is modelled as a plane nonlinear elastic rod with account for bending, tension, and shear; its steady motion is generalized to the case of friction contact;
- the spatial (Eulerian) description of motion is introduced;
- the belt is divided into four segments, two contact and two free segments; the equations for these segments are combined in a single ODE system;
- the formulated BVP is written down in the form appropriate for numerical analysis;
- the simulation results will be further used to substantiate the FEM solutions, presented in [12, 14].

Acknowledgements This research is carried out in the framework of joint project of the Russian Foundation for Basic Research (Grant No. 14–51–15001) and the Austrian Science Fund (FWF, Grant No. I 2093 International Project).

References

1. Antman, S.S.: Nonlinear Problems of Elasticity. Springer, New York (2005)
2. Antman, S.S., Schuricht, F.: The critical role of the base curve for the qualitative behavior of shearable rods. Math. Mech. Solids **8**(1), 75–102 (2003)
3. Belyaev, A.K., Eliseev, V.V., Oborin, E.A.: About one-dimensional models for describing elastic microslip in belt drive. Int. Rev. Mech. Eng. **10**(5), 333–338 (2016)
4. Belyaev, A.K., Eliseev, V.V., Irschik, H., Oborin, E.A.: Contact of two equal rigid pulleys with a belt modelled as Cosserat nonlinear elastic rod. Acta Mech. **228**(12), 4425–4434 (2017)
5. Belyaev, A.K., Eliseev, V.V., Irschik, H., Oborin, E.A.: Static contact of belt and pulleys with account for shear and gravity. J. Phys. Conf. Ser. **1048**(1), 012002 (2018). https://doi.org/10.1088/1742-6596/1048/1/012002
6. Denoël, V., Detournay, E.: Eulerian formulation of constrained elastica. Int. J. Solids Struct. **48**(3–4), 625–636 (2016)
7. Eliseev, V.V.: Mechanics of Deformable Solid Bodies. St. Petersburg Polytechnic University, St. Petersburg (2006)
8. Eliseev, V.V., Zinovieva, T.V.: Nonlinear-elastic strain of underwater pipeline in laying process. Comput. Contin. Mech. **5**(1), 70–78 (2012)
9. Kong, L., Parker, R.G.: Steady mechanics of belt-pulley systems. J. Appl. Mech. **72**(1), 25–34 (2005)
10. Loitsianskii, L.G.: Mechanics of Liquids and Gases. Begell House, Danbury (1995)
11. Nordenholz, T.R., O'Reilly, O.M.: On steady motions of an elastic rod with application to contact problems. Int. J. Solids Struct. **34**(9), 1123–1143 (1997)
12. Oborin, E., Vetyukov, Y., Steinbrecher, I.: Eulerian description of non-stationary motion of an idealized belt-pulley system with dry friction. Int. J. Solids Struct. **147**, 40–51 (2018). https://doi.org/10.1016/j.ijsolstr.2018.04.007
13. Rubin, M.B.: An exact solution for steady motion of an extensible belt in multipulley belt drive systems. J. Mech. Des. **122**(3), 311–316 (2000)
14. Vetyukov, Y.: Non-material finite element modelling of large vibrations of axially moving strings and beams. J. Sound Vib. **414**, 299–317 (2018)
15. Vetyukov, Y.M., Oborin, E.A., Krommer, M., Eliseev, V.V.: Transient modelling of flexible belt drive dynamics using the equations of a deformable string with discontinuities. Math. Comput. Model. Dyn. Syst. **23**(1), 40–54 (2017)

On the Method of Low-Frequency Monitoring of the Initial Stress State of a Body

T. I. Belyankova, O. V. Bocharova, A. V. Sedov, and V. V. Kalinchuk

Abstract A method for low-frequency control of the stress state of structures is proposed, based on an analysis of the parameters of the surface wave field created by the impact. To process the recorded signal, a special method is used, based on the use of optimal orthogonal decompositions of the signal in the base, adaptively tuned to the training sample. A series of computational experiments on simulation of dynamic processes in a prestressed medium was carried out. Studies have shown a high degree of informativeness of the method to various types of initial stress state in the medium and also a high sensitivity to a change in the value of the initial deformation.

1 Introduction

The development of methods for monitoring the structure and stress of composite structures is one of the key problems in the mechanics of solids. A considerable number of publications are devoted to the study of the influence of initial stresses on the processes of wave propagation in an elastic medium [1–3]. In particular, the regularities of the influence of the initial deformation on the velocity of various types of waves are revealed. An equally large number of papers are devoted to the investigation of wave processes on the surface of prestressed media [4–6]. The effect of the initial deformation on the velocity of the Rayleigh waves [7, 8], SH waves [9], or Love waves [10] was studied. Studies have shown that this influence is linear. An alternative to these studies is the method of initial stress control proposed

T. I. Belyankova · V. V. Kalinchuk (✉)
Southern Scientific Center of Russian Academy of Sciences and Southern Federal University, Rostov-on-Don, Russia
e-mail: kalin@ssc-ras.ru

O. V. Bocharova · A. V. Sedov
Southern Scientific Center of Russian Academy of Sciences, Rostov-on-Don, Russia

V. P. Matveenko et al. (eds.), *Dynamics and Control of Advanced Structures and Machines*, https://doi.org/10.1007/978-3-319-90884-7_4

in [11–16]. It is based on recording the change in the resonance properties of the system sensor-layered heterogeneous medium. The advantage of this approach is its integral nature due to the use of low-frequency oscillations. This allows to significantly increase the area monitoring by one sensor and opens the prospect of creating continuous monitoring systems—remote monitoring of the state of constructions and assemblies made of layered composite materials.

2 Resonance Method of Stress Control

The resonant method of stress state control [16] is based on recording the change in the resonance properties of the system "sensor-layered heterogeneous medium." The process of interaction of a massive stamp with a medium is described by the equation of motion of a massive body interacting with an elastic medium

$$w = F\left[Q(\kappa) - m\kappa^2\right]^{-1} \tag{1}$$

Here $Q(\kappa)$ is the dynamic rigidity of the medium, m is the mass of the die, κ is the dimensionless frequency ($\kappa = \omega h V_S^{-1}$, ω is the oscillation frequency, h is the characteristic linear dimension, and V_S is the shear wave velocity). The idea of the method is based on the properties of the function $Q(\kappa)$—the dynamic rigidity of the medium, which is a reaction to the vibrations of a stamp with a given amplitude. Any change in the properties of the medium inevitably leads to a change in the dynamic rigidity and as a consequence, which follows from (1), to a change in the amplitude of the oscillations of a massive body.

If you adjust the mode of oscillation of the body to resonant, then the change in the reaction of the medium will lead to a change in the resonance frequency. As an example in [16] the case of vibrations of a massive body on the surface of a composite medium, which is a layer $0 \le x_3 \le h$ lying on the surface of a half-space $x_3 \le 0$, was investigated. The system performs translational vertical vibrations under the action of force F, applied to the body m. The oscillations are assumed to be steady; friction in the contact region is absent.

Next the following types of initial deformed state are considered: a prestressed layer on a non-stressed half-space (the layer is first stretched or compressed, and then connected to a half-space); an unstressed layer on the prestressed half-space (the half-space is first prestressed, then connected to the layer). As before, the initial deformed state in a layer or half-space can be uniaxial, biaxial, or triaxial. The effect of localization of the initial stressed state on the dynamics of a massive stamp is illustrated by the graphs in Fig. 1 (the prestressed layer, the half-space is free of initial stresses) and Fig. 2 (the half-space is prestressed, the layer is in the natural

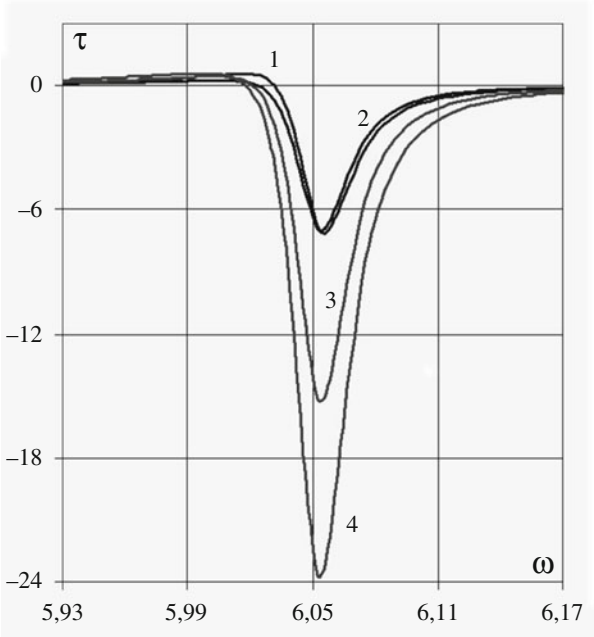

Fig. 1 Influence of various types of initial deformation on the resonance properties of the system "massive die—prestressed two-layer medium." The layer is prestressed

state). The digits 1, 2, and 3 indicate the curves τ calculated for the uniaxial stress state along the axes x_1, x_2, and x_3, respectively, 4—the curve calculated with the triaxial stress state. It is not difficult to see that the maximum influence on the dynamics of a massive body is exerted by a triaxial stress state localized both in the layer and in the half-space. At the same time, there is a sharp difference between the manifestations of prestress in the layer and in the half-space. When the initial stresses localized in the layer (Fig. 1), it has a major influence on the amplitude of the resonance. The resonance frequency does not change—the curves for various initial stresses are embedded to each other. When the initial stresses localized in a half-space (Fig. 2), it has a major influence on the resonance frequency. Curves τ are shifted relative to each other. Each type of initial stresses is characterized by the frequencies of maximum influence and the frequency at which the influence of initial stresses on the amplitude of oscillations of a massive body is absent. This shows the peculiarity of the half-space, which consists in the presence of a maximum and minimum influence in the half-space for each initial state of stress, and the absence of such frequencies near the layer.

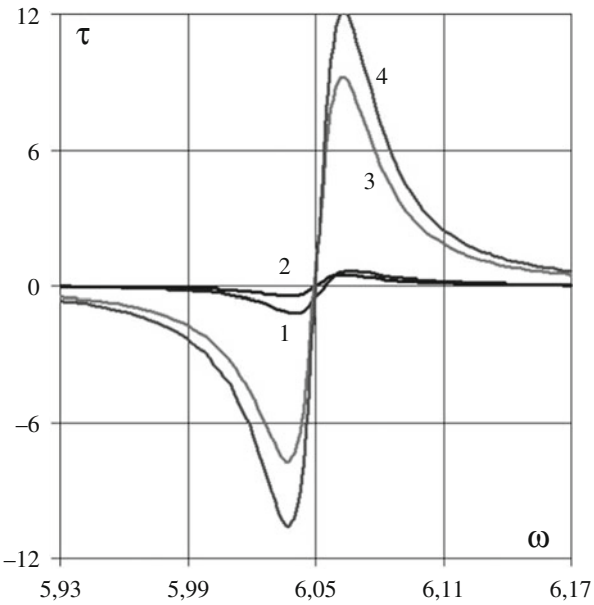

Fig. 2 Influence of various types of initial deformation on the resonance properties of the system "massive die—prestressed two-layer medium." The half-space is prestressed

3 Bispectral Method of Stress Control

Another method that allows controlling the stress state of the medium is a method based on a special treatment of the surface wave field. Figure 3 shows the difference graphs of the displacement amplitudes of the surface point with an initial tension of 0.5×10^{-3} and 1.5×10^{-3} with respect to the initial compression of 1.5×10^{-3}. The question is how to process the signal to get useful information about the stress state. The use of the spectral method, correlation, autocorrelation, and cross correlation did not allow to significantly increase the information content of the signal. In this paper, we propose a bispectral method of signal processing [17].

Next, the results of a numerical experiment on the calculation of the wave-field parameters for different values of the initial stressed state are presented. The following values were used as design values: uniaxial initial stress along the x_1 axis: tensile strength of 0.5×10^{-3}, 1.0×10^{-3}, 1.5×10^{-3}; compression strength of 0.5×10^{-3}, 1.0×10^{-3}, 1.5×10^{-3}. Each graph $f_i(t)$ can be considered as a column-vector of real values $f_i = [f_{i1}, f_{i2}, f_{i3}, \ldots, f_{iN}]^T \in \mathbf{R}^N$ of response change in time. Discretization step Δt in time is selected in accordance with the discretization theorem [17]. Let n be the number of recognizable variations of the defect in the construction. To each of the variations we associate a column-vector $f_i \in \mathbf{R}^N$. Then the test sample for n variations of the defect will be a matrix $f_i = \{f_1, f_2, f_3, \ldots, f_n\} \in \mathbf{R}^{N \times n}$. Initially, a set of vectors $f_i = \{f_1, f_2, f_3, \ldots, f_n\}$ is linearly dependent. This is due to the excessive dimensionality of the vectors $f_i \in \mathbf{R}^N$, precision of the graph forms $f_i(t)$. Base of recognition is the finding of an orthogonal transformation $\Xi \in \mathbf{R}^{N \times m}$ of matrix $\mathbf{f} \in \mathbf{R}^{n \times N}$ into matrix $\mathbf{A} \in \mathbf{R}^{n \times m}$

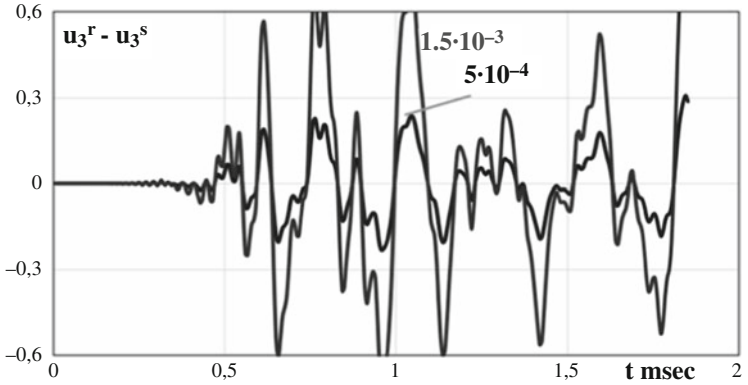

Fig. 3 Amplitude difference of the surface point oscillations under uniaxial initial tension 0.5×10^{-3} and 1.5×10^{-3} multiplied by 10^{12} m relatively to the compression of 1.5×10^{-3}

of the following form $\mathbf{A} = \mathbf{f}\Xi$. The matrix $\Xi = [\xi_1, \xi_2, \xi_3, \ldots, \xi_m]$ defines a linear subspace in $\mathbf{R}^N$, for which it is true that the set of possible linear combinations of the vectors is also a linear space or linear span:

$$\text{span}\,\{\xi_1, \xi_2, \xi_3, \ldots, \xi_m\} = \left\{ \sum_{j=1}^{m} \beta_j \xi_j : \beta_j \in \mathbf{R} \right\} \tag{2}$$

At the same time vectors $\xi_1, \xi_2, \xi_3, \ldots, \xi_m$ form an orthonormal basis in $\mathbf{R}^N$ and for the matrix Ξ, it is true that $\Xi^T \Xi = I_m$. Conventionally, the matrix Ξ can be considered as a matrix of orthogonal compression of linear space $\mathbf{R}^N$ into the space $\mathbf{R}^m$. Vectors $f_i \in \mathbf{R}^N$ of responses are transformed into images $A_i \in \mathbf{R}^m$, using Ξ. In this case the investigated matrix of responses $\mathbf{f}$ transformed into the matrix of images $\mathbf{A} = [A_1, A_2, A_3, \ldots, A_n]^T \in \mathbf{R}^{n \times m}$. In general, the orthogonal decomposition of the original vectors $f_i \in \mathbf{R}^N$ in the basis Ξ can be represented as $f_i = \Xi A_i + A_0$, where A_0 is constant component of the transformation.

The orthonormal basis $\xi_1, \xi_2, \xi_3, \ldots, \xi_m$ is adaptively adjustable and dependent on recognizable sample $f_i = \{f_1, f_2, f_3, \ldots, f_n\} \in \mathbf{R}^{N \times n}$.

When determining the basis, a complex of optimization problems is solved:

1. best reproducibility: $\|\mathbf{f} - \mathrm{A}\Xi^T - \mathrm{A}_0\|_2 \to \min$, where $\mathbf{A_0} \in \mathbf{R}^{n \times N}$ is the matrix of constant transform components, composed of the vectors A_0;
2. orthonormality of the basis: $\|\Xi^T \Xi - I_m\|_2 \to \min$;
3. best distinguishability: $d^2(\mathbf{A}) = \frac{1}{m^2 - m} \sum_{i,j=1, i \neq j}^{m} \|A_i - A_j\|_2 \to \max$.

For the sake of simplicity of physical interpretation, we realized the representation of the images of the initial deformation by images in the two-dimensional feature space. As the two coordinates of the image, we choose those that have the maximum spread spectral sign 1 and spectral sign 2. As the study showed, this size

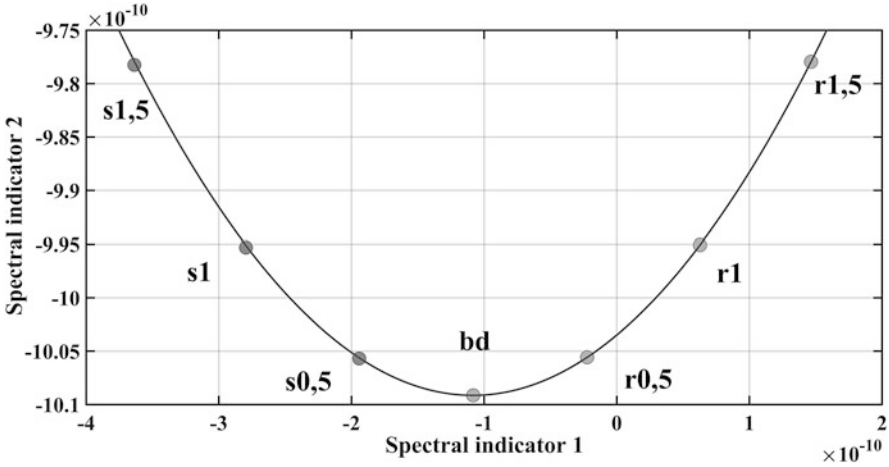

Fig. 4 The results of signal processing for compression and extension along the x_1 axis by the bispectral method

of the spatial space is sufficient to conduct a qualitative diagnosis of the initial stress state of the body.

Figure 4 shows the results of constructing a specific diagnostic space and image arrangement for different values of the uniaxial initial deformation along the x_1 axis. The images are represented in the form of points, the coordinates of which represented in the form of points, the coordinates of which are the coefficients for the expansion of the vectors in the chosen basis. The point bd corresponds to the natural state, the points $r0.5$, $r1.0$, $r1.5$ correspond to the initial stretching values of 0.5×10^{-3}, 1.0×10^{-3}, 1.5×10^{-3}. The points $s0.5$, $s1.0$, $s1.5$ correspond to the initial compression values of 0.5×10^{-3}, 1.0×10^{-3}, 1.5×10^{-3}. It can be noted that the proposed method makes it possible to effectively identify the initial deformed state both in magnitude of strain and in sign (tension or compression). The peculiarity of the result is that the points corresponding to different deformations are located on one parabola.

In Fig. 5 the results of the study of a uniaxial stress state are supplemented by the results of a biaxial stress state along the x_2 and x_3 axes, which provide a given initial deformation along the x1 axis. The points $rr0.5$, $rr1.0$, $rr1.5$ correspond to the initial tension values of 0.5×10^{-3}, 1.0×10^{-3}, 1.5×10^{-3}. The points $ss0.5$, $ss1.0$, $ss1.5$ correspond to the initial compression values of 0.5×10^{-3}, 1.0×10^{-3}, 1.5×10^{-3}. They are also located on a parabola, but the values of the spectral features changed sign and decreased in modulus. Figure 6 illustrates the sensitivity of this approach. It presents images corresponding to different values of uniaxial tension or compression along the x_1 axis with a deformation reduced by a factor of 10.

As follows from the graphs, the proposed method makes it possible to identify different types of initial stress state.

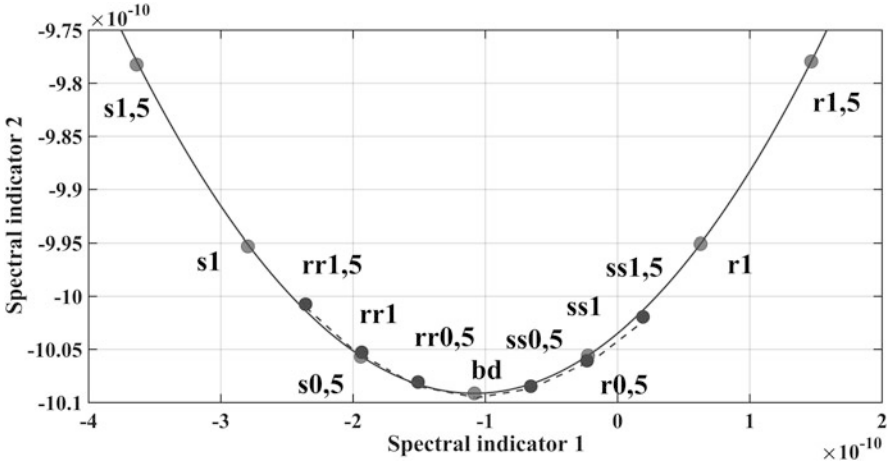

Fig. 5 The results of signal processing for compression and extension along the x_1 axis by the bispectral method. Uniaxial deformation (s, r), biaxial deformation (ss, rr)

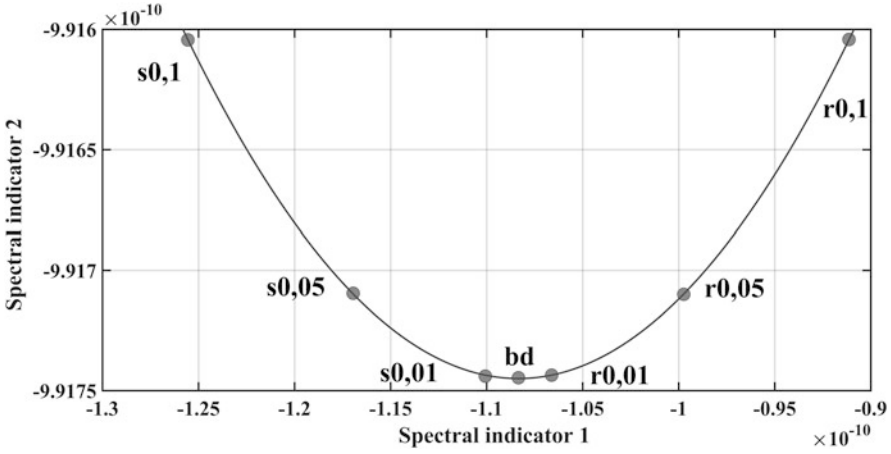

Fig. 6 The results of signal processing for compression and extension along the x_1 axis by the bispectral method. The deformation is reduced by a factor of 10

4 Conclusions

A method for processing signals in problems of controlling the initial stress state is proposed using the response function on the sample surface on the basis of the user adaptive orthonormal basis.

The use of the proposed method provides a clear recognition of the type of the initial stress state and the magnitude of the initial deformation in the diagnostic image space. The method may be of interest for solving the problem of monitoring the stress state of structures.

Acknowledgements This study was supported by the Russian Science Foundation (grant number 14-19-01676).

References

1. Green, J.E.: A note on wave propagation in prestressed elastic solids. J. Mech. Phys. Solids **11**(2), 119–126 (1963)
2. Guz, A.N.: Elastic waves in bodies with initial (residual) stresses. Int. Appl. Mech. **38**(1), 23–59 (2002)
3. Shams, M., Destrade, M., Ogden, R.W.: Initial stresses in elastic solids: constitutive laws and acoustoelasticity. Wave Motion **48**, 552–567 (2011)
4. Hayes, M., Rivlin, R.S.: Surface waves in deformed elastic materials. Arch. Ration. Mech. Anal. **8**(5), 358–380 (1961)
5. Chadwick, P., Jarvis, D.A.: Surface waves in prestressed elastic body. Proc. R. Soc. Lond. A **336**(1727), 517–536 (1979)
6. Nam, N.T., Merodio, J., Ogden, R.W., Vinh, P.C.: The effect of initial stress on the propagation of surface waves in a layered half-space. Int. J. Solids Struct. **88–89**, 88–100 (2016)
7. Iwashimizu, Y., Kobori, O.: The Rayleigh wave in a finitely deformed isotropic elastic material. J. Acoust. Soc. Am. **64**(3), 910–916 (1978)
8. Tanuma, K., Man, C.-S., Chen, Y.: Dispersion of Rayleigh waves in weakly anisotropic media with vertically-inhomogeneous initial stress. Int. J. Eng. Sci. **92**, 63–82 (2015)
9. Wagh, D.K.: Propagation of SH waves in an infinite elastic plate with Cauchy's initial transverse stress. Pure Appl. Geophys. **99**(7), 95–115 (1979)
10. Shams, M.: Effect of initial stress on Love wave propagation at the boundary between a layer and a half-space. Wave Motion **65**, 92–104 (2016)
11. Kalinchuk, V.V., Polyakova, I.B.: Vibration of a die on the surface of a prestressed half-space. Sov. Appl. Mech. **18**(6), 504–509 (1982)
12. Anan'ev, I.V., Kalinchuk, V.V., Poliakova, I.B.: On wave excitation by a vibrating stamp in a medium with inhomogeneous initial stresses. J. Appl. Math. Mech. **47**(3), 408–413 (1983)
13. Kalinchuk, V.V., Lysenko, I.V., Polyakova, I.B.: Singularities of the interaction of a vibrating stamp with an inhomogeneous heavy base. J. Appl. Math. Mech. **53**(2), 235–241 (1989)
14. Belyankova, T.I., Kalinchuk, V.V.: On the interaction between an oscillating die and a prestressed half-space. J. Appl. Math. Mech. **57**(4), 123–134 (1993)
15. Belyankova, T.I., Vorovich, I.I., Kalinchuk, V.V.: Low-frequency resonances in the dynamic interaction of an elastic solid with a semi-bounded medium. J. Appl. Math. Mech. **62**(5), 797–801 (1998)
16. Esipov, Y.V., Mukhortov, V.M., Kalinchuk, V.V.: Test equipment for analyzing the deformation of models of three-dimensional structures. Meas. Tech. **51**(10), 1104–1109 (2008)
17. Sedov, A.V.: Objects with Discrete-Distributed Parameters: A Decomposition Approach (in Russian). Nauka Publishing, Moscow (2010)

Mesomechanical Response of a Soft Magnetic Elastomer to AC Magnetization

A. M. Biller, O. V. Stolbov, and Yu. L. Raikher

Abstract The behavior of a pair of magnetizable spherical particles embedded in a viscoelastic elastomer is studied for the case, where an AC magnetic field is applied along the center-to-center line of the particles. This system is considered as a small-scale (mesoscopic) structure element of a magnetorheological elastomer. Under a quasistatic cycle of the field, the system in question is prone to hysteretic behavior. Namely, the particles initially positioned well apart, at some finite field strength, fall onto one another (cluster) and reside in this state until the field decreases well below the value at which the cluster has been formed. Under dynamic cycling of the field, the viscous friction interferes with the particle displacement process and impedes the occurrence of the magnetodeformational hysteresis of the element. Starting from small-amplitude overdamped oscillations and enhancing the role of magnetic forces over viscous ones, we show how the anharmonicity of the system grows while it approaches the transition threshold, above which the dynamics of the element includes the cluster state. The dynamic hysteresis of magnetization that accompanies the mechanical oscillations of the particles is presented as well.

1 Introduction

For quite a time now, smart materials whose properties can be adjusted to variable working conditions by external or "built-in" control mechanisms are a subject of nonfading interest. A vast majority of smart materials are composites. Uniting in one system the elements sensitive to different stimuli and, at the same time, interacting with each other is, indeed, a direct way to get an entity with a unique combination of properties. In this paper we address the dynamic behavior of the composites of that type known as *magnetorheological elastomers* (MREs), which are elastomer matrices filled with micron-sized magnetizable particles. Under the

A. M. Biller · O. V. Stolbov · Y. L. Raikher (✉)
Institute of Continuous Media Mechanics, Perm, Russia
e-mail: kam@icmm.ru; sov@icmm.ru; raikher@icmm.ru

V. P. Matveenko et al. (eds.), *Dynamics and Control of Advanced Structures and Machines*, https://doi.org/10.1007/978-3-319-90884-7_5

external magnetic field, the particles acquire magnetic moments of their own that makes them interact with the applied field and with each other via ponderomotive forces. Those interactions compel the particles to move at the mesoscopic (of the order of interparticle distance) scale, and, while doing that, the particles entrain the surrounding matrix. The occurring processes, on the one hand, modify the internal structure of a MRE and by that affect its material parameters, rheological ones, in particular. On the other hand, if those changes undergo coherently, (e.g., all the particles attract each other along the direction of the field) cause notable macroscopic deformations of a MRE sample or modify substantially its stress state.

The usage of MREs as essential working components in adaptive dampers, actuators, valves, medical appliances, etc. is an actively developing applicational trend. In such devices, the main exploited effect is the change of rheological characteristics and shape of MRE elements in response to the applied magnetic field or mechanical load in the real-time regime. Therefore, the dependence of the dynamic characteristics of MREs on the applied field and load is an important issue; this is demonstrated by a rather large number of published experimental works on this subject [1–3, 7, 9, 11–13].

2 Two-Particle Element

To understand the internal interactions, which govern the rearrangements of the inner structure of MREs', one should study them at the mesoscopic level, where the matrix and particles are considered separately and each entity is treated as a continuous medium with its own set of properties to which scope the hypotheses on the interaction between the phases are added. In line with this viewpoint, we have proposed a simple model comprising two magnetic particles embedded in an elastic matrix as a basic element of a MRE capable of illustrating the magnetomechanical response of the material [4, 5]. The model element consists of a cylindrical sample whose outer dimensions are chosen under the requirement that a pair of spherical particles occupies about 30% of its geometric volume, which is a typical concentration in MREs of applicational interest. The particles have identical radii a and are positioned symmetrically in such a way that their center-to-center vector $\mathbf{l}$ coincides with the cylinder axis. The latter is taken as the Oz axis of the cylindrical coordinate frame whose origin is placed at the center of the sample.

As well known, the most strong shape changes and magnetic effects are displayed by MREs based on soft polymer matrices with Young's moduli $E \sim$5–30 kPa; see [13], for example. The internal viscosity of those compounds is rather high: the range of experimentally estimated magnetic and stress relaxation times spans from tenths of seconds to a few seconds [10]. This time scale is inherent to MREs filled with microparticles (2–5 μm) of carbonyl iron, which have the initial magnetic susceptibility of the order of 10^4 and saturation magnetization of 1500 kA/m [8].

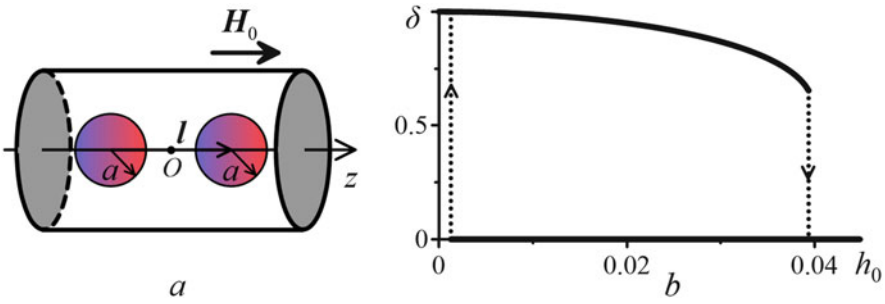

Fig. 1 (**a**) Model mesoscopic two-particle element of a MRE; (**b**) quasistatic magnetomechanical hysteresis loop for a pair of particles with center-to-center distance $q_0 = 3$ and $\beta = 2500$ for definitions of those parameters seen below

When the model element sketched in Fig. 1a is subjected to an external uniform magnetic field $\mathbf{H}_0 = (0, 0, H_0)$, the magnetic polarization of the particles induces their mutual attraction, striving to move them closer. However, as soon as the particles yield to this tendency, the deformed matrix generates restoring elastic forces, so that a new equilibrium state of the pair is defined by the balance of those opposing effects.

The magnetomechanical response of the above-described two-particle element under quasistatic conditions was studied in detail in Refs. [4, 5]. Note that in those works, nonuniform deformation of a nonlinearly elastic elastomer matrix and nonuniform and nonlinear magnetization of the particles were taken into account as well. It turned out that within a certain domain of material parameters of the particles and matrix, the system displays bistable behavior. Namely, when the MRE element is subjected to a quasistatic cycle of the magnetic field, the magnetomechanical hysteresis occurs: the trajectory $z(H)$ along which the particles moves when the field increases does not coincide with that undergone during the field decrease. This is demonstrated in Fig. 1b, where the downward arrow corresponds to the field of cluster formation, whereas the upward arrow corresponds to the field of the cluster breaking apart. In this work, for the sake of simplicity, we deal in the small-strain approximation and assume that the polymer obeys just the Hooke law. Because of that, here the parameter governing the effect is $\beta = 2\mu_0 M_s^2/G$, where μ_0 is the magnetic constant, M_s saturation magnetization of the ferromagnetic material, and G shear modulus. The comparison with [4, 5] shows that the adopted simplifications do not qualitatively change the field-induced behavior of the model. A quantitative difference, however, is that the quasistatic hysteresis loop in Fig. 1b is wider than for the case of a MRE with Mooney-Rivlin matrix.

To characterize the configuration of the two-particle element, we use nondimensional units, scaling all the distances with the particle radius a. Therefore, the current center-to-center distance of the pair and the relative change of the interparticle gap (the closest distance between the particle surfaces) are defined as

$$q = l/a \quad \text{and} \quad \delta = (q - 2)/(q_0 - 2), \tag{1}$$

respectively; here q_0 is the initial interparticle distance and $q = 2$ is the limiting value attained when the particles come into tight contact. As seen, the gap parameter δ varies from unity in the initial state of the element to zero when the particles collapse in a cluster.

The loop presented in Fig. 1b describes the element with initial center-to-center distance $q_0 = l_0/a = 3$ and magnetomechanical parameter $\beta = 2500$ that corresponds to a MRE with $M_s = 1500\,\text{kA/m}$ and Young's modulus of the matrix 8 kPa. Here and below we express the external field strength in nondimensional units as $h_0 = H_0/M_s$. The adopted set of material parameters implies that the polymer is rather soft so that the collapsing field is low: $h_0 \approx 0.039$ that corresponds to $H_0 \sim 60\,\text{kA/m}$ (or 750 Oe) that is rather far from the saturation level of the particle magnetization. Under these conditions, the magnetomechanical hysteresis loops of the linearly and nonlinearly magnetizing particles do not differ much. Further on, after qualitatively understanding the dynamic processes, we restrict the consideration to the linear magnetization approximation, that is, using it for evaluating the interparticle magnetic interaction via the *linear multipole* model; see Ref. [4]. This treatment is not at all unrealistic since carbonyl iron microparticles magnetize virtually linearly in the fields up to a few kOe. Although a linearly magnetizing substance does not have saturation, we keep the adopted value of M_s to scale the field strength; this should be recalled when transforming the results back to dimensional form.

In the case of a time-dependent field, the motion of the particles, besides the potential magnetic and elastic forces, is affected by viscous friction which has two evident sources. One of them stems from the dissipation (Joule heat) due to the eddy currents induced inside the metal grains by the applied field. However, in the low-frequency range (up to a few kHz) that we are interested in, this effect is negligible. The only dissipation mechanism relevant for the considered situation results from the particle displacements relative to the matrix. Provided this motion is not too fast (the frequency of the field is low), the arising viscous force acting on a particle is Stokes-like, i.e., proportional to its velocity.

We begin with the case of small particle displacements, i.e., small matrix strains. In that case, one may assume that the motion of the pair occurs only along the upper branch of the magnetomechanical hysteresis loop; see Fig. 1b. In linear strain approximation, the stress $\hat{\sigma}$ arising in the matrix may be presented as a sum of elastic and viscous parts as

$$\hat{\sigma} = \hat{\sigma}_{el} + \hat{\sigma}_{visc} = \lambda I_1(\hat{\varepsilon})\,\hat{I} + 2G\hat{\varepsilon} + \eta\frac{d}{dt}\hat{\varepsilon}. \tag{2}$$

Here $\hat{\varepsilon}$ is the strain tensor, λ Lamé's first parameter, I_1 the first invariant of tensor $\hat{\varepsilon}$, $\hat{I}$ the unity tensor, and G and η the shear modulus and viscosity coefficient of the matrix, respectively. It is easy to note that the adopted viewpoint corresponds to the Kelvin model of a viscoelastic medium, where the elastic and viscous elements are connected in parallel.

Under linear magnetization law, the interparticle magnetic force may be described with the aid of analytical expressions derived in Ref. [4]. In the set of units that we adopt here, the result of [4] for the vector of magnetic attraction force per particle writes as

$$\mathbf{F}_m = \mu_0 H_0^2 a^2 \underline{\mathbf{F}_m}(q), \tag{3}$$

where nondimensional function $\underline{F_m}$ in a complicated way depends on the interparticle distance q but is independent of the applied field strength. Introducing volume density $\mathbf{f}_m$ of this force in such a way that it is nonzero only inside the particles and is always directed along the local magnetic field, one arrives at the time-dependent force balance equation:

$$\nabla \cdot \hat{\sigma} + \mathbf{f}_m = 0. \tag{4}$$

For the considered materials the inertia terms are omitted as being negligible.

Finally, we introduce the nondimensional time scale $\underline{t} = t/\tau_R$, basing it on the stress relaxation time $\tau_R = \eta/G$ of the Kelvin model. After the pertinent transformation of the strain tensor time derivative, the equation set of the problem takes the form

$$\begin{aligned} &\underline{\nabla} \cdot \underline{\hat{\sigma}} + \kappa h_0^2 \underline{\mathbf{f}_m} = 0, \\ &\underline{\hat{\sigma}} = \frac{\lambda}{G} I_1(\hat{\varepsilon}) \hat{I} + 2\hat{\varepsilon} + \frac{d}{d\underline{t}} \hat{\varepsilon}. \end{aligned} \tag{5}$$

Here the stress is determined as $\underline{\hat{\sigma}} = \hat{\sigma}/G$, the operator as $\underline{\nabla} = a\nabla$, and the coefficient alongside the magnetic force as $\kappa = \mu_0 M_s^2/G$. The problem is completed by imposing stress-free conditions at all the boundaries.

The magnetomechanical problem (5) was solved numerically in axisymmetric formulation by the finite element method with the aid of library fenics for the python language for different field oscillation regimes.

Evidently, the most interesting dynamic issues are the oscillation regimes of the particle pair when the AC field is strong enough to provoke the particle collapse. During some part of the field period, where the field strength is the highest, despite the viscous impediment, the particles would dwell in the cluster state, falling on each other at the beginning of this time interval and falling apart at its end. The chances to obtain this regime analytically, due to its strong nonlinearity, are very poor, and numerical modelling seems the only possible way to describe it. Moreover, even our numerical tools are inept for adequate description of an oscillation that includes the cluster state: the calculation procedure becomes unstable there.

To overcome the difficulty and get some qualitative notion of such regimes, we resort to an interpolation model. Let the particles be connected by a compact Kelvin element whose properties are as close as possible to those of the whole viscoelastic matrix of the mesoscopic model. Therefore, we consider an elastic rod of finite

dimensions set in parallel with a viscous damper. The selection of properties of those two branches is done by fitting their overall responses to those obtained by solving numerically the full problem in the field-frequency domain where the algorithm yet works well. The comparison yields that the shear modulus of the elastic rod should coincide with that of the matrix, whereas the geometry dimensions of the rod serve as fitting parameters. The relaxation time of the Kelvin scheme that is determined by the ratio of its elastic and viscous parameters turns out to be close to the relaxation time of the matrix.

To ensure regular behavior of the model at small interparticle distances, the adopted Kelvin scheme is modified by adding one more branch. This is done on a "technical" purpose: one needs to increase the stability of calculations for the case where the particles are in the cluster state. Although the particle collapse (getting in tight contact) is quite natural from the physical viewpoint, for the software packages that we use, it entails huge computational difficulties as one faces a necessity to solve a contact problem between two solid bodies. To avoid that with minimal effect on the results, we treat the particles as objects with a solid core covered with a thin elastic shell with a high (but not immense) elastic modulus. The abovementioned third branch is responsible for that: it replaces a strictly vertical repulsive potential wall by, although very steep, but inclined ascending one; in other words, it makes the radial dependence of interparticle energy an analytical function.

3 Oscillations of the Interparticle Distance

Let an AC uniform external magnetic field

$$h_0(t) = h_A \sin(\omega t) = h_A \sin(\underline{\omega t}), \quad \underline{\omega} = \omega \tau_R, \quad \underline{t} = t/\tau_R, \tag{6}$$

of amplitude h_A be applied along the axis of the MRE element; here ω is the dimensional frequency. With the usage of the interpolation model, the magnetomechanical problem is solved analytically for any steady field oscillations (6).

As the magnetic particles are just polarizable and do not possess any remanent magnetization, the magnetic force between them does not depend on the direction of the applied field and, thus, would oscillate with doubled frequency. Accordingly, the time dependence of the forced changes of interparticle gap δ would be the same.

The establishment of steady state particle oscillations at low field amplitudes was investigated in our previous work [6]. Here we focus on the oscillations whose regime could be termed *pretransitional*. The results for that case are shown in Fig. 2. Here the amplitude of the applied field exceeds the quasistatic threshold h_* of the particle collapse. In this situation, the transitions of a separated pair to a cluster and back become possible. However, the fact whether or not such a transition would really occur depends on the frequency of the field.

Indeed, in the presence of viscous friction, the transition to the cluster state, i.e., a substantial change of the interparticle distance, needs a finite time τ_*. If, at a given

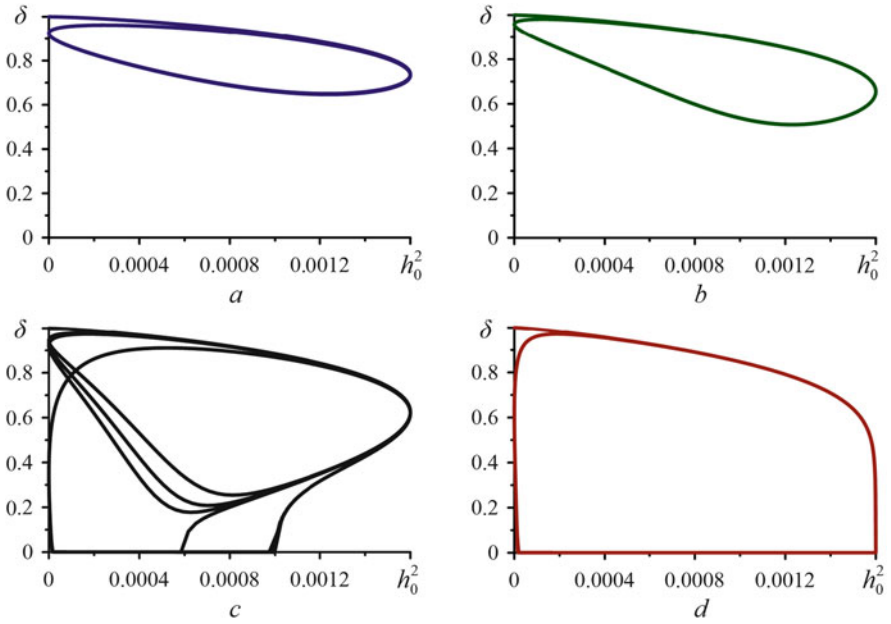

Fig. 2 Steady dynamic magnetodeformational hysteresis cycles of the model element under AC field of amplitude $h_A = 0.04$ and frequencies $\underline{\omega} = 0.8$ (**a**), 0.5 (**b**), 0.44 (**c**), and 0.2 (**d**). We note that smooth smaller loops in pane (**c**)—those similar in shape to that in pane (**b**)—correspond to a transient process; the steady loop is the largest one with "angles"

frequency in each half-period of the AC field, the condition $h_0(t) > h_*$ holds for a time interval longer than τ_*, then the particle clustering should take place. If, to the contrary, this interval is shorter than τ_*, clustering is impossible. Although the time parameter τ_* is not calculable analytically, the numerical plots of Fig. 2 for a certain amplitude imply that for the set of material and model parameters that we use, one has $0.44 < \tau_* < 0.5$. This follows from the difference of the cycle shapes: the one at higher frequency is closed and located at $\delta \geq 0.5$, while the one at lower frequency falls down to $\delta \simeq 0$ after a few cycles. At lower field frequencies, the shape of the dynamic hysteresis loop becomes much the same as the one inherent to the quasistatic case.

4 Magnetization Oscillations

As the MRE element under study is made of magnetically polarizable particles of a finite size, the changes in the interparticle distance, modulating their mutual magnetization, entail cyclic changes of the magnetic moment of the pair. This effect is evaluated from the carried out calculations as well and enables one to obtain the magnetic dynamic hysteresis loops of the studied model system.

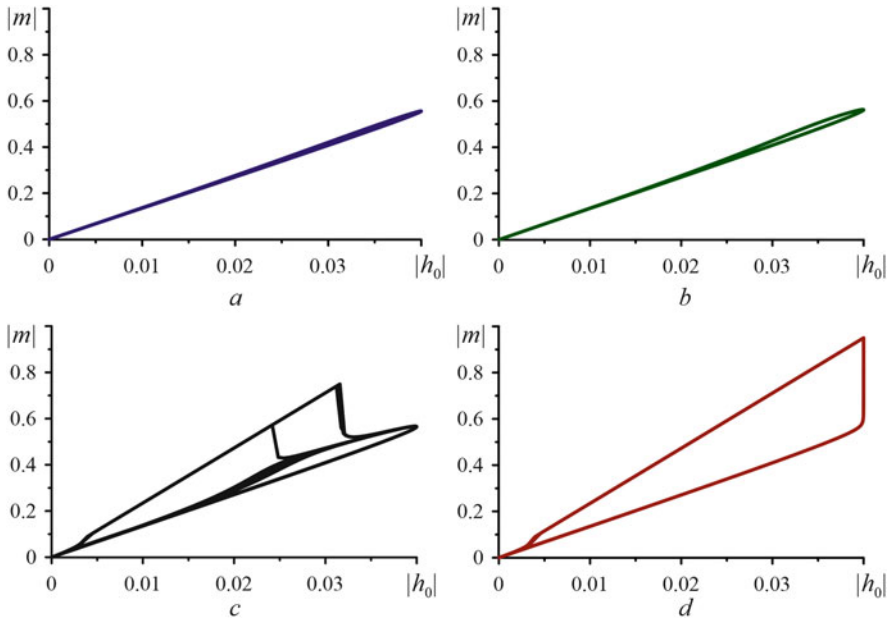

Fig. 3 Steady magnetization curves of the model element under AC field of amplitude $h_A = 0.04$ and frequencies $\underline{\omega} = 0.8$ (**a**), 0.5 (**b**), 0.44 (**c**), and 0.2 (**d**); note that magnetization curves are given in terms of absolute values, i.e., they are valid for both positive and negative m and h_0. We remark that smaller loops in pane (**c**)—those similar in shape to that in pane (**b**)—correspond to a transient process; the steady loop is the largest one

In Fig. 3 the plots of the model element magnetization are presented for the same overcritical field amplitude ($h_0 > h_*$) as in Fig. 2 and different frequencies. Note that, due to the fact that the MRE element contains only magnetically soft particles, the dynamic magnetization curves $m(h_0)$ have "zero-waist" shape: no remanent magnetization in the considered low-frequency (with respect to internal magnetic relaxation) range. At higher frequencies, the elastic effect in the viscoelastic matrix prevails, and the particle displacements (and, thus, magnetization) are tiny and coherent with the field. As a result, the magnetization curve virtually does display any loop; see pane *a*. As the frequency goes down, the amplitude of the particle forced motions becomes greater, and, accordingly, the viscous lag between the field and magnetization enhances. The gradual increase of the phase shift between $h(t)$ and $m(t)$ results in progressive "inflation" of the end loops of the magnetization curves.

5 Conclusion

The mesoscopic oscillatory behavior of ferromagnetic filler particles in a magnetorheological elastomer (MRE) is investigated with the aid of a structure model presenting an element of a MRE as a pair of particles embedded in an elastomer cylinder element. The oscillations are induced by external magnetic field applied to the element. Therefore, they are of the forced type and, due to the small size of the particles, are overdamped: the viscous forces are far greater than the inertial ones. The main phenomenon that affects the process is the bistability of the interparticle gap: in a certain domain of the field and frequency magnitudes, the pair of initially remote particles might collapse in a cluster. This affects the type of the oscillations: from nearly linear (small amplitudes/high frequency) they transform to essentially nonlinear where the part of the field period the pair spends in a collapsed state. As the particles are magnetic, the occurring mechanical motion affects the magnetic moment of the pair as well. This results in a dynamic magnetic hysteresis of the MRE element: its magnetization curves become loop-shaped. In our viewpoint, the above-presented considerations infer that forced oscillations, where the MRE filler particles clusterize, are an interesting issue, whose more detailed investigations—analytical, numerical, and experimental—would be useful for shading light on the internal dynamics of MREs.

Concerning the macroscopic manifestations of the above-described effects we remark the following. On the one hand, they should be strongly smoothed down because of the polydispersity of the MRE filler particles and the distribution of the interparticle gaps. On the other hand, the effect should contribute to the effective values of the dynamic elastic moduli extracted from the measurement data. We remark also that some experimental works, see [1], point out that in some situations the inertial effects (not taken into account here) seem to be important. The presented model could be easily extended to cover that case as well.

Acknowledgements This work was supported by RFBR grants 17-41-590160 and 17-42-590504.

References

1. Alekhina, Yu.A., Makarova, L.A., Rusakova, T.S., Semisalova, A.S., Perov, N.S.: Properties of magnetorheological elastomers in crossed AC and DC magnetic fields. J. Sib. Fed. Univ. Math. Phys. **10**, 45–50 (2016)
2. Becker, T.I., Raikher, Yu.L., Stolbov, O.V., Böhm, V., Zimmermann, K.: Dynamic properties of magneto-sensitive elastomer cantilevers as adaptive sensor elements. Smart Mater. Struct. **26**, 095035 (2017)
3. Bellan, C., Bossis, G.: Field dependence of viscoelastic properties of MR elastomers. Int. J. Mod. Phys. B. **16**, 2447–2453 (2002)
4. Biller, A.M., Stolbov, O.V., Raikher, Yu.L.: Modeling of particle interactions in magnetorheological elastomers. J. Appl. Phys. **116**, 114904 (2014)

5. Biller, A.M., Stolbov, O.V., Raikher, Yu.L.: Mesoscopic magnetomechanical hysteresis in a magnetorheological elastomer. Phys. Rev. E **92**, 023202 (2015)
6. Biller, A.M., Stolbov, O.V., Raikher, Yu.L.: Two-particle element of a magnetorheological elastomer under a cyclic magnetic field. J. Phys. Conf. Ser. **994**, 012001 (2018). https://doi.org/10.1088/1742-6596/994/1/012001
7. Bose, H.: Viscoelastic properties of silicone-based magnetorheological elastomers. Int. J. Mod. Phys. B. **21**, 4790–4797 (2007)
8. Bozorth, R.M.: Ferromagnetism. Wiley/IEEE Press, New York (1993)
9. Chertovich, A.V., Stepanov, G.V., Kramarenko, E.Yu., Khokhlov, A.R.: New composite elastomers with giant magnetic response. Macromol. Mater. Eng. **295**, 336–341 (2010)
10. Kramarenko, E.Yu., Chertovich, A.V., Stepanov, G.V., Semisalova, A.S., Makarova, L.A., Perov, N.S., Khokhlov, A.R.: Magnetic and viscoelastic response of elastomers with hard magnetic filler. Smart Mater. Struct. **24**, 035002 (2015)
11. Makarova, L.A., Alekhina, Yu.A., Perov, N.S.: Peculiarities of magnetic properties of magnetoactive elastomers with hard magnetic filler in crossed magnetic fields. J. Magn. Magn. Mater. **440**, 30–33 (2017)
12. Nikitin, L.V., Mironova, L.S., Stepanov, G.V., Samus, A.N.: The influence of a magnetic field on the elastic and viscous properties of magnetoelastics. Polym. Sci. Ser. A. **43**, 443–450 (2001)
13. Stepanov, G.V., Abramchuk, S.S., Grishin, D.A., Nikitin, L.V., Kramarenko, E.Yu., Khokhlov, A.R.: Effect of a homogeneous magnetic field on the viscoelastic behavior of magnetic elastomers. Polymer **48**, 488–495 (2007)

Two-Dimensional Motions of a Robot Under the Influence of Movable Internal Masses

F. L. Chernousko

Abstract Two-dimensional planar motions of a rigid body carrying movable internal masses are considered. The body can move along a horizontal plane in the presence of dry friction forces obeying Coulomb's law. The motion of the body is controlled by means of internal masses that can perform prescribed movements relative to the body. Two configurations of internal movable masses are considered. For each of them, relative motions of these masses are proposed that ensure the transfer of the system from any given initial state to any prescribed terminal state in the plane. Thus, the controllability of the system by means of internal masses is proven.

1 Introduction

The most well-known locomotion principles for mobile robotic systems presume the use of external devices such as legs, wheels, tracks, propellers, etc., interacting with the exterior environment. However, the motion of a robotic system inside a resistive medium can be based also upon special motions of internal movable masses relative to the main body of the robot. This way of locomotion without external devices can be useful for motion inside hazardous and vulnerable environment.

Mobile robotic systems with internal movable masses are considered in a number of papers and used for micro- and nano-positioning [5, 6]. In [1], optimal periodic motions of systems subjected to dry friction forces and controlled by internal movable masses are analyzed. The obtained optimal control corresponds to the maximum average speed of the periodic motion under constraints imposed upon the relative displacement of the internal mass, its velocity, or acceleration. Experimental data [3, 4] confirm the obtained theoretical results. In earlier papers, only one-

F. L. Chernousko (✉)
Institute for Problems in Mechanics of Russian Academy of Sciences, Moscow, Russia

Moscow Institute of Physics and Technology, Dolgoprudnyi, Moscow Region, Russia
e-mail: chern@ipmnet.ru

V. P. Matveenko et al. (eds.), *Dynamics and Control of Advanced Structures and Machines*, https://doi.org/10.1007/978-3-319-90884-7_6

dimensional motions of systems with internal masses along a horizontal line are discussed.

In this paper, two-dimensional motions of a rigid body carrying internal movable masses are considered. The body contacts a horizontal plane at three support points where normal reactions and dry friction forces are applied to the body. Two versions of internal masses with two degrees of freedom are considered.

A short summary of results concerning optimal one-dimensional motions of a system with an internal mass is given. These results [1] are used for designing controls for two-dimensional motions. For two versions of mechanical systems, the controls are proposed that transfer the systems from any initial position and configuration in the horizontal plane to any prescribed terminal position and configuration in this plane.

2 Mechanical Systems

Consider a rigid body P of mass m_1 that can slide along a fixed horizontal plane OXY. Vertical axis OZ of the Cartesian coordinate system $OXYZ$ is directed upwards. Body P called the main body contacts plane OXY at three support points A_i, $i = 1, 2, 3$. Since in the case of three support points the system is statically determinate, normal reactions N_i at points A_i can be found univalently.

Dry friction forces $\mathbf{F}_i$ acting between points A_i and plane OXY obey Coulomb's law. If point A_i slides along the plane with velocity $\mathbf{v}_i$, the friction force is defined by equation

$$\mathbf{F}_i = -f N_i \mathbf{v}_i / v_i, \quad v_i = |\mathbf{v}_i|, \quad \text{if} \quad v_i \neq 0. \tag{1}$$

Here, f is the coefficient of friction. At the state of rest of body P, we have

$$|\mathbf{F}_i| \leq f N_i, \quad \text{if} \quad v_i = 0, \quad i = 1, 2, 3. \tag{2}$$

We consider two versions of mechanical systems.

Version 1 Main body P carries a point Q of mass m_2 that can move relative to the main body along a horizontal plane parallel to plane OXY (Fig. 1). The point mass Q

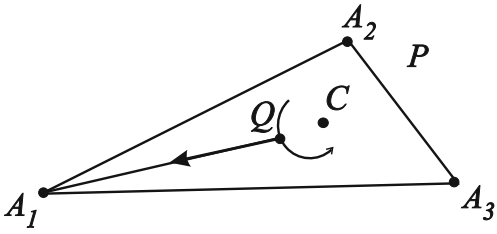

Fig. 1 Two-dimensional motion (Version 1)

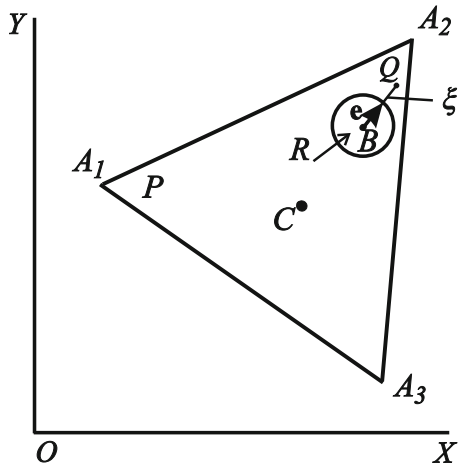

Fig. 2 Two-dimensional motion (Version 2)

has two degrees of freedom relative to the main body and is controlled by actuators installed on the body.

Version 2 Two additional bodies are associated with the main body, namely, point Q of mass m_2 and rotor R of mass m_3. The rotor is a rigid body that can rotate about the vertical axis BZ' which is parallel to OZ and passes through point B of body P. Rotor R is dynamically symmetric with respect to its axis BZ'. A horizontal line directed along the unit vector $\mathbf{e}$ is connected with the rotor and rotates with it. Point mass Q can move along this line; its displacement BQ is denoted by ξ (Fig. 2). As in Version 1, the internal bodies have two degrees of freedom relative to the main body: the angle of rotation of the rotor and displacement ξ. The relative motions of these bodies are controlled by two actuators: one of them rotates rotor R, and the second moves point Q along vector $\mathbf{e}$.

Version 2 can be implemented in different ways [2].

3 Optimal One-Dimensional Motion

Let us consider one-dimensional motion of a system that consists of a main body of mass M and an internal point mass m that can move relative to the main body (Fig. 3). Both masses move along a horizontal axis Ox. The main body interacts with the horizontal plane by means of dry friction forces, whereas the point mass equipped with an actuator interacts only with the main body. Denote by x the horizontal displacement of the main body, by v its velocity, by ξ the displacement of mass m relative to the main body, by u and w its relative velocity and acceleration, respectively. The kinematic equations can be written as follows:

$$\dot{x} = v, \quad \dot{\xi} = u, \quad \dot{u} = w. \tag{3}$$

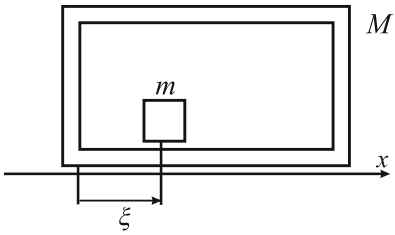

Fig. 3 One-dimensional system

The dynamical equations can be reduced to the relationship:

$$(M+m)\dot{v} = -mw + F, \tag{4}$$

where F is the dry friction force acting upon the main body. This force obeys Coulomb's law (1):

$$F = -f(M+m)g\,\mathrm{sign}v \quad \text{if} \quad v \neq 0; \quad |F| \leq f(M+m)g, \quad \text{if} \quad v = 0, \tag{5}$$

where g is the acceleration of gravity.

Equations (4) and (5) can be presented in the normalized form:

$$\dot{v} = -\mu w - fg\,\mathrm{sign}v, \quad \text{if} \quad v \neq 0; \quad |w| \leq fg\mu^{-1}, \quad \text{if} \quad v = 0, \tag{6}$$

where $\mu = m/(M+m)$. Let us consider relative acceleration w as a control subject to the constraint $|w| \leq W$, where the constant W must satisfy the inequality:

$Y = \mu W(fg)^{-1} > 1$. If this inequality does not hold, then the system cannot be controlled by the motion of the internal mass.

The relative displacement of the internal mass is subject to the constraint:

$$0 \leq \xi \leq L, \tag{7}$$

where L is a given constant.

Let us consider periodic motions of our system satisfying the following boundary conditions:

$$x(0) = v(0) = \xi(0) = u(0) = 0, \quad v(T) = \xi(T) = u(T) = 0, \tag{8}$$

where T is the period of motion. We consider the following optimal control problem.

Problem Find control $w(t)$ subject to constraint $|w| \leq W$ and such that for the solution of system (3), (6) satisfying boundary conditions (8) and constraint (7), the average velocity $V = x(T)/T$ is maximum.

The solution of this problem (in the class of piecewise constant controls $w(t)$) is given in [1]. We describe this solution below for the case where $1 < Y < 2 + 5^{1/2}$.

The optimal control $w(t)$ and the corresponding velocity $v(t)$ are given by

$$w(t) = fg\mu^{-1} \times \begin{cases} 1, & t \in (0, t_1), \\ -Y, & t \in (t_1, t_2), \\ 1, & t \in (t_2, T), \end{cases} \tag{9}$$

$$v(t) = fg\mu^{-1} \times \begin{cases} 0, & t \in (0, t_1), \\ (Y-1)(t-t_1), & t \in (t_1, t_2), \\ [(Y-1)(t_2-t_1) - 2(t-t_2)], & t \in (t_2, t_3), \\ 0, & t \in (t_3, T). \end{cases}$$

Here, the following denotations are introduced:

$$T = 2\tau\sqrt{\frac{Y+1}{Y}}, \quad \tau = \sqrt{\frac{2L\mu}{fg}},$$

$$t_1 = \tau\sqrt{\frac{Y}{Y+1}}, \quad t_2 = T - t_1, \quad t_3 = \tau\left(\sqrt{\frac{Y}{Y+1}} + \sqrt{\frac{Y+1}{Y}}\right).$$

The value of the maximum average speed V and the total displacement x_0 of the system over the period are given by

$$V = \sqrt{\frac{\mu L f g}{2Y(Y+1)}}\,(Y-1), \quad x_0 = VT = \mu L(Y-1)/Y. \tag{10}$$

The control described above can be applied to the displacement of the system for a given distance X. First, let us represent this distance as follows: $X = nx_0 + x_1$, $0 \le x_1 < x_0$, where n is an integer. The total displacement consists of n periods with duration T and displacement x_0 each and one additional interval with duration T_1 and displacement x_1. To determine the control for the additional interval, we consider the relationship similar to (10):

$$x_1 = \mu L(Y_1 - 1)/Y_1. \tag{11}$$

Since $x_1 < x_0$, we have $1 < Y_1 < Y$. Hence, for the additional interval of length x_1, the control can be defined by the same formulas (9) as for the optimal period with the only replacement Y by Y_1 defined by Eq. (11).

Thus, we have determined the control of one-dimensional motion of our two-mass system that ensures its displacement for any given distance X.

The same control is also applicable to a two-body system in its rotational motion about a common axis. Here, the dry friction torque is applied to the main

body, whereas the second body can rotate relative to the main one. Here, linear displacements should be replaced by angles of rotation about the axis, and the masses of bodies by their moments of inertia.

The control of one-dimensional motion can be used as a component part of the control for two-dimensional motions.

4 Control of Motion for Version 1

Let the initial and terminal positions of system $P + Q$ be given, and system is at rest at these positions. This means that the initial and terminal positions of the triangle $A_1A_2A_3$ in plane OXY as well as the initial and terminal positions of point Q relative to this triangle are prescribed. The control problem is to find such motion of point Q relative to body P that transfers the system $P + Q$ from the initial position to the terminal one.

Denote by C the center of mass of body P and assume that the vertical axis passing through point C is the principal central axis of inertia of the body. The projection C' of point C onto plane OXY lies within triangle $A_1A_2A_3$. Point Q can move arbitrarily in a horizontal plane parallel to OXY within a circle $|C'Q'| \le R_0$, where Q' is the projection of Q onto OXY, with an acceleration $\boldsymbol{w}$ relative to body P bounded by the inequality $|\boldsymbol{w}| \le w_0$.

If point Q moves slowly so that its relative acceleration and velocity are small enough, then body P stays at rest. Hence, point Q can move slowly from any initial to any terminal position relative to the stationary body P.

Possible motion of point Q that solves our control problem consists of three stages.

First, point Q moves slowly from its initial position to some position where the distance $C'Q'$ is equal to l, $l \in (0, R_0)$. Body P does not move.

At the second stage, point Q moves along a circle relative to body P so that the distance $C'Q'$ is equal to l. The relative velocity of this motion should be high enough so that body P rotates in the direction opposite to the rotation of point Q. To achieve the rotation of body P, the bound w_0 should be high enough. The motion of body P at this stage is not, generally speaking, a pure rotation; its center of mass C can also move. This stage ends, when body P comes to the rest, and the orientation of the triangle $A_1A_2A_3$ coincides with its terminal orientation.

At the third stage, point Q moves along horizontal straight lines such that its projection Q' moves along lines $C'A_i$, $i = 1, 2, 3$. Suppose point Q' travels along line $C'A_1$; then body P moves translationally, and point C' moves along the same line in the horizontal plane OXY. In this motion, all support points move along lines parallel to $C'Q'A_1$. This motion is feasible because the normal reactions N_i at points A_i, $i = 2, 3$, have equal and opposite torques with respect to line $C'A_1$ and thus counterbalance each other. The torques of friction forces F_2 and F_3 about point C are also equal in value and opposite in direction. Hence, the motion of point Q along line $C'A_1$ results in the translational motion of body P along this line. This motion can

be performed using the control described in Sect. 3. Using two progressive motions of body P along two directions $C'A_i$, it is possible to bring triangle $A_1A_2A_3$ to its terminal position. Point mass Q can reach its prescribed terminal position relative to body P by means of slow motion.

Therefore, it is proven that the system can be brought to the prescribed terminal position.

5 Control of Motion for Version 2

Let the initial and terminal positions of system $P + Q + R$ be given, and the system is at rest at these positions. The problem is to find such motions of rotor R and point Q relative to body P that transfer the system from the initial position to the terminal one.

To simplify the problem, we suppose that the triangle $A_1A_2A_3$ is equilateral, the projection C' of the center of mass C of the whole system $P + Q + R$ (with zero displacement $\xi = 0$ of point Q) lies in the center of the triangle, and the vertical axis CZ' passing through point C is the principal main axis of inertia of the system.

Under these assumptions, the explicit analytical solution of the control problem stated above is feasible [2]. This solution consists of three stages (Fig. 4).

At the first stage, point Q does not move, so that $\xi = 0$. Rotor R rotates about its axis. As a result, body P rotates about axis CZ', whereas point C does not move. The rotation ends at the state of rest, in which projection B' of point B onto plane OXY lies on a line that connects the projections of the initial and terminal positions of point C. At the end of this stage, vector $\mathbf{e}$ should be parallel to the same line.

At the second stage, rotor R stays fixed relative to body P, while point mass Q moves along vector $\mathbf{e}$ that keeps its direction. As a result, body P moves translationally along the same direction. At the end of the second stage, the center of mass C reaches its terminal position, and the whole system comes to the rest with $\xi = 0$.

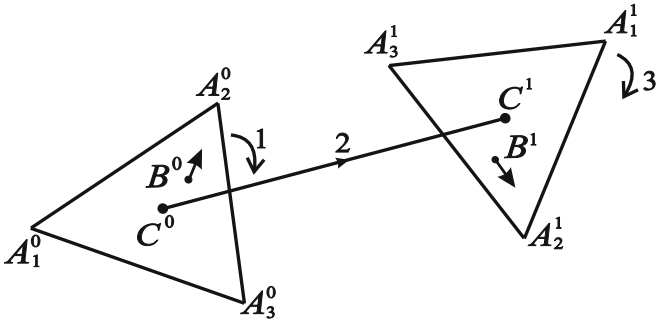

Fig. 4 Stages of motion

At the third stage, as at the first one, the point mass Q stays at rest with $\xi = 0$. Due to the rotation of rotor R, body P rotates about the fixed vertical axis passing through its center of mass C that stays fixed. The rotation ends at the state of rest, in which triangle $A_1A_2A_3$ comes to its terminal position. Also, point B and vector $\mathbf{e}$ reach their terminal states.

At all three stages, the motions are essentially one-dimensional: rotations at the first and third stages, and translation at the second one. They can be described by formulas for controls given in Sect. 3. Thus, the solution of the control problem stated above is obtained.

6 Conclusions

It is shown that the mechanical system consisting of a main body and internal movable masses attached to it and controlled by actuators can be transferred from an initial state to any terminal state in the horizontal plane. The motion occurs in the presence of dry friction forces acting upon the main body. Two versions of internal masses associated with the main body are considered; both of them have two degrees of freedom relative to the body. The motions of internal masses that bring the system to the desired position include several stages, rotations and translations, that are reduced to one-dimensional motions considered earlier. The results obtained can be useful for mobile robots moving in hazardous or vulnerable environment; these robots have no external devices and may be hermetic.

Acknowledgements The work was supported by the Russian Foundation for Basic Research, Project No. 17-01-00652, and by the Program No. 29 "Advanced Topics of Robotic Systems" of the Presidium of the Russian Academy of Sciences.

References

1. Chernousko, F.L.: Analysis and optimization of the motion of a body controlled by a movable internal mass. J. Appl. Math. Mech. **70**(6), 915–941 (2006)
2. Chernousko, F.L.: Two-dimensional motions of a body containing internal moving masses. Meccanica **51**(12), 3203–3209 (2016)
3. Li, H., Firuta, K., Chernousko, F.L.: A pendulum-driven cart via internal force and static friction. In: Proceedings of International Conference "Physics and Control", St. Petersburg, pp. 15–17 (2005)
4. Li, H., Firuta, K., Chernousko, F.L.: Motion generation of the Capsubot using internal force and static friction. In: Proceedings of the 45th IEEE Conference Decision and Control, San Diego, pp. 6575–6580 (2006)
5. Schmoeckel, F., Worn, H.: Remotely controllable mobile microrobots acting as nano positioners and intelligent tweezers in scanning electron microscopes (SEMs). In: Proceedings of International Conference Robotics and Automation, pp. 3903–3913. IEEE, New York (2001)
6. Vartholomeos, H., Papadopoulos, E.: Dynamics, design and simulation of a novel micro-robotic platform employing vibration microactuators. J. Dyn. Syst. Meas. Control. **128**(1), 122–133 (2006)

Splitting of Strain Solitons upon Their Interaction in the Auxetic Rod

Vladimir I. Erofeev, Vladimir V. Kazhaev, and Igor S. Pavlov

Abstract The problem of longitudinal wave propagation in a rod made from an auxetic material is considered. It is shown that a negative Poisson's ratio leads to a qualitatively different (anomalous) dispersion behavior of linear waves. Accounting for geometric and physical elastic nonlinearities leads to the possibility of generating in a rod of stationary strain waves of a substantially non-sinusoidal profile—solitons and their periodic analogues. By means of numerical simulation it is shown that qualitatively different scenarios of interaction of solitons depend on the relative collision velocity.

1 Introduction

At present, models and structures of auxetic rods [1] used as elements of a new class of composites [2] are actively developed, and auxetic polymeric foams [3, 4] and auxetic crystalline materials [5, 6] are synthesized and studied. Considerable attention is paid to the study of characteristic features of the propagation of elastic waves, primarily, of the ultrasonic range, in materials with a negative Poisson's ratio (auxetics) [1, 7–13], since such studies will contribute to the development of methods for acoustic non-destructive testing of new advanced materials.

The aim of this paper is an investigation of the propagation of longitudinal waves in a rod made from an auxetic material.

V. I. Erofeev (✉) · V. V. Kazhaev · I. S. Pavlov
Mechanical Engineering Research Institute of the Russian Academy of Sciences, Nizhny Novgorod, Russia
e-mail: erof.vi@yandex.ru

V. P. Matveenko et al. (eds.), *Dynamics and Control of Advanced Structures and Machines*, https://doi.org/10.1007/978-3-319-90884-7_7

2 The Nonlinear Mathematical Model

The nonlinear equation generalizing the Bishop model of longitudinal vibrations of a rod has the form [14]:

$$\frac{\partial^2 u}{\partial t^2} - c_0^2 \left(1 + \frac{6\alpha}{E}\frac{\partial u}{\partial x}\right)\frac{\partial^2 u}{\partial x^2} - \nu^2 R^2 \left(\frac{\partial^4 u}{\partial x^2 \partial t^2} - c_x^2 \frac{\partial^4 u}{\partial x^4}\right) = 0 \tag{1}$$

Here R is the polar radius of inertia, and the coefficient α determining the contribution of the geometric and physical nonlinearities is equal to $\alpha = \frac{E}{2} + \frac{\nu_1}{6}(1 - 6\nu) + \nu_2(1 - 2\nu) + \frac{4}{3}\nu_3$, where ν_1, ν_2, and ν_3 are Lame constants of the third order.

Let us introduce dimensionless variables $t' = c_0 t/R$, $x' = x/R$, $u' = \alpha u/R$ in Eq. (1) and then omit dashes over the dimensionless variables:

$$\frac{\partial^2 u}{\partial t^2} - \left(1 + \beta\frac{\partial u}{\partial x}\right)\frac{\partial^2 u}{\partial x^2} - \frac{\partial^4 u}{\partial x^2 \partial t^2} + c^2 \frac{\partial^4 u}{\partial x^4} = 0 \tag{2}$$

The dimensionless parameter β defines a rod with a "rigid" ($\beta = 1$) or a "soft" ($\beta = -1$) type of nonlinearity.

In Eq. (2) the dimensionless parameter c is equal to the ratio of the velocities $c = c_\tau/c_0$ and $c \leq 1$ for all the positive values of the Poisson's ratio. But if the Poisson's ratio is negative, various cases are possible, when the rod velocity c_0 exceeds the shear wave velocity c_τ ($c < 1$ for $-0.5 < \nu < 0$) or, vice versa, $c_\tau > c_0$ ($c > 1$ for $-1 < \nu < -0.5$). The degenerated case, when both velocities coincide, yields $c = 1$ for $\nu = -0.5$.

3 Strain Solitons in an Auxetic Rod

Let us consider a rod with a "rigid" nonlinearity. We shall search for solutions of Eq. (2) among stationary strain waves $U(\xi) = \partial u/\partial\xi$ where $\xi = x - Vt$ is the "travelling" coordinate and $V = const$ is the stationary wave velocity. Some solutions of Eq. (2) describe a nonlinear stationary wave (soliton) having a bell shape:

$$U(\xi) = \frac{A^*}{ch^2((x - Vt)/\Delta)} \tag{3}$$

where ch is the hyperbolic cosine. The amplitude A^* and the width Δ of a wave are related to its velocity V by the following relations:

$$A^* = 3\left(V^2 - 1\right), \qquad \Delta = 2\sqrt{\left(c^2 - V^2\right)/\left(1 - V^2\right)} \tag{4}$$

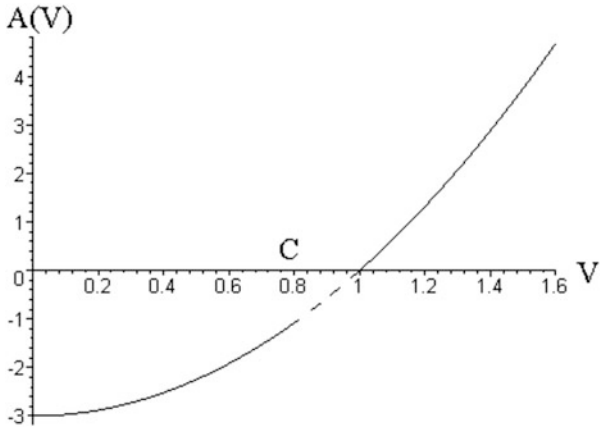

Fig. 1 The dependence of the amplitude for $\nu > -0.5$

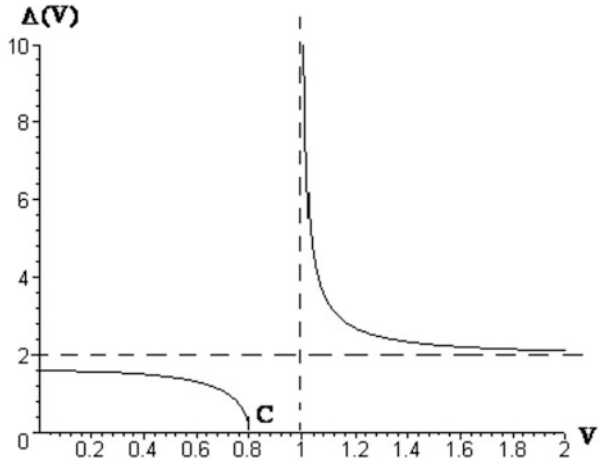

Fig. 2 The dependence of the width on the soliton velocity for $\nu > -0.5$

If Poisson's ratio exceeds -0.5 (i.e., $c < 1$), then "subsonic" solitons ($0 < V < c$) of a negative polarity and "supersonic" ($V > 1$) solitons of a positive polarity can propagate in a rod. The dependences of the amplitude and the width on the soliton velocity are plotted in Figs. 1 and 2, accordingly.

When $\nu \in (-1; 0.5)$, "subsonic" solitons ($0 < V < 1$) have a negative polarity too, whereas "supersonic" ($V > c$) solitons possess a positive polarity. The dependences of the amplitude and the width on the soliton velocity are plotted in Figs. 3 and 4, respectively.

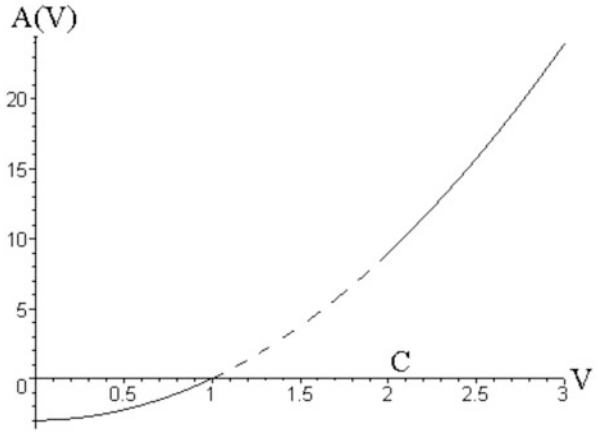

Fig. 3 The dependence of the amplitude on the soliton velocity for $-1 < \nu < -0.5$

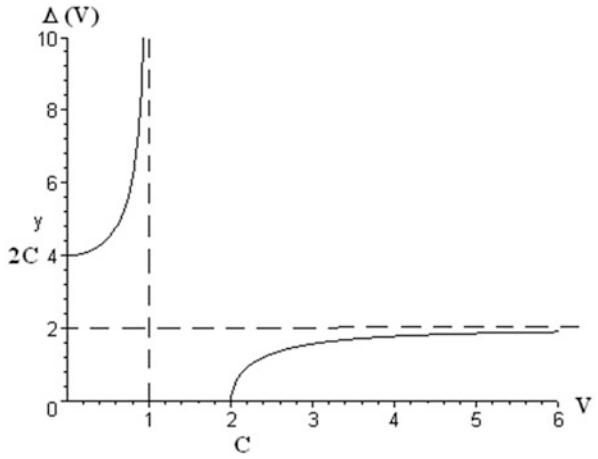

Fig. 4 The dependence of the width on the soliton velocity for $-1 < \nu < -0.5$

4 Numerical Simulation of Soliton Interactions

Numerical simulation of Eq. (2) was carried out using the developed finite-difference algorithm realizing an implicit three-layer scheme with the approximation order $o\left(\tau^2, \eta^2\right)$, where τ is the time step and η is the space step of the grid. The difference scheme is uniformly stable for the following relation between the steps: $\tau \leq 0.85\eta^2/\sqrt{2\eta^2\left(1 + |u_x|\right) + 8c^2}$.

By means of numerical simulation it is shown that qualitatively different scenarios of interaction of solitons depend on the relative collision velocity. A collision of only supersonic solitons was considered, as any collision velocities can be realized for them.

If the relative velocity is small ($\Delta V = 0.0466$), the collision occurs like the exchange interaction of the classical solitons described by the Korteweg–de Vries equation. A fast soliton overtakes a slow soliton, they are not unified but they exchange their characteristics and continue to move with the just received velocities. In this case the secondary solitons are completely identical to the primary solitons.

When the relative velocity is greater ($\Delta V = 0.1$), the collision of solitons is already inelastic. During the interaction, solitons lose a part of their energy, which is realized in a packet of quasiharmonic waves moving behind the slowest supersonic soliton with the velocity of linear waves.

As a result of further increasing of the collision velocity ($\Delta V = 0.4$), the fast soliton overtakes the slow soliton and they are unified. The amplitude of the unified soliton is less than the algebraic sum of the amplitudes of the interacting solitons. Then the solitons go away from each other losing some of the energy. This energy is distributed between two wave packets, one of which propagates in the opposite direction to the motion of the solitons with the velocity of quasilinear waves, and the other one overtakes, with the same velocity, supersonic solitons.

The great collision velocities ($\Delta V \geq 0.5$) lead to the effect of splitting of solitons, which means generation of a larger number of secondary solitons than in the beginning of interaction. Figure 5 demonstrates the process of splitting for collision of the solitons with velocities $V_1 = 3$ and $V_2 = 1.5$. Since the amplitudes of the interacting solitons differ by almost two orders of magnitude, for the convenience of visual perception, Fig. 5 is executed in a logarithmic scale. From this figure it is visible that a high-speed soliton, after overtaking a slow soliton, is rapidly removed from the interaction zone. And in this case a wave packet arises that propagates in the opposite direction to the soliton motion. It is shown in the enlarged scale in the left circle, below its evolution is demonstrated. Next, a second soliton is extracted and a nonstationary wave packet (the right circle) follows for it (its evolution is shown below). Later, another supersonic soliton is formed from this packet. Then again a quasilinear wave packet and a slow (subsonic) soliton of a negative polarity are generated. All the characteristics of the secondary solitons completely coincide with the solutions (3) and (4).

The soliton interaction occurring with very high speeds ($\Delta V > 2$) looks most effectively for the counter collision of identical solitons (Fig. 6). After the collision, a high-speed secondary soliton with amplitude A_{11} is released. This amplitude is not much smaller than the amplitude A_0 of the primary soliton. A second secondary soliton is formed behind it, the amplitude A_{12} of which is much smaller than A_0. Next, a nonlinear wave packet is formed (on an enlarged scale it is shown in the oval). If to observe the soliton interaction for a long time, it should be noticed that

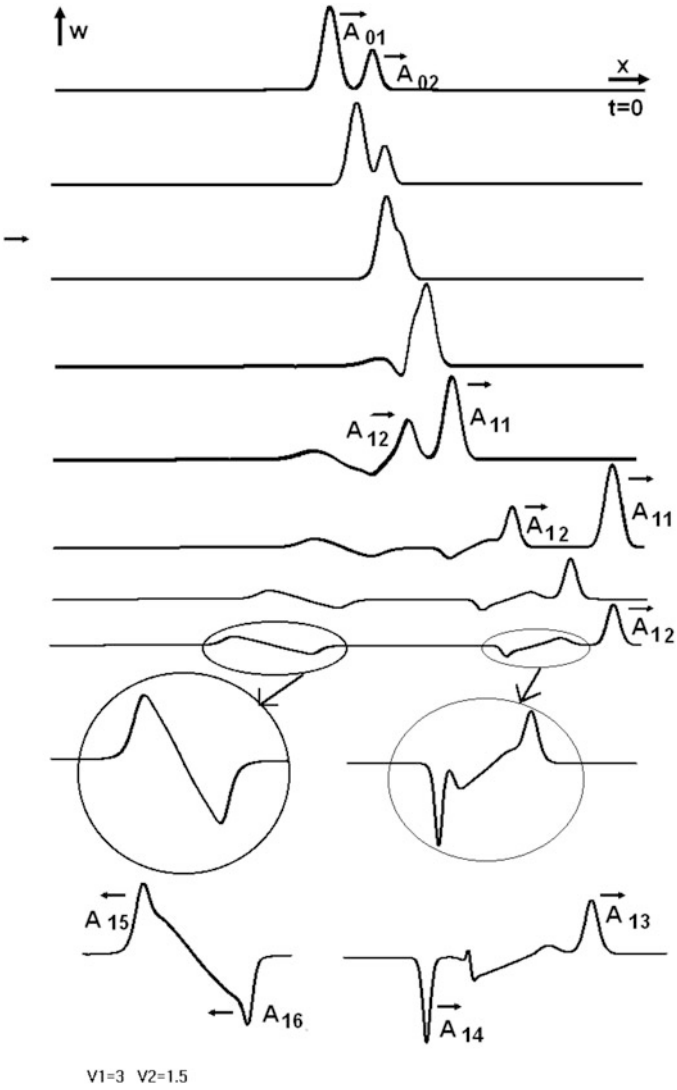

Fig. 5 Collision of the solitons with the relative velocity $\Delta V \geq 0.5$: the splitting effect

solitons can be further generated from this packet and, at last, the slow subsonic soliton, whose amplitude A_{13} is almost equal to A_{12}, will travel behind them. In general, any number of supersonic solitons can arise from a wave packet, since their amplitude and energy can be practically zero.

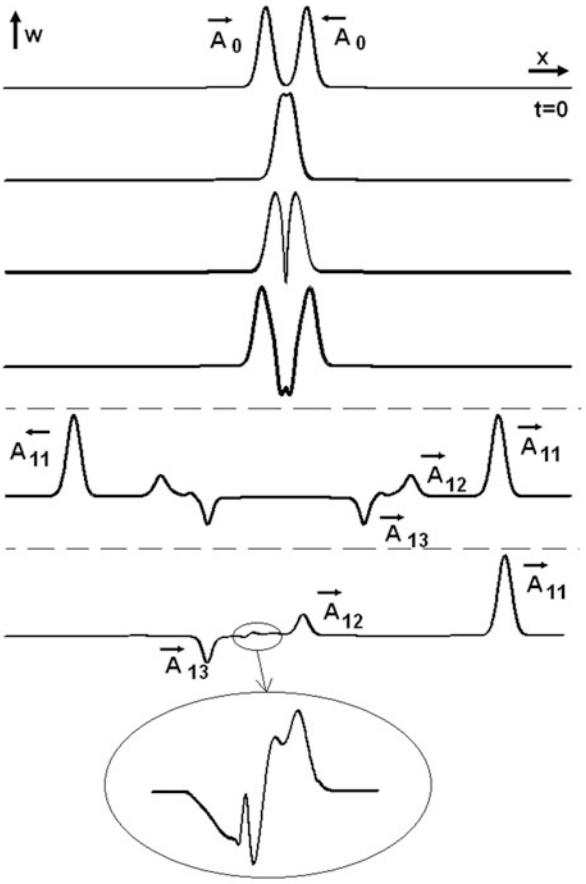

Fig. 6 Counter interaction of solitons with relative velocities $\Delta V > 2$

5 Conclusions

Longitudinal wave propagation in an auxetic rod has been considered. A qualitatively different (anomalous) dispersion behavior of linear waves is shown to be possible in such a rod. Accounting for geometric and physical elastic nonlinearities, in its turn, leads to the possibility of generating in a rod of stationary strain waves of a substantially non-sinusoidal profile—solitons and their periodic analogues.

By means of numerical simulation it is shown that qualitatively different scenarios of interaction of solitons depend on the relative collision velocity. So, if the velocity is small, the collision occurs like the exchange interaction of the classical Korteweg–de Vries solitons, i.e., secondary solitons possess the same velocity, amplitude, and width as the primary solitons have. When the relative velocity is greater, the collision of solitons is inelastic: during the interaction, solitons lose a

part of their energy, which is realized in a packet of quasiharmonic waves moving with the velocity of linear waves. A further increasing of the collision velocity leads to the effect of splitting of solitons that means generation of a larger number of secondary solitons than in the beginning of interaction.

Acknowledgement The research was carried out under the financial support of the Russian Scientific Foundation (Project No. 14-19-01637).

References

1. Lim, T.-C.: Auxetic Materials and Structures. Engineering Materials. Springer, Singapore (2015)
2. Bilski, M., Wojciechowski, K.W.: Tailoring Poisson's ratio by introducing auxetic layers. Phys. Status Solidi B **253**, 1318–1323 (2016)
3. Lakes, R.S.: Foam structures with a negative Poisson's ratio. Science **235**, 1038–1040 (1987)
4. Friis, E.A., Lakes, R.S., Parks, J.B.: Negative Poisson's ratio polymeric and metal foams. J. Mater. Sci. **23**, 4406–4414 (1988)
5. Alderson, K.L., Simkins, V.R., Coenen, V.L., Davies, P.J., Alderson, A., Evans, K.E.: How to make auxetic fibre reinforced composites. Phys. Status Solidi B **242**, 509–518 (2005)
6. Krasavin, V.V., Krasavin, A.V.: Auxetic properties of cubic metal single crystals. Phys. Status Solidi B **251**, 2314–2320 (2014)
7. Koenders, M.A.: Wave propagation through elastic granular and granular auxetic materials. Phys. Status Solidi B **246**, 2083–2088 (2009)
8. Kolat, P., Maruszewski, B.T., Wojciechowski, K.W.: Solitary waves in auxetic plates. J. Non-Cryst. Solids **356**, 2001–2009 (2010)
9. Kolat, P., Maruszewski, B.T., Tretiakov, K.V., Wojciechowski, K.W.: Solitary waves in auxetic rods. Phys. Status Solidi B **248**, 148–157 (2011)
10. Malischewski, P.G., Lorato, A., Scarpa, F., Ruzzene, M.: Unusual behaviour of wave propagation in auxetic structures: P-waves on free surface and S-waves in chiral lattices with piezoelectrics. Phys. Status Solidi B **249**, 1339–1346 (2012)
11. Dinh, T.B., Long, V.C., Xuan, K.D., Wojciechowski, K.W.: Computer simulation of solitary waves in a common or auxetic elastic rod with both quadratic and cubic nonlinearities. Phys. Status Solidi B **249**, 1386–1392 (2012)
12. Goldstein, R.V., Gorodtsov, V.A., Lisovenko, D.S.: Rayleigh and Love surface waves in isotropic media with negative Poisson's ratio. Mech. Solids **49**, 422–434 (2014)
13. Sobieszczyk, P., Majka, M., Kuźma, M., Lim, T.-C., Zieliński, P.: Effect of longitudinal stress on wave propagation in width-constrained elastic plates with arbitrary Poisson's ratio. Phys. Status Solidi B **252**, 1615–1619 (2015)
14. Erofeev, V.I., Klyueva, N.V.: Solitons and nonlinear periodic strain waves in rods, plates, and shells (a review). Acoust. Phys. **48**, 643–655 (2002)

Analysis of Acoustic Second-Harmonic Generation in a Multilayered Structure with Nonlinear Interfaces

Yosuke Ishii and Tadaharu Adachi

Abstract The one-dimensional longitudinal wave propagation in a multilayered structure consisting of alternating layers and nonlinear spring-type interlayer interfaces is analyzed theoretically to investigate the acoustic second-harmonic generation due to the interfacial nonlinearity. Assuming that the nonlinearity is sufficiently weak, the second-harmonic components contained in the reflected and transmitted waves when a monochromatic longitudinal wave impinges perpendicularly on the structure are derived using a perturbation approach and the transfer-matrix method. Some numerical results of frequency dependence of second-harmonic amplitudes are shown and discussed with the aid of the band structure of layered structures.

1 Introduction

Nonlinear acoustic wave propagation in layered structures was widely studied theoretically to explore the amplitude-dependent dispersion relation [1], the localized solutions [2], and the second-harmonic generation [3]. These foregoing studies [1–3] dealt with the nonlinear acoustic phenomena caused by material nonlinearity, whereas the nonlinear acoustics at imperfect interfaces between solid media have attracted much attention in the field of nondestructive testing as a sensitive measure of contacting interface, weak bonds, kissing bonds, closed cracks, and so on. In particular, the higher-harmonic generation at an imperfect interface was extensively investigated theoretically and experimentally [4, 5]. These studies demonstrated that the second- or higher-harmonic generation at a contacting interface between two solids was reasonably described by modeling it as a spring-type interface with quadratic nonlinearity. This modeling was utilized to analyze the frequency-dependent second-harmonic generation in multiple interface structures, namely multilayered structures consisting of layers having identical elastic properties

Y. Ishii (✉) · T. Adachi
Toyohashi University of Technology, Tempaku-cho, Toyohashi, Japan
e-mail: ishii@me.tut.ac.jp; adachi@me.tut.ac.jp

V. P. Matveenko et al. (eds.), *Dynamics and Control of Advanced Structures and Machines*, https://doi.org/10.1007/978-3-319-90884-7_8

and nonlinear interlayer interfaces, where the interlayer interfaces were solely responsible for the formation of frequency pass and stop bands [6, 7]. On the other hand, in the case of dissimilar layers, the wave scattering can occur at interlayer interfaces due not only to the finite stiffness of interfaces but also to the mismatch of acoustic impedances between neighboring layers. Therefore, understanding the resulting frequency dependence of the second-harmonic generation is of academic interest and important from a practical perspective for nondestructive evaluation of layered structure with dissimilar layers.

In this study, the acoustic second-harmonic generation in a multilayered structure consisting of alternating layers of two linear elastic solids and nonlinear spring-type interlayer interfaces is analyzed theoretically by a perturbation approach and the transfer-matrix method [8] to investigate the frequency dependence of second-harmonic amplitudes of reflected and transmitted waves when the structure is subjected to the normal incidence of a monochromatic longitudinal wave. The formulation is briefly summarized in Sect. 2 and some numerical results are shown in Sect. 3.

2 Analysis

2.1 Formulation

The one-dimensional longitudinal wave propagation in the layering direction (x direction) of a multilayered structure shown in Fig. 1 is considered. The structure consists of $N-1$ alternating layers of two different types of linear elastic media, denoted by "Layer 0" (density ρ_0, wave speed c_0, and thickness h_0) and "Layer 1" (density ρ_1, wave speed c_1, and thickness h_1), and is embedded between two linear elastic semi-infinite media with the same material properties as the Layer 1. All these media are bonded each other by N spring-type interfaces at $x = X_m (m = 1, 2, \ldots, N)$, where N is a positive even number.

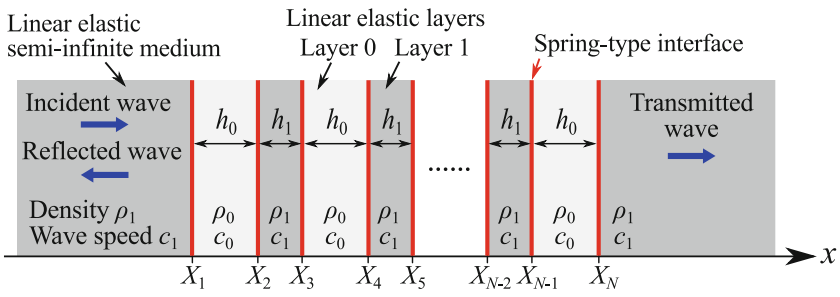

Fig. 1 Computational model

The displacement in the structure, denoted as $u(x,t)$ where t is the time, is governed by the linear equation of motion as

$$\frac{\partial^2 u}{\partial t^2} = c_\alpha^2 \frac{\partial^2 u}{\partial x^2}, \tag{1}$$

where $\alpha = 0$ in the Layer 0 and $\alpha = 1$ in the Layer 1 (and the surrounding semi-infinite media). At each interface, the stress given by $\sigma(x,t) = \rho_\alpha c_\alpha^2 \partial u/\partial x$ is continuous while the discontinuity is allowed in the displacement. With the spring-type interfaces possessing weak quadratic nonlinearity, the boundary conditions at $x = X_m$ are given as [5]

$$\sigma(X_{m+},t) = \sigma(X_{m-},t) = K\left[1 - \beta_m y_m(t)\right] y_m(t), \tag{2}$$

where the subscripts "$m+$" and "$m-$" denote the limit of a field variable when x approaches X_m from $x > X_m$ and $x < X_m$, respectively. In Eq. (2), K is the linear interfacial stiffness and assumed to be the same for all interfaces because they are all located between two phases. Furthermore, β_m is a positive parameter representing the nonlinearity of the mth interface, and $y_m(t) \equiv u(X_{m+},t) - u(X_{m-},t)$ is the jump of displacement at $x = X_m$.

In this paper, the amplitudes of the nonlinearly generated second-harmonic component in the reflected and transmitted waves for $x < X_1$ and $x > X_N$, respectively, are analyzed when a monochromatic longitudinal wave with angular frequency ω_0 and amplitude A_{inc} impinges perpendicularly upon the multilayered structure from $x < X_1$. Assuming that $\max_m(\beta_m)A_{\mathrm{inc}}$ is sufficiently small, and that the time dependence term is given by $\exp(-\mathrm{i}\omega t)$ where i is the imaginary unit and ω is the angular frequency, the governing equations and the boundary conditions for the fundamental wave ($\omega = \omega_0$) and its second-harmonic component ($\omega = 2\omega_0$) are written by performing the perturbation analysis [6] as follows.
For $\omega = \omega_0$, we have

$$\frac{\mathrm{d}^2 U_1}{\mathrm{d}x^2} + \left(\frac{\omega_0}{c_\alpha}\right)^2 U_1 = 0, \tag{3}$$

$$\rho_\chi c_\chi^2 \frac{\mathrm{d}U_1}{\mathrm{d}x}(X_{m-}) = \rho_\kappa c_\kappa^2 \frac{\mathrm{d}U_1}{\mathrm{d}x}(X_{m+}) = K Y_{1m}, \quad m = 1,2,\ldots,N, \tag{4}$$

where $\chi = 1$ and $\kappa = 0$ when m is odd and $\chi = 0$ and $\kappa = 1$ when m is even.
For $\omega = 2\omega_0$, we have

$$\frac{\mathrm{d}^2 U_2}{\mathrm{d}x^2} + \left(\frac{2\omega_0}{c_\alpha}\right)^2 U_2 = 0, \tag{5}$$

$$\begin{aligned}\rho_\chi c_\chi^2 \frac{\mathrm{d}U_2}{\mathrm{d}x}(X_{m-}) &= \rho_\kappa c_\kappa^2 \frac{\mathrm{d}U_2}{\mathrm{d}x}(X_{m+}) \\ &= K Y_{2m} - \frac{1}{2}\beta_m K Y_{1m}^2, \quad m = 1,2,\ldots,N.\end{aligned} \tag{6}$$

In Eqs. (3)–(6), U_1 and U_2 (Y_{1m} and Y_{2m}) are the complex-valued time-harmonic displacements (jumps of displacement at the mth interface) of the fundamental wave and its second-harmonic component, respectively.

2.2 Propagation of Fundamental Wave

Using the classical transfer-matrix method [8] for Eqs. (3) and (4), the complex amplitude reflection and transmission coefficients of the fundamental wave, $R(\Omega)$ and $T(\Omega)$, can be given as,

$$R(\Omega) = -\frac{L_{21}(\Omega)}{L_{22}(\Omega)} \exp\left(2\mathrm{i}\Omega \hat{X}_1\right), \tag{7}$$

$$T(\Omega) = \frac{L_{11}(\Omega)L_{22}(\Omega) - L_{12}(\Omega)L_{21}(\Omega)}{L_{22}(\Omega)} \exp\left[-\mathrm{i}\Omega\left(\hat{X_N} - \hat{X_1}\right)\right], \tag{8}$$

where $\Omega = \omega_0 h_0/c_0$ and $\hat{X}_q = c_0 X_q/(c_1 h_0)(q = 1, N)$ represent the normalized frequency and the normalized positions of the leftmost and rightmost interfaces, respectively. In Eqs. (7) and (8), $L_{IJ}(\Omega)(I, J = 1, 2)$ are the elements of the global transfer matrix given by

$$\boldsymbol{L}(\Omega) = \begin{bmatrix} L_{11}(\Omega) & L_{12}(\Omega) \\ L_{21}(\Omega) & L_{22}(\Omega) \end{bmatrix} = \boldsymbol{P}_1^{-1}(\Omega)\boldsymbol{H}^{\frac{N}{2}}(\Omega), \tag{9}$$

where $\boldsymbol{H}(\Omega) \equiv \boldsymbol{P}_1(\Omega)\boldsymbol{S}_{01}(\Omega)\boldsymbol{P}_0(\Omega)\boldsymbol{S}_{10}(\Omega)$, and

$$\boldsymbol{S}_{10}(\Omega) = \frac{1}{2}\begin{bmatrix} 1 + 1/\zeta + \mathrm{i}\Lambda\Omega & 1 - 1/\zeta - \mathrm{i}\Lambda\Omega \\ 1 - 1/\zeta + \mathrm{i}\Lambda\Omega & 1 + 1/\zeta - \mathrm{i}\Lambda\Omega \end{bmatrix}, \tag{10}$$

$$\boldsymbol{S}_{01}(\Omega) = \frac{1}{2}\begin{bmatrix} 1 + \zeta + \mathrm{i}\Lambda\Omega & 1 - \zeta - \mathrm{i}\Lambda\Omega \\ 1 - \zeta + \mathrm{i}\Lambda\Omega & 1 + \zeta - \mathrm{i}\Lambda\Omega \end{bmatrix} \tag{11}$$

are the scattering matrices at the interfaces at $x = X_m(m = 1, 3, \ldots, N-1)$ and at $x = X_m(m = 2, 4, \ldots, N)$, respectively. Furthermore,

$$\boldsymbol{P}_0(\Omega) = \begin{bmatrix} \exp(\mathrm{i}\Omega) & 0 \\ 0 & \exp(-\mathrm{i}\Omega) \end{bmatrix}, \quad \boldsymbol{P}_1(\Omega) = \begin{bmatrix} \exp(\mathrm{i}\Omega\eta) & 0 \\ 0 & \exp(-\mathrm{i}\Omega\eta) \end{bmatrix}, \tag{12}$$

are the propagator matrices in the Layer 0 and Layer 1, respectively. In the above expressions, the non-dimensional parameters

$$\Lambda \equiv \frac{\rho_0 c_0^2}{K h_0}, \qquad \zeta \equiv \frac{\rho_1 c_1}{\rho_0 c_0}, \qquad \eta \equiv \frac{h_1 c_0}{h_0 c_1}, \tag{13}$$

represent the relative linear compliance of the interfaces, the acoustic impedance ratio between the two phases, and the ratio of the times of flight in the Layer 0 and Layer 1, respectively. Using Eqs. (10)–(12) with the so-obtained reflection coefficient $R(\Omega)$ from Eq. (7), the jump of displacement at the mth interface ($m = 1, 2, \ldots, N$) due to the fundamental wave propagation can be calculated as

$$Y_{1m}(\Omega) = \begin{cases} \boldsymbol{e}[\boldsymbol{S}_{10}(\Omega) - \boldsymbol{I}]\boldsymbol{H}^{\frac{m-1}{2}}(\Omega)\boldsymbol{U}_1(X_{1-}), & m = 1, 3, \ldots, N-1, \\ \boldsymbol{e}[\boldsymbol{S}_{01}(\Omega) - \boldsymbol{I}]\boldsymbol{P}_0(\Omega)\boldsymbol{S}_{10}(\Omega)\boldsymbol{H}^{\frac{m-2}{2}}(\Omega)\boldsymbol{U}_1(X_{1-}), & m = 2, 4, \ldots, N, \end{cases} \tag{14}$$

where $\boldsymbol{e} \equiv (1, 1)$, $\boldsymbol{I}$ represents the 2×2 identity matrix, and

$$\boldsymbol{U}_1(X_{1-}) = \begin{pmatrix} A_{\text{inc}} \exp\left(\mathrm{i}\Omega \hat{X}_1\right) \\ R(\Omega) A_{\text{inc}} \exp\left(-\mathrm{i}\Omega \hat{X}_1\right) \end{pmatrix}. \tag{15}$$

2.3 Generation and Propagation of Second Harmonics

By applying the transfer-matrix method again to Eqs. (5) and (6), the second-harmonic amplitudes of reflected and transmitted waves, A_{R2} and A_{T2}, can be given as,

$$A_{\text{R2}} = -\frac{b_2(\Omega)}{L_{22}(2\Omega)} \exp\left(2\mathrm{i}\Omega \hat{X}_1\right), \tag{16}$$

$$A_{\text{T2}} = \frac{b_1(\Omega)L_{22}(2\Omega) - b_2(\Omega)L_{12}(2\Omega)}{L_{22}(2\Omega)} \exp\left(-2\mathrm{i}\Omega \hat{X_N}\right), \tag{17}$$

where

$$\boldsymbol{b}(\Omega) \equiv \begin{pmatrix} b_1(\Omega) \\ b_2(\Omega) \end{pmatrix} = \frac{1}{4} \sum_{j=1}^{N/2} \boldsymbol{M}^{\frac{N}{2}-j}(2\Omega) \left[\beta_{2j-1} Y^2_{1(2j-1)}(\Omega) \boldsymbol{S}_{01}(2\Omega) \boldsymbol{P}_0(2\Omega) + \beta_{2j} Y^2_{1(2j)}(\Omega)\right], \tag{18}$$

and $\boldsymbol{M}(\Omega) \equiv \boldsymbol{S}_{01}(\Omega)\boldsymbol{P}_0(\Omega)\boldsymbol{S}_{10}(\Omega)\boldsymbol{P}_1(\Omega)$.

3 Numerical Examples

The frequency dependence of second-harmonic amplitudes due to a single nonlinear interface located at $x = X_6$ ($\beta_6 = \beta > 0$, $\beta_m = 0$ for $m \neq 6$) when $N = 10$, $\Lambda = 0.1$, $\zeta = 1$, and $\eta = 1$ is shown in Fig. 2, together with the amplitude transmission coefficient of fundamental wave $|T(\Omega)|$ in Eq. (8) and the jump of displacement at the nonlinear interface $|Y_{16}(\Omega)|$ in Eq. (14). Likewise, the results when $\zeta = 0.7$ are shown in Fig. 3. Furthermore, the spatial distributions of fundamental and second-harmonic displacements corresponding to Figs. 2 and 3 are illustrated in Figs. 4 and 5, respectively.

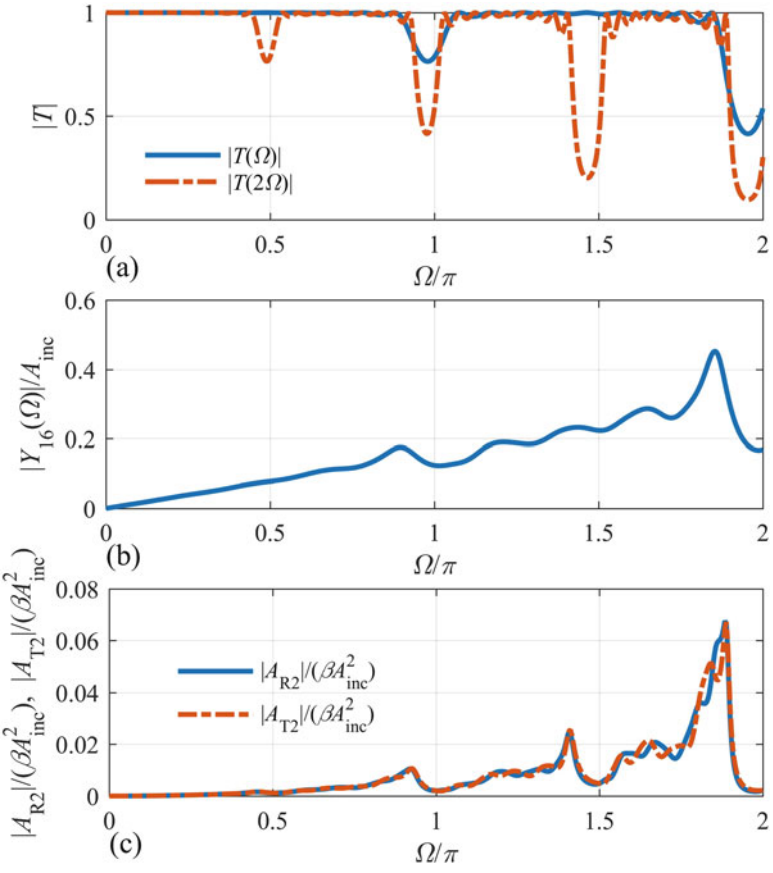

Fig. 2 Frequency dependence of fundamental and second-harmonic components when $N = 10$, $\Lambda = 0.1$, $\zeta = 1$, and $\eta = 1$. (**a**) Amplitude transmission coefficient of fundamental wave. (**b**) Opening displacement at the nonlinear interface at $x = X_6$. (**c**) Second-harmonic amplitudes of reflected and transmitted waves

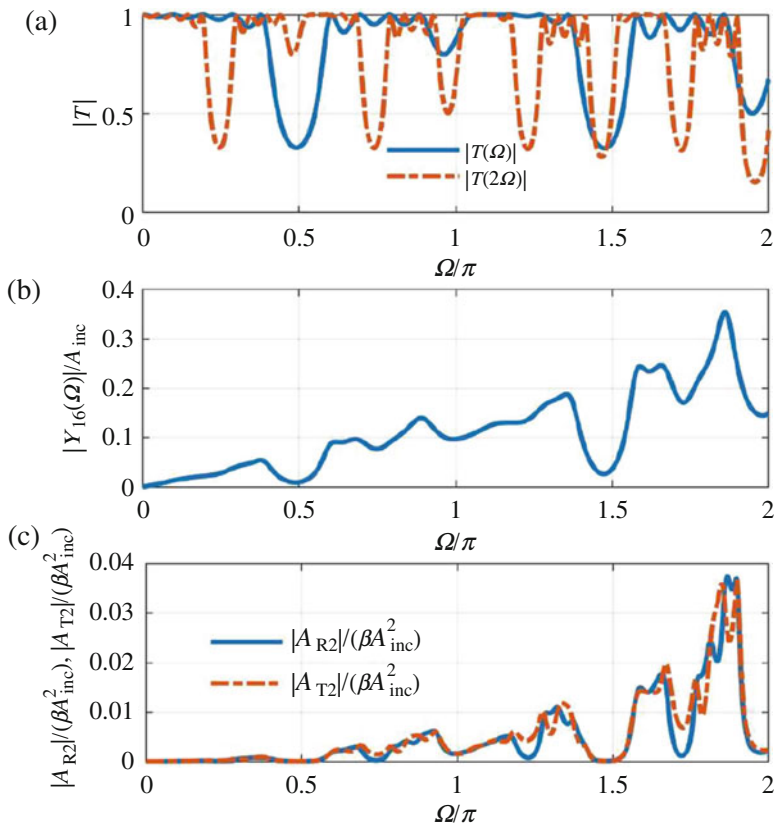

Fig. 3 Same as Fig. 2, but for $N = 10$, $\Lambda = 0.1$, $\zeta = 0.7$, and $\eta = 1$

In Fig. 2a, the bandgaps can be seen at around $\Omega/\pi = 1$ and 2, where the transmission coefficient $|T(\Omega)|$ drops to relatively low levels due to the constructive interference of scattered waves from the interfaces. When $\zeta = \eta = 1$ in Fig. 2, Layer 0 and Layer 1 have the identical material properties, so the finite interfacial stiffness (finite Λ) is solely responsible for the wave scattering at the interfaces. After being generated at the nonlinear interface, the second harmonics propagate in the layered structure linearly, namely that the second-harmonic components contained in the reflected and transmitted waves are influenced by not only the opening displacement at the nonlinear interface $|Y_{16}(\Omega)|$ in Fig. 2b but also the transmission coefficient at the double frequency $|T(2\Omega)|$ shown in Fig. 2a. For example, when $\Omega/\pi = 1.9$ in Fig. 2, the second-harmonic component generated at the nonlinear interface decays with the distance from $x = X_6$ as can be seen in

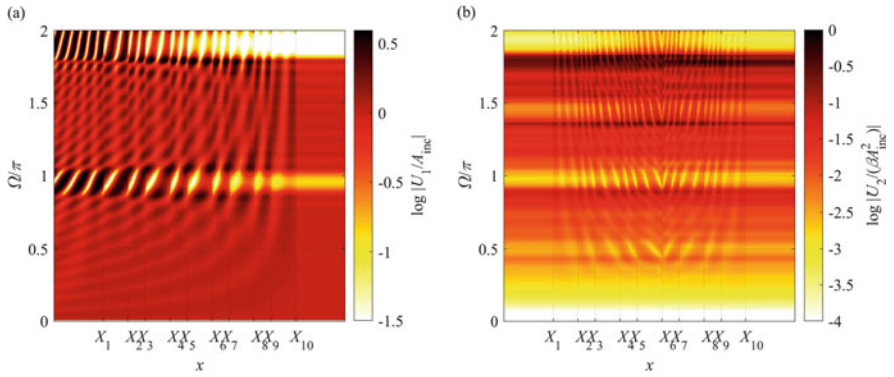

Fig. 4 Spatial distributions of displacements when $N = 10$, $\Lambda = 0.1$, $\zeta = 1$, $\eta = 1$, and $h_1/h_0 = 0.7$. (**a**) Fundamental component. (**b**) Second-harmonic component when the nonlinear interface is located at $x = X_6$

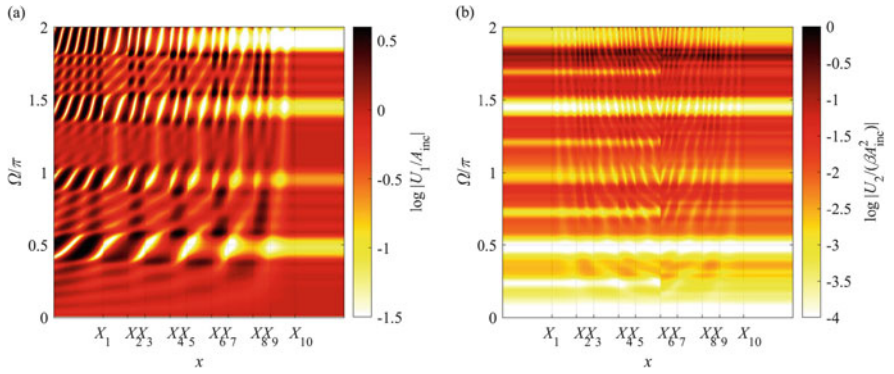

Fig. 5 Same as Fig. 4, but for $N = 10$, $\Lambda = 0.1$, $\zeta = 0.7$, $\eta = 1$, and $h_1/h_0 = 0.7$

Fig. 4b because the double frequency lies in the bandgap in Fig. 2a, which results in the smaller second-harmonic amplitudes in the reflected and transmitted fields in Fig. 2c.

On the other hand, when $\zeta (= \rho_1 c_1/(\rho_0 c_0)) = 0.7$ in Figs. 3 and 5, the mismatch of acoustic impedances between neighboring layers also contributes to the wave scattering. Hence, more bandgaps are formed in the transmission spectrum in Fig. 3a in comparison with Fig. 2a. As a consequence, the second-harmonic amplitudes in Fig. 3c have the more complicated band structure than the one in Fig. 2c. However, its generation mechanism can still be explained in the same manner as mentioned above in Figs. 2 and 4.

References

1. Manktelow, K., Narisetti, R.K., Leamy, M.J., Ruzzene, M.: Finite-element based perturbation analysis of wave propagation in nonlinear periodic structures. Mech. Syst. Signal Process. **39**, 32–46 (2013)
2. Vakakis, A.F., King, M.E.: Nonlinear wave transmission in a monocoupled elastic periodic system. J. Acoust. Soc. Am. **98**, 1534–1546 (1995)
3. Yun, Y., Miao, G.O., Zhang, P., Huang, K., Wei, R.J.: Nonlinear acoustic wave propagating in one-dimensional layered system. Phys. Lett. A **343**, 351–358 (2005)
4. Buck, O., Morris, W.L., Richardson, J.M.: Acoustic harmonic generation at unbonded interfaces and fatigue cracks. Appl. Phys. Lett. **33**, 371–373 (1978)
5. Biwa, S., Nakajima, S., Ohno, N.: On the acoustic nonlinearity of solid-solid contact with pressure-dependent interface stiffness. Trans. ASME J. Appl. Mech. **71**, 508–515 (2004)
6. Biwa, S., Ishii, Y.: Second-harmonic generation in an infinite layered structure with nonlinear spring-type interfaces. Wave Motion **63**, 55–67 (2016)
7. Ishii, Y., Biwa, S., Adachi, T.: Second-harmonic generation in a multilayered structure with nonlinear spring-type interfaces embedded between two semi-infinite media. Wave Motion **76**, 28–41 (2018)
8. Thomson, T.: Transmission of elastic waves through a stratified solid medium. J. Appl. Phys. **21**, 89–93 (1950)

Experimental and Analytical Examination in Solid Sensible Cylindrical Heat Storage Block Consisted of Ferronickel Slag

Ryuusuke Kawamura, Kozo Onoue, Yoshinori Nagase, and Shigeki Tomomatsu

Abstract Using ferronickel slag as heat storage medium, low cost solid sensible heat storage system for concentrating solar thermal power generation plant has been considered. Effects of ferronickel slag mix on amount of heat storage of mortar block specimen using ferronickel slag as a fine aggregate are evaluated. It has been shown that amount of heat storage increases as volume fraction of ferronickel slag increases in heat storage test. On the other hand, it has been shown that variation of amount of heat storage with volume fraction of ferronickel slag differs between numerical results in steady state and those in unsteady state in numerical calculations based on theoretical analysis. The reason is explained by variations of specific heat capacity and thermal conductivity in the block with volume fraction of ferronickel slag. Variation of amount of heat storage in the block in unsteady state with volume fraction of ferronickel slag has been clarified.

1 Introduction

Effective use of solar energy becomes an important issue all over the world, since solar energy has been promising as one of the renewables which enables to reduce greenhouse gas emissions. Concentrating solar thermal power generation (CSP) [1] is one of the effective technologies using solar energy for preventing from global warming. It is necessary to introduce heat storage system in CSP to be able to supply electric power in cloudy day or in the night. In general, introducing heat storage system into CSP increases electric generating capacity meanwhile it increases investments in CSP. Therefore, low cost solid sensible heat storage using concrete as heat storage medium has been investigated to reduce cost of power

R. Kawamura (✉) · Y. Nagase · S. Tomomatsu
Institute of Education and Research for Engineering, University of Miyazaki, Miyazaki, Japan
e-mail: rkawamura@cc.miyazaki-u.ac.jp

K. Onoue
Faculty of Advanced Science and Technology, Kumamoto University, Kumamoto, Japan

V. P. Matveenko et al. (eds.), *Dynamics and Control of Advanced Structures and Machines*, https://doi.org/10.1007/978-3-319-90884-7_9

generation [2, 3]. It is an important subject to develop low cost solid sensible heat storage for central power tower plants which have an advantage in energy efficiency.

In this study, ferronickel slag [4] is used as a concrete fine aggregate for heat storage medium. Ferronickel slag is an industrial by-product in refining of ferronickel at 1600–1900 °C. The slag is harmless to health, and it can be expected as inexpensive heat storage medium at elevated temperature, which also contributes to effective use of unused industrial wastes. However, applicability of the slag as heat storage medium has not been made clear. The aim of this study is to develop mortar hollow circular cylinder blocks using ferronickel slag as a fine aggregate for heat storage medium in low cost solid sensible heat storage system of concentrating solar thermal power generation plant. Effects of ferronickel slag mix on amount of heat storage in the block are evaluated by both heat storage tests and numerical calculations based on unsteady heat conduction analysis.

2 Heat Storage Test

2.1 Fabrication of Heat Storage Block Specimen

Using ferronickel slag (FNS) as a fine aggregate of mortar, mortar hollow circular cylinder block specimens for heat storage are fabricated. FNS is a granulated slag produced when processing ferronickel which is used as a raw material of stainless steel. Appearance of FNS is shown in Fig. 1. Chemical composition of FNS is shown in Table 1. Chemical composition of FNS is mainly composed of silica and magnesia. Considering workability of mortar, three kinds of mix proportions listed in Table 2 are nominated. As shown in Fig. 2, a mortar hollow circular cylinder

Fig. 1 Appearance of FNS

Table 1 Chemical composition of FNS (in weight (%))

Total Fe	SiO_2	MgO	CaO	Al_2O_3	Cr	Ni
8.34	52.9	31.3	0.52	2.04	0.88	0.06

Table 2 Mix proportion of mortar

Block	Water [g]	Cement [g]	FNS [g]
No. 1	225	449	1499
No. 2	240	481	1424
No. 3	256	512	1349

Fig. 2 Appearance of mortar block

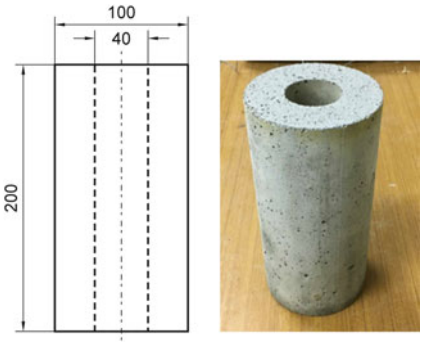

block has a length of 200 mm, an outer diameter of 100 mm, and an inner diameter of 40 mm. A piece of heat storage block specimen consists of five hollow circular cylinder blocks which are bonded in series with high temperature ceramic and graphite adhesives.

2.2 Experimental Apparatus and Test Procedures

Heat storage tests of the block specimens have been performed to examine effects of mix proportion of FNS on amount of heat storage in the specimen. Heat storage tank for the test is shown in Fig. 3. A piece of the specimen is filled in a stainless duct. Air generated by electric heater is flowed from top of the duct to bottom. Inner and outer surfaces of the specimen are heated by air at 200 °C for 60 min. Heat storage tests for three kinds of specimens No. 1–No. 3 which have different mix proportions shown in Table 2 are performed four times for each specimen. After warming up operation for 2 min. to keep air temperature generated by the heater constant, charging the specimen is started by inserting a nozzle of the heater into a stainless reducer of the tank. K-type sheath thermocouples are embedded at a depth of 15 mm from outer surface to measure temperatures of the specimen. Temperatures of air at inlet and outlet of the specimen are also measured by the thermocouples. Temperatures of both the specimen and the air are recorded by a data logger.

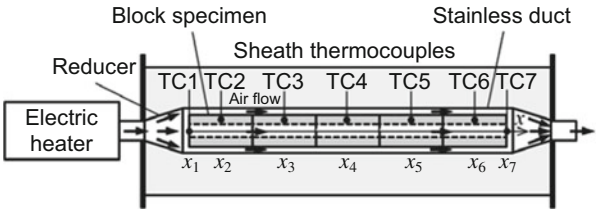

Fig. 3 Schematic view of heat storage tank

Table 3 Volume fraction of FNS, specific heat, and density in blocks

Block	Volume fraction V_{FNS}	Specific heat [kJ/kg K]	Density [kg/m^3]
No. 1	0.582	0.984	3022
No. 2	0.553	0.990	3028
No. 3	0.524	0.996	3035

2.3 Specific Heat and Density of Block Specimens

Specific heat c and density ρ in the specimen are estimated as

$$c = \frac{c_{\mathrm{FNS}}\rho_{\mathrm{FNS}}V_{\mathrm{FNS}} + c_{\mathrm{c}}\rho_{\mathrm{c}}V_{\mathrm{c}}}{\rho_{\mathrm{FNS}}V_{\mathrm{FNS}} + \rho_{\mathrm{c}}V_{\mathrm{c}}}, \tag{1}$$

$$\rho = \rho_{\mathrm{FNS}}V_{\mathrm{FNS}} + \rho_{\mathrm{c}}V_{\mathrm{c}}, \tag{2}$$

in which c_{FNS}, ρ_{FNS}, V_{FNS}, c_{c}, ρ_{c}, V_{c} are specific heat, density, and volume fractions of FNS and Portland cement, respectively. Volume fraction of FNS, specific heat, and density in blocks are shown in Table 3.

2.4 Calculation of Amount of Heat Storage of Block Specimen

Amount of heat storage of the specimen is calculated by using temperature changes in the specimen measured by the thermocouples. We assume that temperature of the specimen is constant in radial direction and changes only in axial direction. Temperature change $T(x)$ at position x in the specimen is evaluated by

$$T(x) = \frac{x_{j+1} - x}{x_{j+1} - x_j}T_j + \frac{x - x_j}{x_{j+1} - x_j}T_{j+1} \quad (j = 1, \ldots, 6), \tag{3}$$

in which x_j $(j = 1, \ldots, 7)$ are positions in axial direction of the specimen, and T_j $(j = 1, \ldots, 7)$ are temperature changes at positions x_j. Temperature changes T_1

and T_7 at both edges ($x = x_1, x_7$) are calculated as

$$T_1 = T(x_1) = \frac{x_3 - x_1}{x_3 - x_2} T_2 + \frac{x_1 - x_2}{x_3 - x_2} T_3, \tag{4}$$

$$T_7 = T(x_7) = \frac{x_6 - x_7}{x_6 - x_5} T_5 + \frac{x_7 - x_5}{x_6 - x_5} T_6. \tag{5}$$

Assuming that specific heat in the specimen does not depend on temperature but is constant, amount of heat storage in the specimen is expressed in a dimensionless form as

$$\bar{Q} = \frac{\pi}{8} \left(\bar{d}_{\mathrm{o}}^2 - \bar{d}_{\mathrm{i}}^2 \right) \bar{c} \bar{\rho} \sum_{j=1}^{6} \left(\bar{x}_{j+1} - \bar{x}_j \right) \left(\bar{T}_j + \bar{T}_{j+1} \right), \tag{6}$$

in which dimensionless quantities introduced in Eq. (6) are defined as

$$(\bar{d}_{\mathrm{o}}, \bar{d}_{\mathrm{i}}) = \frac{(d_{\mathrm{o}}, d_{\mathrm{i}})}{l}, \quad \bar{c} = \frac{c}{c_0}, \quad \bar{\rho} = \frac{\rho}{\rho_0}, \quad \bar{x}_j = \frac{x_j}{l} \ (j = 1, \ldots, 7), \tag{7}$$

$$\bar{T}_j = \frac{T_j}{\Delta T_0} \ (j = 1, \cdots, 7), \quad \bar{Q} = \frac{Q}{c_0 \rho_0 \Delta T_0 l^3}, \tag{8}$$

in which d_{o}, d_{i} are outer and inner diameters of the specimen; l is a length of the specimen; c_0, ρ_0 are typical quantities of specific heat and density; ΔT_0 is a typical temperature change.

3 Theoretical Analysis of Amount of Heat Storage

3.1 Unsteady Heat Conduction Analysis of Hollow Circular Cylinder Block Model

Effects of mix of FNS on amount of heat storage in the specimen are evaluated by numerical calculations based on unsteady heat conduction analysis.

Let the specimen be a hollow circular cylinder of inner radius a and outer radius b composed of homogeneous material subjected to heat supply at inner and outer surfaces by surrounding media. Disregarding axial variation of temperature change of the cylinder, theoretical analysis of plane axisymmetric unsteady heat conduction problem of the cylinder is developed. We assume that temperature of the cylinder is initially at uniform temperature θ_0, and that heat transfer between boundary surfaces of the cylinder and surrounding media at constant temperatures θ_{a}, θ_{b} occurs by convection with constant coefficients of heat transfer γ_{a}, γ_{b}, as shown in Fig. 4.

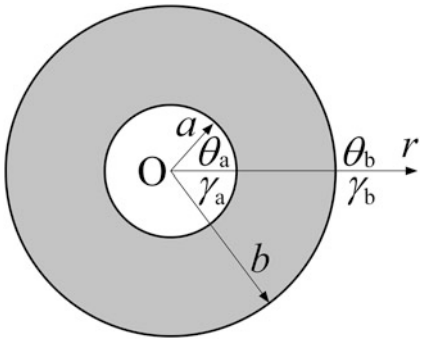

Fig. 4 Hollow circular cylinder block model

Temperature, thermal conductivity, thermal diffusivity in the model are denoted as θ, λ, κ, and coordinate in radial direction, time are denoted as r, t, respectively. Temperature changes are introduced as

$$T = \theta - \theta_0\,,\ T_a = \theta_a - \theta_0\,,\ T_b = \theta_b - \theta_0, \tag{9}$$

in which T is temperature change in the model; θ_a, θ_b are temperature changes of surrounding media. Fundamental equation of unsteady heat conduction, initial condition, and thermal boundary conditions for the model are expressed in dimensionless forms as follows:

$$\frac{\partial \bar{T}}{\partial \tau} = \bar{\kappa}\left(\frac{\partial^2 \bar{T}}{\partial \bar{r}^2} + \frac{1}{\bar{r}}\frac{\partial \bar{T}}{\partial \bar{r}}\right), \tag{10}$$

$$\bar{T} = 0 \quad \text{at} \quad \tau = 0, \tag{11}$$

$$-\frac{\partial \bar{T}}{\partial \bar{r}} + \bar{h}_a\left(\bar{T} - \bar{T}_a\right) = 0 \quad \text{at} \quad \bar{r} = \bar{a}, \tag{12}$$

$$-\frac{\partial \bar{T}}{\partial \bar{r}} + \bar{h}_b\left(\bar{T}_b - \bar{T}\right) = 0 \quad \text{at} \quad \bar{r} = \bar{b} \tag{13}$$

Dimensionless quantities introduced in Eqs. (10)–(13) are defined as follows:

$$\left(\bar{T}, \bar{T}_a, \bar{T}_b\right) = \frac{(T, T_a, T_b)}{T_0}\,,\ \left(\bar{r}, \bar{a}, \bar{b}\right) = \frac{(r, a, b)}{l}\,,\ \bar{\kappa} = \frac{\bar{\lambda}}{\bar{c}\bar{\rho}},$$
$$\bar{\lambda} = \frac{\lambda}{\lambda_0}\,,\ \bar{\rho} = \frac{\rho}{\rho_0}\,,\ \bar{c} = \frac{c}{c_0}\,,\ \tau = \frac{\lambda_0}{c_0\rho_0 l^2}t\,,\ \bar{h}_a = \frac{l\gamma_a}{\lambda}\,,\ \bar{h}_b = \frac{l\gamma_b}{\lambda}, \tag{14}$$

in which T_0, λ_0 are typical quantities of temperature change and thermal conductivity.

Using Laplace transformation method, analytical solution of temperature change in the model T is expressed in a dimensionless form as

$$\bar{T}(\bar{r},\tau) = \sum_{m=1}^{\infty} \frac{2e^{-{\omega_m}^2\tau}}{\omega_m \Delta'_{\mathrm{ut}}(\omega_m)} \left\{ \bar{A}_m J_0\left(\frac{\omega_m}{\sqrt{\bar{\kappa}}}\bar{r}\right) + \bar{B}_m Y_0\left(\frac{\omega_m}{\sqrt{\bar{\kappa}}}\bar{r}\right) \right\} + \frac{1}{\Delta_{\mathrm{st}}}\left(\bar{A}' + \bar{B}' \ln \bar{r}\right), \tag{15}$$

in which J_0, Y_0 are Bessel functions of first and second kinds with order zero; ω_m is m-th positive eigenvalue; $\bar{A}_m$, $\bar{B}_m$, $\Delta'_{\mathrm{ut}}(\omega_m)$ are coefficients; and $\bar{A}'$, $\bar{B}'$, Δ_{st} are constants, whose detailed expressions are omitted.

3.2 Amount of Heat Storage Per Unit Length

Using the solution of temperature change in the model, amount of heat storage per unit length q in the model is expressed in a dimensionless form as

$$\bar{q} = 2\pi\bar{c}\bar{\rho}\left[\left[\sum_{m=1}^{\infty} \frac{2e^{-{\omega_m}^2\tau}}{\omega_m \Delta'_{\mathrm{ut}}(\omega_m)} \left[\bar{A}_m \left\{\bar{b} J_1\left(\frac{\omega_m}{\sqrt{\bar{\kappa}}}\bar{b}\right) - \bar{a} J_1\left(\frac{\omega_m}{\sqrt{\bar{\kappa}}}\bar{a}\right)\right\} + \bar{B}_m \left\{\bar{b} Y_1\left(\frac{\omega_m}{\sqrt{\bar{\kappa}}}\bar{b}\right) - \bar{a} Y_1\left(\frac{\omega_m}{\sqrt{\bar{\kappa}}}\bar{a}\right)\right\}\right] + \frac{1}{\Delta_{\mathrm{st}}}\left[\frac{\bar{A}'}{2}\left(\bar{b}^2 - \bar{a}^2\right) + \bar{B}'\left\{\frac{\bar{b}^2}{2}\left(\ln \bar{b} - \frac{1}{2}\right) - \left(\ln \bar{a} - \frac{1}{2}\right)\right\}\right]\right]\right], \tag{16}$$

in which J_1, Y_1 are Bessel functions of first and second kinds with order one. Dimensionless quantity introduced in Eq. (16) is defined as

$$\bar{q} = \frac{q}{c_0 \rho_0 l^2 T_0}. \tag{17}$$

4 Results and Discussion

Experimental results in heat storage tests for the specimens which have three different kinds of FNS mix are presented.

Table 4 Temperature change of thermocouple TC2 and amount of heat storage

Block	Volume fraction V_{FNS}	Temperature change T_2 [°C]	Amount of heat storage Q [kJ]
No. 1	0.582	179	2127
No. 2	0.553	178	2063
No. 3	0.524	176	2019

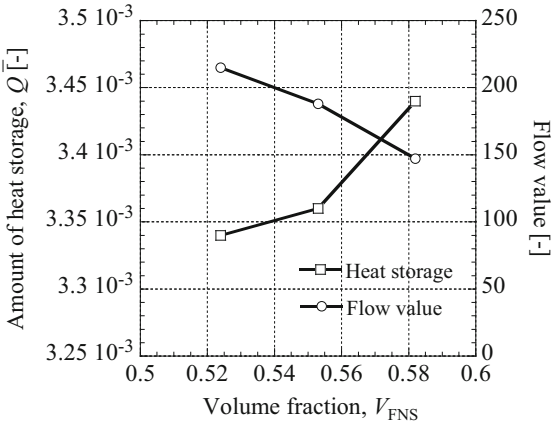

Fig. 5 Variations of amount of heat storage and flow value with volume fraction V_{FNS}

Table 4 shows the volume fractions V_{FNS}, temperature changes of thermocouple TC2 of the specimens, and amounts of heat storage. Temperature change of the specimen No. 1 in which the volume fraction V_{FNS} is the largest among three specimens is the highest and amount of heat storage is also the largest. Figure 5 shows variations of amount of heat storage $\bar{Q}$ in the specimen and flow value of fresh mortar with the volume fraction V_{FNS}. As the volume fraction V_{FNS} increases, amount of heat storage $\bar{Q}$ increases, while flow value of fresh mortar decreases. It is found that the specimen, which has the high volume fraction V_{FNS}, exhibits high performance in terms of heat storage. Because flow value of fresh mortar decreases, it is necessary to take fabrication of block into account. Next, numerical results of amount of heat storage per unit length q in the model based on unsteady heat conduction analysis are presented. Table 5 shows numerical parameters, and Fig. 6 shows variations of specific heat capacity $c\rho$ and thermal conductivity λ with the volume fraction V_{FNS}. Thermal conductivity λ is estimated by Kerner's law of mixture. As the volume fraction V_{FNS} increases, specific heat capacity $c\rho$ decreases, while thermal conductivity λ increases.

Figure 7 shows time evolutions of amount of heat storage per unit length $\bar{q}$ for three kinds of the models, and Fig. 8 is an enlarged drawing of Fig. 7 near steady state. The amount of heat storage $\bar{q}$ in steady state for Block No. 3 is the largest among the three blocks. As the volume fraction V_{FNS} increases, the amount of heat storage $\bar{q}$ in steady state decreases. Figure 9 shows variation of the amount of heat storage $\bar{q}$ in unsteady state ($t = 570$ s) with the volume fraction V_{FNS}. As

Table 5 Numerical parameters

Inner radius a [m]	0.02
Outer radius b [m]	0.05
Initial temperature θ_0 [°C]	17.9
Temperature of inner surrounding medium θ_a [°C]	194.5
Temperature of outer surrounding medium θ_b [°C]	194.5
Typical value of temperature change T_0 [°C]	200
Coefficient of heat transfer at inner surface γ_a [W/m^2 K]	12
Coefficient of heat transfer at outer surface γ_b [W/m^2 K]	12
Length of block specimen l [m]	1

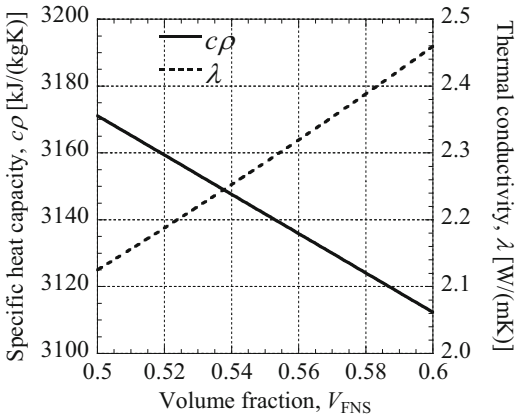

Fig. 6 Variations of specific heat capacity and thermal conductivity with volume fraction V_{FNS}

the volume fraction V_{FNS} increases, the amount of heat storage $\bar{q}$ in steady state increases. It is found that variation of the amount of heat storage $\bar{q}$ in unsteady state with the volume fraction V_{FNS} turns out the opposite of one $\bar{q}$ in steady state with the volume fraction V_{FNS}. As the volume fraction V_{FNS} increases, thermal conductivity λ increases as shown in Fig. 6, and temperature change in unsteady state also increases. The amount of heat storage $\bar{q}$ in unsteady state for Block No. 1 is the largest among the three blocks because the amount of heat storage $\bar{q}$ depends on product of specific heat capacity $c\rho$ and temperature change. The amount of heat storage $\bar{q}$ depends on specific heat capacity $c\rho$ because temperatures in steady state for three kinds of blocks are same with the volume fraction V_{FNS}. Figure 10 shows comparison of experimental results of amount of heat storage per unit length with analytical one after a lapse of an hour of heating. Experimental results of amount of heat storage per unit length are larger than analytical one. The reason is that radial variation of temperature change of the block is not considered when calculating experimental results of amount of heat storage. In heat storage tests,

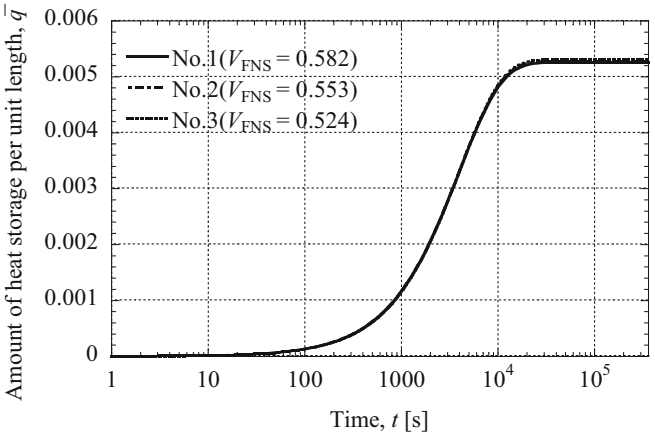

Fig. 7 Time evolutions of amount of heat storage per unit length

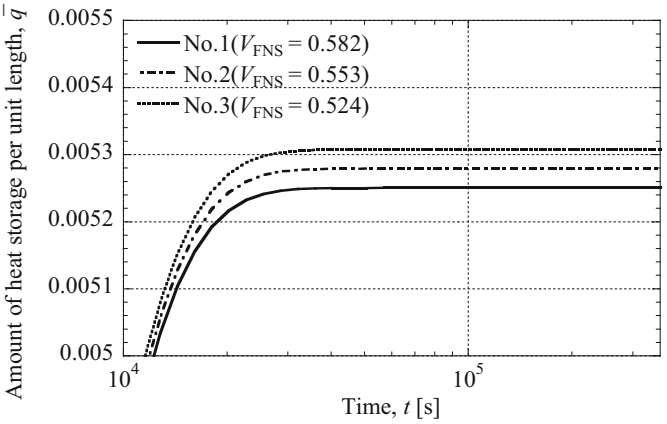

Fig. 8 Time evolutions of amount of heat storage per unit length (enlarged Fig. 7)

temperatures of the block are measured by the thermocouples embedded in the block at a depth of 15 mm from its outer surface to measure, and amount of heat storage is calculated under assumption that temperature is constant in radial direction of the block. Therefore, it is necessary to consider radial variation of temperature change in the block to obtain amount of heat storage of block.

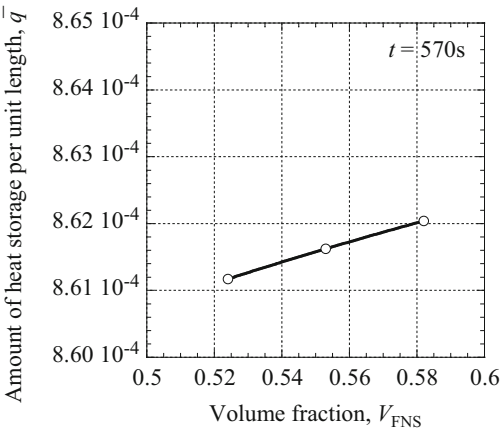

Fig. 9 Variation of amount of heat storage per unit length with volume fraction V_{FNS} in unsteady state ($t = 570$ s)

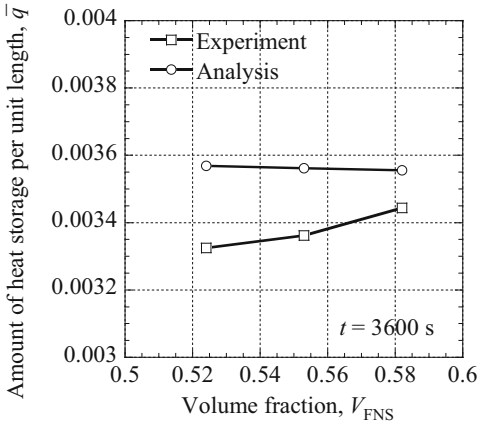

Fig. 10 Comparison of experimental result of amount of heat storage with analytical one

5 Conclusions

The following conclusions are drawn from results of heat storage tests and numerical calculations based on theoretical analysis on effects of volume fraction of ferronickel slag on amount of heat storage in mortar hollow circular cylinder blocks.

1. In heat storage tests, amount of heat storage increases, while flow value of fresh mortar decreases as volume fraction of ferronickel slag increases.
2. In numerical calculations based on theoretical analysis, variation of amount of heat storage in unsteady state with volume fraction of ferronickel slag turns out the opposite of one in steady state with volume fraction of the slag.
3. It is necessary to measure temperatures on inner and outer surfaces to evaluate amount of heat storage of the block accurately.

Consequently, effects of volume fraction of ferronickel slag on amount of heat storage in the mortar hollow circular cylinder block in unsteady state are revealed.

Acknowledgements This work was supported by JSPS KAKENHI Grant Number JP15K05680. The authors would like to thank Mr. Kentaro Yasui of University of Miyazaki for the support to prepare specimens, and to thank Mr. Kensuke Hayase, Mr. Jin Ikeda, Mr. Katsunori Takagi, Mr. Shohei Iwakiri, Mr. Zhiyun Zhou, Ms. Yukiko Nakanishi, Mr. Masataka Takei, and Mr. Makoto Yokota for the assistances with experiments and numerical calculations in this study.

References

1. New Energy and Industrial Technology Development Organization (NEDO): White paper on renewable energy technologies, 2nd edn. (2014) (in Japanese)
2. Laing, D., Steinmann, W.D., Tamme, R., Richter, C.: Solid media thermal storage for parabolic trough power plants. Sol. Energy **80**, 1283–1289 (2006)
3. Laing, D., Lehmann, D., Fiß, M.: Test results of concrete thermal energy storage for parabolic trough power plants. Trans. ASME J. Sol. Energy Eng. **131**, 041007-1–041007-6 (2009)
4. Sumitomo Metal Mining Co. Ltd. http://smm.co.jp/E/products/refining/greensand/

A Complete Direct Approach to Modeling of Dielectric Elastomer Plates as Material Surfaces

Michael Krommer and Elisabeth Staudigl

Abstract In this paper we present a complete direct approach to modeling nonlinear plates, which are made of incompressible dielectric elastomer layers. In particular, the layers are assumed to exhibit a neo-Hookean elastic behavior and the effect of electrostatic forces is incorporated by a purely electrical contribution to the Helmholtz free energy. In our previous work on this subject, two-dimensional constitutive relations for the plate were derived by numerical integration of the three-dimensional augmented free energy through the plate thickness imposing a plane stress assumption and an a-priori assumption concerning the distribution of the strain through the thickness of the plate. In contrast, we directly postulate the form of the two-dimensional augmented free energy for the structural plate problem in this paper. Results computed within the framework of this novel approach are compared to results from our previous work, which are well tested against existing solutions in the literature. A very good agreement is found.

1 Introduction

The general theory of elastic dielectrics dates back to [1], and has been further developed in, e.g., [2–4] and [5]. Elastic dielectrics belong to the class of so-called smart or intelligent materials, which are often used as structurally integrated materials to put structures into practice, which exhibit both, sensing and actuating authority. Such structures are denoted as smart structures. Prominent examples are piezoelectric materials, but also electro-active polymers. Concerning the latter we refer to, e.g., [6] or [7]. Due to the large deformations in electro-active polymers, nonlinear and electro-mechanically coupled formulations are required, in which two types of coupling are typically accounted for: coupling by means of electrostatic forces and constitutive coupling through coupling effects like electrostriction, see,

M. Krommer (✉) · E. Staudigl
Institute of Mechanics and Mechatronics, TU Wien, Vienna, Austria
e-mail: michael.krommer@tuwien.ac.at; elisabeth.staudigl@tuwien.ac.at

V. P. Matveenko et al. (eds.), *Dynamics and Control of Advanced Structures and Machines*, https://doi.org/10.1007/978-3-319-90884-7_10

e.g., [6]. For three-dimensional Eulerian and Lagrangian formulations, we refer to [8] and [9].

A practically important sub-class of electro-active polymers are dielectric elastomers, for which the constitutive coupling is often assumed negligible, and the actuation is then caused solely by the electrostatic forces. Practical applications of such dielectric elastomer actuation devices can be found, e.g., in [10–12] and [13]. In general problems of dielectric elastomer actuators numerical methods, such as the Finite Element method, are applied implementing solid elements for general three-dimensional problems [9, 14, 15] or solid shell elements to account for the typical thinness of the dielectric elastomer actuators, as developed in [16].

In our own previous work, see [17], we proposed a strategy for the modeling of thin dielectric elastomer plates, in which the plate was considered as a material surface with mechanical and electrical degrees of freedom, and the specific constitutive relations were obtained from the three-dimensional ones by the assumption of a plane stress and an a-priori assumption concerning the distribution of the strain through the thickness of the plate. Numerical integration was applied to compute the structural two-dimensional constitutive relations. In elasticity such an approach has been successfully used for elastic plates and shells [18, 19] and [20], and extended to the electro-mechanically coupled problem of piezoelectric plates and shells in [21] and [22].

In this paper we directly postulate the form of the two-dimensional augmented free energy for the structural plate problem, from which structural two-dimensional constitutive relations follow as a consequence from an extension of the principle of virtual work to the electro-mechanically coupled problem. We compute results with the proposed direct approach and compare them to validated results reported in [17].

2 Nonlinear Dielectric Elastomer Plates as Material Surfaces

In this section we briefly summarize the governing equations of thin plates modeled as material surfaces with mechanical and electrical degrees of freedom. For details concerning these equations we refer the reader to [17] and [22]. In particular, we consider the plate as a two-dimensional continuum of "needles" with five mechanical degrees of freedom, three translations $\delta\mathbf{r}$, and two rotations $\delta\mathbf{k}$, in which the variation of the unit normal vector $\mathbf{k}$ lies in the tangential plane. This resembles the notion of a single director attached to each particle of the plate, introduced in [23]. Concerning the electrical degrees of freedom, we use only the dominant one—the electric potential difference V.

2.1 Strain Measures

The material surface is plane in the reference configuration, and it is denoted as reference surface. In the deformed or actual configuration the deformed material surface is denoted as actual surface. The first metric tensor of the reference surface $\mathbf{A} = \mathbf{I}$ plays the role of the two-dimensional identity tensor. The second metric tensor is zero for the plane reference surface, $\mathbf{B} = \mathbf{0}$. For the actual surface the first and second metric tensors are $\mathbf{a}$ and $\mathbf{b}$. The reference configuration and the actual configuration of the material surface are related to each other by means of a deformation gradient tensor $\mathbf{F} = (\nabla \mathbf{r})^T$ with the position vector $\mathbf{r}$ of points of the actual surface and the differential operator ∇ of the reference surface. With the aid of the deformation gradient tensor, we introduce two tensor valued Green strain measures for the material surface, which are defined as the difference between the two metric tensors in the two configurations; yet, with the proper transformation by means of $\mathbf{F}$ applied to the metric tensors of the actual surface $\mathbf{a}$ and $\mathbf{b}$. These two strain measures are

$$\boldsymbol{\varepsilon} = \frac{1}{2}\left(\mathbf{F}^T \cdot \mathbf{a} \cdot \mathbf{F} - \mathbf{I}\right), \quad \boldsymbol{\kappa} = -\mathbf{F}^T \cdot \mathbf{b} \cdot \mathbf{F}, \tag{1}$$

with the right-Cauchy Green tensor $\mathbf{C}$ of the material surface as $\mathbf{C} = \mathbf{F}^T \cdot \mathbf{a} \cdot \mathbf{F} = \mathbf{F}^T \cdot \mathbf{F}$. Both strain measures remain constant, if and only if the motion of the material surface is a rigid body motion, see [24] for a discussion.

2.2 Principle of Virtual Work

We introduce a generalized principle of virtual work as

$$\int_A \delta(\eta_0 \Omega) dA + \int_A \sigma \delta V dA + \delta A^e = 0, \tag{2}$$

with the mass η_0 per unit undeformed area. Integration is done over the domain A of the reference surface. $\eta_0 \Omega$ is the plate augmented free energy per unit area in the reference configuration, δA^e is the virtual work of external forces and moments, which through boundary forces and moments involves mechanical and electrical sources, and the second integral accounts for the external electric charge σ per unit reference area with δV being the variation of the electric potential. It has been shown before, see [17], that the augmented free energy of the plate has the form $\eta_0 \Omega = \eta_0 \Omega(\boldsymbol{\varepsilon}, \boldsymbol{\kappa}, V)$, such that its variation reads

$$\delta(\eta_0 \Omega) = \eta_0 \frac{\partial \Omega}{\partial \boldsymbol{\varepsilon}} \cdot\cdot \delta \boldsymbol{\varepsilon} + \eta_0 \frac{\partial \Omega}{\partial \boldsymbol{\kappa}} \cdot\cdot \delta \boldsymbol{\kappa} + \eta_0 \frac{\partial \Omega}{\partial V} \delta V. \tag{3}$$

Moreover, stress measures $\boldsymbol{\tau}$ and $\boldsymbol{\mu}$ as well as the internal charge q per unit reference area are obtained through the constitutive relations

$$\boldsymbol{\tau} = \eta_0 \frac{\partial \Omega}{\partial \boldsymbol{\varepsilon}} = 2\eta_0 \frac{\partial \Omega}{\partial \mathbf{C}}\,,\ \boldsymbol{\mu} = \eta_0 \frac{\partial \Omega}{\partial \boldsymbol{\kappa}}\,,\ q = -\eta_0 \frac{\partial \Omega}{\partial V}, \tag{4}$$

and the variation becomes $\delta(\eta_0 \Omega) = \boldsymbol{\tau} \cdot\cdot\, \delta\boldsymbol{\varepsilon} + \boldsymbol{\mu} \cdot\cdot\, \delta\boldsymbol{\kappa} - q\delta V$.

With the extended principle of virtual work at hand, we can derive the governing equations or use the principle as a starting point for a numerical solution. In any case, it remains to derive the specific form for the plate augmented free energy $\eta_0 \Omega(\boldsymbol{\varepsilon}, \boldsymbol{\kappa}, V)$.

2.3 Augmented Free Energy

First, we study a single layer dielectric elastomer plate with the thickness h. The material is assumed to exhibit a neo-Hookean behavior and to be incompressible. Moreover, we consider the thickness center surface as the material surface. In analogy to the three-dimensional case, we decompose the structural augmented free energy into a purely mechanical part $\eta_0 \Omega^{mech}$ and an electrical part $\eta_0 \Omega^{elec}$. The mechanical part is further additively composed of a membrane part and a bending part, $\Omega^{mech} = \Omega_m^{mech} + \Omega_b^{mech}$. With the right Cauchy–Green tensor $\mathbf{C}$ of the material surface, we introduce the membrane part of the mechanical contribution to the structural augmented free energy in analogy to a plane stress augmented free energy for an incompressible neo-Hookean material as

$$\eta_0 \Omega_m^{mech} = \frac{1}{2}\frac{A}{4}\left(\mathrm{tr}\mathbf{C} + (\det\mathbf{C})^{-1} - 3\right), \tag{5}$$

with the extensional stiffness $A = Yh(1-\nu^2)^{-1}$ known from linear plate theory. In the latter incompressibility is accounted for by means of $\nu = 0.5$ and Young's modulus becomes $Y = 3\mu$; then, $A = 4\mu h$ holds. Next, we introduce the bending part Ω_b^{mech} of the structural augmented free energy in analogy to the bending energy of an isotropic incompressible Kirchhoff plate as

$$\eta \Omega_b^{mech} = \frac{1}{2}\tilde{D}\left(\frac{1}{2}(\mathrm{tr}\tilde{\boldsymbol{\kappa}})^2 + \frac{1}{2}\tilde{\boldsymbol{\kappa}} \cdot\cdot\, \tilde{\boldsymbol{\kappa}}\right), \tag{6}$$

in which all entities are referred to the actual configuration. $J = \det\mathbf{F}$ is the area change from the undeformed to the deformed configuration, $\eta = J^{-1}\eta_0$ is the mass per unit area in the deformed configuration, $\tilde{\boldsymbol{\kappa}} = -\mathbf{b} = \mathbf{F}^{-T} \cdot \boldsymbol{\kappa} \cdot \mathbf{F}^{-1}$ is the negative second metric tensor of the actual surface, and the thickness change is accounted for in the definition of a plate stiffness $\tilde{D} = J^{-3}D$. $D = Yh^3/12(1-\nu^2)^{-1}$ is the classical plate stiffness, which for an incompressible material with $\nu = 0.5$ is

$D = \mu h^3/3$. Therefore, we have

$$\eta_0 \Omega_b^{mech} = \frac{1}{2}(\det\mathbf{C})^{-1} D \left((\mathrm{tr}\tilde{\boldsymbol{\kappa}})^2 - \det\tilde{\boldsymbol{\kappa}} \right) \tag{7}$$

for the bending part of the augmented free energy. Concerning the electrical contribution to the augmented free energy we write $2\eta\Omega^{elec} = -\tilde{c}V^2$, with the voltage V and the capacity $\tilde{c}$ per unit deformed area, which is related to the capacity per unit undeformed area c by $\tilde{c} = Jc$. Therefore, we have

$$\eta_0 \Omega^{elec} = -\frac{1}{2} c V^2 (\det\mathbf{C}). \tag{8}$$

We summarize our result. In the nonlinear case we have the augmented free energy of a single layer incompressible dielectric elastomer plate

$$\begin{aligned} \eta_0 \Omega(\mathbf{C}, \tilde{\boldsymbol{\kappa}}, V^2) = {} & \frac{1}{2}\frac{A}{4}\left(\mathrm{tr}\mathbf{C} + (\det\mathbf{C})^{-1} - 3 \right) \\ & + \frac{1}{2}(\det\mathbf{C})^{-1} D \left((\mathrm{tr}\tilde{\boldsymbol{\kappa}})^2 - \det\tilde{\boldsymbol{\kappa}} \right) - \frac{1}{2} c V^2 (\det\mathbf{C}), \end{aligned} \tag{9}$$

in which $\mathbf{C} = 2\boldsymbol{\varepsilon} + \mathbf{I}$ holds. Moreover, we note the identities $\mathrm{tr}\tilde{\boldsymbol{\kappa}} = \mathrm{tr}(\mathbf{C}^{-1} \cdot \boldsymbol{\kappa})$ and $\det\tilde{\boldsymbol{\kappa}} = \det(\mathbf{C}^{-1} \cdot \boldsymbol{\kappa})$, from which we conclude that $\Omega = \Omega(\boldsymbol{\varepsilon}, \boldsymbol{\kappa}, V)$ is true.

Change of Material Surface Our formulation holds only for a single layer dielectric elastomer plate, for which the physical thickness center surface is taken as the material surface. Using a different physical surface as the material surface, we must extend the form of the augmented free energy accordingly. Owing to the thinness of the plate, we assume the curvature tensor $\boldsymbol{\kappa}$ to be invariant under such a change of the material surface. In contrast, the right Cauchy–Green tensor $\mathbf{C}$ is not invariant, but transforms according to $\mathbf{C} \to \mathbf{C} + 2\lambda_m \boldsymbol{\kappa}$, in which λ_m is a geometry parameter accounting for the change of the material surface. Moreover, λ_m is of the same order of smallness as the plate thickness h. We start the derivation with the membrane energy $\eta_0 \Omega_m^{mech} = \eta_0 \Omega_m^{mech}(\mathbf{C})$ by replacing $\mathbf{C}$ with $\mathbf{C} + 2\lambda_m \boldsymbol{\kappa}$ and conducting a formal expansion with respect to λ_m up to terms of order λ_m^3. This results into

$$\begin{aligned} \eta_0 \Omega_m^{mech} \approx {} & \frac{1}{2}\frac{A}{4}\left(\mathrm{tr}\mathbf{C} + (\det\mathbf{C})^{-1} - 3 \right) + \frac{1}{2}\frac{A}{2}\lambda_m \left(\mathrm{tr}\boldsymbol{\kappa} - (\det\mathbf{C})^{-1} \mathrm{tr}\tilde{\boldsymbol{\kappa}} \right) \\ & + \frac{1}{2} A \lambda_m^2 (\det\mathbf{C})^{-1} \left((\mathrm{tr}\tilde{\boldsymbol{\kappa}})^2 - \det\tilde{\boldsymbol{\kappa}} \right) \\ & + \frac{1}{2} 2A \lambda_m^3 (\det\mathbf{C})^{-2} \mathrm{tr}\tilde{\boldsymbol{\kappa}} \left(2\det\boldsymbol{\kappa} - \det\mathbf{C} (\mathrm{tr}\tilde{\boldsymbol{\kappa}})^2 \right). \end{aligned} \tag{10}$$

Likewise, we treat the electrical part of the energy and find the exact result

$$\eta_0 \Omega^{elec} = -\frac{1}{2} c V^2 \left(\det\mathbf{C} \, (1 + 2\lambda_m \mathrm{tr}\tilde{\boldsymbol{\kappa}}) + 4\lambda_m^2 \det\boldsymbol{\kappa} \right). \tag{11}$$

Concerning the bending energy we note that it is proportional to h^3 rather than the membrane energy, which is only proportional to h. Therefore, the order of smallness of the bending energy is already λ_m^2 and it is sufficient to have a formal expansion with respect to λ_m up to terms of order λ_m; hence,

$$\begin{aligned} \eta_0 \Omega_b^{mech} \approx & \frac{1}{2} (\det\mathbf{C})^{-1} D \left((\mathrm{tr}\tilde{\boldsymbol{\kappa}})^2 - \det\tilde{\boldsymbol{\kappa}} \right) \\ & + \frac{1}{2} 6 D \lambda_m (\det\mathbf{C})^{-2} \mathrm{tr}\tilde{\boldsymbol{\kappa}} \left(2\det\boldsymbol{\kappa} - \det\mathbf{C} (\mathrm{tr}\tilde{\boldsymbol{\kappa}})^2 \right). \end{aligned} \tag{12}$$

In conclusion, we write the augmented free energy for the single layer dielectric elastomer plate as

$$\begin{aligned} \eta_0 \Omega = & \frac{1}{2} \frac{A}{4} \left(\mathrm{tr}\mathbf{C} + (\det\mathbf{C})^{-1} - 3 \right) + \frac{1}{2} \frac{A}{2} \lambda_m \left(\mathrm{tr}\boldsymbol{\kappa} - (\det\mathbf{C})^{-1} \mathrm{tr}\tilde{\boldsymbol{\kappa}} \right) \\ & + \frac{1}{2} \left(D + A\lambda_m^2 \right) (\det\mathbf{C})^{-1} \left((\mathrm{tr}\tilde{\boldsymbol{\kappa}})^2 - \det\tilde{\boldsymbol{\kappa}} \right) \\ & + \frac{1}{2} 2 \left(A\lambda_m^2 + 3D \right) \lambda_m (\det\mathbf{C})^{-2} \mathrm{tr}\tilde{\boldsymbol{\kappa}} \left(2\det\boldsymbol{\kappa} - \det\mathbf{C} (\mathrm{tr}\tilde{\boldsymbol{\kappa}})^2 \right) \\ & - \frac{1}{2} c V^2 \left(\det\mathbf{C} \, (1 + 2\lambda_m \mathrm{tr}\tilde{\boldsymbol{\kappa}}) + 4\lambda_m^2 \det\boldsymbol{\kappa} \right), \end{aligned} \tag{13}$$

in which A and D are stiffnesses referring to the center surface of the plate, whereas λ_m characterizes the distance of the material surface from this center surface. However, we are not so much interested in the derivation of these parameters, but rather in the functional dependency of the different terms of the augmented free energy on the strain measures. To identify the material parameters as well as the sources of actuation we will linearize our formulation and compare the result to the well-known linear theory.

Small Strain Regime Finally, we linearize the augmented free energy in the small strain regime, in which we have $\mathbf{C} = \mathbf{I} + 2\lambda\boldsymbol{\varepsilon}$ with λ as a formal small parameter; also $\boldsymbol{\kappa}$ is formally replaced by $\lambda\boldsymbol{\kappa}$. Concerning the voltage V we assume its square to be of order λ. Then, an expansion in the vicinity of $\lambda = 0$ finds the principal term λ^1 of the augmented free energy to be independent from any deformation measure. Therefore, the leading order term for the plate theory is of order λ^2 and it reads

$$\begin{aligned} \eta_0 \Omega^{lin} = & \frac{1}{2} \left(A \left((\mathrm{tr}\boldsymbol{\varepsilon})^2 - \det\boldsymbol{\varepsilon} \right) - 2cV^2 \mathrm{tr}\boldsymbol{\varepsilon} \right) + \frac{1}{2} A \lambda_m \left(\mathrm{tr}\boldsymbol{\varepsilon} \mathrm{tr}\boldsymbol{\kappa} + \boldsymbol{\varepsilon} \cdot\cdot \boldsymbol{\kappa} \right) \\ & + \frac{1}{2} \left(\left(D + A\lambda_m^2 \right) \left((\mathrm{tr}\boldsymbol{\kappa})^2 - \det\boldsymbol{\kappa} \right) - 2c\lambda_m V^2 \mathrm{tr}\boldsymbol{\kappa} \right). \end{aligned} \tag{14}$$

On the other hand, the linear theory of thin plates with eigenstrains is well studied, see [25]; for the case of an isotropic incompressible material obeying Hooke's law using any other surface than the neutral surface as a reference surface we have

$$\eta_0\Omega^{Hooke} = \frac{1}{2}\left(\bar{A}\left((\mathrm{tr}\boldsymbol{\varepsilon})^2 - \det\boldsymbol{\varepsilon}\right) - 2\tau^*\mathrm{tr}\boldsymbol{\varepsilon}\right) + \frac{1}{2}\bar{B}\left(\mathrm{tr}\boldsymbol{\varepsilon}\mathrm{tr}\boldsymbol{\kappa} + \boldsymbol{\varepsilon}\cdot\cdot\boldsymbol{\kappa}\right) + \frac{1}{2}\left(\bar{D}\left((\mathrm{tr}\boldsymbol{\kappa})^2 - \det\boldsymbol{\kappa}\right) - 2\mu^*\mathrm{tr}\boldsymbol{\kappa}\right), \tag{15}$$

in which the actuation enters classically by means of so-called *Eigenspannungsquellen* τ^* and $\mu^* = Z_m\tau^*$, provided the corresponding source is constant through the thickness. Z_m is the thickness position of the neutral surface, which is in the thickness center of the plate. The extensional stiffness $\bar{A}$, the coupling stiffness $\bar{B}$, and the bending stiffness $\bar{D}$ as well as the *Eigenspannungsquellen* are defined as

$$\begin{aligned}(\bar{A}, \bar{B}, \bar{D}) &= 4\mu\int_{Z_o}^{Z_o+h}(1, Z, Z^2)dZ,\\ (\tau^*, \mu^*) &= \int_{Z_o}^{Z_o+h}\varepsilon_0\varepsilon_r\left(\frac{V}{h}\right)^2(1, Z)dZ,\\ Z_m &= \frac{1}{h}\int_{Z_o}^{Z_o+h}ZdZ.\end{aligned} \tag{16}$$

Z_o is the thickness coordinate of the upper side of the plate and ε_0 and ε_r are the permittivity in vacuum and the relative permittivity. This specific type of actuation is due to Coulomb forces. Comparing the linearized version of the nonlinear theory to the linear theory we identify the material parameters and the actuation of the nonlinear theory, and eventually write the augmented free energy as

$$\begin{aligned}\eta_0\Omega = &\frac{1}{2}\frac{\bar{A}}{4}\left(\mathrm{tr}\mathbf{C} + (\det\mathbf{C})^{-1} - 3\right) + \frac{1}{2}\frac{\bar{B}}{2}\left(\mathrm{tr}\boldsymbol{\kappa} - (\det\mathbf{C})^{-1}\mathrm{tr}\tilde{\boldsymbol{\kappa}}\right)\\ &+ \frac{1}{2}\bar{D}(\det\mathbf{C})^{-1}\left((\mathrm{tr}\tilde{\boldsymbol{\kappa}})^2 - \det\tilde{\boldsymbol{\kappa}}\right) + \frac{1}{2}2\bar{K}(\det\mathbf{C})^{-2}\mathrm{tr}\tilde{\boldsymbol{\kappa}}\left(2\det\boldsymbol{\kappa} - \det\mathbf{C}(\mathrm{tr}\tilde{\boldsymbol{\kappa}})^2\right)\\ &- \frac{1}{2}\tau^*\left(\det\mathbf{C}\,(1 + 2Z_m\mathrm{tr}\tilde{\boldsymbol{\kappa}}) + 4Z_m^2\det\boldsymbol{\kappa}\right).\end{aligned} \tag{17}$$

with $\tau^* = cV^2$ and $ch = \varepsilon_0\varepsilon_r$. By analogy, we identify the corresponding higher order coupling stiffness $\bar{K}$ as

$$\bar{K} = 4\mu\int_{Z_o}^{Z_o+h}Z^3dZ. \tag{18}$$

This completes the discussion of the augmented free energy. Having this energy at hand we can easily study layered plates as well, because the choice of the material surface as any physical surface is possible.

3 Validation

As a simple example, we are studying a rectangular plate with dimension $a \times b \times h = 100\,\text{mm} \times 50\,\text{mm} \times 1\,\text{mm}$ made of two perfectly connected layers; the material parameters are $\varepsilon_r = 4.7$ and $\mu = 20{,}698\,\text{Pa}$. An electrode at the connecting interface is grounded and a voltage can be applied at the two outer electrodes. In particular, the voltage is applied at the lower electrode and the upper one is grounded as well; this configuration will result into a bending actuator. The plate is fully clamped at $x = 0$ and free at the other edges. As no external forces are applied and the voltage is prescribed, the principle of virtual work reduces to a stationarity principle,

$$\delta \Sigma = 0 \quad \text{with } \Sigma = \int_A \eta_0 \Omega(\boldsymbol{\varepsilon}, \boldsymbol{\kappa}, V) dA. \tag{19}$$

As we are mainly interested in verifying the proposed form of the augmented free energy, we compute solutions with a simple Ritz approximation within the framework of the von-Karman and Tsien theory, see [26], rather than for the fully geometric nonlinear theory. Therefore, the strain measures $\boldsymbol{\varepsilon}$ and $\boldsymbol{\kappa}$ are approximated as

$$\boldsymbol{\varepsilon} = \frac{1}{2}\left(\nabla \mathbf{u}^S + \nabla w \nabla w\right) , \quad \boldsymbol{\kappa} = -\nabla\nabla w, \tag{20}$$

in which w is the plate deflection and $\mathbf{u}$ the in-plane displacement vector; $\nabla \mathbf{u}^S$ denotes the symmetric part of the displacement gradient tensor. For the Ritz-Ansatz we set

$$u(x, y) = \sum_{i=1}^{5} x^i u_i , \quad v(x, y) = 0 , \quad w(x, y) = \sum_{i=1}^{5} x^{i+1} w_i. \tag{21}$$

We increase the voltage in the bottom layer starting with $V = 0\,\text{V}$ up to $V = 2000\,\text{V}$ and show results for the non-dimensional end point deflection w/h and the non-dimensional end point axial position x/h in the center of the free end in the top row of Fig. 1. Results are presented for four different physical surfaces used as the material surface—the bottom and the top surface of the plate, the center surface of the plate, which represents the neutral plane, with $\bar{B} = 0$ and $\bar{K} = 0$, and the center surface of the actuated bottom layer, which is the neutral plane of the bottom layer. One can see that the deflection and the axial positions are close to each other

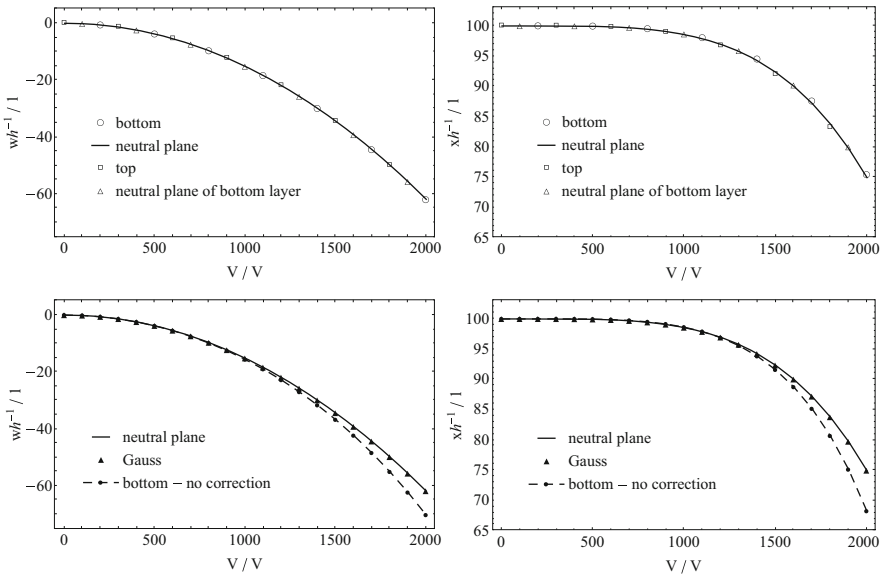

Fig. 1 Non-dimensional end point deflection w/h and the non-dimensional end point axial position x/h for different physical surfaces

independent from the choice of the material surface. These results verify the proper modeling concerning the choice of the material surface; yet, they still need to be validated against other results. This is done in the two plots in the bottom row of Fig. 1. Here, *neutral plane* refers to the present theory using the center surface as the material surface and *bottom—no correction* to the present theory using the bottom surface as the material surface, but setting $\bar{K} = 0$. Clearly, one can see the significance of the material parameter $\bar{K}$, if the material surface is not the neutral plane of the plate. *Gauss* refers to the result computed with the same Ritz-Ansatz within the von-Karman and Tsien approximation, but with the augmented free energy as

$$\varrho_0 \Omega_3 = \frac{1}{2}\mu \left(\mathrm{tr}\mathbf{C}_3 + (\det \mathbf{C}_3)^{-1} - 3 \right) - \frac{1}{2}\varepsilon_0 \varepsilon_r \det \mathbf{C}_3 \left(\frac{V}{h/2} \right)^2 , \tag{22}$$

with $\mathbf{C}_3 = 2(\boldsymbol{\varepsilon} + Z\boldsymbol{\kappa}) + \mathbf{I}$. A numerical integration through the thickness then finds the plate augmented free energy. This type of modeling is already well tested against results from the literature in [17] using finite elements within the geometrically exact formulation. As the present results—*neutral plane*—coincide very well with the ones using the numerical integration—*Gauss*—we conclude that the plate augmented free energy, as given in Eq. (17), is a proper formulation.

4 Conclusions

In this paper we primarily focused on postulating a specific form for the two-dimensional augmented free energy of a thin plate made of layers of incompressible dielectric elastomers. The particular case of a neo-Hookean material was considered. The resulting novel formulation was validated against results based on a-priori assumptions imposed on the state of stress and the distribution of the strain through the thickness of the plate, which are already well tested. A very good agreement was obtained.

Acknowledgement This work was partially supported by the Linz Center of Mechatronics (LCM) in the framework of the Austrian COMET-K2 Program.

References

1. Toupin, R.A.: The elastic dielectric. J. Ratio. Mech. Anal. **5**(6), 849–915 (1956)
2. Pao, Y.H.: Electromagnetic forces in deformable continua. In: Nemat-Nasser, S. (ed.) Mechanics Today, pp. 209–306. Pergamon Press, Oxford (1978)
3. Prechtl, A.: Eine Kontinuumstheorie elastischer Dielektrika. Teil 1: Grundgleichungen und allgemeine Materialbeziehungen (in German). Arch. Elektrotech. **65**(3), 167–177 (1982)
4. Prechtl, A.: Eine Kontinuumstheorie elastischer Dielektrika. Teil 2: Elektroelastische und elastooptische Erscheinungen (in German). Arch. Elektrotech. **65**(4), 185–194 (1982)
5. Maugin, G.A.: Continuum Mechanics of Electromagnetic Solids. North-Holland, Amsterdam (1988)
6. Pelrine, R.E., Kornbluh, R.D. Joseph, J.P.: Electrostriction of polymer dielectrics with compliant electrodes as a means of actuation. Sens. Actuators A Phys. **64**, 77–85 (1998)
7. Bar-Cohen, Y.: Electroactive Polymer (EAP) Actuators as Artificial Muscles: Reality, Potential, and Challenges. SPIE, Bellingham (2004)
8. Dorfmann, A., Ogden, R.W.: Nonlinear electroelasticity. Acta Mech. **174**, 167–183 (2005)
9. Vu, D.K, Steinmann, P., Possart, G.: Numerical modelling of non-linear electroelasticity. Int. J. Numer. Methods Eng. **70**, 685–704 (2007)
10. Choi, H.R., Jung, K., Ryew, S., Nam, J.D., Jeon, J., Koo, J.C., Tanie, K.: Biomimetic soft actuator: design, modeling, control, and applications. IEEE/ASME Trans. Mechatron. **10**, 581–593 (2005)
11. Carpi, F., Migliore, A., Serra, G., Rossi, D.D.: Helical dielectric elastomer actuators. Smart Mater. Struct. **14**, 1–7 (2005)
12. Carpi, F., Salaris, C.,Rossi, D.D.: Folded dielectric elastomer actuators. Smart Mater. Struct. **16**, S300–S305 (2007)
13. Arora, S., Ghosh, T., Muth, J.: Dielectric elastomer based prototype fiber actuators. Sens. Actuators A Phys. **136**, 321–328 (2007)
14. Gao, Z., Tuncer, A.,Cuitiño, A.: Modeling and simulation of the coupled mechanical-electrical response of soft solids. Int. J. Plast. **27**(10), 1459–1470 (2011)
15. Skatulla, S., Sansour, C., Arockiarajan, A.: A multiplicative approach for nonlinear electroelasticity. Comput. Methods Appl. Mech. Eng. **245–246**, 243–255 (2012)
16. Klinkel, S., Zwecker, S., Mueller, R.: A solid shell finite element formulation for dielectric elastomers. J. Appl. Mech. **80**, 021026-1–021026-11 (2013)
17. Staudigl, E., Krommer, M., Vetyukov, Y.: Finite deformations of thin plates made of dielectric elastomers: modeling, numerics and stability. J. Intell. Mater. Syst. Struct. **29**(17), 3495–3513 (2018)

18. Opoka, S., Pietraszkiewicz, W.: On modified displacement version of the non-linear theory of thin shells. Int. J. Solids Struct. **46**(17), 3103–3110 (2009)
19. Eliseev, V.V., Vetyukov, Y.: Finite deformation of thin shells in the context of analytical mechanics of material surfaces. Acta Mech. **209**(1–2), 43–57 (2010)
20. Vetyukov, Y.: Finite element modeling of Kirchhoff-Love shells as smooth material surfaces. Z. Angew. Math. Mech. **94**, 150–163 (2014)
21. Krommer, M., Vetyukov, Y., Staudigl, E.: Nonlinear modelling and analysis of thin piezoelectric plates: buckling and post-buckling behaviour. Smart Struct. Syst. **18**(1), 155–181 (2016)
22. Vetyukov, Y., Staudigl, E., Krommer, M.: Hybrid asymptotic-direct approach to finite deformations of electromechanically coupled piezoelectric shells. Acta Mech. **229**(2), 953–974 (2018)
23. Naghdi, P.: The theory of shells and plates. In: Flügge, S., Truesdell, C. (eds.) Linear Theories of Elasticity and Thermoelasticity. Handbuch der Physik, vol. VIa/2, pp. 425–640. Springer, Berlin (1972)
24. Vetyukov, Y.: Nonlinear Mechanics of Thin-Walled Structures: Asymptotics, Direct Approach and Numerical Analysis. Springer, Vienna (2014)
25. Ziegler, F.: Mechanics of Solids and Fluids, 2nd edn. Springer, Vienna (1998)
26. von Kármán, Y., Tsien, H.S.: The buckling of thin cylindrical shells under axial compression. J. Aeronaut. Sci. **8**, 303–312 (1941)

Harmonic Balance Method and Stability of Discontinuous Systems

E. V. Kudryashova, N. V. Kuznetsov, O. A. Kuznetsova, G. A. Leonov, and R. N. Mokaev

Abstract The development of the theory of discontinuous dynamical systems and differential inclusions was not only due to research in the field of abstract mathematics but also a result of studies of particular problems in mechanics. One of the first methods, used for the analysis of dynamics in discontinuous mechanical systems, was the harmonic balance method developed in the thirties of the twentieth century. In our work, the results of analysis obtained by the method of harmonic balance, which is an approximate method, are compared with the results obtained by rigorous mathematical methods and numerical simulation.

1 Introduction

The development of the theory of discontinuous dynamical systems and differential inclusions was not only due to research in the field of abstract mathematics in the thirties of the last twentieth century but also a result of studies of particular problems in mechanics. In the thirties and forties of the twentieth century, J. Hartog,

E. V. Kudryashova · O. A. Kuznetsova
Saint-Petersburg State University, Saint-Petersburg, Russia

N. V. Kuznetsov (✉)
Saint-Petersburg State University, Saint-Petersburg, Russia

University of Jyväskylä, Jyväskylä, Finland

Institute of Problems of Mechanical Engineering RAS, Saint-Petersburg, Russia
e-mail: n.v.kuznetsov@spbu.ru

G. A. Leonov
Saint-Petersburg State University, Saint-Petersburg, Russia

Institute of Problems of Mechanical Engineering RAS, Saint-Petersburg, Russia

R. N. Mokaev
Saint-Petersburg State University, Saint-Petersburg, Russia

University of Jyväskylä, Jyväskylä, Finland

V. P. Matveenko et al. (eds.), *Dynamics and Control of Advanced Structures and Machines*, https://doi.org/10.1007/978-3-319-90884-7_11

A. Andronov, N. Bautin, and M. Keldysh were among the first who rigorously treated the mathematical peculiarities of discontinuous dynamical models [1–3] on the examples of mechanical models. One of the first methods, used for the analysis of stability and oscillations in discontinuous dynamical models was the harmonic balance method (or the describing function method) developed in the thirties of the twentieth century [4]. This method is not strictly mathematically justified and is one of the approximate methods of analysis of oscillation in nonlinear systems. Nowadays, we can apply various rigorous analytical and reliable numerical methods, which have been developed from that time till now: mathematical theory of differential inclusions (see, e.g., [5–9] and others), direct Lyapunov method and frequency methods (see, e.g., [6, 10]), and special numerical approaches for solving differential inclusions (see, e.g., [11–13]).

In our work for the Hartog, Keldysh, and modified Fitts models, we compare the results of analysis obtained by the method of harmonic balance with the results obtained by rigorous mathematical methods and numerical simulation.

2 Hartog Model

In 1930, J. Hartog studied vibrations in a mechanical model with dry friction[1] described by the following equation [1]:

$$m\ddot{x} + kx = -\varphi(\dot{x}), \quad \varphi(\dot{x}) = F_0 \mathrm{sign}(\dot{x}) \tag{1}$$

where $m > 0$ is the mass, $k > 0$ is spring stiffness, and $F_0 > 0$ is the dry friction coefficient. Following the mechanical sense, Hartog defined sign(0) as a value from $[-F_0, F_0]$ and, thus, the discontinuous differential equation (1) has a segment of equilibria (rest segment).

Following the theory of differential inclusion, for the model (1) we consider the discontinuity manifold: $S = \{\dot{x} : \ \dot{x} = 0\}$ on the phase space $(x, \dot{x})$, define $\varphi(\dot{x})$ on S as the set $[-F_0, +F_0]$, and get differential inclusion:

$$m\ddot{x} + kx \in -\hat{\varphi}(\dot{x}), \quad \hat{\varphi}(\dot{x}) = \begin{cases} \varphi(\dot{x}), & \text{if } \dot{x} \neq 0, \\ [-F_0, +F_0], & \text{if } \dot{x} = 0. \end{cases} \tag{2}$$

The solutions of (2) are considered in the sense of Filippov [5]. Remark that here solutions cannot slide on the discontinuity manifold S but can tend to the rest segment:

$$\Lambda = \{ -F_0/k \leq x \leq F_0/k, \dot{x} = 0\} \subset S,$$

or pierce the manifold $S \backslash \Lambda$. The phase portrait of (2) is shown in Fig. 1.

[1] The history of the dry friction law can be found, e.g., in [14].

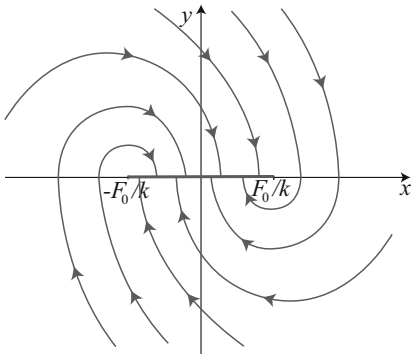

Fig. 1 Phase portrait of system (1): trajectories tend toward the rest segment $\{|x| \le F_0/k,\ y = 0\}$

For Eq. (2), the harmonic balance methods states that there are no periodic oscillations for any values of the parameters. This result can be rigorously justified by the analog direct Lyapunov method for differential inclusions [6, Lemma 1.5, p. 58]. Consider Lyapunov function:

$$V(x, \dot{x}) = \frac{1}{2}(m\dot{x}^2 + kx^2). \tag{3}$$

Then, we have

$$\dot{V}(x, \dot{x}) = -F_0 \dot{x}\,\mathrm{sign}(\dot{x}) < 0, \quad \forall \dot{x} \notin S$$

and the equality $V(x(t), \dot{x}(t)) \equiv \mathrm{const}$ can hold only for $x \in \Lambda$. Thus, any solution of (2) converges to the rest segment Λ.

3 Two-Dimensional Keldysh Model

M. Keldysh, in 1944, studied a two-dimensional model of damping flutter in aircraft control systems with dry friction [3]:

$$J\ddot{x} + kx = -\mu\dot{x} - \varphi(\dot{x}), \quad \mu = \lambda - h,\ \varphi(\dot{x}) = (F_0 + \kappa\dot{x}^2)\mathrm{sign}(\dot{x}), \tag{4}$$

where $J > 0$ is the moment of inertia, $k > 0$ is spring stiffness, $h\dot{x}$ is an excitation force proportional to the angular velocity $\dot{x}$, $f(\dot{x}) = \lambda\dot{x} + \varphi(\dot{x})$ is the nonlinear characteristic of hydraulic damper with dry friction, $F_0 > 0$ is the dry friction coefficient, and $\lambda > 0$ and $\kappa > 0$ are parameters of the hydraulic damper.

Using the harmonic balance method, Keldysh formulated the following result: *If*

$$-2.08\sqrt{F_0\kappa} = \delta_K < \mu$$

then all trajectories of (4) converge to the rest segment; if $\mu < -2.08\sqrt{F_0\kappa}$, *then there are two periodic trajectories (limit cycles)* $\approx a_{\pm}\cos(\omega t)$ *with amplitudes*:

$$a_{\pm}(\mu) = \frac{3}{8\kappa}\sqrt{\frac{J}{k}}\left(\pi\mu \pm \sqrt{\pi^2\mu^2 - \frac{32}{3}\kappa F_0}\right); \tag{5}$$

Other trajectories behave as follows. The trajectories, emerging from infinity, tend to the external limit cycle. The domain between two limit cycles is filled with trajectories unwinding from the internal (unstable) limit cycle and winding onto external (stable) limit cycle. The stability domain bounded by the internal limit cycle is filled with trajectories tending to one of the possible equilibria on the rest segment.

By analogy with the above consideration of the Hartog model, we transform the Keldysh model to the differential inclusion:

$$J\ddot{x} + kx + \mu\dot{x} \in -\hat{\varphi}(\dot{x}), \quad \hat{\varphi}(\dot{x}) = \begin{cases} \varphi(\dot{x}) & \dot{x} \neq 0, \\ [-F_0, +F_0] & \dot{x} = 0, \end{cases} \tag{6}$$

consider Lyapunov function (3) with $m = J$, and get

$$\dot{V}(x, \dot{x}) = -\mu\dot{x}^2 - \dot{x}\varphi(\dot{x}) < 0, \quad \forall \dot{x} \notin S.$$

Thus, if $\dot{x}\varphi(\dot{x}) > 0$ for $\dot{x} \neq 0$, that is:

$$-2\sqrt{F_0\kappa} < \mu,$$

then any solution of (6) converges to the rest segment Λ [15]. Here, the estimate obtained by direct Lyapunov method is close to the Keldysh estimate obtained by the harmonic balance method.

To check the second part of Keldysh's result, we use numerical simulation [13]. The qualitative behavior of trajectories in the case of two coexisting limit cycles is shown in Fig. 2.

Here, the largest limit cycle is a hidden attractor [16–23] and corresponds to the flutter. Figure 3 shows the bifurcation of collision of the limit cycles and the rest segment. In the right subfigure of Fig. 3, both limit cycles have disappeared and trajectories tend to the rest segment, while the second part of the Keldysh estimate is valid.

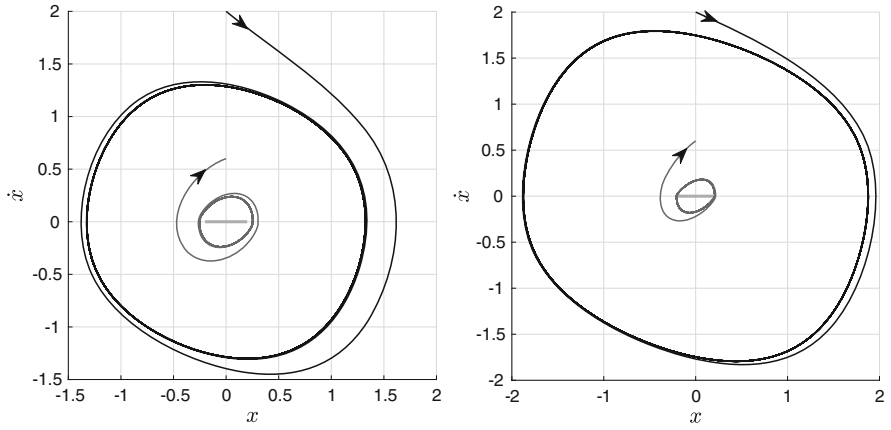

Fig. 2 Numerical experiment with $F_0 = 0.2$, $J = 1, k = 1$, and $\kappa = 1$. Outer trajectory winds onto stable limit cycle, and inner trajectory unwinds from unstable limit cycle and winds onto the stable limit cycle (hidden attractor). Left subfigure: $\mu = -1.3967\delta_K$: $a_+(\mu) \gg a_-(\mu) > F_0$. Right subfigure: $\mu = -1.7847\delta_K$: $a_+(\mu) \gg F_0 > a_-(\mu)$

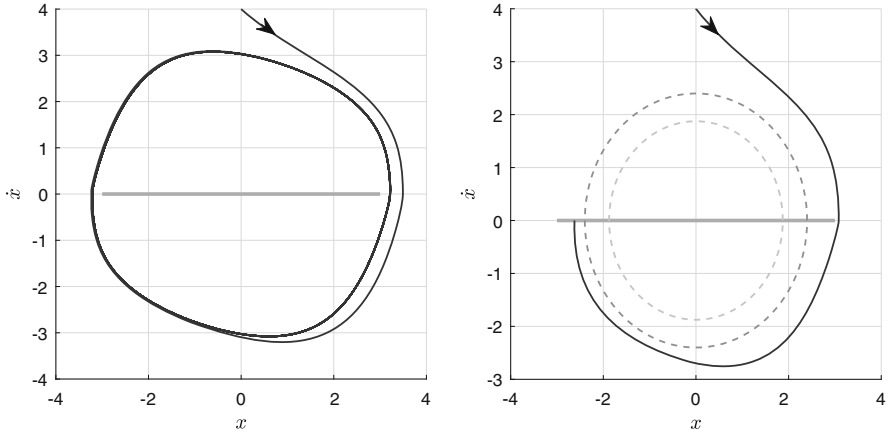

Fig. 3 Numerical experiment with $F_0 = 3$, $J = 1, k = 1$, and $\kappa = 1$. Left subfigure: $\mu = -1.0713\delta_K$, $a_+(\mu) \gtrapprox F_0 > a_-(\mu)$; outer trajectory winds onto stable limit cycle, and internal unstable limit cycle is not revealed numerically (due to stiffness). Right subfigure: $\mu = -1.0076\delta_K$, $F_0 \gtrapprox a_+(\mu) > a_-(\mu)$ (dash circles); outer trajectory approaches the stationary segment, both limit cycles have disappeared

4 Discontinuous Modification of the Fitts Counterexample

It is known that the harmonic balance method may lead to wrong conclusion on the global stability. For example, it states that the Aizerman and Kalman conjectures on the global stability of nonlinear control systems are valid, while

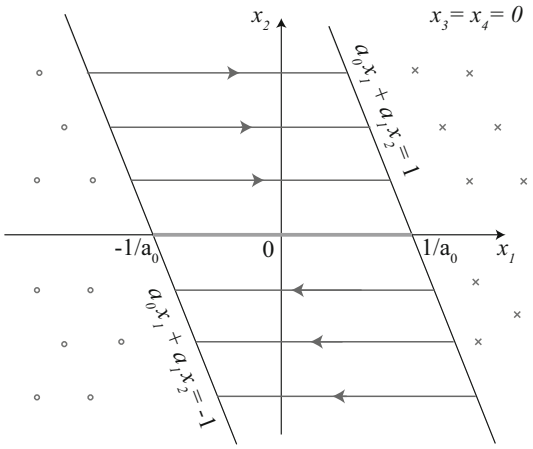

Fig. 4 Sliding mode surface $\{(x_1, x_2, x_3, x_4) \in \mathbb{R}^4 \mid x_3 = x_4 = 0, -1 \le a_0x_1 + a_1x_2 \le 1\}$ for system (7). Arrowed lines define the motion on the surface, and thick line defines the rest segment

various counterexamples with hidden attractors have been found (see, e.g., [16, 24–32]). Consider a modification of one of the first counterexamples to the Kalman conjecture [33]:

$$\begin{aligned} &\dot{x}_1 = x_2, \qquad \dot{x}_2 = x_3, \qquad \dot{x}_3 = x_4, \\ &\dot{x}_4 \in -a_0x_1 - a_1x_2 - a_2x_3 - a_3x_4 + \hat{\varphi}(-x_3), \quad \hat{\varphi}(\dot{x}) = \begin{cases} \operatorname{sign}(-x_3) & x_3 \neq 0, \\ [-1, 1] & x_3 = 0, \end{cases} \end{aligned} \tag{7}$$

where $a_i > 0$.

The sliding mode surface for the system (7) is given by:

$$D = \{(x_1, x_2, x_3, x_4) \in \mathbb{R}^4 \mid x_3 = x_4 = 0, -1 \le a_0x_1 + a_1x_2 \le 1\}$$

and the rest segment is (Fig. 4)

$$\Lambda = \left\{(x_1, x_2, x_3, x_4) \in \mathbb{R}^4 \mid x_2 = x_3 = x_4 = 0, -\tfrac{1}{a_0} \le x_1 \le \tfrac{1}{a_0}\right\}.$$

This system has infinite sector of the linear stability and, thus, the harmonic balance method cannot reveal any periodic solutions [16]. However, for parameters $a_0 = 0.981919$, $a_1 = 0.121308$, $a_2 = 2.0254$, and $a_3 = 0.12$, it can be found numerically periodic solution (see Fig. 5) with initial data [33, 34]:

$$\begin{aligned} (x_1^0, x_2^0, x_3^0, x_4^0) = (&-0.625205162606931095343423624907 23, \\ &-3.732409707265061046582527856259 4, \\ &0, \\ &3.475416972869712079398927411163 6) \end{aligned} \tag{8}$$

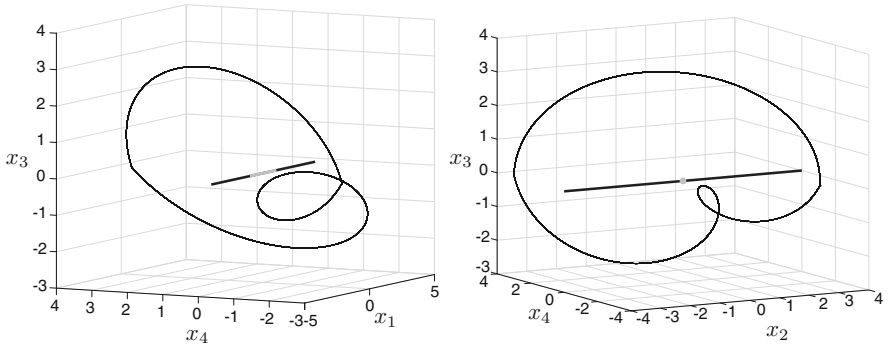

Fig. 5 Periodic solution of system (7) for parameters $a_0 = 0.981919$, $a_1 = 0.121308$, $a_2 = 2.0254$, and $a_3 = 0.12$. Thick dark gray line defines the projection of the sliding mode surface on the corresponding three-dimensional hyperspace (x_1, x_3, x_4) (or (x_2, x_3, x_4)), and light gray line (or dot) defines the projection of the rest segment

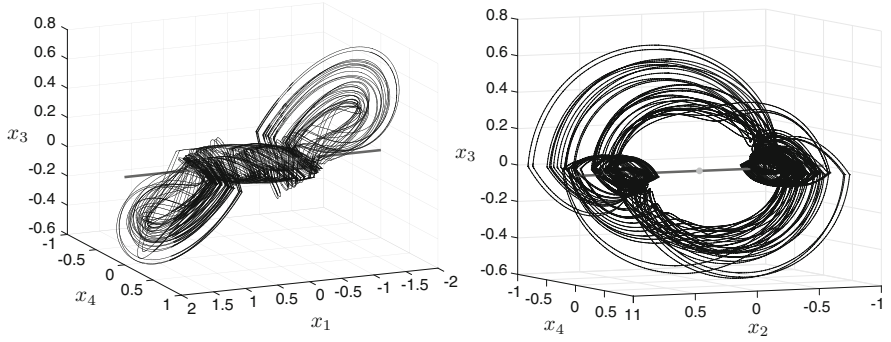

Fig. 6 Nonperiodic oscillating solution of system (7) for parameters $a_0 = 1.0004$, $a_1 = 4.08$, $a_2 = 2.08$, and $a_3 = 0.4$. Thick dark gray line defines the projection of the sliding mode surface on the corresponding three-dimensional hyperspace (x_1, x_3, x_4) (or (x_2, x_3, x_4)), and light gray line (or dot) defines the projection of the rest segment

Using the continuation procedure and passing from parameters $a_0 = 0.981919$, $a_1 = 0.121308, a_2 = 2.0254$, and $a_3 = 0.12$ to parameters $a_0 = 1.0004, a_1 = 4.08$, $a_2 = 2.08$, and $a_3 = 0.4$, it is possible to localize nonperiodic oscillating solution (see Fig. 6).

5 Conclusions

While harmonic balance method is widely used for the study of stability and oscillations of nonlinear dynamical systems, it may lead to wrong results. Some limitations of the use of harmonic balance method for the study of systems with dry friction and rest segment are demonstrated.

Acknowledgement This work was supported by the grant NSh-2858.2018.1 of the President of Russian Federation for the Leading Scientific Schools of Russia (2018–2019).

References

1. Hartog, J.D.: Lond. Edinb. Dubl. Philos. Mag. J. Sci. **9**(59), 801 (1930)
2. Andronov, N., Bautin, A.A.: Dokl. Akad. Nauk SSSR (in Russian) **43**(5), 197 (1944)
3. Keldysh, M.: TsAGI Tr. (in Russian) **557**, 26 (1944)
4. Krylov, N., Bogolyubov, N.: Introduction to Non-linear Mechanics (in Russian). AN USSR, Kiev (1937) (English transl: Princeton Univ. Press, 1947)
5. Filippov, A.F.: Differential Equations with Discontinuous Right-Hand Sides. Kluwer, Dordrecht (1988)
6. Gelig, A., Leonov, G., Yakubovich, V.: Stability of Nonlinear Systems with Nonunique Equilibrium (in Russian). Nauka, Moscow (1978) (English transl: Stability of Stationary Sets in Control Systems with Discontinuous Nonlinearities, 2004, World Scientific)
7. Orlov, Y.: Discontinuous Systems: Lyapunov Analysis and Robust Synthesis Under Uncertainty Conditions. Communications and Control Engineering. Springer, New York (2008)
8. Boiko, I.: Discontinuous Control Systems: Frequency-Domain Analysis and Design. Springer, London (2008)
9. Adly, S.: A Variational Approach to Nonsmooth Dynamics: Applications in Unilateral Mechanics and Electronics. SpringerBriefs in Mathematics. Springer International Publishing, Cham (2018)
10. Leonov, G., Ponomarenko, D., Smirnova, V.: Frequency-Domain Methods for Nonlinear Analysis. Theory and Applications. World Scientific, Singapore (1996)
11. Aizerman, M., Pyatnitskiy, E.: Autom. Remote Control (in Russian) 7 **8**, 33 (1974)
12. Dontchev, A., Lempio, F.: SIAM Rev. **34**(2), 263 (1992)
13. Piiroinen, P.T., Kuznetsov, Y.A.: ACM Trans. Math. Softw. **34**(3), 13 (2008)
14. Zhuravlev, V.: Herald of the Bauman Moscow State Technical University. Series Natural Sciences (2(53)), 21 (2014)
15. Leonov, G.A., Kuznetsov, N.V.: On flutter suppression in the Keldysh model. Dokl. Phys. **63**(9), 366–370 (2018). https://doi.org/10.1134/S1028335818090021
16. Leonov, G., Kuznetsov, N.: Int. J. Bifurcation Chaos **23**(1) (2013) art. no. 1330002. https://doi.org/10.1142/S0218127413300024
17. Leonov, G., Kuznetsov, N., Mokaev, T.: Eur. Phys. J. Spec. Top. **224**(8), 1421 (2015). https://doi.org/10.1140/epjst/e2015-02470-3
18. Kuznetsov, N.: Lect. Notes Electr. Eng. **371**, 13 (2016). https://doi.org/10.1007/978-3-319-27247-4_2. Plenary lecture at International Conference on Advanced Engineering Theory and Applications 2015
19. Kiseleva, M., Kudryashova, E., Kuznetsov, N., Kuznetsova, O., Leonov, G., Yuldashev, M., Yuldashev, R.: Int. J. Parall. Emerg. Distrib. Syst. (2018). https://doi.org/10.1080/17445760.2017.1334776
20. Stankevich, N., Kuznetsov, N., Leonov, G., Chua, L.: Int. J. Bifurcation Chaos **27**(12) (2017). Art. num. 1730038
21. Chen, G., Kuznetsov, N., Leonov, G., Mokaev, T.: Int. J. Bifurcation Chaos **27**(8) (2017). Art. num. 1750115
22. Kuznetsov, N., Leonov, G., Mokaev, T., Prasad, A., Shrimali, M.: Nonlinear Dyn. (2018). https://doi.org/10.1007/s11071-018-4054-z
23. Danca, M.F., Fečkan, M., Kuznetsov, N., Chen, G.: Nonlinear Dyn. **91**(4), 2523 (2018)
24. Pliss, V.A.: Some Problems in the Theory of the Stability of Motion (in Russian). Izd LGU, Leningrad (1958)
25. Fitts, R.E.: Trans. IEEE **AC-11**(3), 553 (1966)

26. Barabanov, N.E.: Sib. Math. J. **29**(3), 333 (1988)
27. Bernat, J., Llibre, J.: Dyn. Contin. Discrete Impuls. Syst. **2**(3), 337 (1996)
28. Leonov, G., Bragin, V., Kuznetsov, N.: Dokl. Math. **82**(1), 540 (2010). https://doi.org/10.1134/S1064562410040101
29. Bragin, V., Vagaitsev, V., Kuznetsov, N., Leonov, G.: J. Comput. Syst. Sci. Int. **50**(4), 511 (2011). https://doi.org/10.1134/S106423071104006X
30. Leonov, G., Kuznetsov, N.: Dokl. Math. **84**(1), 475 (2011). https://doi.org/10.1134/S1064562411040120
31. Alli-Oke, R., Carrasco, J., Heath, W., Lanzon, A.: IFAC Proceedings Volumes (IFAC-PapersOnline), vol. 7, p. 27 (2012). https://doi.org/10.3182/20120620-3-DK-2025.00161
32. Heath, W.P., Carrasco, J., de la Sen, M.: Automatica **60**, 140 (2015)
33. Leonov, G., Kuznetsov, N., Kiseleva, M., Mokaev, R.: Differ. Equ. **53**(13), 1671 (2017)
34. Leonov, G., Mokaev, R.: Dokl. Math. **96**(1), 1 (2017). https://doi.org/10.1134/S1064562417040111

Optimization of the Dissipative Properties of Electroelastic Bodies with Electric Circuits Through the Analysis of Natural Vibrations

V. P. Matveenko, N. A. Yurlova, N. V. Sevodina, D. A. Oshmarin, and M. A. Yurlov

Abstract This paper presents a formulation and equations for the problem of natural vibrations of electroelastic bodies with external electric circuits that contain resistive, capacitive, and inductive elements. As one of its applications, the results of the solution of this problem are suggested for determining external electric circuit parameters that ensure optimal damping of one or several vibration modes. In order to illustrate the proposed approach, there are presented results of definition of optimal parameters of external series RL-circuit, shunting piezoelectric element attached to the surface of thin-walled shell in the form of half-cylinder and providing the best variants of damping for one or two vibration modes.

1 Introduction

The possibility of controlling the dynamic characteristics of structures by means of the attached piezoelements and the electric circuits connected to these piezoelements was first demonstrated in [1]. A technique for determining parameters for external shunting circuits that ensure optimal damping of structures was proposed in [2]. The technique is based on the transfer function analysis of the electromechanical system under consideration. A review of the literature has shown that the above-mentioned approach prevails in the analysis of the dynamic behavior of electroelastic systems with piezoelements shunted with passive electric circuits [2–9].

Another more general variant of the analysis of the dynamic characteristics of electroelastic bodies (elastic deformable body with attached deformable piezoelement) with external electric circuits suggests the usage of the equations of solid mechanics and Maxwell's equations. Within this approach, an estimate of the

V. P. Matveenko · N. A. Yurlova (✉) · N. V. Sevodina · D. A. Oshmarin · M. A. Yurlov
Institute of Continuous Media Mechanics Ural Branch of RAS, Perm, Russia
e-mail: mvp@icmm.ru; yurlova@icmm.ru; natsev@icmm.ru; oshmarin@icmm.ru; yurlovm@icmm.ru

V. P. Matveenko et al. (eds.), *Dynamics and Control of Advanced Structures and Machines*, https://doi.org/10.1007/978-3-319-90884-7_12

dissipative properties of the system can be obtained using the results of the solution of one of the two well-known problems. The first problem is concerned with studying free vibrations. In this case, the system dissipation manifests itself in the decay of vibrations, and the rate of decay of vibrations estimates quantitatively the dissipative properties of the system. The second problem focuses on steady-state forced vibrations. The dissipation of the system is determined in this case by the values of resonance amplitudes of the examined variables.

For the electroelastic systems under consideration, it is of great practical significance to find appropriate parameters, including external electric circuit parameters that provide optimal and, as a rule, maximum damping of vibrations in the prescribed frequency range. Determination of optimal parameters through numerical simulations requires multiple solutions of problems that give a quantitative evaluation of the dissipative properties of the system.

The problems of damped free vibrations and steady-state forced vibrations have disadvantages when they are used in optimization algorithms. For instance, in the case of free vibrations an optimal solution is obtained for specified boundary and initial conditions and the change in these conditions generates a need for a novel optimal solution. When addressing the problem of steady-state forced vibrations, an additional drawback arises regarding the necessity to construct an amplitude–frequency response for getting the values of amplitudes in the prescribed frequency range. This requires multiple solutions to the problem of steady-state forced vibrations at each step of the optimization algorithm.

A more acceptable problem for using in optimization algorithms is the problem of natural vibrations of dissipative systems. One of the results of the solution of such problems is the spectrum of complex eigenfrequencies of vibrations, where the real parts characterize resonance frequencies and the imaginary parts—the rate of decay at a certain frequency. The first formulation of these problems was associated with the consideration of the natural vibrations of viscoelastic bodies [10], whose mechanical behavior was described by the complex modulus, the components of which were calculated using the relations of the hereditary theory of viscoelasticity. A formulation for the problem of natural vibrations of deformable bodies with attached piezoelectric elements connected via electrode surfaces to external electric circuits is given in [11, 12].

This paper considers the application of a natural vibration problem to the optimization of the dissipative characteristics of electroelastic systems via the determination of external electric circuit parameters that ensure maximum damping of vibrations.

2 Equations of the Problem of Natural Vibrations of Electroelastic Systems

We consider a piecewise-homogeneous body of volume $V = V_1 + V_2$, where the volume V_1 consists of homogeneous elastic elements, and the volume V_2 consists of homogeneous electroelastic (piezoelectric) elements. The passive electric circuit of arbitrary configuration, which contains resistive (R), capacitive (C), and inductive (L) elements, is connected to the electrode surface of the piezoelement. "Passivity" implies the absence of external sources of energy.

The variational equation of motion of the body consisting of elastic/viscoelastic and piezoelectric elements is formulated using the relations of the linear theory of elasticity, Maxwell's equations in quasistatic approximation, and the well-known relations of electrical engineering [11]. A solution to the natural vibration problem is found as:

$$u_i(\bar{x}, t) = u_i(\bar{x})e^{i\omega t}, \varphi(\bar{x}, t) = \varphi(\bar{x})e^{i\omega t} \tag{1}$$

where $\omega = \omega_{\mathrm{Re}} + \mathrm{i}\omega_{\mathrm{Im}}$ is the complex eigenfrequency, the real part of which ω_{Re} corresponds to the circular natural frequency of vibrations and its imaginary part ω_{Im} is the damping coefficient characterizing the rate of decay of vibrations; $u_i(\bar{x})$, $\varphi(\bar{x})$ are the eigenmodes of components of displacement and electric potential. The variation equation for the natural vibration problems takes the form [11]:

$$\begin{aligned}
&\int_{V_1} (\sigma_{ij}\delta\varepsilon_{ij} + \rho_1 \ddot{u}_i \delta u_i) dV + \int_{V_2} (\sigma_{ij}\delta\varepsilon_{ij} - D_i\delta E_i + \rho\ddot{u}_i\delta u_i) dV \\
&+ \sum_{p=1}^{n_L} \frac{1}{L_p} \int\int (\varphi_1^{L_p} - \varphi_2^{L_p})\delta\varphi dt^2 + \sum_{q=1}^{n_R} \frac{1}{R_q} \int (\varphi_1^{R_q} - \varphi_2^{R_q})\delta\varphi dt \\
&+ \sum_{r=1}^{n_C} C_r(\varphi_1^{C_r} - \varphi_2^{C_r})\delta\varphi = 0.
\end{aligned} \tag{2}$$

where D_i, E_i are the components of electric flux density and electric field intensity vectors; σ_{ij} are the components of a Cauchy stress tensor; ε_{ij} are the components of the tensor of linear strains; u_i are the components of the displacement vector; ρ_1 is the volume density of the elastic material; ρ_2 is the volume density of the piezoelectric material; φ is the electric potential; $\varphi_1^{cir} - \varphi_2^{cir}$ is the potential difference of the corresponding element of the electric circuit $cir = L_p, R_q, C_r$, $p = 1, \ldots, n_L, q = 1, \ldots, n_R, r = 1, \ldots, n_C$, where n_L, n_R, n_C is the number of inductive, resistive, and capacitive elements, respectively, and L_p, R_q, C_r are the values of inductance, resistance, and capacitance of the corresponding circuit element; and δ is the variation of the corresponding variable.

3 Optimization of Dissipative Properties on the Basis of Natural Vibration Problem

The resonant RL-circuit consisting of series-connected resistance (R) and inductance (L) is most commonly used for damping the vibrations of electroelastic systems. A piezoelement exhibits capacitive properties and, along with the resonant circuit, forms a series RLC oscillatory circuit. This makes it possible to generate, in the main frequency spectrum of electroelastic system vibrations, an additional eigenfrequency due to the interaction between the inductive element (inductance coil or gyrator) and the piezoelement capacitance. This frequency can vary in a fairly wide range owing to changes in external electric circuit parameters.

The use of an external electric RL-circuit in damping structural vibrations at the prescribed frequency requires the adjustment of the additional vibrational frequency of the electric circuit. "Adjustment" is realized through changes in the external electric circuit parameters, which causes shifts in the additional frequency and brings it closer to the eigenfrequency of the electroelastic structure, until they coincide [2].

In [12], it was shown that in the space of possible values of the parameters R and L there may appear such values at which the imaginary parts of the main complex eigenfrequencies ω^n, related directly to the structure, have pronounced extrema (the only ones for each frequency), corresponding to the maximum rate of decay of vibrations at a frequency corresponding to the real part. The vibrational frequency of the electric circuit ω^e (additional frequency) has in this case a great number of local extrema of imaginary part corresponding to the adjustment of a shunting circuit to a specified vibration frequency of the structure (Fig. 1).

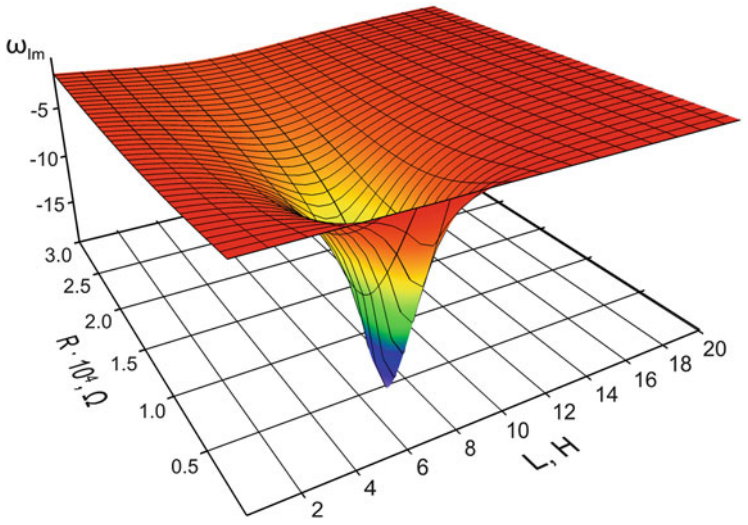

Fig. 1 Dependence of the imaginary part ω_{Im} of the first complex eigenfrequency on the circuit parameters R and L

This allows us to formulate the condition, which unambiguously defines the optimal values of shunting circuit parameters R_{opt} and L_{opt} at which the highest rate of decay of the corresponding vibration mode of the main spectrum is achieved [12]:

$$\left|\omega_{\mathrm{Im}}^{n}\right| \rightarrow max \tag{3}$$

According to [2], the use of a series-resonant electric circuit shunting the piezoelement makes it possible to damp vibrations only at a single chosen frequency, to which the electric circuit is adjusted through the selection of appropriate parameters R and L.

Analysis of the behavior of the imaginary parts ω_{Im} in the space of parameters R and L has revealed some variants of the coincidence at different eigenfrequencies but at the same parameters of the electric circuit, i.e., the rate of decay of vibrations at these frequencies is equal [13].

It has been found that the parameters of the external electric circuit that provide optimal damping of a few vibration modes should correspond to the point in the space of parameters $R - L$ where the coincident moduli of damping coefficients for some modes are maximum:

$$max\left(\left|\omega_{\mathrm{Im}}^{k}\right| = \left|\omega_{\mathrm{Im}}^{l}\right|\right) \tag{4}$$

Here, k, l are the numbers of vibration modes for which one can observe the point of coincidence of damping coefficients.

4 The Results of Determination of Optimal Parameters of External Electric Circuit

To demonstrate the validity of the proposed approach, we consider a thin-walled shell in the form of a half-cylinder, which was rigidly clamped at both ends and freely supported along the generatries (Fig. 2).

The geometrical parameters of the shell are: radius $r_1 = 76\,\mathrm{mm}$, length $l_1 = 300\,\mathrm{mm}$, and thickness $h_1 = 0.25\,\mathrm{mm}$. The shell is made of an elastic isotropic material with the following physical–mechanical characteristics: $E{=}2{\times}10^{11}\,\mathrm{N/m^2}$, $\nu = 0.3$, and $\rho = 7700\,\mathrm{kg/m^3}$.

The piezoelement made of piezoceramics PZT-4 was attached to the shell. It was polarized along the axis r and had standard physical–mechanical characteristics described in [11] and the following dimensions: length of 50 mm, width of 20 mm, and thickness of 0.36 mm. The center of mass of the piezoelement was located at a distance of 15 mm from the clamped ends and it was shifted by 90° with respect to the angular coordinate from the lower base.

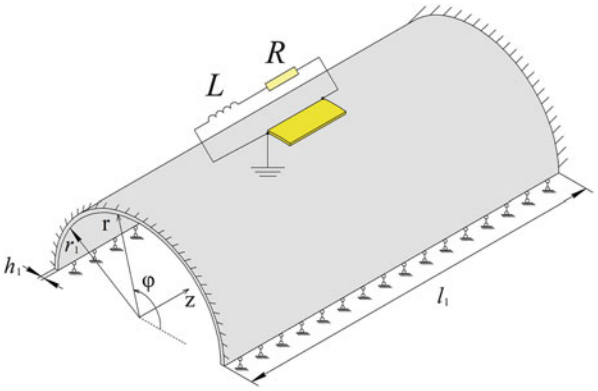

Fig. 2 Computational scheme for the shell in the form of a half-cylinder with a piezoelement and a series RL-circuit

The solution of the problem of natural vibrations of the shell has shown that in the range from 0 Hz up to 1500 Hz there are 15 eigenfrequencies. With the prescribed location of the piezoelement, only five vibration modes (first, fourth, fifth, twelfth, and fifteenth) can be damped. The remaining modes are such that the piezoelement is either not deformed or a zero potential is generated on its surface, which does not allow controlling the dissipative characteristics of the structure by means of the external electric circuit.

For each of these modes, the values of optimal parameters of the shunting circuit and the corresponding values of complex eigenfrequencies are given in Table 1. Figure 1 shows the dependence of the imaginary part of the first complex eigenfrequency on the circuit parameters R and L in the vicinity of their optimal values. This dependence gives an idea of possible strategies for finding optimal solutions.

The results for determining circuit parameters R and L under condition (4) that provides high damping coefficients of a few vibration modes (in the considered variant, modes 4, 5 or modes 12 and 15) are summarized in Table 2. The values of the imaginary parts of corresponding complex eigenfrequencies demonstrate that there exist some variants of the series external RL-circuit parameter values that can

Table 1 The values of eigenfrequencies at optimal parameters of the external circuit

Frequency number	Circuit parameters L(H), R (kΩ)	Eigenfrequencies of the shell with external electric circuit $\omega = \omega_{\mathrm{Re}} + \mathrm{i}\omega_{\mathrm{Im}}$
1	$L = 6.9$, $R = 5.3$	$554 - \mathrm{i}\,28.3$
4	$L = 3.7$, $R = 4.1$	$751 - \mathrm{i}\,32.1$
5	$L = 3.7$, $R = 4.0$	$814 - \mathrm{i}\,31.1$
12	$L = 1.3$, $R = 2.2$	$1308 - \mathrm{i}\,48.2$
15	$L = 1.0$, $R = 2.6$	$1493 - \mathrm{i}\,81.5$

Table 2 External electric circuit parameters that ensure the maximum values of coincident imaginary parts of eigenfrequencies for two vibration modes

1st frequency	4th frequency	5th frequency	12th frequency	15th frequency
$R = 4.41\,\text{k}\Omega$, $L = 3.57\text{H}$				
$552 - \text{i}\,2.0$	$755 - \text{i}\,23.8$	$792 - \text{i}\,23.6$	$1296 - \text{i}\,0.7$	$1486 - \text{i}\,0.8$
$R = 2.45\,\text{k}\Omega$, $L = 1.19\text{H}$				
$553 - \text{i}\,0.5$	$754 - \text{i}\,1.1$	$799 - \text{i}\,0.9$	$1281 - \text{i}\,25.4$	$1507 - \text{i}\,25.8$

ensure sufficiently high damping coefficients in the vicinity of modes 4, 5 and modes 12 and 15 in comparison with other modes.

The comparison of the results from Tables 1 and 2 led us to conclude that two modes of vibrations of the electroelastic structure can be damped using one series-resonant electric circuit with the parameters selected under condition (4). Although the damping coefficients of the considered frequencies are lower than those adjusted for damping only one vibration mode (Table 1), these coefficients are significantly higher compared to other vibration modes.

5 Conclusions

In this work, we have demonstrated the application of the problem of natural vibrations of piecewise-homogeneous bodies containing piezoelements and external electric circuits for selecting variants that ensure an increase in the dissipative properties of the system for one and several vibration modes in the presence of one external circuit consisting of inductive and resistive elements connected in series.

Determination of the optimal dissipative characteristics of the system is based on the analysis of the imaginary part of the eigenfrequency, which specifies the damping coefficient of the corresponding vibration modes in the space of electrical circuit parameters (inductance and resistance).

It is shown that the approach developed in this work can be used to optimize the dissipative characteristics of the electroelastic system for one or several vibration modes.

Acknowledgement The work was supported by RFBR under grant no. 17-41-590152- r-ural-a.

References

1. Forward, R.L.: Electronic damping of vibrations in optical structures. Appl. Opt. **18**, 690–697 (1979)
2. Hagood, N.W., von Flotow A.: Damping of structural vibrations with piezoelectric materials and passive electrical networks. J. Sound Vib. **146**(2), 243–268 (1991)
3. Park, C.H., Inman D.J.: Enhanced piezoelectric shunt design. Shock Vib. **10**(2), 127–133 (2003)

4. Fleming, A.J., Moheimani S.O.R.: Control orientated synthesis of high-performance piezoelectric shunt impedances for structural vibration control. IEEE Trans. Control Syst. Technol. **13**(1), 97–113 (2005)
5. Wu, D., Yang Z., Sun H.: Vibration control efficiency of piezoelectric shunt damping system. Front. Mech. Eng. **4**(4), 441–446 (2009)
6. Thomas, O., Durcane, J., Deu, J.-F.: Performance of piezoelectric shunts for vibration reduction. Smart Mater. Struct. **21**(1) (2011). https://doi.org/10.1088/0964-1726/21/1/015008
7. Berardengo, M., Cigada A., Manzoni S., Vanali N.: Vibration control by means of piezoelectric actuators shunted with LR impedances: performance and robustness analysis. Shock Vib. **2015** (2015). https://doi.org/10.1155/2015/704265
8. Høgsberg, J., Krenk S.: Balanced calibration of resonant piezoelectric RL shunts with quasi-static background flexibility correction. J. Sound Vib. **341**, 16–30 (2015)
9. Park, C.H., Inman D.J.: Uniform model for series R-L and parallel R-L shunt circuits and power consumption. Proc. SPIE Conf. Smart Struct. Integr. Syst. **3668**, 797–804 (1999)
10. Kligman, E.P., Matveenko, V.P.: Natural vibration problem of viscoelastic solids as applied to optimization of dissipative properties of constructions. Int. J. Vib. Control **3**(1), 87–102 (1997)
11. Matveenko, V.P., Oshmarin, D.A., Sevodina, N.V., Yurlova, N.A.: Natural vibration problem for electroviscoelastic body with external electric circuits and finite-element relations for its numerical implementation. Comput. Contin. Mech. **9**(4), 476–485 (2016)
12. Oshmarin, D ., Sevodina, N., Iurlov, M., Iurlova, N.: A search for optimal parameters of resonance circuits ensuring damping of electroelastic structure vibrations based on the solution of natural vibration problem. IOP Conf. Ser. Mater. Sci. Eng. **208** (2017). https://doi.org/10.1088/1757-899X/208/1/012030
13. Oshmarin, D.A., Iurlov, M.A., Sevodina, N.V., Iurlova, N.A.: Passive multimodal damping of vibrations in structures with piezoelectric elements and external electric circuits. In: Guemes, A., Benjeddou, A., Rodellar, J., Leng, J. (eds.) 8th ECCOMAS Thematic Conference on Smart Structures and Materials and 6th International Conference on Smart Materials and Nanotechnology in Engineering (SMART 2017), pp. 1125–1136 (2017)

Multiscale Dynamics of Damage-Failure Transitions and Structures Control Under Intensive Loading

O. B. Naimark

Abstract High-cycle and very-high-cycle fatigue is the most important fundamental and engineering problem for a variety of applications. Series of accidents caused by the gas turbine engine failure (Cowles, Int J Fract 80:147–163, 1996; Shanyavsky, Simulation of fatigue fracture of metals. Synergetics in aviation. Monografiya, Ufa, 2007), along with high costs of service life estimation and potential costs of development of new constructions, stimulated advanced concepts of national programs for high-cycle and very-high-cycle fatigue (Bathias and Paris, Gigacycle fatigue in mechanical practice. Dekker Publisher Co., Marcel, 2005; Botvina, Fracture: kinetics, mechanisms, general laws. Nauka, Moscow, 2008; Hong et al., Metall Mater Trans A 43(8):2753–2762, 2012; Mughrabi, Int J Fatigue 28:1501–1508, 2006; Nicolas, Int J Fatigue 21:221–231, 1999; Nicholas, High cycle fatigue. A mechanics of material perspective. Elsevier, Oxford, 2006; Paris et al., Eng Fract Mech 75:299–305, 2008; Peters and Ritchie, Eng Fract Mech 67:193–207, 2000; Sakai, J Solid Mech Mater Eng 3(3):425–439, 2009; Shanyavsky, Simulation of fatigue fracture of metals. Synergetics in aviation. Monografiya, Ufa, 2007), as being based on new fundamental results of fatigue evaluation. The programs aim at developing approaches using basic research findings, modern methods of laboratory modeling, and quantitative analysis of structural changes in order to reveal fracture stages and "criticality" mechanisms in transition to macroscopic fracture. A strong interest in the gigacycle range (10^9 cycles) of fatigue loads is provided by the progress in the creation of new (nano- and submicrostructural) materials with a very-high-cycle fatigue life and by breakthrough tendencies in technologies requiring such life in aviation motor industry (Nicolas, Int J Fatigue 21:221–231, 1999).

O. B. Naimark (✉)
Institute of Continuous Media Mechanics UB RAS, Perm, Russia
e-mail: naimark@icmm.ru

V. P. Matveenko et al. (eds.), *Dynamics and Control of Advanced Structures and Machines*, https://doi.org/10.1007/978-3-319-90884-7_13

1 Special Features of Crack Initiation in the Very-High-Cycle Fatigue Regime

To distinguish stages of initiation and propagation of fatigue cracks is one of the key problems of fatigue failure [9, 15–17, 24, 26], which is solved using the methodology of investigation of damage kinetics, crack nucleation and propagation as well as by means of experimental technique for registration of specific fracture stages. It was previously noted [5, 15, 17] that a promising approach to evaluating the very-high-cycle fatigue life is the consistent description of stages of damage accumulation with regard to its multiscale kinetics until the leader crack appears whose size would allow a use of fracture mechanics approaches. The role of the initiation stage is particularly important for gigacycle loading regimes, which are characterized by the generation of the fracture cite of a "fish-eye" shape in the material bulk [6]. The stage of fatigue crack growth in the very-high-cycle regime may be short as the major part of the fatigue life is accounted for the time of formation of the initiation zone [5, 12, 15–17, 20, 25].

Fatigue damage is traditionally associated with microplastic deformation [15, 16] under cyclic loading that induces various microstructural mechanisms of control of the fatigue life, being dependent on the origin and initial structure of material. For plastic metals, there is a special type of localized fatigue (cyclic) deformation (persistent slip bands), usually initiating cracks in the near-surface zone. Fatigue fracture of high-strength steels is another case that implies the generation of damages (cracks) in the vicinity of inclusions at low-load amplitudes corresponding to very-high-cycle fatigue. Thus, in contrast to conventional studies of very-high-cycle fatigue focusing on the crack propagation stage, we pose a fundamental problem of initiation of a fatigue crack during multiscale processes of damage accumulation associated with various defects (localized plastic shear bands, microcracks, and pores). In so doing, a qualitative difference of very-high-cycle fatigue is the fatigue crack initiation in the material bulk [5, 12, 15, 25]. This radically alters the statement of the problem of fatigue life evaluation and implies the development of new methods for studying fracture stages, formation of critical conditions for the transition from disperse to macroscopic fracture, experimental and structural methods of assessment of fracture stages. Mughrabi and Höppel also noted that fracture stages are characterized by the irreversibility effects appearing due to localized shears that govern the fatigue crack initiation [15, 16].

2 Fatigue Crack Growth

The study of the crack kinetics is one of the important fundamental problems of the mechanics and physics of fracture, which considers crack propagation in the damaged medium in new statements, being a distinctive feature of fracture under very-high-cycle fatigue. Paris analyzed a large amount of experimental data and

dependences of the crack growth rate $\mathrm{d}a/\mathrm{d}N$ on the stress intensity factor K and its range ΔK and found the power law of crack growth [5, 23]:

$$\frac{\mathrm{d}a}{\mathrm{d}N} = C\,(\Delta K)^m\,, \tag{1}$$

where C and m are the material-dependent constants.

The stress intensity factor range is defined as $\Delta K = K_{max} - K_{min}$, where K_{max} and K_{min} are the maximum and minimum stress intensity factors under cyclic loading. In addition to the Paris kinetics, the existence of the threshold value ΔK_{th} is anticipated, under which the crack will not propagate.

Once formed, a crack grows further in the material by certain mechanisms that can be divided into the following three stages. Figure 1 is a kinetic diagram of fatigue fracture [5], which describes the crack growth. Stage 1 is a near-threshold growth of the fatigue crack at the crack rate in the range 10^{-6}–10^{-5} mm/cycle; stage 2 is a stable growth of the fatigue crack (more than 10^{-5} but less than 10^{-3} mm/cycle); stage 3 is an unstable growth of the fatigue crack at 10^{-3} mm/cycle and higher. The Paris law describes a linear portion of the kinetic diagram with the "upper bound" at the first stage. At stage 3, the crack growth rate proves to be much higher than that predicted by the Paris equation.

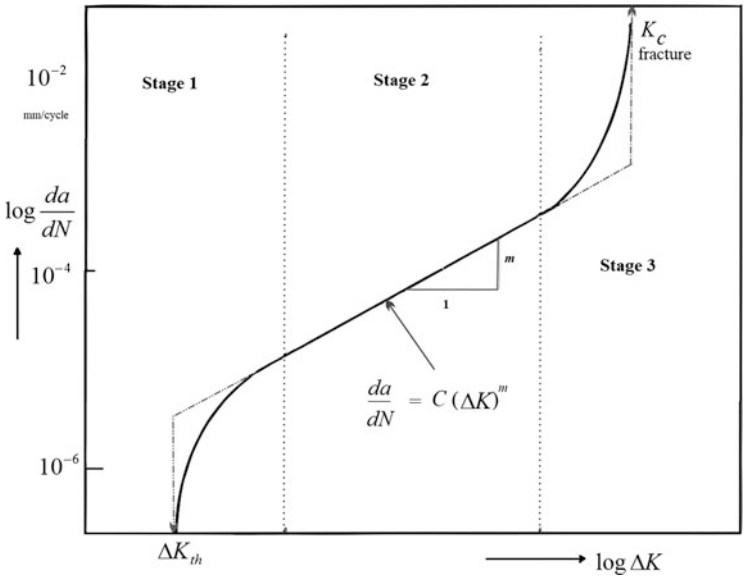

Fig. 1 Kinetic diagram of fatigue fracture, crack growth stages [5]. Stage 1 is a strong influence of the microstructure, average stress, maximum stress of the environment; stage 2 is a strong influence of maximum stresses, a weak influence of the microstructure, average stress of the environment; and stage 3 is a strong influence of the microstructure, average stress, a weak influence of the environment

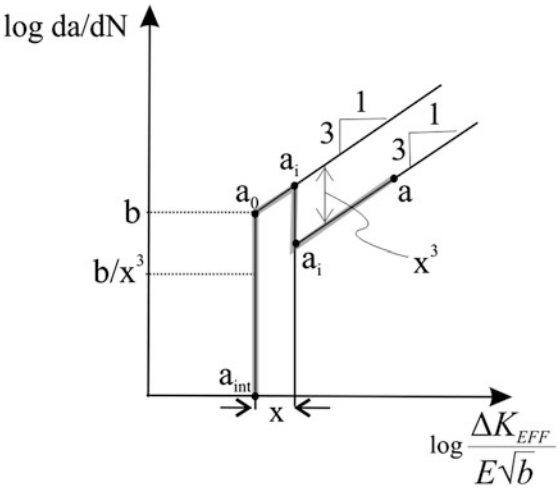

Fig. 2 Schematic diagram of fatigue crack growth depending on the crack size [13]

The kinetic diagram is indicative of the two main characteristics of the cyclic crack resistance: the threshold stress intensity factor range ΔK_{th}, below which a fatigue crack does not grow, and the critical stress intensity factor range ΔK_{fc}, at which a catastrophic fatigue failure occurs. Fatigue failure in the Paris regime is determined by the applied stress and crack length (and its orientation) [14]. However, for small cracks or low stresses when the crack growth kinetics is significantly affected by the structure and damage of the surrounding material, the Paris law cannot be used in its traditional formulation.

To describe the growth kinetics of cracks smaller than "Paris cracks," Miller and Hertzberg [11, 13] proposed a phenomenological relation, which, along with the macroscopic characteristics of the stress state at the crack tip ΔK, includes a parameter of the dislocation subsystem, namely, the Burgers vector modulus b (Fig. 2):

$$\frac{\mathrm{d}a}{\mathrm{d}N} = b\left(\frac{\Delta K}{E\sqrt{b}}\right)^{\alpha}, \tag{2}$$

where E is Young's modulus. This relation finds wide applications, even for "Paris cracks" due to the introduction of the effective value ΔK_{eff}.

3 Kinetic Equation of Fatigue Crack Growth

The versatility of kinetics mechanisms determining the relationship between the fatigue crack growth rate and stress intensity factor change ΔK is the subject of intensive experimental and theoretical research. Power-law dependence (1)

reflects the self-similar nature of fatigue crack growth due to nonlinear damage accumulation in the vicinity of the crack tip (process zone).

Self-similar features of crack growth were studied by methods of the theory of similarity and dimensions [4, 8]. The crack growth rate $\mathrm{d}a/\mathrm{d}N$ (a is the crack length and N is the number of cycles) is dependent on the following parameters:

$$\frac{\mathrm{d}a}{\mathrm{d}N} = F\left(\Delta K, E, l_{sc}, L_{pz}\right), \tag{3}$$

where ΔK is the stress intensity factor range, E is Young's modulus, l_{sc} is the minimum spatial scale in the vicinity of the crack tip (fracture process zone) on which scale-invariant laws of the fracture surface relief begin to show up, and L_{pz} is the scale of the fracture process zone at the crack tip. The values L_{pz} and l_{sc} are experimentally determined based on the study of correlation properties using the scale invariant (Hurst exponent) obtained from the analysis of the correlation function of fracture surface profiles. Following the Π-theorem [4] in a dimensionless form, function (3) can be represented as:

$$\frac{\mathrm{d}a}{\mathrm{d}N} = \Phi\left(\frac{\Delta K}{E\sqrt{l_{sc}}}, \frac{L_{pz}}{l_{sc}}\right). \tag{4}$$

By evaluating $\Delta K/\left(E\sqrt{l_{sc}}\right) \ll 1$ and $L_{pz}/l_{sc} \gg 1$, we can suggest the intermediate asymptotic nature of crack growth kinetics and write (4) in the form:

$$\frac{\mathrm{d}a}{\mathrm{d}N} = l_{sc}\left(\frac{\Delta K}{E\sqrt{l_{sc}}}\right)^{\alpha}\left(\frac{L_{pz}}{l_{sc}}\right)^{\beta}, \tag{5}$$

where α and β are exponents reflecting the intermediate asymptotic nature of crack growth kinetics versus dimensionless variables. We introduce the parameter $\Delta K_{eff} = \Delta K\left(L_{pz}/l_{sc}\right)^{\beta/\alpha}$ and write (5) in the form:

$$\frac{\mathrm{d}a}{\mathrm{d}N} = l_{sc}\left(\frac{\Delta K_{eff}}{E\sqrt{l_{sc}}}\right)^{\alpha}. \tag{6}$$

At $l_{sc} \to b$ where b is the Burgers vector modulus, $L_{pz} \to l_{sc}$, and consequently $\Delta K_{eff} \to \Delta K$ the derived equation of crack growth kinetics will tend to be written as Herzberg (2) [11].

The scales L_{pz} and l_{sc} were previously determined by the profilometry data at the fatigue crack tip for R4 steel [21]. These data presented in logarithmic coordinates in accordance with (6) allow an assessment of the critical scale l_{sc}. The lower limit of the spatial scale L_{min} is taken as the critical scale l_{sc} (Fig. 3).

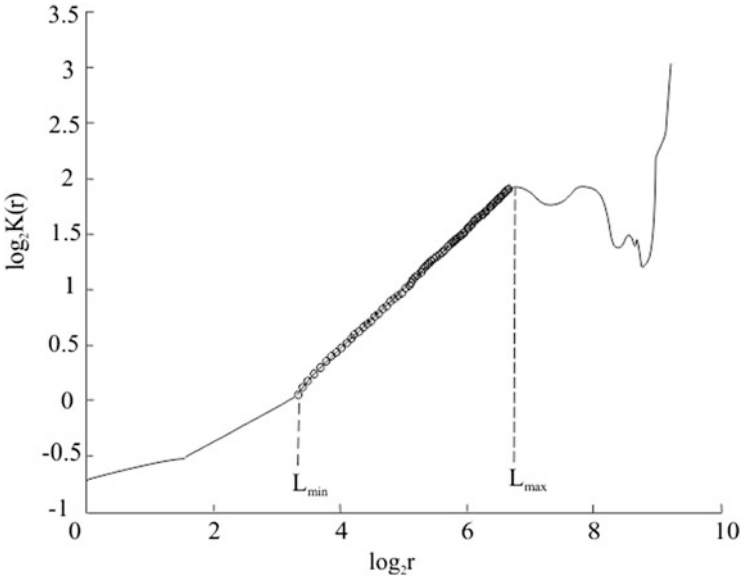

Fig. 3 Typical form of the dependence of $\ln K(r)$ on the fracture surface relief

4 Quantitative Fractography of Fracture Surfaces

Mechanisms of fatigue failure in the very-high-cycle regime are studied by quantitative fractography based on the data of optical microscopy and high-resolution profilometry of the fracture surface (New View 5000 interferometer–profilometer).

Specimens made of titanium and its alloys with a characteristic fracture ("fish-eye"), whose cite is in the material bulk, demonstrate zones with pronounced roughness around the crack nucleus (zone I), which are about 100 µm in diameter for pure Grade-4 titanium and 300 µm in diameter for alloy VT-6 (Fig. 4). The rest and the largest part of the fracture surface is zone II which is smoother.

5 Methods of the Fracture Surface Analysis

5.1 Scale Kink Method

Methods for evaluating the correlation length are tested with the use of processing of roughness profiles of high-strength steel obtained by the New View 5000 interferometer–profilometer (Fig. 5).

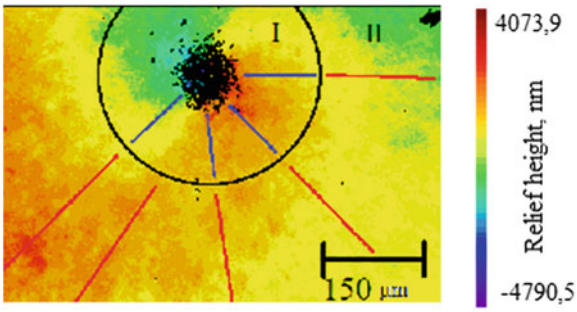

Fig. 4 Images of the fatigue crack nucleus and specific zone of increased roughness around it taken by the New View 5010 interferometer. Solid and dashed lines show the investigated one-dimensional profiles in zones I and II, respectively

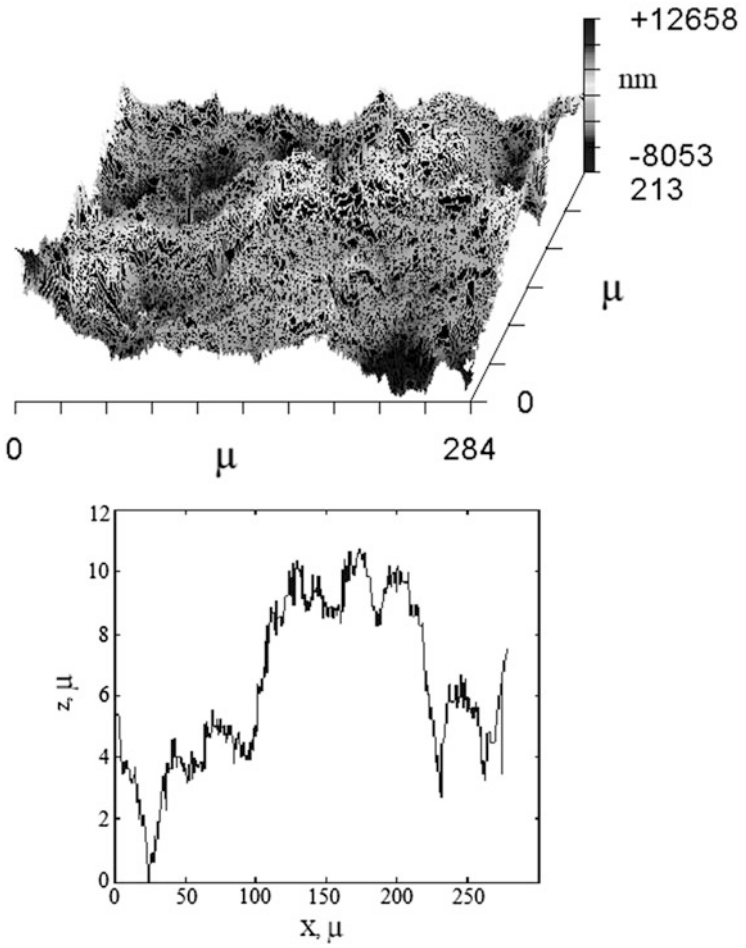

Fig. 5 3D-image of the fracture surface of steel R5 and the analyzed one-dimensional profile

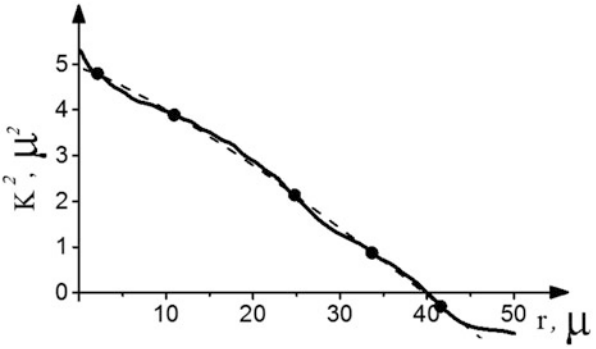

Fig. 6 Oscillations of the correlation function and the assessment of the correlation scales. The solid line is the experimentally obtained correlation function, and the dashed line is the power-law extrapolation

The structural scaling parameter is introduced at calculating the correlation function [1–3, 7, 10, 18, 21, 22]:

$$K(P) \equiv \sqrt{\langle (h(x+R) - h(x))^2 \rangle}, \tag{7}$$

provided that there are scales $R \ll \xi$ (ξ is the correlation length) on which the relief reveals correlated fluctuations which are indicative of the power-law dependence:

$$K(P) \propto R^H, \tag{8}$$

where H is the relief scaling (surface roughness) index (Hurst exponent). Therefore, the correlation length is determined as the scale, at which the structural scaling parameter begins to deviate from the power-law dependence, meaning that the crack behavior is not determined by the material state on scales $R \gg \xi$. The correlation scale can be thus associated with the scale of a zone in the vicinity of the crack tip defining its kinetics.

The proposed approach can be used with sufficient accuracy for long profiles of the fracture surface. However, if the length of the experimental profile is limited, this approach can demonstrate a sufficiently wide scatter of the correlation function values. In addition, oscillations might be responsible for the ambiguous definition of intersection points of the correlation function and power-law dependence (Fig. 6). In accordance with the standard procedure, each of the five intersection points can be taken as the correlation length.

6 Results and Discussion

Various mechanisms of initiation and propagation of fatigue cracks in metals under high-cycle and very-high-cycle fatigue have a variety of qualitative and quantitative fractographic signs of fracture surfaces. The developed methods of

multiscale analysis enable a determination of scale-invariant characteristics (scaling parameters) of specific zones of fatigue fracture (initiation and propagation of cracks), which are related to various mechanisms and stages of defect development and fatigue crack growth.

A quantitative analysis of the surface morphology according to high-resolution profilometry made it possible to find the scale invariance of the fracture surface relief and to relate it to the self-similar nature of fatigue crack growth in the very-high-cycle fatigue regime. Characteristic scales L_{pz} and l_{sc} which determine boundaries of the zone of the correlated behavior of defects at the crack tip are related to phenomenological relations describing the fatigue crack kinetics.

The analysis of the experimental data shows that an increasing number of cycles in very-high-cycle fatigue testing lead to an increase in softening of Armco iron specimens, i.e., increases the damage degree associated with defects (dislocations, microscopic pores, and cracks). The studies performed demonstrate that fracture occurs in the central part of the specimen. The experimental data allow us to conclude that the detected softening in specimens when tested for very-high-cycle fatigue is due to the formation of pores and microcracks that decrease the density of the specimen. Independent measurements of the elastic modulus, which decreases on account of the formation of pores and microcracks, confirm the formation of the fracture site in the specimen bulk.

Acknowledgement Research was supported by the Russian Foundation of Basic Research (project n. 17-01-00687a).

References

1. Abaimov, S.G.: Statistical Physics of Non-thermal Phase Transitions (From Foundations to Applications). Series in Synergetics. Springer, Cham (2015)
2. Bannikov, M., Oborin, V., Naimark, O.: Experimental study of crack initiation and propagation in high- and gigacycle fatigue in titanium alloys. AIP Conf. Proc. **1623**, 55 (2014)
3. Bannikov, M.V., Naimark, O.B., Oborin, V.A.: Experimental investigation of crack initiation and propagation in high- and gigacycle fatigue in titanium alloys by study of morphology of fracture. Frattura ed Integrità Strutturale **35**, 50–56 (2016)
4. Barenblatt, G.I.: Scaling phenomena in fatigue and fracture. Int. J. Fract. **138**, 19–35 (2006)
5. Bathias, C., Paris, P.C.: Gigacycle Fatigue in Mechanical Practice. Dekker Publisher Co., Marcel (2005)
6. Botvina, L.R.: Fracture: Kinetics, Mechanisms, General Laws. Nauka, Moscow (2008)
7. Bouchaud, E.: Scaling Properties of Cracks. J. Phys. Condens. Matter. **9**, 4319–4344 (1997)
8. Ciavarella, M., Paggi, M., Carpinteri, A.: One, no one, and one hundred thousand crack propagation laws: a generalized Barenblatt and Botvina dimensional analysis approach to fatigue crack growth. J. Mech. Phys. Solids **56**, 3416–3432 (2008)
9. Cowles, B.A.: High cycle fatigue in aircraft gas turbines—an industry perspective. Int. J. Fract. **80**, 147–163 (1996)
10. Froustey, C., Naimark, O., Bannikov, M., Oborin, V.: Microstructure scaling properties and fatigue resistance of pre-strained aluminium alloys. Eur. J. Mech. A Solids **29**, 1008–1014 (2010)
11. Hertzberg, R.W.: On the calculation of closure-free fatigue crack propagation data in monolithic metal alloys. Mater. Sci. Eng. A **190**, 25–32 (1995)

12. Hong, Y., Zhao, A., Qian, G., Zhou, C.: Fatigue strength and crack: initiation mechanism of very-high-cycle fatigue for low alloy steels. Metall. Mater. Trans. A **43**(8), 2753–2762 (2012)
13. Marines-Garcia, I., Paris, P.C., Tada, H., Bathias, C.: Fatigue crack growth from small to long cracks in VHCF with surface initiations. Int. J. Fatigue **29**(9–11), 2072–2078 (2007)
14. Miller, K.J.: Materials science perspective of metal fatigue resistance. Mater. Sci. Tech. **9**(6), 453–462 (1993)
15. Mughrabi, H.: Specific features and mechanisms of fatigue in the ultra-high-cycle regime. Int. J. Fatigue **28**, 1501–1508 (2006)
16. Mughrabi, H.: Microstructural fatigue mechanisms: cyclic slip irreversibility, crack initiation, non-linear elastic damage analysis. Int. J. Fatigue **57**, 2–8 (2013)
17. Mughrabi, H., Höppel, H.W.: Cyclic deformation and fatigue properties of very fine-grained metals and alloys. Int. J. Fatigue **32**(9), 1413–1427 (2010)
18. Naimark, O.B., Bayandin, Yu.V., Leontiev, V.A., Panteleev, I.A., Plekhov, O.A.: Structural-scaling transitions and thermodynamic and kinetic effects in submicro-(nano-)crystalline bulk materials. Phys. Mesomech. **12**(5–6), 239–248 (2009)
19. Nicholas, T.: High Cycle Fatigue. A Mechanics of Material Perspective. Elsevier, Oxford (2006)
20. Nicolas, T.: Critical issues in high cycle fatigue. Int. J. Fatigue **21**, 221–231 (1999)
21. Oborin, V.A., Bannikov, M.V., Naimark, O.B., Palin-Luc, T.: Scaling invariance of fatigue crack growth in gigacycle loading regime. Tech. Phys. Lett. **36**(11), 1061–1063 (2010)
22. Oborin, V., Bannikov, M., Naimark, O., Froustey, C.: Long-range-correlation large-scale interactions in ensembles of defects: estimating reliability of aluminium alloys under dynamic cycling and fatigue loading. Tech. Phys. Lett. **37**(3), 241–243 (2011)
23. Paris, P.C., Lados, D., Tada, H.: Reflections on identifying the real ΔKeffective in the Threshold Region and Beyond. Eng. Fract. Mech. **75**, 299–305 (2008)
24. Peters, J.O., Ritchie, R.O.: Influence of foreign-object damage on crack initiation and early crack growth during high-cycle fatigue of Ti-6Al-4V. Eng. Fract. Mech. **67**, 193–207 (2000)
25. Sakai, T.: Review and prospects for current studies on high cycle fatigue of metallic materials for machine structural use. J. Solid Mech. Mater. Eng. **3**(3), 425–439 (2009)
26. Shanyavsky, A.A.: Simulation of Fatigue Fracture of Metals. Synergetics in Aviation. Monografiya, Ufa (2007)

Influence of Sensors and Actuators on the Design of the Modal Control System

V. A. Polyanskiy, A. K. Belyaev, N. A. Smirnova, and A. V. Fedotov

Abstract The efficiency of the active vibration control of flexible systems is limited by the delay in the feedback loop, which causes instability at higher frequencies. In order to design the transfer functions of the feedback control system, it is necessary to use the frequency response functions of the control object. In the case where these functions cannot be measured experimentally, they can be derived from the model of the object. We consider the object model with and without taking into account the influence of sensors and actuators on its dynamics, and the results demonstrate that if this influence is neglected in the model, the efficiency of the control system can significantly decrease. We consider modal control of bending vibrations of a metal beam using piezoelectric sensors and actuators.

Keywords Active vibration control · Modal control · Identification · Sensors · Actuators

1 Introduction

Material savings and lightweight design lead to the appearance of flexible systems practically in all new constructions, from bridges to robots. At the same time, there is a cheapening of sensors and actuators. All this gives completely new opportunities in the solution of engineering problems by methods of active control. Such smart structure control methods have been intensively developed over the past 25 years.

Piezoelectric sensors and actuators are widely used as the control elements in the modern smart systems due to their high operational characteristics. A review of functional materials used in smart structures is given by Tani et al. [10]. One of important applications of the smart structure technology is the active vibration

V. A. Polyanskiy · A. K. Belyaev (✉) · N. A. Smirnova · A. V. Fedotov
Institute for Problems in Mechanical Engineering, Russian Academy of Sciences, Saint-Petersburg, Russia

V. P. Matveenko et al. (eds.), *Dynamics and Control of Advanced Structures and Machines*, https://doi.org/10.1007/978-3-319-90884-7_14

control. Concerning the literature on the active vibration control and the smart systems used for this purpose, the reader is referred to cf. [1, 9].

An important part of such smart structures is the electronic control system. Due to the limited dynamics of all digital and electronic components, there are limitations on the accuracy of control. All processes are fast in the case of active vibration suppression. The limited dynamics of electronic and digital components can play a decisive role in control. These problems lead to residual vibrations in the smart structures that are observed during the experiments [3, 7]. Additional difficulties are associated with the presence of a large number of resonances and small internal damping of elastic smart systems. Instability may cause the resonance peaks for the cutoff frequency of the open-loop system. In [3], we showed theoretically and experimentally that modal control has significant advantages over the local one. This is achieved by knowledge of the model of the controlled object, and its eigenfrequencies and eigenmodes.

There arises the problem of identification, which is almost always solved by calculation, either by the finite element method [5, 8] or by means of an analytical solution of the oscillation problem [4, 6]. At the same time, thin piezoelectric patches influence own frequencies and modes, even on a steel beam. In fact, using the model modes we try to control an object using its inaccurate model. It is important to understand how serious control errors this can cause.

2 Modal Control of the Distributed Elastic Object

The purpose of the control is to reduce the amplitude of forced vibrations of the distributed elastic object in the frequency range, which includes several of its lower eigenfrequencies. It is assumed that the displacement of the object $u(\mathbf{r}, t)$ can be expressed as an infinite series in eigenmodes of the object:

$$u(\mathbf{r}, t) = \sum_{k=1}^{\infty} w_k(\mathbf{r})\beta_k(t). \tag{1}$$

Let the control system include r sensor–actuator pairs. The principal coordinates $\beta_k(t)$ can be found as the solution of the following system:

$$\begin{aligned} &\ddot{\beta}_k(t) + 2\xi_k\lambda_k\dot{\beta}_k(t) + \lambda_k^2\beta_k(t) = f_k + y_k \\ &y_k = \sum_{i=1}^{r} \theta_{ki}^a U_i \end{aligned}, \tag{2}$$

where λ_k is the k-th natural frequency of the object, ξ_k is the damping ratio, f_k is the external disturbance, y_k is the control influence on the k-th eigenmode of the object, U_i is the control signal applied to the i-th actuator, and θ_{ki}^a is the coefficient of influence of the i-th actuator on the k-th mode. In terms of system (2), the purpose

of the control is to reduce the moduli of the first m principal coordinates by selecting the control signals U_i. The modal control algorithm has the following form [3]:

$$\begin{aligned} U_{r\times 1} &= F K_{m\times m} T Y_{r\times 1} \\ Y_{r\times 1} &= \theta^s_{r\times m}\beta_{m\times 1} + \widetilde{Y} \end{aligned}, \tag{3}$$

where $K_{m\times m}$ is the diagonal matrix of gain factors (the subscript indicates the dimension of the matrix object), $F_{r\times m}$, $T_{m\times r}$ are the modal matrices to be selected, $Y_{r\times 1}$ is the vector of sensor signals, $\theta^s_{r\times m}$ is the weighting matrix to be identified, and vector $\widetilde{Y}$ contains only higher principal coordinates, but not the first m coordinates. Then, the first m equations of the system (2) can be expressed in the matrix form:

$$\begin{aligned} &\ddot{\beta}_{m\times 1} + 2\xi_{m\times m}\dot{\beta}_{m\times 1} + \Lambda_{m\times m}\beta_{m\times 1} \\ &\quad = f_{m\times 1} + \theta^a_{m\times r} F_{r\times m} K_{m\times m} T_{m\times r}\theta^s_{r\times m}\beta_{m\times 1} + \Delta_{m\times 1}, \end{aligned}$$

where $\Lambda_{m\times m} = diag\{\lambda_k^2\}$ is the diagonal matrix of squares of the eigenfrequencies of the object, $\xi_{m\times m} = diag\{\xi_k\lambda_k\}$ is the diagonal damping matrix, $f_{m\times 1}$ is the vector of external disturbances, and vector $\Delta_{m\times 1}$ contains only higher harmonics.

The modal approach assumes the independent control of the lower eigenmodes of the object, and therefore, the diagonal structure of matrix $M = \theta^a F K T \theta^s$. For this purpose, the modal matrices F and T must be selected as follows:

$$F_{r\times m} = \theta^{aT}_{r\times m}(\theta^a_{m\times r}\theta^{aT}_{r\times m})^{-1},\ T_{m\times r} = (\theta^{sT}_{m\times r}\theta^s_{r\times m})^{-1}\theta^{sT}_{m\times r}.$$

The task in defining the control algorithm is to determine the matrices $\theta^a_{m\times r}$ and $\theta^s_{r\times m}$, which change as a result of attaching sensors and actuators to the object. It is also necessary to select the transfer functions $k_1(s), \ldots, k_m(s)$, which are the elements of the diagonal matrix $K_{m\times m}$, so as to improve the quality of suppression of the lower modes and ensure the stability of higher ones.

3 Functional Models of Sensors and Actuators

This section describes the operation of rectangular piezoelectric patch sensors and actuators used to control bending vibrations of a beam. Two functional models of control elements are obtained: a full one, which takes into account their mechanical properties, and a simplified one, which does not take into account the size of the control elements and their effect on the mechanical properties of the beam.

Let the sensors and the actuators be located in pairs on both sides of the beam between the sections $x = a_i$ and $x = A_i, i = 1, \ldots, r$, $A_i - a_i = l_p$, where l_p is the length of the piezopatch. According to the piezo-actuator model [9], the application of the electric voltage V to the actuator electrodes is equivalent to the application of

a pair of bending moments M_p in sections $x = a_i$ and $x = A_i$, equal in magnitude and opposite in direction: $M_p = e_{31} b z_m V$, where e_{31} is the piezoelectric constant of the material, b is the width of the electrode, and z_m is the distance between the midplanes of the beam and the piezopatch. According to the piezo-sensor model [9], the signal of the i-th sensor is proportional to the difference between the rotation angles $\phi(t, x)$ of beam sections $x = a_i$ and $x = A_i$. We assume here the dynamics of the beam limited to its n lower bending modes. Then, the control influence on the k-th vibration mode y_k and the signal of the i-th sensor Y_i in the full model will take the following form:

$$\begin{aligned} y_k &= \int_0^l \vartheta_k(x) \left(\sum_{i=1}^r M_{pi} [\delta(x - A_i) - \delta(x - a_i)] \right) dx \\ &= k_a \sum_{i=1}^r [\vartheta_k(A_i) - \vartheta_k(a_i)] U_i = \sum_{i=1}^r \theta_{ki}^a U_i, \\ Y_i &= \frac{e_{31} b z_m}{C} (\phi(t, A_i) - \phi(t, a_i)) \\ &= k_s \sum_{k=1}^n [\vartheta_k(A_i) - \vartheta_k(a_i)] \beta_k(t) \\ &= \sum_{k=1}^n \theta_{ik}^a \beta_k(t), \end{aligned}$$

where C is the capacitance of the sensor; $k_a = e_{31} b z_m$ and $k_s = e_{31} b z_m / C$ are the coefficients common to all actuators and sensors; the influence coefficient $\theta_{ki}^a = k_a [\vartheta_k(A_i) - \vartheta_k(a_i)]$ and the weighting coefficient $\theta_{ik}^s = k_s [\vartheta_k(A_i) - \vartheta_k(a_i)]$ are calculated from the k-th mode of the rotation angle of the beam section taking into account the influence of the control elements attached to the beam $\vartheta_k(x)$.

In simplified models, we assume the curvature of the vibration modes constant over the actuator length, while the modes themselves are obtained without taking into account the control elements attached to the beam. In this case, the control influence $\hat{y}_k$ and the sensor signal $\hat{Y}_i$ are determined by the following formula:

$$\hat{y}_k = k_a \sum_{i=1}^r l_p \frac{d^2}{dx^2} \hat{w}_k \left(\frac{a_i + A_i}{2} \right) U_i = \sum_{i=1}^r \hat{\theta}_{ki}^a U_i,$$

$$\hat{Y}_i = k_s \sum_{k=1}^n l_p \frac{d^2}{dx^2} \hat{w}_k \left(\frac{a_i + A_i}{2} \right) \beta_k(t) = \sum_{k=1}^n \hat{\theta}_{ik}^s \beta_k(t),$$

where the influence coefficients $\hat{\theta}_{ki}^a = k_a l_p \frac{d^2}{dx^2} \hat{w}_k \left(\frac{a_i + A_i}{2} \right)$ and the weighting coefficients $\hat{\theta}_{ik}^s = k_s l_p \frac{d^2}{dx^2} \hat{w}_k \left(\frac{a_i + A_i}{2} \right)$ are calculated from the vibration modes of the beam without taking into account the piezopatches $\hat{w}_k(x)$.

4 The Influence of the Model of Piezopatches on the Efficiency of the Modal Control

We consider a simply supported aluminum beam of length $l = 1$ m with a rectangular cross-section $S = 3 \times 35$ mm^2. The external disturbance is the bending moment μ_0 applied at the beam section $x_0 = 0.4$ m. The purpose of the control is to suppress forced resonant vibrations of the beam with the first and the second natural frequencies. The modal control (3) includes $m = 2$ vibration modes. The numerical model includes $n = 20$ lower modes with the same damping factor $\xi = 0.01$. Two pairs of piezoelectric sensors and actuators ($r = 2$) with dimensions $60 \times 30 \times 0.5$ mm are attached to the beam between the sections $x = a_i$ and $x = A_i$, $i = 1, 2$. Their locations are chosen so as to provide the most effective separation of the first and the second modes: $a_1 = 0.22$ m, $A_1 = 0.28$ m, $a_2 = 0.47$ m, and $A_2 = 0.53$ m.

Attaching piezopatches has a significant effect on the properties of the beam: the linear density of the corresponding beam segments changes from 0.284 to 0.518 kg/m, and their bending stiffness increases from 5.51 to 12.3 N m^2. Figure 1 shows the frequency response functions of the beam for the first actuator and the first sensor, which are obtained using both models of the control elements.

Taking into account the mechanical properties of the piezopatches leads to significant lowering of the frequency response function of the beam. This is explained by the fact that the control elements considerably increase the bending

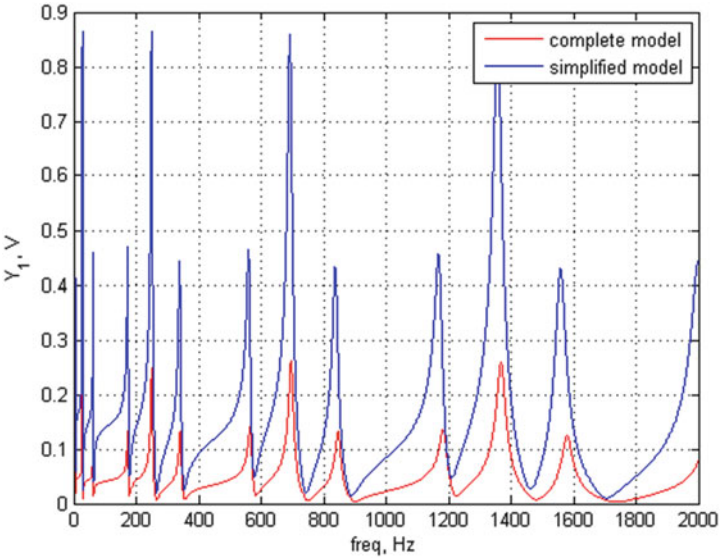

Fig. 1 FRFs of the beam for the 1st actuator and the 1st sensor using the complete (red line) or the simplified (blue line) model of the piezopatches

stiffness of the beam segments to which they are attached, therefore the curvature of these segments decreases for each vibration mode. These changes should be taken into account in the numerical model of the object, which serves as a starting point for the synthesis of the modal control algorithm.

To implement the modal control algorithm (3), it is necessary to specify the modal matrices T and F and the elements of matrix K. Meanwhile, K includes the dynamics of the electronic and digital parts of the control system, which is modeled with the transfer function $H_e(s) = \frac{1}{0.0005s+1}$. Thus, the elements of matrix K take the following form:

$$K_{11}(s) = \frac{1}{0.0005s+1} R_1(s),\ K_{22}(s) = \frac{1}{0.0005s+1} R_2(s),$$

where $R_1(s)$ and $R_2(s)$ are the transfer functions of the first and the second control loops, respectively. The modal matrices $F_{2\times2}$ and $T_{2\times2}$ are obtained by inverting the matrices $\theta^a_{2\times2}$ and $\theta^s_{2\times2}$, which are related due to the pair placement of the sensors and the actuators: $\theta^a = \frac{k_a}{k_s}\theta^{sT}$. Therefore, the modal matrices are defined by the following formula:

$$F = \frac{k_s}{k_a} T^T = (\theta^a)^{-1}, \tag{4}$$

where the matrix θ^a is obtained using the complete or the simplified model of the actuators.

The transfer functions $R_1(s)$ and $R_2(s)$ are selected in order to provide the desired frequency response functions of the open-loop system. For this purpose, the FRFs of the control object corresponding to both control loops are used. These FRFs can be obtained using either full or simplified model of piezopatches. During the synthesis of the transfer functions, their order was increased until it was possible to significantly increase the gain factor at the lower frequencies provided that the closed-loop system is stable. The transfer functions are designed independently for each control loop. When the control loops are switched on simultaneously, the gain factors should be reduced to ensure the stability of the closed-loop system. The described approach to the synthesis of the transfer functions was applied on the experimental setup, and the results are reported in the article [3].

To estimate the efficiency of vibration suppression in the resonance regimes, the steady-state value of the vibration intensity was calculated: $E = \sup_t \sqrt{\int_0^l u^2(x,t)\,dx}$, where $u(x,t)$ is the displacement of the beam from the formula (1). For each variant of the control system, the coefficient of vibration suppression $K_u^{(i)}$ was calculated according to the formula $K_u^{(i)} = \left(1 - \frac{E^{(i)}}{E_0^{(i)}}\right) \cdot 100\%$, where $E^{(i)}$ and $E_0^{(i)}$ denote the vibration intensity at the i-th resonance with and without control.

We considered four different variants of the control system. Variants 1A and 2A use modal matrices, calculated using the simplified model of sensors and actuators:

$$F = \begin{pmatrix} 0 & -169 \\ -675 & 119 \end{pmatrix}, \; T = 10^{-5} \cdot \begin{pmatrix} 0 & -4.62 \\ -1.16 & 0.82 \end{pmatrix}.$$

Variants 1B and 2B use modal matrices on the basis of the full model of the piezopatches:

$$F = \begin{pmatrix} 11.3 & -350 \\ -1453 & 249 \end{pmatrix}, \; T = 10^{-5} \cdot \begin{pmatrix} 0.077 & -9.95 \\ -2.4 & 1.71 \end{pmatrix}.$$

Variants 1A and 1B use first-order transfer functions:

$$R_1(s) = K_{p1}^{(1)} R_1^{(1)}(s), \; R_2(s) = K_{p2}^{(1)} R_2^{(1)}(s), \; R_1^{(1)}(s) = \frac{1 + 0.4s}{1 + 0.002s},$$

$$R_2^{(1)}(s) = \frac{1 + 0.067s}{1 + 0.00033s}.$$

Variants 2A and 2B use more complicated transfer functions of higher order:

$$R_1(s) = K_{p1}^{(2)} R_1^{(2)}(s), \; R_2(s) = K_{p2}^{(2)} R_2^{(2)}(s),$$

$$R_1^{(2)}(s) = \frac{1 + 0.015s + 0.000625s^2}{1 + 0.0012s + 0.0004s^2}, \; R_2^{(2)}(s) = \frac{1 + 0.00235s + 0.000035s^2}{1 + 0.000054s + 0.000029s^2}.$$

For each variant, the configurations of the control system with only one or both control loops were tested; for these cases, the gain factors K_{p1} and K_{p2} were different. The magnitude of the gain factors is limited by the onset of instability at the higher resonance frequencies of the system. For the variants 1A and 2A, the gain factors are determined based on the FRFs obtained using the simplified model of the piezopatches. In contrast, the gain factors for the variants 1B and 2B are determined based on the real FRFs of the beam. Table 1 shows the gain values in cases of separate and simultaneous work of the control loops. Table 2 shows the

Table 1 Gain factors for different variants of the control system

	Gain factors			
	One control loop		Two control loops together	
Control system	K_{p1}	K_{p2}	K_{p1}	K_{p2}
1A	0.6	8	0.33	4.4
1B	0.4	5.5	0.22	3.03
2A	65	800	32.5	400
2B	45	620	22.5	310

Table 2 Coefficients of vibration suppression at the 1st and the 2nd resonances for different variants of the control system

	Coefficients of vibration suppression K_u, %			
	One control loop		Two control loops together	
Control system	$K_u^{(1)}$	$K_u^{(2)}$	$K_u^{(1)}$	$K_u^{(2)}$
1A	5.7	3.4	3.3	2
1B	15	9.3	9.3	7.4
2A	48	47	32	32
2B	70	59	59	57

corresponding values of the coefficients of vibration suppression at the first and the second resonances.

We can see that the use of simple transfer functions (variants 1A and 1B) is ineffective, in contrast to more complex transfer functions (variants 2A and 2B). In the case where both control loops operate simultaneously, the efficiency of vibration suppression is considerably lower than in the cases where the loops work separately, because of the lower gain values in the first case. Comparison of the data presented shows that the efficiency of the modal control, based on the complete model of sensors and actuators (1B and 2B), significantly exceeds the efficiency of control based on the simplified model of piezopatches (1A and 2A). This means that the synthesis of the control systems should be based either on the adequate model of the object, with correctly calculated eigenmodes, or on the experimental identification of the modal matrices, in accordance with the algorithm proposed in [2]. The design of the transfer functions and the optimization of the gain factors should be carried out using the real frequency response functions of the object.

It is found out that the delay in the control channel leads to instability of higher modes, limiting the gain factors. Numerical studies usually neglect the dynamics of the electronic part, considering the delay in the control loop to be not significant. Results show that this small delay, approximately two orders less than the periods of vibrations suppressed in the system, has a very significant effect on the maximum possible coefficient of vibration suppression.

5 Conclusion

Modeling of the elastic beam with and without taking into account the mechanical properties of sensors and actuators has shown that these elements have considerable effect on the dynamical properties of the controlled object. The combination of this effect with the delay in the control loop imposes strong restrictions on the operation of the smart system.

The results of the numerical modeling has shown that in order to design correctly the modal matrices and the transfer function in the control loops, it is necessary

either to precisely calculate the eigenfrequencies and eigenmodes of the object taking into account the characteristics of the control elements, or directly identify all the parameters on the controlled object.

References

1. Alkhatib, R., Golnaraghi, M.F.: Active structural vibration control: a review. Shock Vib. Dig. **35**, 367–383 (2003)
2. Belyaev, A.K., Polyanskiy, V.A., Smirnova, N.A., Fedotov, A.V.: Identification procedure in the modal control of a distributed elastic system. St. Petersburg Polytech. Univ. J. Phys. Math. (2017). https://doi.org/10.1016/j.spjpm.2017.06.004
3. Belyaev, A.K., Fedotov, A.V., Irschik, H., Nader, M., Polyanskiy, V.A., Smirnova, N.A.: Experimental study of local and modal approaches to active vibration control of elastic systems. J. Struct. Control Health Monit. (2018). https://doi.org/10.1002/stc.2105
4. Biglar, M., Gromada, M., Stachowicz, F., Trzepiecinski, T.: Optimal configuration of piezoelectric sensors and actuators for active vibration control of a plate using a genetic algorithm. Acta Mech. (2015). https://doi.org/10.1007/s00707-015-1388-1
5. Braghin, F., Cinquemani, S., Resta, F.: A new approach to the synthesis of modal control laws in active structural vibration control. J. Vib. Control (2012). https://doi.org/10.1177/1077546311430246
6. Canciello, G., Cavallo, A.: Selective modal control for vibration reduction in flexible structures. Automatica (2017). https://doi.org/10.1016/j.automatica.2016.09.043
7. He, C., Jha, R.: Experimental evaluation of augmented UD identification based vibration control of smart structures. J. Sound Vib. **274**, 1065–1078 (2004)
8. Mirafzal, S.H., Khorasani, A.M., Ghasemi, A.H.: Optimizing time delay feedback for active vibration control of a cantilever beam using a genetic algorithm. J. Vib. Control (2015). https://doi.org/10.1177/1077546315569863
9. Preumont, A.: Vibration Control of Active Structures: An Introduction, 3rd edn. Springer, Berlin (2011)
10. Tani, J., Takagi, T., Qiu, J.: Intelligent material systems: application of functional materials. Appl. Mech. Rev. **51**, 505–521 (1998)

Control of Beam Vibrations by Casimir Functions

Hubert Rams, Markus Schöberl, and Kurt Schlacher

Abstract This contribution presents a port-Hamiltonian (pH) framework for the modeling and control of a certain class of distributed-parameter systems. Since the proposed pH-formulation can be seen as a direct adoption of the calculus of variations on jet bundles, it is especially suited for mechanical systems exhibiting a variational character. Besides the pH-framework, an energy-based control scheme making heavy use of structural invariants (casimir functions) is presented on the example of a boundary-controlled Euler–Bernoulli beam.

1 Introduction

Geometric methods turned out to build an effective framework for the description and analysis of mechanical systems, see [1] for example. In particular, differential-geometric approaches can be used in a very beneficial manner for the pure covariant formulation of classical field theories, see, e.g., [3], specifically for continuum mechanics find [9]. From a control engineering point of view, especially port-Hamiltonian formulations are very beneficial since they provide insight into the power flow within the system and how the system exchanges power with other systems. These formulations therefore naturally lead to energy-based control schemes, see, e.g., [15], which turned out to result in robust and physically reasonable controls. Unfortunately, for control systems governed by partial differential equations (pdes) there exists no unique pH-framework. For example, in [12] different pH-formulations are demonstrated by means of a Mindlin plate. In this contribution, however, we restrict ourselves to a pH-framework based on jet-bundle structures, see [11], as it is very well suited for the formulation and the energy-based controller design of mechanical systems, see [10, 14]. Having said that, it should be emphasized that in [10, 14] only 1st-order Hamiltonians, i.e., Hamiltonian densities

H. Rams · M. Schöberl (✉) · K. Schlacher
Institute of Automatic Control and Control Systems Technology, Linz, Austria
e-mail: markus.schoeberl@jku.at; kurt.schlacher@jku.at

V. P. Matveenko et al. (eds.), *Dynamics and Control of Advanced Structures and Machines*, https://doi.org/10.1007/978-3-319-90884-7_15

depending on derivative coordinates up to 1st-order, are considered. Therefore, in this paper, we extend this pH-formulation to 2nd-order Hamiltonians with the restriction on one-dimensional spatial domains and demonstrate the energy-based control by means of Casimir functions in the example of an Euler–Bernoulli beam formulated in terms of this framework.

2 Geometrical Framework

To define the representation of systems governed by pdes in a pH-setting, we first introduce some geometrical structures. Hence, we start with defining the (so-called) state-space bundle $\pi : E \to B$, where the base manifold B (spatial domain) is equipped with the independent (spatial) coordinate z, and the total space E comprises the dependent (fiber) coordinates x^α, $\alpha = 1, \ldots, n$, as well as the coordinate z. Furthermore, π is a surjective submersion from the manifold E to the manifold B and is referred to as projection. Consequently, the bundle $\pi : E \to B$ allows us to distinguish strictly between dependent and independent coordinates. Note that the time t remains in the role of an evolution parameter in this setting, i.e., we confine ourselves to the time-invariant scenario solely. A section $\sigma : B \to E$ of the bundle $\pi : E \to B$ is a smooth mapping which relates the independent coordinates to the dependent ones in the manner of $x^\alpha \circ \sigma = \sigma^\alpha(z) \in C^\infty(B)$.

By means of the first, second, third, and fourth *jet manifold*, which are denoted as $J^1(E)$, $J^2(E)$, $J^3(E)$, and $J^4(E)$, respectively, the so-called *derivative coordinates* or *jet variables* can be introduced. As coordinates on these manifolds we have $(z, x^\alpha, x^\alpha_z)$, $(z, x^\alpha, x^\alpha_z, x^\alpha_{zz})$, $(z, x^\alpha, x^\alpha_z, x^\alpha_{zz}, x^\alpha_{zzz})$, and $(z, x^\alpha, x^\alpha_z, x^\alpha_{zz}, x^\alpha_{zzz}, x^\alpha_{zzzz})$, respectively; here, x^α_z, x^α_{zz}, x^α_{zzz}, and x^α_{zzzz} denote the first, second, third, and fourth derivative coordinates, respectively. For these coordinates, the important relation $x^\alpha_{z\cdots z} \circ \sigma = \partial^l \sigma^\alpha / \partial z^l$ holds, where l is the cardinality of the subscripted index set of $x^\alpha_{z\cdots z}$. To clarify notation, we have $x^\alpha_{zzz} \circ \sigma = \partial^3 \sigma^\alpha / \partial z^3$, for example.

Of particular interest is also the vertical tangent bundle $v_E : V(E) \to E$ where a section $v : E \to V(E)$ forms a vertical vector field given as $v = v^\alpha \partial_\alpha$ with $v^\alpha \in C^\infty(E)$ in local coordinates. Based on certain pullback-bundle constructions, see [3, 8] for example, we are able to introduce the so-called evolutionary or generalized vertical vector fields $v = v^\alpha \partial_\alpha$ with $v^\alpha \in C^\infty(J^l(E))$, $l \geq 0$, i.e., the coefficients v^α are allowed to depend on derivative coordinates. Furthermore, the second prolongation of a (generalized) vertical vector field v is given by:

$$j^2(v) = v^\alpha \partial_\alpha + d_z(v^\alpha)\partial^z_\alpha + d_z(d_z(v^\alpha))\partial^{zz}_\alpha \tag{1}$$

using the total derivative $d_z = \partial_z + x^\alpha_z \partial_\alpha + x^\alpha_{zz} \partial^z_\alpha + x^\alpha_{zzz} \partial^{zz}_\alpha + \cdots$ as well as the abbreviation $\partial^{z\cdots z}_\alpha = \partial / \partial x^\alpha_{z\cdots z}$.

Other important bundles are the cotangent bundles $\tau^*_E : T^*(E) \to E$ and $\tau^*_B : T^*(B) \to B$. Sections of these bundles are 1-forms (covectors) and read as $\omega = \omega_\alpha \mathrm{d}x^\alpha + \bar{\omega} \mathrm{d}z$ and $\theta = \bar{\theta} \mathrm{d}z$, where $\omega_\alpha, \bar{\omega} \in C^\infty(E)$ and $\bar{\theta} \in C^\infty(B)$, in

local coordinates, respectively. Again, by forming an appropriate pullback bundle $W_0^l(E) = T^*(B) \to J^l(E)$, we can introduce special densities $h\mathrm{d}z$ with $h \in C^\infty(J^l(E))$, $l \geq 0$, i.e., the function h may depend on derivative coordinates as well.

The natural contraction between a vector field $v = v^\alpha \partial_\alpha + \bar{v}\partial_z$ and a 1-form $\omega = \omega_\alpha \mathrm{d}x^\alpha + \bar{\omega}\mathrm{d}z$ is denoted by $v \rfloor \omega$ and results in $v \rfloor \omega = v^\alpha \omega_\alpha + \bar{v}\bar{w}$. Note that here and in the sequel Einstein's summation convention is applied.

Moreover, covector-valued densities $\eta_\alpha \mathrm{d}x^\alpha \wedge \mathrm{d}z$ with $\eta_\alpha \in C^\infty(J^l(E))$, $l \geq 0$, can be built as sections of the pullback bundle $W_1^l(E) = T^*(E) \wedge T^*(B) \to J^l(E)$.

Based on the above bundle constructions, we introduce the Euler–Lagrange operator, which is henceforth referred to as domain operator, $\delta : W_0^2(E) \to W_1^4(E)$:

$$\delta(h\mathrm{d}z) = \delta_\alpha(h)\mathrm{d}x^\alpha \wedge \mathrm{d}z \tag{2}$$

including the variational derivative $\delta_\alpha = \partial_\alpha - d_z(\partial_\alpha^z) + d_z(d_z(\partial_\alpha^{zz}))$ as well as both the (so-called) boundary operators of the special form:

$$\delta^{\partial,1}(h\mathrm{d}z) = \delta_\alpha^{\partial,1}(h)\mathrm{d}x^\alpha = (\partial_\alpha^z h - d_z(\partial_\alpha^{zz}h))\mathrm{d}x^\alpha \tag{3a}$$

$$\delta^{\partial,2}(h\mathrm{d}z) = \delta_\alpha^{\partial,2}(h)\mathrm{d}x_z^\alpha = \partial_\alpha^{zz}(h)\mathrm{d}x_z^\alpha. \tag{3b}$$

Finally, it is of particular interest how the integrated quantity $H = \int_B h\mathrm{d}z$ evolves along a vertical vector field $v = v^\alpha \partial_\alpha$ which might be generalized, i.e., we shall consider the expression $\int_B j^2(v)(h\mathrm{d}z)$. To this end, we state the following theorem.

Theorem 1 (Decomposition Theorem) *Let $h \in C^\infty(J^2(E))$ be a 2nd-order density, and $v \in V(E)$ an evolutionary vector field. Then, the integral $\int_B j^2(v)(h\mathrm{d}z)$ can be decomposed into:*

$$\int_B j^2(v)(h\mathrm{d}z) = \int_B v \rfloor \delta(h\mathrm{d}z) + \int_{\partial B} v \rfloor \delta^{\partial,1}(h\mathrm{d}z) + \int_{\partial B} j^1(v) \rfloor \delta^{\partial,2}(h\mathrm{d}z) \tag{4}$$

with the domain operator (2) as well as both the boundary operators (3).

Proof Using the prolongation of v according to (1), we find

$$\int_B j^2(v)(h\mathrm{d}z) = \int_B (v^\alpha \partial_\alpha h + d_z(v^\alpha)\partial_\alpha^z h + d_z(d_z(v^\alpha))\partial_\alpha^{zz}h)\mathrm{d}z,$$

and after successive integration by parts, we unambiguously obtain

$$\int_B j^2(v)(h\mathrm{d}z) = \int_B v^\alpha \delta_\alpha(h)\mathrm{d}z + \int_B d_z(v^\alpha[\partial_\alpha^z h - d_z(\partial_\alpha^{zz}h)] + v_z^\alpha[\partial_\alpha^{zz}h])\mathrm{d}z.$$

Finally, applying the theorem of Stokes, see [2, p. 260] for example, yields (4) where we exploited the operators (2) and (3). Note that $(\cdot)|_{\partial B}$ denotes the restriction of an expression to the boundary ∂B of the domain B. □

In case the evolutionary vector field v in Theorem 1 can be linked to the solution of the corresponding evolutionary pdes of the form $\dot{x}^\alpha = v^\alpha$, we use the notation $\dot{H} = \int_B j^2(v)(h\mathrm{d}z)$ to emphasize that the formal expression $\int_B j^2(v)(h\mathrm{d}z)$ then describes how the integrated quantity H evolves along the solutions of the underlying pdes. Furthermore, we stress that if H corresponds to an energy, then (4) states a power balance relation.

3 A PH-Framework for Distributed-Parameter Systems

In the following, we state a port-Hamiltonian system-representation structure for evolutionary equations of the type $\dot{x}^\alpha = f(z, x^\alpha, x^\alpha_z, x^\alpha_{zz}, x^\alpha_{zzz}, x^\alpha_{zzzz})$ that makes extensive use of the balance relation (4) of Theorem 1. This system structure shall enable us to introduce collocation on the boundary, i.e., it enables the "power" exchange with external systems through the boundary of the spatial domain.

Definition 1 (ipH-Systems) Let $H = h\mathrm{d}z$ be a 2nd-order Hamiltonian, i.e., $h \in C^\infty(J^2(E))$. Then, a distributed-parameter port-Hamiltonian system with 2nd-order Hamiltonian and one-dimensional spatial domain is of the form:

$$\dot{x} = (J - R)(\delta H) \tag{5}$$

where J and R are linear mappings $J, R : W_1^4(E) \to V(E)$ with the properties that J is skew symmetric, and R is symmetric as well as positive semidefinite.

Therefore, the local coordinate expression of (5) is

$$\dot{x}^\alpha = (J^{\alpha\beta} - R^{\alpha\beta})\delta_\beta h\,, \qquad \alpha, \beta = 1, \ldots, n \tag{6}$$

where the mappings enjoy the properties $J^{\alpha\beta} = -J^{\beta\alpha}$, $R^{\alpha\beta} = R^{\beta\alpha}$ as well as $[R^{\alpha\beta}] \geq 0$ (positive semidefinite).

Consequently, applying Theorem 1 with $v = \dot{x}$ of (6), we find that the Hamiltonian $H = \int_B h\mathrm{d}z$ evolves along trajectories of (6) as:

$$\dot{H} = -\int_B \delta_\alpha(h) R^{\alpha\beta} \delta_\beta(h)\mathrm{d}z + [\dot{x}^\alpha \delta^{\partial,1}_\alpha(h) + \dot{x}^\alpha_z \delta^{\partial,2}_\alpha(h)]\big|_{\partial B}. \tag{7}$$

Hence, (7) reveals that the "power balance" equation of (6) generally comprises dissipation within the domain (first term), and two classes of possible boundary (power) ports (second and third term). Now, we divide ∂B into an actuated part ∂B_a

and an unactuated part ∂B_u. For ∂B_u, we set $\dot{x}^\alpha \delta_\alpha^{\partial,1}(h) = \dot{x}_z^\alpha \delta_\alpha^{\partial,2}(h) = 0$; for ∂B_a, we set

$$\dot{x}^\alpha \delta_\alpha^{\partial,1}(h)|_{\partial B_a} = \hat{u}^{\hat{\xi}} \hat{y}_{\hat{\xi}}, \qquad \dot{x}_z^\alpha \delta_\alpha^{\partial,2}(h)|_{\partial B_a} = \tilde{u}^{\tilde{\xi}} \tilde{y}_{\tilde{\xi}}, \tag{8}$$

with $\hat{\xi}_1 = 1, \ldots, m_1$ and $\tilde{\xi} = 1, \ldots, m_2$; thus, we obtained the collocated boundary inputs $\hat{u}$, $\tilde{u}$ and boundary outputs $\hat{y}$, $\tilde{y}$, respectively, which can be used in many applications (if they exist) to either extract or deliver "power" to the system through the boundary of the domain. Obviously, the assignment of $\hat{u}$, $\tilde{u}$ and $\hat{y}$, $\tilde{y}$ in (8) is not unique, cf. [13]. Hence, in the following, we restrict ourselves to the assignment:

$$\begin{aligned} \delta_\alpha^{\partial,1}(h)|_{\partial B_a} &= \hat{B}_{\alpha\hat{\xi}} \hat{u}^{\hat{\xi}} & \qquad \delta_\alpha^{\partial,2}(h)|_{\partial B_a} &= \tilde{B}_{\alpha\tilde{\xi}} \tilde{u}^{\tilde{\xi}} \\ \hat{B}_{\alpha\hat{\xi}} \dot{x}^\alpha|_{\partial B_a} &= \hat{y}_{\hat{\xi}} & \qquad \tilde{B}_{\alpha\tilde{\xi}} \dot{x}_z^\alpha|_{\partial B_a} &= \tilde{y}_{\tilde{\xi}} \end{aligned} \tag{9}$$

that will be suitable for the mechanical example under consideration.

In view of the 1st-order Hamiltonian case, see [10, 14], we want to stress the following facts. That is, for 1st-order Hamiltonians the first and second term in (7) are also present; however, the second boundary-port class, more specifically the boundary operator (3b), does not appear. Of course, if we restrict the density to $h \in C^\infty(J^1(E))$, i.e., to a 1st-order density, in (7)–(9) the second boundary-port category disappears, since $\partial_\alpha^{zz} h = 0$ clearly holds in that case, and thus (7)–(9) degenerates precisely to the boundary ports obtained in [10, 14] for 1st-order densities.

Casimir Functions In light of the findings presented in [10, 14], we define a *structural invariant* or *casimir function* to be of the form:

$$C = \int_B c \mathrm{d}z, \qquad c \in C^\infty(J^2(E)). \tag{10}$$

We say that (10) is a casimir function of (6), if $\dot{C} = 0$ holds independently of h, i.e., C is then a conserved quantity along the trajectories of the ipH-system. This implies that the conditions:

$$\delta_\alpha(c)(J^{\alpha\beta} - R^{\alpha\beta}) = 0 \tag{11a}$$

$$[\dot{x}^\alpha \delta_\alpha^{\partial,1}(c) + \dot{x}_z^\alpha \delta_\alpha^{\partial,2}(c)]\big|_{\partial B} = 0 \tag{11b}$$

are met independently of h. It is remarkable that in the infinite-dimensional as well as in the finite-dimensional case, the interconnection and dissipation mappings characterize the casimir functions. More specifically, casimir functions are subject to the pdes (11a) with the boundary conditions (11b).

Note that since the variational derivative δ_α always annihilates total derivatives, see [6, Theorem 4.7] for example, the differential equations (11a) can be satisfied

trivially by the choice $c = d_z(\varphi)$ with $\varphi \in J^1(E)$. In that case, therefore only the boundary conditions (11b) have to be investigated.

Example 1 Consider the Euler–Bernoulli beam equation (see [5] for example):

$$\rho A \ddot{x}^1(z,t) + EIx^1_{zzzz}(z,t) = 0 \tag{12}$$

on the spatial domain $B = \{z | z \in (0, L)\}$ with the boundary $\partial B = \{0, L\}$. We suppose the beam to be pivoted at one end ($z = 0$) and fully actuated at the other ($z = L$). Hence, ∂B can be divided into an actuated part $\partial B_a = \{L\}$ and an unactuated part $\partial B_u = \{0\}$. Consequently, the beam vibrations $x^1(z,t)$ are also subject to the boundary conditions $x^1(0,t) = EIx^1_{zz}(0,t) = 0$ and $-EIx^1_{zzz}(L,t) = u^1(t)$ as well as $EIx^1_{zz}(L,t) = u^2(t)$, where u^1 and u^2 represent controlled variables. Note that $EIx^1_{zz}(z,t)$ and $-EIx^1_{zzz}(z,t)$ correspond to the bending moment and shear force, respectively.

To formulate (12) in the pH-structure (5), we first introduce the momentum $x^2 = \rho A \dot{x}^1$ and consider the total energy of the beam structure as Hamiltonian, i.e., $H = \int_0^L \left(\frac{1}{2\rho A}(x^2)^2 + \frac{EI}{2}(x^1_{zz})^2 \right) \mathrm{d}z$. Then, we find that (12) can be formulated as:

$$\begin{bmatrix} \dot{x}^1 \\ \dot{x}^2 \end{bmatrix} = \begin{bmatrix} 0 & 1 \\ -1 & 0 \end{bmatrix} \begin{bmatrix} \delta_1(h) \\ \delta_2(h) \end{bmatrix}. \tag{13}$$

Moreover, evaluating (7) yields $\dot{H} = [\dot{x}^1(-EIx^1_{zzz}) + \dot{x}^1_z(EIx^1_{zz})]|_{\partial B_a}$; therefore, we have $[\dot{x}^1(-EIx^1_{zzz})]|_{\partial B_a} = \hat{u}^1\hat{y}_1$ and $[\dot{x}^1_z(EIx^1_{zz})]|_{\partial B_a} = \tilde{u}^1\tilde{y}_1$ with the assignment according to (9), i.e., $-EIx^1_{zzz}(L) = \hat{u}^1$ and $\dot{x}^1(L) = \hat{y}_1$ as well as $EIx^1_{zz}(L) = \tilde{u}^1$ and $\dot{x}^1_z(L) = \tilde{y}_1$. Note that the construction of the maps $\hat{B}_{\alpha\hat{\xi}}$ and $\tilde{B}_{\alpha\tilde{\xi}}$ is straightforward in this case.

The objective of the next section shall be to stabilize the particular rest position $x^{1,d} = az$ with $a \in \mathbb{R}$ of the beam structure of Example 1. That is, the minimum of the closed-loop Hamiltonian must be shaped appropriately, and damping must be injected to achieve stabilization of the desired rest position. To this end, power-conserving interconnection and casimir functions shall be exploited.

4 Control by Interconnection and Casimir Functions on the Example of an Euler–Bernoulli Beam

In this section, we discuss the power-conserving interconnection between an ipH-system and a lumped-parameter pH-controller as well as the energy-based control exploiting casimir functions of the closed loop, all on the example of the boundary-controlled Euler–Bernoulli beam of Example 1.

Interconnection and Damping Injection Consequently, the power-conserving interconnection must satisfy

$$\hat{u}^1\hat{y}_1 + \tilde{u}^1\tilde{y}_1 + \hat{u}_c\hat{y}_c + \tilde{u}_c\tilde{y}_c = 0, \tag{14}$$

where the controller ports have already been splitted into two parts to take account of the 2nd-order Hamiltonian. As pH-controller structure we use

$$\begin{aligned} \dot{x}_c^{\alpha_c} &= (J_c^{\alpha_c\beta_c} - R_c^{\alpha_c\beta_c})\partial_{\beta_c}H_c + \hat{G}^{\alpha_c}\hat{u}_c + \tilde{G}^{\alpha_c}\tilde{u}_c, \qquad \alpha_c, \beta_c = 1, \ldots, 4 = n_c \\ \hat{y}_c &= \hat{G}^{\alpha_c}\partial_{\alpha_c}H_c, \text{ and } \tilde{y}_c = \tilde{G}^{\alpha_c}\partial_{\alpha_c}H_c \end{aligned} \tag{15}$$

with $J_c^{\alpha_c\beta_c} = -J_c^{\beta_c\alpha_c}$, $R_c^{\alpha_c\beta_c} = R_c^{\beta_c\alpha_c}$, and $[R_c^{\alpha_c\beta_c}] \geq 0$; see, e.g., [10] for a concise introduction of the geometric structure behind (15). Note that the controller Hamiltonian H_c evolves along solutions of (15) as $\dot{H}_c = -\partial_{\alpha_c}(H_c)R_c^{\alpha_c\beta_c}\partial_{\beta_c}(H_c) + \hat{u}_c\hat{y}_c + \tilde{u}_c\tilde{y}_c$. As power-conserving feedback structure we simply choose

$$\hat{u}_c = \hat{y}_1, \quad \hat{u}^1 = -\hat{y}_c \text{ and } \tilde{u}_c = \tilde{y}_1, \quad \tilde{u}^1 = -\tilde{y}_c \tag{16}$$

clearly satisfying (14). Consequently, due to (16), the closed-loop Hamiltonian $H_{cl} = \int h\mathrm{d}z + H_c$ evolves along solutions of the closed loop (well-posedness provided) as:

$$\dot{H}_{cl} = -\int_B \delta_\alpha(h)R^{\alpha\beta}\delta_\beta(h)\mathrm{d}z - \partial_{\alpha_c}(H_c)R_c^{\alpha_c\beta_c}\partial_{\beta_c}(H_c)\,, \tag{17}$$

thus the controller injects additional damping into the closed loop.

Next, we investigate casimir functions of the plant (13) coupled with the controller (15) via the feedback structure (16), to relate (some) plant states to (some) controller states to shape H_{cl} such that its minimum is shifted to $x^{1,d}$.

Control by Means of Casimir Functions (Energy Shaping) Motivated by the results of [7, 10, 14], we are interested in casimir functions of the form:

$$C^\lambda = x_c^\lambda + \int_B c^\lambda \mathrm{d}z, \qquad c \in C^\infty(J^2(E)), \qquad \lambda = 1, \ldots, \bar{n} \leq n_c, \tag{18}$$

which have to be constant along the closed-loop trajectories, i.e., conserved quantities, to be able to relate (some) plant states to (some) controller states; thus, we require $\dot{C}^\lambda = 0$ independently of h and H_c. In that case, the casimir functions (18) enable us to easily express the controller states in terms of the plant states via $x_c^\lambda = -\int_B c^\lambda \mathrm{d}z + \kappa^\lambda$, where $\kappa^\lambda = C^\lambda|_{t=t_0}$ are constants that only depend on the plant and controller initial data. As a result, it may be possible to shape H_{cl} properly. For more details on the general framework, see [7], where a similar beam setup is considered as application example.

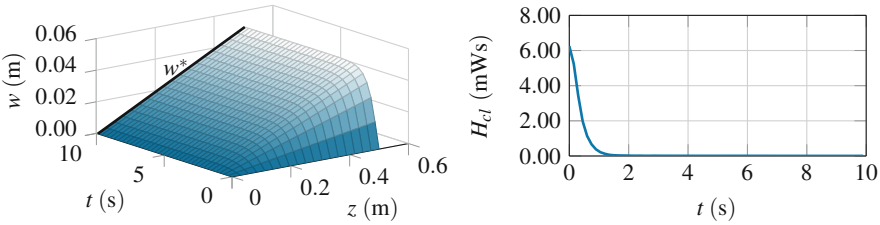

Fig. 1 *Left:* Beam deflection $w(z,t)$ plotted against time t and space variable z. Note that w^* indicates the rest position to be stabilized. *Right:* Closed-loop Hamiltonian H_{cl} plotted against t. Controller parameter: $J^{34} = 4.1$, $R^{33} = 10$, $R^{34} = 6$, $R^{44} = 12$, $\hat{G}^3 = 2.4$, $\hat{G}^4 = 0.8$, $\tilde{G}^3 = 0.9$, and $\tilde{G}^4 = 2.8$; beam parameter: $EI = 15\,\mathrm{Nm}^2$, $\rho A = 2.1\,\mathrm{kg/m}$, $L = 0.5\,\mathrm{m}$, and $a = 0.1\,\mathrm{m}$

With regard to stabilizing the rest position $x^{1,d} = az$ of the considered beam structure, we are thus interested in relations of the form $x_c^1 = x^1(L) + \kappa^1$ and $x_c^2 = x_z^1(L) + \kappa^2$. Fortunately, we find that both the functions (total derivatives) $c^1 = \frac{-1}{L} d_z(zx^1)$ and $c^2 = \frac{-1}{L} d_z(zx_z^1)$ are able to yield such relations if the controller maps are appropriately restricted. In particular, c^1 and c^2 are only casimir functions of the closed loop if the controller maps are restricted to $J_c^{\lambda\beta_c} - R_c^{\lambda\beta_c} = 0$ with $\lambda = 1, 2$, and $\hat{G}^1 = \tilde{G}^2 = 1$ as well as $\hat{G}^2 = \tilde{G}^1 = 0$. Consequently, if we set (with H from Example 1) $H_{cl} = H + \frac{1}{2}(x_c^1 - x_c^{1,d})^2 + \frac{1}{2}(x_c^2 - x_c^{2,d})^2 + \frac{1}{2}(x_c^3)^2 + \frac{1}{2}(x_c^4)^2$, as closed-loop Hamiltonian for example, it is obvious that $x^{1,d} = az$ is part of the strict minimum of H_{cl} due to the validity of the relations $x_c^1 = x^1(L) + \kappa^1$ and $x_c^{1,d} = aL + \kappa^1$ as well as $x_c^2 = x_z^1(L) + \kappa^2$ and $x_c^{2,d} = a + \kappa^2$. Note that the controller states x_c^1 and x_c^2 are responsible for the "energy-shaping" part—cf. H_{cl}, whereas x_c^3 and x_c^4 are responsible for the "damping-injection" part—cf. (17).

Finally, Fig. 1 presents simulation results that confirm the theoretical findings.

Remark 1 By exploiting functional-analytic methods, see [4] for example, it can be proven that the controller (15) stabilizes the rest position $x^{1,d}$ of the plant (13) asymptotically if the conditions $\hat{G}^3\tilde{G}^4 - \tilde{G}^3\hat{G}^4 \neq 0$ and $[R_c^{kl}] > 0, k, l = 3, 4$, are met.

Acknowledgement This work was partially supported by the Linz Center of Mechatronics (LCM) in the Framework of the Austrian COMET-K2 Program.

References

1. Abraham, R., Marsden, J.E.: Foundations of Mechanics, 2nd edn. Addison, Boston (1994)
2. Boothby, W.M.: An Introduction to Differentiable Manifolds and Riemannian Geometry, 2nd edn. Academic, New York (1986)
3. Giachetta, G., Mangiarotti, L., Sardanashvily, G.: New Lagrangian and Hamiltonian Methods in Field Theory. World Scientific, Singapore (1997)

4. Luo, Z.-H., Guo, B.-Z., Morgul, O.: Stability and Stabilization of Infinite Dimensional Systems with Applications. Springer, New York (1998)
5. Meirovitch, L.: Analytical Methods in Vibrations. Macmillan Publishing Co., Inc., New York (1967)
6. Olver, P.J.: Applications of Lie Groups to Differential Equations, 2nd edn. Springer, New York (1993)
7. Rams, H., Schöberl, M.: On structural invariants in the energy based control of port-Hamiltonian systems with second-order Hamiltonian. In: Proceedings of the American Control Conference (ACC), pp. 1139–1144 (2017)
8. Saunders, D.J.: The Geometry of Jet Bundles. Cambridge University Press, Cambridge (1989)
9. Schöberl, M., Schlacher, K.: Covariant formulation of the governing equations of continuum mechanics in an Eulerian description. J. Math. Phys. **48**(5), 052902 (2007)
10. Schöberl, M., Siuka, A.: On Casimir functionals for field theories in port-Hamiltonian description of control purposes. In: Proceeding of the 50th IEEE Conf. Decision and Control and European Control Conf. (CDC-ECC), pp. 7759–7764 (2011)
11. Schöberl, M., Siuka, A.: On the port-Hamiltonian representation of systems described by partial differential equations. In: Proceedings of the 4th IFAC Workshop on Lagrangian and Hamiltonian Methods for Non Linear Control, vol. 45, pp. 1–6 (2012)
12. Schöberl, M., Siuka, A.: Analysis and comparison of port-Hamiltonian formulations for field theories - demonstrated by means of the Mindlin plate. In: Proceeding of the European Control Conference (ECC), pp. 548–553 (2013)
13. Schöberl, M., Ennsbrunner, H., Schlacher, K.: Modelling of piezoelectric structures - a Hamiltonian approach. Math. Comput. Model. Dyn. Syst. **14**(3), 179–193 (2008)
14. Siuka, A., Schöberl, M., Schlacher, K.: Port-Hamiltonian modelling and energy-based control of the Timoshenko beam - an approach based on structural invariants. Acta Mech. **222**(1), 69–89 (2011)
15. van der Schaft, A.J.: L2-Gain and Passivity Techniques in Nonlinear Control. Springer, New York (2000)

A Modular Solver for Mechanical System Dynamics Under One-Sided Contact Constraints

Alexander Schirrer and Sebastian Thormann

Abstract A modular and flexible solver for mechanical system dynamics with one-sided (inequality) contact constraints is proposed. In each time step, an active set method constructs the current set of active constraints, the α-RATTLE time integration method is employed to solve the equality-constrained subproblem, and a Newton iteration is applied to solve the implicit system of update equations. The purely geometric formulation of the constraint functions allows an efficient modeling of system couplings where the constraint forces are solved for as part of the solution. A test case showing a ball bouncing on a string illustrates the solver's functionality.

1 Introduction

Many technical applications of mechanical systems involve transient contacts between solid (rigid or deformable) bodies. Even everyday examples like a tennis racket hitting the ball—two deformable bodies colliding abruptly—represents a difficult computational problem. The resulting constraint forces and the shape of the contact region depend on each other. Both evolve over time as part of the solution in such a way that no penetration occurs. These contact problems are commonly solved numerically using the finite element method (FEM) in combination with penalty techniques (minimize penetration) or Lagrange multiplier methods (exact solution) as described in Ref. [8, ch. 10.3]. The (nonlinear) FEM for mechanical problems [2, ch. 6.2] is commonly based on D'Alembert's principle, using a Lagrangian (material) formulation of the problem.

A. Schirrer (✉) · S. Thormann
Institute of Mechanics and Mechatronics, Technische Universität Wien, Vienna, Austria
e-mail: alexander.schirrer@tuwien.ac.at; sebastian.thormann@tuwien.ac.at

V. P. Matveenko et al. (eds.), *Dynamics and Control of Advanced Structures and Machines*, https://doi.org/10.1007/978-3-319-90884-7_16

The focus of this work is the dynamics of rigid and/or elastic bodies coupled by generalized contacts. For this application field, we introduce a flexible solver architecture for transient contact problems. Its efficiency is illustrated via a planar test problem in which a ball bounces on an elastic string.

The presented solver is based on the α-RATTLE method [7] which is inspired by the RATTLE method [1] of molecular dynamics, extending the generalized α-method [3] with algebraic constraints. Special parameter cases of the generalized α-method lead to, e.g., the Newmark or the Hilber–Hughes–Taylor integration methods. The α-RATTLE method is a numerical time integration scheme for Lagrange's equations of the first kind (following from D'Alembert's principle) stabilized by additional degrees of freedom. This extended system formulation with global index two was derived in Ref. [5]. A numerical solution was proposed in Ref. [4], highlighting the advantages over former methods based on the Euler–Lagrange equation (i.e., state-space form or Lagrange's equation of the second kind).

Lagrange's equations of the first kind allow for modularization of the system (and solver) structure since the mechanical subsystems add equations independent of the other systems. The coupling between subsystems is formulated via generalized contact constraints. These are represented as algebraic constraint equalities or inequalities. Consequently, constraint forces need not be modeled explicitly—instead, they are determined as part of the solution. The constrained system takes the form of an inequality-constrained differential-algebraic equation (DAE).

2 Problem Statement

The proposed algorithm solves the inequality-constrained DAE system:

$$M\ddot{q} + G^{\mathrm{T}}\lambda = f\left(\dot{q}, q, t\right) \tag{1}$$

$$g_{\mathrm{eq}}\left(q, t\right) = 0 \tag{2}$$

$$g_{\mathrm{iq}}\left(q, t\right) \leq 0 \tag{3}$$

over time t. The generalized coordinate vector q, velocities $\dot{q}$, and accelerations $\ddot{q}$, as well as the constraint force vector $G^{\mathrm{T}}\lambda$ constitute the unknowns. Here, (1) is called the equation of motion, which is a vector-valued balance of inertial forces $M\ddot{q}$, constraint forces, and active forces f given as a function $f = f\left(\dot{q}, q, t\right)$. Such formulation is readily obtained, for example, after applying the FEM on a solid-body problem. The square mass matrix M is assumed to be constant and invertible. From the principle of sufficient reason, it follows that the vector $G^{\mathrm{T}}\lambda$ is orthogonal to the (time-varying) contact surfaces [6, ch. 2]. The constraint Jacobian G projects the auxiliary vector of Lagrange multipliers λ accordingly.

Constraints are formulated via scalar functions either in the form of equalities (e.g., clamping) or inequalities (e.g., no penetration between two bodies). Herein, these constraints are interpreted as displacement-level constraints, and the constraint functions represent the (generalized) displacement residuals. They can be explicitly time dependent (rheonomic) but are assumed independent of $\dot{q}$. Multiple scalar constraint functions are then stacked into vectors $g_{\mathrm{eq}} = g_{\mathrm{eq}}(q,t)$ and $g_{\mathrm{iq}} = g_{\mathrm{iq}}(q,t)$ for equality and inequality constraint functions, respectively.

All quantities in (1)–(3) are time dependent (except for M) and real valued. The initial values $q_0 = q\ (t = t_0)$ and $\dot{q}_0 = \dot{q}\ (t = t_0)$ are given.

3 Solution Strategy

The problem (1)–(3) is solved over the time interval $t \in [t_0, t_{\mathrm{end}}]$ by combining:

1. An active-set management strategy,
2. The α-RATTLE method [7] for numerical time integration, and
3. A dynamic equilibrium iteration using the Newton–Raphson scheme [2, ch. 8.4.1].

The combination of these methods results in an algorithm structure consisting of three nested iteration levels, outlined in Fig. 1. Hereafter, these three levels will be called Time Stepper, Active Set Manager, and Dynamic Equilibrium (DE) Solver. The DE Solver operates on a stacked unknown vector x (including q and $\dot{q}$) as explained below.

The Time Stepper constructs the solution over a major time grid spanning $[t_0; t_{\mathrm{end}}]$. For each time step, the Active Set Manager (and therein, to the DE Solver) is called to obtain the solution. If convergence of either the active set or the equilibrium iterations fails, shorter (minor) time steps are attempted.

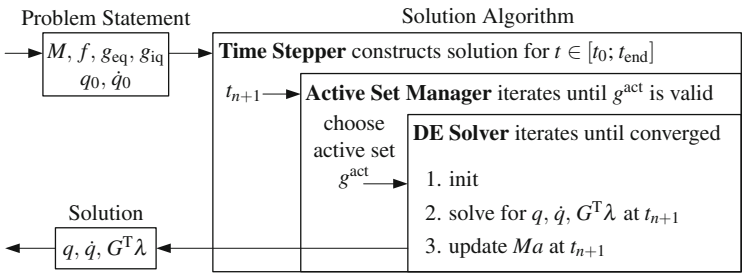

Fig. 1 Solver architecture

3.1 Active Set Manager

Since a direct solution to the original system (1)–(3) is difficult because of the inequality (3), an active set method is employed. All formulated scalar constraint functions together form the candidate set $\bar{g} = g_{\mathrm{eq}} \cup g_{\mathrm{iq}}$.

For each time step, the Active Set Manager iteratively updates the active set $g^{\mathrm{act}} \subseteq \bar{g}$ until it is valid (satisfies the Hertz–Signorini–Moreau conditions [8]). As a result:

$$g^{\mathrm{act}}(q, t) = 0 \tag{4}$$

replaces the equalities (2) and inequalities (3). If g^{act} is valid, then the DAE system (1), (4) is locally (at this point in time) equivalent to the inequality-constrained DAE system (1)–(3). The set g_{eq} is always part of the active set g^{act}. The set g_{iq} is partitioned into two subsets: the active inequality functions $g_{\mathrm{iq}}^{\mathrm{act}}$ and the inactive ones $g_{\mathrm{iq}}^{\mathrm{ina}}$, hence $g_{\mathrm{iq}} = g_{\mathrm{iq}}^{\mathrm{act}} \cup g_{\mathrm{iq}}^{\mathrm{ina}}$ and $g_{\mathrm{iq}}^{\mathrm{ina}} = g_{\mathrm{iq}} \setminus g^{\mathrm{act}}$ hold.

Since each element of $\bar{g}$ corresponds to a component of the vector λ, also the set of active inequality functions $g_{\mathrm{iq}}^{\mathrm{act}} \subseteq \bar{g}$ corresponds to a part of λ, denoted by the vector $\lambda_{\mathrm{iq}}^{\mathrm{act}}$. Analogously, the vector $\lambda_{\mathrm{iq}}^{\mathrm{ina}}$ is that part of λ which corresponds to the set $g_{\mathrm{iq}}^{\mathrm{ina}}$. It holds that

$$\text{Eq. (4)} \ \wedge \ g_{\mathrm{iq}}^{\mathrm{ina}} < 0 \ \wedge \ \lambda_{\mathrm{iq}}^{\mathrm{act}} \geq 0 \ \wedge \ \lambda_{\mathrm{iq}}^{\mathrm{ina}} = 0 \quad \Longrightarrow \quad g^{\mathrm{act}} \text{ is valid}. \tag{5}$$

The active set iteration starts with an initial guess for g^{act}. A useful guess is the valid g^{act} from the last time step. Violated inequality constraints $g_{\mathrm{iq}}^{\mathrm{vio}}$ are not in g^{act} but nonnegative, meaning that $g_{\mathrm{act}}^{\mathrm{vio}} = \{g_{\mathrm{iq}}^{\mathrm{ina}} \geq 0\}$. Inequality constraint functions which correspond to negative-valued $\lambda_{\mathrm{iq}}^{\mathrm{act}}$ cause (incorrect) "sticking" constraint forces, denoted by $g_{\mathrm{iq}}^{\mathrm{neg}}$. The update rule:

$$g^{\mathrm{act}} \rightarrow \left(\left(g_{\mathrm{iq}}^{\mathrm{act}} \cup g_{\mathrm{iq}}^{\mathrm{vio}} \right) \setminus g_{\mathrm{iq}}^{\mathrm{neg}} \right) \cup g_{\mathrm{eq}} \tag{6}$$

is therefore applied until g^{act} is valid according to (5). If this procedure fails, a shorter time step is attempted.

3.2 Dynamic Equilibrium Solver

Considering the DAE system of (1), (4) where the active set $g = g^{\mathrm{act}}$ is defined locally at one active set iteration step, the α-RATTLE method [7] is applied, which

implicitly defines the new unknowns x via:

$$\overbrace{\begin{bmatrix} M & 0 & -\alpha_4 G_n^{\mathrm{T}} - \alpha_5 G_{n+1}^{\mathrm{T}} & 0 \\ 0 & M & 0.5h G_n^{\mathrm{T}} & 0.5h G_{n+1}^{\mathrm{T}} \\ 0 & G_{n+1} & 0 & 0 \\ 0 & 0 & 0 & 0 \end{bmatrix}}^{D(x_{n+1})} \overbrace{\begin{bmatrix} q_{n+1} \\ v_{n+1} \\ \lambda_{n+1}^{+} \\ \lambda_{n+1}^{-} \end{bmatrix}}^{x_{n+1}}$$

$$= \overbrace{\begin{bmatrix} \alpha_3 f_{n+1} + \alpha_2 f_n + M(q_n + h v_n + \alpha_1 a_n) \\ \alpha_8 f_{n+1} + \alpha_7 f_n + M(v_n + \alpha_6 a_n) \\ -\dot{g}_{n+1} \\ g_{n+1} \end{bmatrix}}^{R(x_{n+1})} \tag{7}$$

and

$$M a_{n+1} = \alpha_9 f_n + \alpha_{10} f_{n+1} + \alpha_{11} M a_n \,. \tag{8}$$

The system (7), (8) describes the discrete time evolution from t_n to t_{n+1} (time step size $h = t_{n+1} - t_n$) of five vectors : the coordinates $q_n = q(t_n)$, the velocities $v_n = \dot{q}(t_n)$, the auxiliary variables a_n, and the approximations of the Lagrange multipliers for the next point in time $\lambda_{n+1}^{+} \simeq \lambda(t_{n+1})$ and for the last one $\lambda_{n+1}^{-} \simeq \lambda(t_n)$. Here, the term $\dot{g}_{n+1}$ stems from the consideration of rheonomic constraints and the scalars α_i are given below. Since the matrix D and the vector R depend (nonlinearly) on components of the unknowns at the next time step x_{n+1}, a direct solution is typically not possible.

Hence, the nonlinear implicit root finding problem:

$$F(x_{n+1}) := D(x_{n+1}) x_{n+1} - R(x_{n+1}) = 0 \,, \tag{9}$$

is solved iteratively via the Newton–Raphson approach in each time step, obtained by a Taylor expansion of F (iteration index k):

$$F(x_{n+1}^k + \Delta x_{n+1}^k) \doteq F(x_{n+1})|_{x_{n+1}^k} + \left.\frac{\partial F(x_{n+1})}{\partial x_{n+1}}\right|_{x_{n+1}^k} \Delta x_{n+1}^k$$

$$= -B + A\ \Delta x_{n+1}^k := 0 \,. \tag{10}$$

Therefore, the dynamic equilibrium update is given by:

$$x_{n+1}^{k+1} := x_{n+1}^k + \Delta x_{n+1}^k \quad \text{with} \quad A\ \Delta x_{n+1}^k = B \,, \tag{11}$$

with the coefficient matrix A and the right-hand side B (the indices $n+1$ for the next point in time t_{n+1} and k for the current iteration are suppressed for the symbols q, v, f, λ^+, λ^-, K, C, g, $\dot{g}$, G, $\dot{G}$, H_v, H_λ^+, and H_λ^-) defined by:

$$A = \begin{bmatrix} M + \alpha_3 K - \alpha_5 H_\lambda^+ & \alpha_3 C & -\alpha_4 G_n^{\mathrm{T}} - \alpha_5 G^{\mathrm{T}} & 0 \\ \alpha_8 K + 0.5h H_\lambda^- & M + \alpha_8 C & 0.5h G_n^{\mathrm{T}} & 0.5h G^{\mathrm{T}} \\ H_v + \dot{G} & G & 0 & 0 \\ -G & 0 & 0 & 0 \end{bmatrix} \tag{12}$$

$$B = \begin{bmatrix} M(q_n - q) + hMv_n + (\alpha_4 G_n^{\mathrm{T}} + \alpha_5 G^{\mathrm{T}})\lambda^+ + \alpha_1 M a_n + \alpha_2 f_n + \alpha_3 f \\ M(v_n - v) - 0.5h(G_n^{\mathrm{T}}\lambda^+ + G^{\mathrm{T}}\lambda^-) + \alpha_7 f_n + \alpha_8 f + \alpha_6 M a_n \\ -Gv - \dot{g} \\ g \end{bmatrix} \tag{13}$$

The matrices A and B contain derivatives of the forcing f: tangent stiffness matrix K and damping matrix C. They also contain derivatives of the vector g corresponding to the active set of constraint functions: the vector $\dot{g}$, and the matrices G, $\dot{G}$, H_v, H_λ^+, and H_λ^-. These derivatives are defined as:

$$K = -\frac{\partial f\,(\dot{q}, q, t)}{\partial q}\,,\quad C = -\frac{\partial f\,(\dot{q}, q, t)}{\partial \dot{q}}\,,\quad \dot{g} = \frac{\partial g\,(q, t)}{\partial t}\,,\quad G = \frac{\partial g\,(q, t)}{\partial q}\,,$$

$$\dot{G} = \frac{\partial^2 g\,(q, t)}{\partial q\,\partial t}\,,\quad H_v = \frac{\partial\,(Gv)}{\partial q}\,,\quad H_\lambda^+ = \frac{\partial\left(G^{\mathrm{T}}\lambda^+\right)}{\partial q}\,,\quad \text{and}\quad H_\lambda^- = \frac{\partial\left(G^{\mathrm{T}}\lambda^-\right)}{\partial q}\,.$$

The scalars α_i in (7), (8), and (11) are given by:

$$\alpha_1 = \tfrac{h^2}{2}\tfrac{1-\alpha_\mathrm{m}-2\beta}{1-\alpha_\mathrm{m}}\,,\ \alpha_2 = h^2\beta\tfrac{\alpha_\mathrm{f}}{1-\alpha_\mathrm{m}}\,,\ \alpha_3 = h^2\beta\tfrac{1-\alpha_\mathrm{f}}{1-\alpha_\mathrm{m}}\,,\ \alpha_4 = h^2\left(\bar{\beta} - \tfrac{1}{2}\right)\,,$$
$$\alpha_5 = -h^2\bar{\beta}\,,\qquad \alpha_6 = h\tfrac{1-\gamma-\alpha_\mathrm{m}}{1-\alpha_\mathrm{m}}\,,\ \alpha_7 = h\gamma\tfrac{\alpha_\mathrm{f}}{1-\alpha_\mathrm{m}}\,,\quad \alpha_8 = h\gamma\tfrac{1-\alpha_\mathrm{f}}{1-\alpha_\mathrm{m}}$$
$$\alpha_9 = \tfrac{\alpha_\mathrm{f}}{1-\alpha_\mathrm{m}}\,,\qquad \alpha_{10} = \tfrac{1-\alpha_\mathrm{f}}{1-\alpha_\mathrm{m}}\,,\qquad \text{and } \alpha_{11} = -\tfrac{\alpha_\mathrm{m}}{1-\alpha_\mathrm{m}}\,.$$

Further details on the coefficients of the integration scheme (α_f, α_m, β, $\bar{\beta}$, *and* γ), and accuracy and numerical damping properties of the α-RATTLE method are given in [7]. Summing up, one call of the Dynamic Equilibrium Solver:

1. Prepares the initial values of the vector x,
2. Iterates x (11) until a terminal condition is met (e.g., Δx sufficiently small), and
3. Finally updates the vector Ma by (8).

4 Implementation Aspects

To illustrate the proposed solver, a two-dimensional contact problem between a rigid ball and an elastic rope is shown. The rigid ball is modeled via a point mass P. Its spatial extension (circle with radius R) is considered by one-sided radius constraints (inequalities), which prevent penetrations between the ball and the rope nodes. The rope is modeled by nonlinear finite elements E and clamped at points a and b, see Fig. 2. In the initial state of the simulation, both bodies are at rest, the rope forms a straight line from a to b, and the ball is located above the rope without contact. Gravity accelerates P downwards until the first contact occurs. Figure 2 shows a snapshot of both bodies in contact, where cross markers indicate active constraints. Dotted lines represent snapshots of the rope at several times after the first contact.

The inequality-constrained DAE system (1)–(3) can be formulated by first modeling the unconstrained solid bodies and then adding the constraint functions g_{eq} and g_{iq}. Newton's second law for point mass P states, with regard to its coordinates $q_P = [x_P \; y_P]^{\text{T}}$ and mass m_P, that

$$\begin{bmatrix} m_P & 0 \\ 0 & m_P \end{bmatrix} \begin{bmatrix} \ddot{x}_P \\ \ddot{y}_P \end{bmatrix} = \begin{bmatrix} 0 \\ -m_P\, a_{\text{g}} \end{bmatrix} \quad \Longleftrightarrow \quad M_P \ddot{q}_P = f_P$$

holds, where the scalar a_{g} is the gravitational acceleration. Therefore, all necessary quantities of P are known: its coordinate vector q_P, mass matrix M_P, and active forces $f_P = const.$

The rope is assembled out of N_E nonlinear truss elements E according to Ref. [2, ch. 6.3.3]. Each of these isoparametric two-node elements (four degrees of freedom per element) is formulated in the form of:

$$M_E\,(\rho A, L_0)\,\ddot{q}_E = f_E\left(q_E, \rho A, EA, a_{\text{g}}, L_0\right) ,$$

with specific mass ρA, spring constant EA, and relaxed length L_0 of E. Assembling both subsystems (point mass P and rope) yields the global stacked coordinate vector:

$$q = \left[x_P \; y_P \; x_1 \; y_1 \; x_2 \; y_2 \; \ldots \; y_{N_E} \; x_{N_E+1} \; y_{N_E+1}\right]^{\text{T}} ,$$

mass matrix M, and active forces f in the equation of motion (1) of the full system.

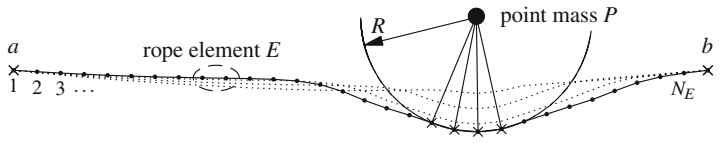

Fig. 2 Snapshots of the bouncing ball test problem

Equality constraint functions in g_{eq} realize the clamping of the nodes at a and b; inequality constraint functions in g_{iq} prevent penetrations between the ball with radius R and the nodes of the rope:

$$g_{\text{eq}} = \begin{bmatrix} x_1 - x_a \\ y_1 - y_a \\ x_{N_E+1} - x_b \\ y_{N_E+1} - y_b \end{bmatrix}, \; g_{\text{iq}} = \begin{bmatrix} \sqrt{(x_P - x_1)^2 + (y_P - y_1)^2} - R \\ \sqrt{(x_P - x_2)^2 + (y_P - y_2)^2} - R \\ \vdots \end{bmatrix} = r\,(q) - R\,,$$

where $r(q)$ is the vector of current distances and the vector g_{iq} has $N_E + 1$ components. The candidate Jacobian matrix $\bar{G}$ of the candidate set $\bar{g}$ has the form:

$$\bar{G} = \begin{bmatrix} \frac{\partial g_{\text{eq}}}{\partial x_P} & \frac{\partial g_{\text{eq}}}{\partial y_P} & \cdots & \frac{\partial g_{\text{eq}}}{\partial y_{N_E+1}} \\ \frac{\partial g_{\text{iq}}}{\partial x_P} & \frac{\partial g_{\text{iq}}}{\partial y_P} & \cdots & \frac{\partial g_{\text{iq}}}{\partial y_{N_E+1}} \end{bmatrix} \quad \text{with e.g.,} \quad \frac{\partial g_{\text{iq}}}{\partial x_P} = \begin{bmatrix} \frac{x_P - x_1}{r_1} \\ \frac{x_P - x_2}{r_2} \\ \vdots \end{bmatrix}.$$

The Jacobian matrix G of the current active set g^{act} is always a part of the matrix $\bar{G}$. Here, the derivatives $\dot{g}$ and $\dot{G}$ are zero since $\bar{g}$ is not explicitly time dependent; for simplicity, the derivatives H_v, H_λ^+, and H_λ^- are neglected here. This is admissible because these terms do not affect the right-hand side B (13) and thus correctness of the solution. Perturbations in the coefficient matrix A (12) potentially do affect the convergence speed and stability of the Newton–Raphson scheme, but no according effects have been seen here.

Figure 3 shows the transient build-up and bounce-off of the ball over time. Vertical ball position y_P, the varying number of active radius constraints, and the total vertical constraint force V_P acting on the ball demonstrate the solver's ability to solve this one-sided contact problem effectively.

Summing up, a flexible solver architecture for solid-body problems with equality and inequality constraints (representing two-sided respectively one-sided contacts)

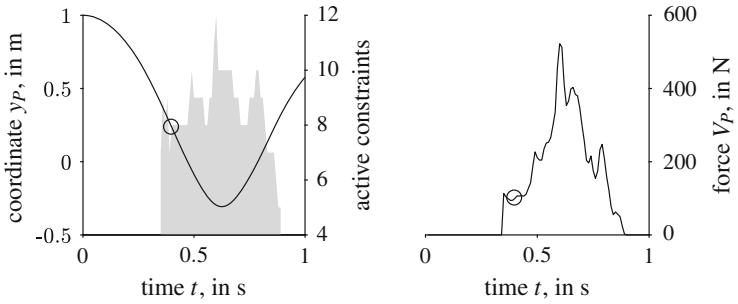

Fig. 3 Bouncing ball test problem: vertical ball position y_P, number of active constraints, and total vertical constraint force V_P on the ball plotted over time; the circle indicates the time of the main snapshot shown in Fig. 2

has been proposed. An active set strategy has been combined with DAE solving techniques (the α-RATTLE method), allowing an efficient and strongly modularized treatment of assembled system dynamics.

Acknowledgements The authors gratefully acknowledge partial funding by grant no. 854381 (Competence Headquarters) of the Austrian Research Promotion Agency (FFG).

References

1. Andersen, H.C.: Rattle: a "velocity" version of the shake algorithm for molecular dynamics calculations. J. Comput. Phys. **52**(1), 24–34 (1983)
2. Bathe, K.-J.: Finite Element Procedures, 2nd edn. Klaus-Jürgen Bathe, Berlin (2006)
3. Chung, J., Hulbert, G.M.: A time integration algorithm for structural dynamics with improved numerical dissipation: the generalized-α method. J. Appl. Mech. **60**(2), 371–375 (1993)
4. Führer, C., Leimkuhler, B.J.: Numerical solution of differential-algebraic equations for constrained mechanical motion. Numer. Math. **59**(1), 55–69 (1991)
5. Gear, C.W., Leimkuhler, B.J., Gupta, G.K.: Automatic integration of Euler-Lagrange equations with constraints. J. Comput. Appl. Math. **12**, 77–90 (1985)
6. Hamel, G.: Theoretische Mechanik: eine einheitliche Einführung in die gesamte Mechanik (Engl.: Theor. Mechanics: A Unified Introduction into the Entirety of Mechanics). Springer, New York (1949)
7. Lunk, C., Simeon, B.: Solving constrained mechanical systems by the family of Newmark and α-methods. ZAMM-J. Appl. Math. Mech./Zeitschrift für Angewandte Mathematik und Mechanik **86**(10), 772–784 (2006)
8. Wriggers, P.: Computational Contact Mechanics. Springer Science & Business Media, Berlin (2006)

Shock Absorption Effect of Semi-active Mass Control Mechanism for Structure

Ming-Hsiang Shih and Wen-Pei Sung

Abstract Taiwan is located in the Circum-Pacific Seismic Zone and also at the junction of the Eurasian plate and the Philippine Sea plate, initiating sensible earthquakes to threaten the structural safety. Therefore, in order to enhance the seismic proof capability of structure, a new structural control mechanism, emerged passive control and active control, is proposed in this study. This mechanism can execute the "release" and "capture" of control mass block and only produce "negative" work on structure, based on the active mass control principle without power supply. A mathematical model of control law of this proposed mechanism is derived and the parameter study for single degree of freedom is executed to compare with those of structures without control and with passive tuned mass damper to obtain the optimal design parameters. Analysis results display that amplification of steady state reaction for structure with this semi-active control is much less than those of structure with passive control under within 0.03–0.07 and around 0.6–1.6. This proposed mechanism can "capture" and "release" the active control mass based on the direction and velocity of movement of the structural displacement.

1 Introduction

There are many reasons to enhance the intensity of natural disasters such as strong earthquakes, typhoons, and hurricanes. Especially, Taiwan is located in the Circum-Pacific Seismic Zone and also at the junction of the Eurasian plate and the Philippine Sea plate, initiating sensible earthquakes every year, for example, 6.4 Richter scale earthquake magnitudes, happened in southern Taiwan, led to the 16-story building collapsed on the ground, causing heavy casualties in 2016, before Chinese New Year

M.-H. Shih (✉)
Department of Civil Engineering, National Chi Nan University, Nan-Tou, Taiwan

W.-P. Sung
Department of Landscape Architecture, Integrated Research Center for Green Living Technologies, National Chin-Yi University of Technology, Taichung, Taiwan
e-mail: wps@ncut.edu.tw

V. P. Matveenko et al. (eds.), *Dynamics and Control of Advanced Structures and Machines*, https://doi.org/10.1007/978-3-319-90884-7_17

and 5.6 Richter scale earthquake magnitudes, happened in Hualien, eastern Taiwan, led to many buildings collapse. The main reason for building collapse is lack of earthquake resistance capability. To maintain the safety of buildings to resist seismic force and other dynamical excitations, structural control theorems and equipment are widely applied in Architecture and Civil Engineering. In this study, a semi-active mass control mechanism is proposed to combine the advantages of a tuned mass damper with active mass damper. This new proposed mechanism is adopted to improve passive control damper and active control damper as a semi-active mass control mechanism. This mechanism can execute the "release" and "capture" of control mass block, based on the active mass control principle without power supply.

Presently, structural control techniques have been divided into passive control [1–4], active control [5–8], and semi-active control [9–12]. The disadvantage of passive control is that such approaches provide insufficient strength to counter large deformation. Active control [5–8] requires a supply of external energy to exert a control force. An active control system must be ready to detect structural responses according to predetermined control laws, transmit a control signal, and output commands to the system to produce a moderate control force. Therefore, semi-active control [9–12], emerged passive control and active control, is proposed to improve the disadvantages of these two control dampers. A new structural control method, a semi-active mass control mechanism, is proposed in this research to improve these two kinds of dampers as a semi-active mass control mechanism. The control power of these two control methods is derived from the vibrations of structural responses. This control mechanism has a variable control system that provides different natural frequencies to control structural displacement. A mathematical model and the control logic of this semi-active control mechanism are provided in this paper. Then, the parameter study of this proposed method, installed in single degree of freedom structure, is analyzed, discussed, and compared with those of structures without control and with passive control to obtain the optimal design parameters.

2 Methodology

2.1 Mathematical Model of Semi-active Mass Control Method

The structural control mechanism of this proposed method is based on active mass control principle to execute the action of "release" and "capture" of control mass block. It is a variable control system to provide with different natural frequency of structure according to the changeable system of this proposed control method. This proposed control method does not have obvious natural frequency, and so resonance phenomenon does not exist. This proposed structural control mechanism, installed in structure, is shown in Fig. 1.

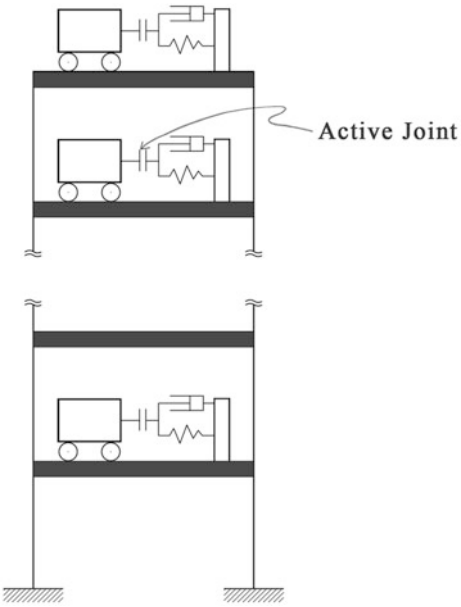

Fig. 1 The proposed semi-active mass control mechanism

According to Fig. 1, the equation of motion of this proposed system can be derived as follows:

$$\left[\underline{\underline{M}}\ \underline{\underline{m}}\right]\left\{\begin{matrix}\ddot{\underline{X}}\\ \ddot{\underline{x}}\end{matrix}\right\}+\left[\underline{\underline{C}}\ \underline{\underline{c}}\right]\left\{\begin{matrix}\dot{\underline{X}}\\ \dot{\underline{x}}\end{matrix}\right\}+\left[\underline{\underline{K}}\ \underline{\underline{k}}\right]\left\{\begin{matrix}\underline{X}\\ \underline{x}\end{matrix}\right\}=\underline{P}(t), \tag{1}$$

$$\underline{\underline{M}}\,\ddot{\underline{X}}(t)+\underline{\underline{C}}\,\dot{\underline{X}}(t)+\underline{\underline{K}}\,\underline{X}(t)=\underline{P}(t)-\left\{\underline{\underline{m}}\,\ddot{\underline{x}}(t)+\underline{\underline{c}}\,\dot{\underline{x}}(t)+\underline{\underline{k}}\,\underline{x}(t)\right\}. \tag{2}$$

Let control force be $\underline{u}_i(t) = -\left\{\underline{\underline{m}}\,\ddot{\underline{x}}(t)+\underline{\underline{c}}\,\dot{\underline{x}}(t)+\underline{\underline{k}}\,\underline{x}(t)\right\}$. Therefore, control force $\underline{u}_i(t)$ of Eq. (3) is active changeable. Equation (2) can be rewritten as follows:

$$\underline{\underline{M}}\,\ddot{\underline{X}}(t)+\underline{\underline{C}}\,\dot{\underline{X}}(t)+\underline{\underline{K}}\,\underline{X}(t)=\underline{P}(t)+\underline{u}_i(t), \tag{3}$$

in which $\underline{u}_i(t)=\underline{u}_1(t)+\underline{u}_2(t)+\cdots+\underline{u}_M(t)$ and $\underline{u}_i(t)=\underline{u}_i^C(t)$ or $\underline{u}_i(t)=\underline{u}_i^R(t)$ for $i=1,\ldots,M$.

In this proposed method, the equivalent control force $\underline{u}_i^C(t)$ and $\underline{u}_i^R(t)$ of each control mass block for "captured state" and "released state" can be obtained based on the detecting reaction state of structure and control mass blocks. Therefore, $\underline{u}_i(t)$ actively changes and only produced negative power for the structure to be controlled. Then, the control logic will be described in Sect. 2.2.

2.2 Control Logic of the Proposed Method

This proposed mechanism is a changeable system and choose the optimal combination of active mass block to reduce the structural dynamic responses under excitation of earthquake force. In order to execute the "release" state and "capture" state at the best time, the control command is carried out based on the sign of the velocity of the control mass block. The sign of the velocity of the control mass block relative to that of the structure and the sign of the structural velocity at the control mass block of a placed degree of freedom (DOF) is a contrary sign. When the relative displacement of the control mass block at the placed DOF to the structural displacement at the control mass block of the placed DOF is zero, the active control joint begins to be released. The sign of the velocity of the control mass block relative to that of the structure and the sign of the structural velocity at the control mass block of the placed DOF is the same sign. The duration for the structure to capture the active mass block is half the natural frequency of the control mass block system.

The control flowchart of this proposed system is presented in Fig. 2. In Fig. 2, x_i^s and x_i^m denote the displacement response of structure at which the i-th control mass installed and of the i-th control mass, respectively, and ε_i denote the strain or force exerted by the i-th control mass on the structure.

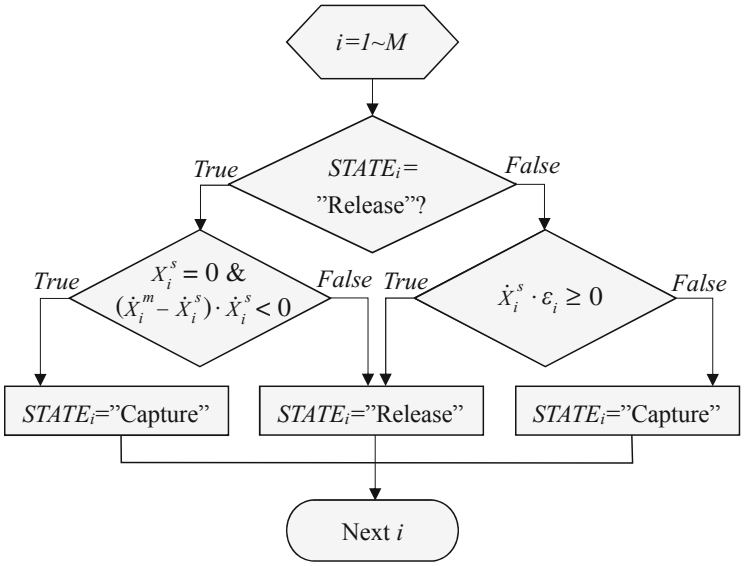

Fig. 2 The flowchart of the control logic for this proposed mechanism

3 Analysis Results and Discussions

In order to compare the structural control effects of structure under control of different structural control method, a single degree of freedom (SDOF) structure is executed to compare the energy dissipation behavior of the structure under passive control in the resonance state and the random loading state with those of this proposed control method in this section. This SDOF is with mass of structure = 1 kg, stiffness = 40 N/m, damping ratio = 0.03, passive tuned mass block = 0.04 kg, and spring constant = 1.6 N/m. In this study, two design parameters are defined as: η is the ratio of the mass summation of the control mass blocks to the total mass of the structural system, and Ω, the ratio of the frequency of the control mass block to the fundamental natural frequency of the structural system. In order to investigate the influence of the loading frequency, β is defined as the ratio of frequency of a periodic load to the fundamental natural frequency of the structure. This structure is subjected to periodic loads $\beta = 0.2, 0.4, 0.6, 0.8, 1.0, 1.2, 1.4, 1.8, 2.0$. Then the single DOF building without control, with passive control $\Omega = 1$, and with semi-active $\Omega = 4$ with ratios of mass variation of $\eta = 0.01, 0.02, 0.03, 0.04, 0.05, 0.06, 0.07, 0.08, 0.09, 0.10$ under excitation of various β is compared with the steady state reaction and the relationship of the amplification factor to β. The results of analysis of the amplification of the steady state reaction for the structure without control and those with passive and semi-active control are listed in Table 1. The relationship of the amplification factor to β for the structure without control and those with passive and semi-active control are presented in Fig. 3.

Analysis results of Table 1 show that the amplification of steady state response for SDOF with this semi-active control is much less than those of SDOF with

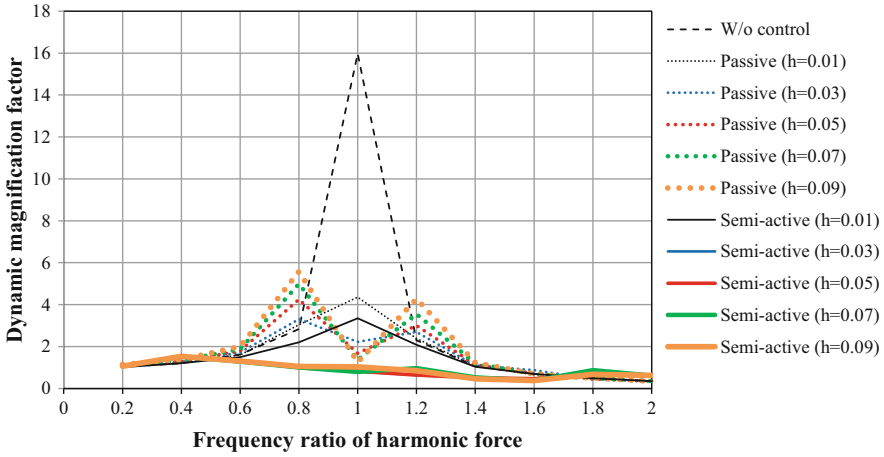

Fig. 3 Dynamic magnification factor of various mass ratio for different control method

Table 1 Amplification of steady state reaction for structure without control and with passive control and semi-active control for SDOF structure

$\eta(\%)/\beta$	0.2	0.4	0.6	0.8	1.0	1.2	1.4	1.6	1.8	2.0
Dynamic magnitude without control										
–	1.03	1.21	1.62	2.83	15.98	2.30	1.07	0.69	0.50	0.35
Dynamic magnitude with passive control										
1	1.06	1.21	1.60	3.04	4.36	2.39	1.08	0.65	0.46	0.34
2	1.07	1.24	1.70	3.25	2.85	2.48	1.12	0.70	0.48	0.34
3	1.08	1.26	1.72	3.31	2.22	2.70	1.10	0.88	0.45	0.33
4	1.10	1.27	1.79	3.97	1.98	2.91	1.13	0.89	0.45	0.35
5	1.11	1.28	1.80	4.25	1.68	3.01	1.13	0.71	0.45	0.35
6	1.12	1.32	1.82	4.51	1.43	3.21	1.17	0.68	0.48	0.35
7	1.13	1.34	1.88	4.99	1.37	3.55	1.20	0.68	0.50	0.35
8	1.14	1.35	1.94	3.34	1.30	3.99	1.24	0.70	0.50	0.35
9	1.15	1.37	2.01	5.57	1.25	4.28	1.23	0.70	0.49	0.35
10	1.17	1.40	2.08	6.51	1.23	4.62	1.22	0.69	0.49	0.36
Dynamic magnitude with semi-active control										
1	1.01	1.21	1.50	2.20	3.35	2.09	1.04	0.69	0.49	0.35
2	1.02	1.25	1.41	1.72	2.09	1.44	0.95	0.70	0.47	0.32
3	1.04	1.35	1.37	1.37	1.25	1.01	0.79	0.64	0.65	0.61
4	1.06	1.43	1.34	1.12	1.19	0.80	0.62	0.55	0.63	0.61
5	1.07	1.51	1.31	0.99	0.82	0.64	0.51	0.47	0.63	0.63
6	1.08	1.53	1.28	0.89	0.70	0.53	0.43	0.46	0.66	0.62
7	1.07	1.52	1.28	1.00	0.79	0.97	0.53	0.37	0.88	0.62
8	1.07	1.52	1.29	0.98	1.39	0.91	0.49	0.41	0.70	0.61
9	1.06	1.53	1.31	1.05	1.03	0.85	0.46	0.38	0.68	0.62
10	1.05	1.50	1.32	1.02	1.28	0.66	0.53	0.38	0.67	0.62

passive control under η within $0.03 \approx 0.07$ and β around $0.6 \approx 1.6$. As shown in Fig. 3, the greater the η is, the less the resonance amplitude is for passive control. However, the amplification factors increase on both sides of $\beta = 1$. Particularly, when β is lower than $\beta = 1$, a greater η leads to an amplification factor. The resonance amplitudes are even almost the same as those of the structure without control. Actually, resonance still occurs by the natural frequencies of the structure with passive control. When η is lower, the two frequencies are close to each other and cause an interaction phenomenon. There are no very large amplification factors. Nevertheless, the larger the η is, the greater the difference between the two frequencies. The dynamic characteristics of the structure with passive control tend toward two degrees of freedom. Therefore, a large peak exists at low frequency. The structural control effect of the structure under random load may necessarily be negative for larger η. The passive control effect is not stable with the increase in η.

Figure 3 shows that the structure control effects of the structure with semi-active control achieve a better control effect for a larger η. But variance of the control effect tends to ease quickly. The amplitude is large for a large η with a high frequency

load. The greater the control mass is, the greater the effect of the semi-active control within the range of the allowable device. This semi-active control mass need not be large. A small control mass can achieve almost the limit of the control effect.

4 Conclusions

The semi-active mass control method is proposed in this study. According to the results of numerical simulation, the conclusions of this study can be obtained as follows:

1. This proposed mechanism can "capture" and "release" the active control mass based on the direction and velocity of movement of the structural displacement.
2. Amplification of steady state reaction for structure with this semi-active control is much less than those of structure with passive control under η within $0.03 \approx 0.07$ and β around $0.6 \approx 1.6$.

This proposed mechanism can perform well shock absorption effect and avoid the disadvantages of passive and active mass dampers. Therefore, structural control effects of multiple degree of freedom structure with this proposed mechanism should be carefully studied and discussed to demonstrate the actual shock absorption benefits.

Acknowledgements The authors would like to acknowledge the support of Taiwan Ministry of Science and Technology through grant No. MOST-106-2221-E-260-003.

References

1. Yao, J.T.P., Natke, H.G.: Effect of active control to structural reliability. In: Probabilistic Mechanics and Structural and Geotechnical Reliability, Proceedings of the Specialty Conference, pp. 373–376 (1992)
2. Symans, M.D., Constantinou, M.C.: Passive fluid viscous damping systems for seismic energy dissipation. ISET J. Earthq. Technol. **35**(4), 185–206 (1998)
3. Murase, M., Tsuji, M., Takewaki, I.: Smart passive control of buildings with higher redundancy and robustness using base-isolation and inter-connection. Earthq. Struct. **4**(6), 649–670 (2013)
4. Cacciola, P., Tombari, A.: Vibrating barrier: a novel device for the passive control of structures under ground motion. Proc. Math. Phys. Eng. Sci. **471**(2179), 20150075 (2015)
5. Zhang, Y., Iwan, W.D.: Active interaction control of civil structures. Part 2: MDOF systems. Earthq. Eng. Struct. Dyn. **31**, 179–194 (2002)
6. Fallah, N., Ebrahimnejad, M.: Active control of building structures using piezoelectric actuators. Appl. Soft Comput. **13**(1), 449–461 (2013)
7. Liu, K., Chen, L.X., Cai, G.P.: Active control of buildings with bilinear hysteresis and time delay. Int. J. Struct. Stab. Dyn. **13**(5) (2013). https://doi.org/10.1142/S0219455413500272
8. Zeng, X., Peng, Z., Mo, L.G., Su, Y.: Active control based on prediction of structural vibration feedback. In: 2014 Fifth International Conference on Intelligent Systems Design and Engineering Applications (2014). https://doi.org/10.1109/ISDEA.2014.35

9. Shih, M.H., Sung, W.P., Go, C.G.: Development of accumulated semi-active hydraulic damper. Exp. Tech. **26**(5), 29–32 (2002)
10. Shih, M.H., Sung, W.P.: A design concept of autonomous controller for improving seismic proof capability of semi-active control device. Exp. Tech. **34**(4), 20–26 (2010)
11. Pourzeynali, S., Jooei, P.: Semi-active control of building structures using variable stiffness device and fuzzy logic. Int. J. Eng. Trans. A Basics **26**(10), 1169–1182 (2013)
12. Uz, M.E., Sharafi, P.P.: Investigation of the optimal semi-active control strategies of adjacent buildings connected with magnetorheological damper. Int. J. Optim. Civil Eng. **6**(4), 523–547 (2016)

Hierarchical Modeling of Damage and Fracture in a Structurally Inhomogeneous Materials Subjected to Deformation

Sergey V. Smirnov, Marina V. Myasnikova, and Yury V. Khalevitsky

Abstract Two computational models of deformation are presented: the first one models aluminum matrix composite with silicon carbide reinforcement; the second models complexly alloyed brass. The models account for material internal structure, as well as for rheological properties of material constituents. Material deformation on micro- and macroscale has been simulated. It is shown that damage mechanics is applicable for simulating fracture of both malleable and brittle constituents of the materials. In numerical simulations an empirically obtained model of composite matrix limiting plasticity is used, which correlates limiting plasticity with stress stiffness coefficient and Lode-Nadai stress state coefficient. On an example of the brass, a technique is developed, that allows one to derive the dependence of limiting deformation of brittle inclusions of metal alloys, on stress stiffness coefficient.

1 Introduction

Developing a hierarchical model with several structural levels of deformation and fracture in solid body subjected to external mechanical effects enables simulations of material behavior at various scale levels. Experimental investigations and numerical simulation of the plastic deformation of structurally inhomogeneous materials are successfully pursued within this research area [1–3]. We propose to remove the sentence, since it is not clear where to insert it specifically. The use of a hierarchical approach to deformation and fracture of materials allows one to solve two important problems for industrial applications: (1) to develop and optimize pressure forming technological processes for a specific material; (2) to develop and optimize the

S. V. Smirnov
Federal State Budgetary Scientific Institution "Institute of Engineering Science, Ural Branch of the Russian Academy of Sciences" (IES UB RAS), Ekaterinburg, Russia
e-mail: smirnov@imach.uran.ru

M. V. Myasnikova (✉) · Yu. V. Khalevitsky
IES UB RAS, Ekaterinburg, Russia
e-mail: marina@imach.uran.ru; me@dijkstra.ru

V. P. Matveenko et al. (eds.), *Dynamics and Control of Advanced Structures and Machines*, https://doi.org/10.1007/978-3-319-90884-7_18

composition of the material so the technological processes result in required strength of produced parts.

This work uses the concept of multilevel material description and damage mechanics failure criteria to simulate plastic deformation and fracture in structural components of heterophase material. Randomly chosen microscopic volumes of metal matrix composite (MMC) and complexly alloyed brass have been chosen as models. The model materials are chosen in a way to demonstrate two different fracture mechanisms: in case of the composite fracture develops in malleable matrix, but reinforcement particles have high strength and hardly experience any strain at all; in contrary, complexly alloyed brass fracture initiates in brittle inclusions enclosed in malleable base. The models explicitly account for internal structure of material, as well as constituent rheology.

2 Material and Investigation Procedures

A specific metal matrix composite has been chosen to be the first model material. The constituents of the composite are 99.8% commercially pure aluminum and silicon carbide reinforcement particles. The dominant particle shape is considered to be irregularly prismatic; particle sizes are in ranges of 1–5 and 15–20 µm. The composite microstructure is depicted in Fig. 1a. As tensile tests show, a MMC damage process is initiated and then governed by the emergence and development of cracks in the matrix, while SiC inclusions demonstrate high strength and do not undergo any substantial strain [4]. Considering this failure behavior, the stress–strain response evolution and damage accumulation in matrix under uniaxial loading conditions has been studied.

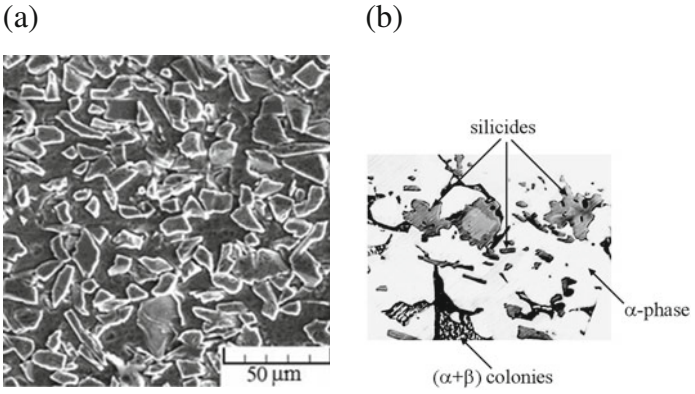

Fig. 1 The microstructure of model materials. (**a**) The model material matrix composite microstructure. (**b**) The microstructure of complexly alloyed brass, ×400

A complexly alloyed brass has been chosen as the second model material. The brass has the following chemical composition, mass %: 71.13 Cu; 1.82 Fe; 5.27 Al; 2.06 Si; 7.04 Mn; 0.04 Ni; 0.94 Pb; the rest Zn. The brass contains three main structural constituents, namely a ductile base—an α-phase, solid solution of zinc and alloying elements in copper with low values of microhardness; the strengthening β-phase, which is present in the form of an $(\alpha + \beta)$ mechanical mixture and characterized by higher hardness and lower plasticity; silicide inclusions Mn_5Si_3 and $(Fe, Mn)_5Si_3$ high hardness and playing a reinforcing role in the material. A typical alloy structure is depicted in Fig. 1b. Silicide particles in the alloy are columnar and globular [2]. Investigations show that the brass deformation under upset takes place mainly in malleable matrix—solid α-phase and colonies of phases $(\alpha + \beta)$. The brittle silicide inclusions are fractured first. This distinctly differs the brass from the metal matrix composite, in which the fracture is initiated in ductile matrix by microscopic crack emergence. Experimental investigations of microcrack initiation and development in the brass as dependent on the amount of strain were made by series of upsetting tests on prismatic specimens. Experimental apparatus featured polished heads and lubrication. The experimental procedure allowed us to sufficiently accurately reproduce the plane strain loading conditions.

After each stage of loading the fractured inclusions have been counted. Microcrack emergence has been chosen as failure criterion. Since it does not seem possible to evaluate the equivalent plastic strain of silicides ε^{sil} directly from experiments, finite element simulation results were used.

The computational models of the composite and the brass leverage the two-level structural-phenomenological approach for coupling the micro- and macroscale material behavior [5]. According to this approach, the material is considered to be a homogeneous isotropic medium with isotropic hardening on the macroscale. On the microscale, the material is considered to be an inhomogeneous medium partitioned into connected non-intersecting domains which represent corresponding constituents.

According to the approach, the composite volume on microlevel is modeled by a cube with 30 µm edge size, which represents the aluminum matrix with embedded silicon carbide particles. The microstructural properties of the metal matrix composite have been chosen according to metallographic investigation [4]. The structurally inhomogeneous microvolume is surrounded with a buffer layer. The layer has smeared macroscopic mechanical properties of the composite and dilates evenly from microvolume borders. The volume thickness is equal to the microvolume linear size (Fig. 2). Rheological properties of commercially pure aluminum were set as strain-hardening curves according to compression tests with cylindrical specimens on macroscale [6]. Tests were conducted with a strain rate of $1\,s^{-1}$ at 300 °C.[1]

[1]Experimental investigations have been made using the Centre of Collective Usage Plastometry of IES UB RAS equipment.

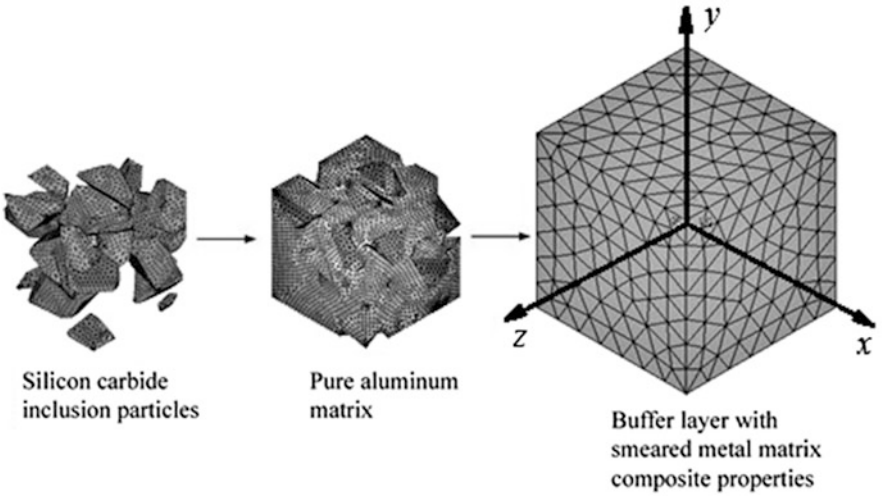

Fig. 2 Three-dimensional metal matrix composite computational model

To develop a computational model of brass on the microlevel, we dealt with structurally inhomogeneous cells (microcells) being an array of structural-phase constituents specified as a system of interconnected regions, with their geometries, dimensions, and properties corresponding to those of actual structural constituents of the brass tested. The initial image of the brass structure was determined by the results of a quantitative metallographic analysis with the application of the statistical Monte Carlo method. Coordinates of the metallographic section points in whose vicinity the structure was photographed were selected as random values (Fig. 3a). The images of microstructure have been digitized and further used to develop geometrical models of deforming areas. The area size has been chosen to be approximately $140 \times 160\,\mu m$ in size and has been enclosed in buffer layer with smeared material properties. Altogether there were 10 photographs treated, and this ensured adequate sampling for subsequent statistical averaging of the results. The buffer layer was composed of eight identical homogeneous and isotropic cells, their sizes being consistent with that of the central microcell (Fig. 3b).

Strain resistance of the buffer layer was assumed equal to that of the brass. The strain resistance of the constituents of brass was determined with the micro-indentation technique [7] based on the identification of the stress–strain dependence by experimental results and a numerical solution of the inverse problem. The stress–strain curves for the brass and its constituents are published in [2]. The numerical simulation of metal matrix composite and brass deformation has been conducted in the quasi-static statement. Boundary conditions, ensuring uniaxial loading conditions of the MMC model and upsetting under the plane strain state of the brass model, have been specified in displacements of the faces of the buffer layer of each computational model.

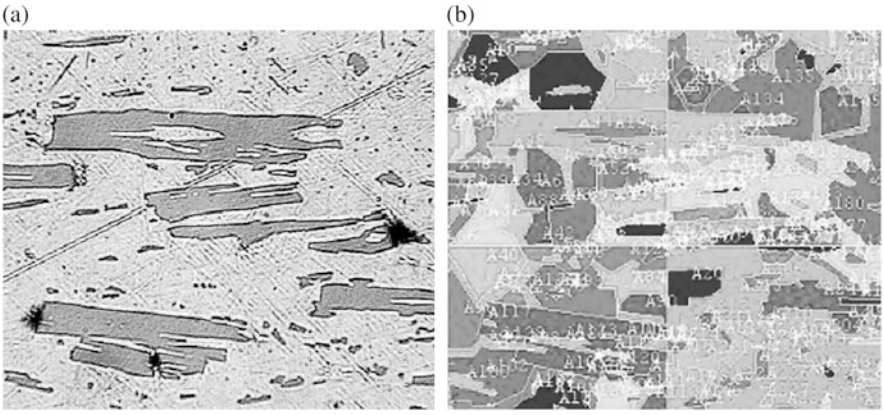

Fig. 3 The microstructure and the model of the brass. (**a**) A photograph of the brass microstructure, 140 × 160 μm. (**b**) A microcell surrounded by a buffer layer

The simulation allowed us to obtain stress tensor σ_{mp} and strain increment $\Delta\varepsilon_{mp}$ tensor data in each node of the finite element models. The data have been further used to determine the stress stiffness coefficient $k_i = \frac{\sigma^i}{T^i}$ and the Lode-Nadai coefficient $\mu_{\sigma i} = 2\frac{\sigma_2^i - \sigma_3^i}{\sigma_1^i - \sigma_3^i}$ at each finite element mesh nodes of the models on i-th computation step. σ^i denotes mean normal (hydrostatic) stress, T denotes tangential stress intensity equal to shear yield stress in the plastic region. σ_1, σ_2 σ_3 denote principal stresses on i-th computational step. The equivalent (von Mises) strain increment on i-th computation step has been expressed in terms of strain tensor component increments $\Delta\varepsilon_{mp}$ obtained on this step as $\Delta\varepsilon_i = \sqrt{\frac{2}{3}\Delta\varepsilon_{mp}\Delta\varepsilon_{mp}}$. Thereafter, the whole accumulated equivalent deformation ε in every node is computed as amount of equivalent strain increments after n total computational step number for deformation ($i = 1 \ldots n$).

The phenomenological theory authored by Vadim Kolmogorov [8] has been used for studying the materials damage accumulation. This theory assumes that material damage ω lies in range 0–1, where 0 means undeformed material and 1 implies material failure and crack emergence. The material damage on computational step of deformation is equal to the ratio of equivalent strain increment to equivalent plastic strain to fracture ε_f and damage accumulation considered to be linear. A node has been considered to be fractured if the damage level in the node reaches 1. The condition of fracture after n steps is stated as follows:

$$\omega = \sum_{i=1}^{n} \frac{\Delta\varepsilon_i}{\varepsilon_f(k_i, \mu_{\sigma i})} = 1. \tag{1}$$

3 Results and Discussion

3.1 Metal Matrix Composite

Numerical simulation has shown that rigid silicon carbide particles clamp a thin matrix layer. Clamping leads to the emergence of local plastic deformation regions. On the other hand, stiff silicon carbide inclusion particles distributed in the ductile matrix make tensile stress areas in their proximity. This has been shown by computing the stress stiffness coefficient k in the finite element nodes pertaining to matrix of composite. Maximum k values caused by inclusion proximity appear to occur in distinctive microcrack initiation areas observed in experiments. It is known that severe tensile stresses contribute to intensive plastic dilatancy and accelerate fracture process [8]. This conclusion is also confirmed by numerical simulations of damage ω accumulation in the matrix metal within microvolume of MMC.

The fracture locus of commercially pure aluminum (composite matrix material) for 300 °C has been taken from the experimental investigation [9]. A fracture locus determines the dependence of ultimate shear strain Λ_f at fracture on stress state parameters k and μ_σ: $\Lambda_f = \Lambda_f(k, \mu_\sigma)$. Ultimate strain at fracture ϵ_f was calculated as follows: $\epsilon_f = \Lambda_f/\sqrt{3}$.

It is found that the most possible regions of failure initiation (i.e., regions, where equation 1 holds true) are strain localization regions where adverse tensile stresses prevail. As an example, Fig. 4 depicts accumulated damage distribution in central cross-section xy of the metal matrix within the microvolume depending on equivalent macroscopic strain ε for uniaxial tension. The results of the damage simulation of MMC are discussed in more detail in [6].

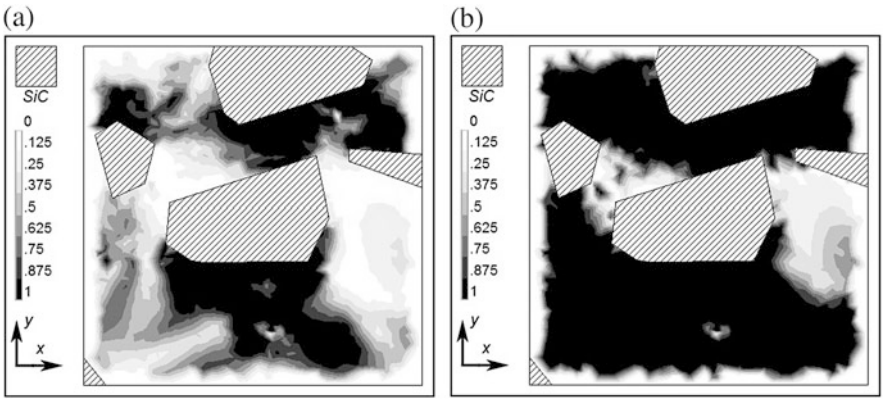

Fig. 4 Damage ω distribution in the matrix. Central xy cross-section of metal matrix microvolume, tension simulation. (**a**) $\varepsilon = 0.04$. (**b**) $\varepsilon = 0.2$

3.2 Complexly Alloyed Brass

The experimental investigations have shown that $(Fe, Mn)_5Si_3$ particles of any geometry, which are, in the average, bigger in size (10–80 μm) and contain iron, are more prone to fracture than smaller manganic Mn_5Si_3 particles (10–20 μm) under identical deformation conditions. Besides, a negative effect is exerted by the non-uniform stress–strain state of the material on the mesolevel, whereas the geometry of silicides scarcely affects their ability to fracture. Therefore in the subsequent discussion our consideration is restricted to the ultimate plasticity of acicular iron-containing $(Fe, Mn)_5Si_3$ silicides. The features of the fracture of silicides in brass are discussed in more detail in [2]. The analysis of the calculation results has revealed the non-uniformity of the stress state of silicides on the microlevel at a fixed moment loading. A fairly wide range of the values of the stress stiffness coefficient k and its variation in the course of specimen upsetting enabled us to use the identification procedure for determining the diagram relating the amount of ultimate equivalent strain prior to silicide fracture ε_f^{sil} to the stress stiffness coefficient k. The description of diagrams of the kind by the exponential function is the most commonly used for metal alloys [8], therefore, to describe the diagram of ultimate equivalent strain of $(Fe, Mn)_5Si_3$ silicides, it was also reasonable to use the function of the form $\varepsilon_f^{sil} = a \exp(-bk)$, where a and b denote empirical coefficients obtained by the identification.

Let the mean value of μ_σ be constant on every step of upset in plate strain conditions. Then the fracture criterion (1) can be used to compute damage in every node of finite element mesh of silicides, on every computation step. It is assumed in the calculation that a silicide will fracture when the above-mentioned fracture condition is fulfilled on the average over the nodes belonging to this silicide. The number of fractured silicides at each stage of deformation was determined similarly. The model was identified from the condition of the best agreement between the experimental and calculated data, reasoning from the minimization of the value of the quadratic residual. For the quadratic residue $S = 0.22$, the following empirical coefficients were obtained: $a = 0.005$, $b = 6.1$.

With the obtained diagram and the linear model of damage accumulation [8] the simulation of the deformation and fracture of silicides in the course of specimen upsetting was performed. A treated fragment of brass microstructure, about 70×80 μm in dimensions, was used as a structurally heterogeneous microcell. Figure 5, a shows simulation results at equivalent macroscopic strain $\varepsilon = 0.04$ in upsetting. It shows areas corresponding to the zones of the most probable fracture of silicides. It is possible to reduce the probability of silicide fracture, i.e., to increase the durability of the brass, through the use of "milder" stress schemes offering a higher level of compressive stresses—sufficient for minimizing the "adverse" tensile stress zones. Figure 5b shows results of the simulation of damage accumulation in silicides prior to fracture at equivalent macroscopic strain $\varepsilon = 0.25$ in upsetting under plane strain with an additional external hydrostatic pressure of 850 MPa. The simulation has demonstrated that this loading scheme enables brass to be deformed with a fairly

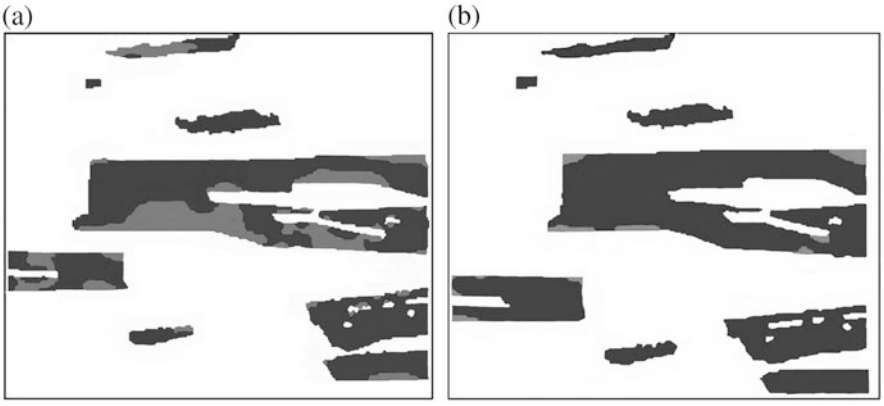

Fig. 5 Damage distribution among silicides at equivalent macroscopic strain in upsetting. Additional 850 MPa hydrostatic pressure is applied in (**b**). Fractured areas are colored gray (**a**) $\varepsilon = 0.04$. (**b**) $\varepsilon = 0.25$

high value of strain and minimum internal fractures (with only slight spalling at silicide edges).

4 Conclusion

Both two and three-dimensional computational models of inhomogeneous material deformation have been developed. The two-level structural-phenomenological approach has been applied to couple macroscopic boundary condition and microscopic model. The model takes into account the complex rheological properties of its components. The developed models have been implemented numerically on the example of simulating the loading of the random microstructure subvolume of an aluminum matrix composite with silicon carbide reinforcement for uniaxial tension and compression as well as for simulating the loading of the random microstructure portion of complexly alloyed brass in upsetting under the plane strain state.

The principal possibility of applying phenomenological damage theory for damage accumulation simulations of the materials under loading has been shown. The evolution of stress–strain state parameters (the stress stiffness coefficient and the Lode-Nadai coefficient) has been taken into account. A technique has been proposed for relating the ultimate strains of brittle particles in the soft phase of alloys to the stress stiffness coefficient. The technique has been applied to construct a diagram of ultimate strain for $(Fe, Mn)_5Si_3$ silicides of complexly alloyed brass. Damage accumulation in ((Fe, Mn)$_5$Si$_3$ silicides prior to fracture has been simulated.

Acknowledgements This work was partially supported by Russian Science Foundation (project 14-19-01358) in the part of metal matrix composite model development.

References

1. Smirnov, S.V., Myasnikova, M.V., Pugacheva, N.B.: Hierarchical simulation of plastic deformation and fracture of complexly alloyed brass. Int. J. Damage Mech. **25**(2), 251–265 (2016). https://doi.org/10.1177/1056789515577401
2. Pyo, S.H., Lee, H.K.: Micromechanics-based elastic-damage analysis of laminated composite structures. Int. J. Solids Struct. **46**(17), 3138–3149 (2009)
3. Pavan, R.C., Creus, G.J., Maghous, S.: Compos. Struct. **91**(1), 84–94 (2009)
4. Pugacheva, N.B., Michurov, N.S., Bykova, T.M.: Structure and properties of the Al/SiC composite material. Phys. Met. Metallogr. **117**(6), 654–660 (2016). https://doi.org/10.1134/S0031918X16060119
5. Haritos, G.K., Hager, J.W., Amos, A.K., et al.: Mesomechanics: The microstructure-mechanics connection. Int. J. Solids Struct. **24**(11), 1081–1096 (1988)
6. Smirnov, S.V., Konovalov, A.V., Myasnikova, M.V., Khalevitsky, Y.V., Smirnov, A.S.: Hierarchical modeling of deformation and damage of metal matrix composite under uniaxial loading conditions. IOP Conf. Ser. Mater. Sci. Eng. **208**, 012037 (2017). https://doi.org/10.1088/1757-899X/208/1/012037
7. Smirnov, S.V., Pugacheva, N.B., Tropotov, A.V., Soloshenko, A.N.: Resistance to deformation of structural constituents of a high-alloy brass. Phys. Met. Metallogr. **91**(2), 210–215 (2001)
8. Kolmogorov, V.: Metal Forming Mechanics (Mechanika obrabotki metallov davleniem), 2nd edn. GOU VPO "UGTU-UPI", Ekaberinburg (2001) (in Russian)
9. Smirnov S.V., Vichuzhanin D.I., Nesterenko A.V., Igumnov A.S.: A fracture locus for commercially pure aluminum at 300 °C. AIP Conf. Proc. **1785**, 040067 (2016). https://doi.org/10.1063/1.4967124

Effect of Lattice Misfit Strain on Surface Acoustic Waves Propagation in Barium Titanate Thin Films

P. E. Timoshenko, V. V. Kalinchuk, V. B. Shirokov, and A. V. Pan'kin

Abstract The finite-element approaches are used to the analysis of the properties of acoustoelectronic devices on surface acoustic waves (SAWs) made using thin-film technologies. The device consists of a barium titanate $BaTiO_3$ film placed on a magnesium oxide substrate MgO. The barium titanate (BT) film is studied in the c-, r-, and aa-phases. The interdigital transducer (IDT) is attached to the free surface of the ferroelectric film and consists of a system parallel electrodes (pins) alternately connected to each other via common buses. The commercial software COMSOL is used for two-dimensional finite-element analysis and modeling the processes of excitation and propagation of SAW. The resonance and antiresonance frequencies are calculated for different film thicknesses and values of the lattice misfit strain. The significant influence of the film thickness and strains near the phase transitions and in r-phase on the resonant and antiresonant frequencies is discussed. In addition, a two-dimensional model of a SAW filter consisting of 40 pair pins of transmitting and receiving IDTs spaced 1.8 mm apart is considered. The frequency dependences of scattering parameters (S-parameters) have calculated and are presented.

Keywords Ferroelectrics · Finite-element method · Scattering parameters

1 Introduction

The progress in obtaining high perfection films [1, 2] stipulates a wide range of their applications in various branches of science and technology. High-efficiency dynamic deformation sensors of the generator type have been obtained [3, 4] on the

P. E. Timoshenko (✉) · A. V. Pan'kin
Faculty of Physics, Southern Federal University, Rostov-on-Don, Russia

V. V. Kalinchuk · V. B. Shirokov
Southern Scientific Center of the Russian Academy of Science, Rostov-on-Don, Russia
e-mail: kalin@ssc-ras.ru

V. P. Matveenko et al. (eds.), *Dynamics and Control of Advanced Structures and Machines*, https://doi.org/10.1007/978-3-319-90884-7_19

basis of thin ferroelectric films, which allowed to take a new look at the problem of monitoring the dynamic behavior of complex systems [4–6].

Another promising direction of using thin-film technologies are microwave devices and acoustic-electronic radio components on surface acoustic waves (SAW) for analog signal processing in real time in a wide frequency range from 1 MHz to 15 GHz. In traditional elements using SAW, an increase in the central frequency of the operating frequency band is achieved in two ways: using a sound-conducting substrate with a higher sound velocity and reducing the geometric dimensions (gap and electrode width) of the emitting and receiving interdigital transducer (IDT) [7]. Both of these methods have their own natural limitations: a fixed speed of sound in the substrate and significant technological difficulties in obtaining a gap width of less than 0.5 μm using a lithographic method. An alternative way is to improve the design of acoustic-electronic devices by using thin films of various piezoelectric materials [8–12]. Experience has shown that the properties of acoustic-electronic devices depend significantly on the quality of the film. The using of high perfection films allowed to provide acoustic-electronic devices with fundamentally new capabilities, for example, increasing the operating frequencies or the adjustable sensitivity [13, 14].

The miniaturization and application of thin ferroelectric films, on the one hand, and the presence of external electric fields and initial stresses, on the other hand, require the use of rigorous mathematical methods that allow accounting of all external influences and emerging internal stresses, revealing new regularities and creating fundamentally new types of devices, based on the use of the identified physical effects. The properties of thin films can perform a special role in the design of the acoustic-electronic device due to the presence of internal stresses that arise when the film is applied to a substrate crystal lattices of which have different sizes [15, 16]. The properties of films can depend on the geometrical parameters of the film (thickness) and technological conditions (deposition temperature) [17–26].

2 Resonant and Antiresonant Frequencies

The problem of finding the resonant and antiresonant frequencies at different values of the forced deformation of the barium titanate film does not differ from the problem of finding the natural frequencies, and, consequently, we can consider a two-dimensional periodic problem.

The model for the solution of the two-dimensional problem is a barium titanate (BT) film with thickness h_{BT} (area Ω_1 in Fig. 1) on a substrate of magnesium oxide (Ω_2) with thickness h_{MgO}, on which a high-frequency IDT is put, which consists of parallel flat aluminum electrodes Ω_3, Ω_4 located on the surface of the piezoelectric material and alternately connected to each other via common bars. The width of the electrodes making up the IDT is s, their period is p, the thickness is h_s.

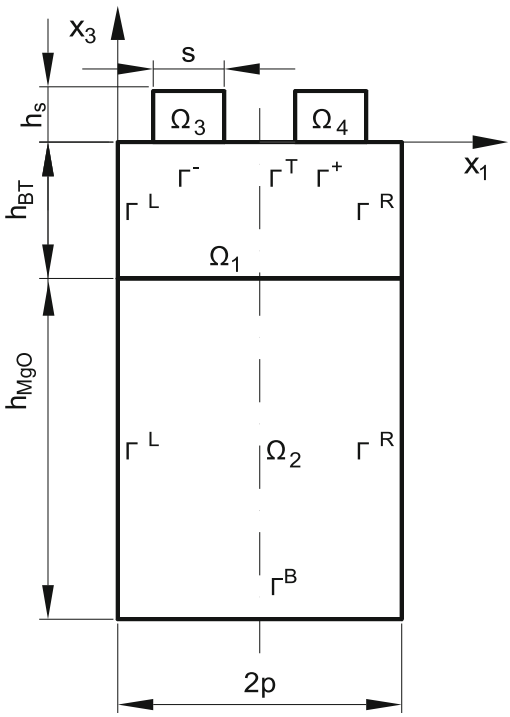

Fig. 1 The computational domain contains a single period of IDT

The problem is considered in the Cartesian coordinates x_1, x_3. Surface waves propagate in both directions along the coordinate x_1, and x_3 is the direction of their attenuation. The wave parameters do not depend on the coordinate x_2. In general, due to the anisotropy of the ferroelectric material properties, all three components of the mechanical displacements exist, which we will denote as u_1, u_2, u_3 (respectively, in the x_1, x_2, x_3 axis direction). We also introduce the electric potential V to describe the electric field. The extended vector $u = (u_1, u_2, u_3, V)^T$ fully characterizes such piezoelectric system. The use of these variables allows to determine all the mechanical and electrical parameters in the quasistatic approximation. The equations of piezoacoustics in the time domain are given in the tensor form [26] (summation is made over repeated indices):

$$\begin{cases} C^E_{ijkl}\frac{\partial^2 u_i}{\partial x_j \partial x_k} + e_{kij}\frac{\partial^2 V}{\partial x_j \partial x_k} = \rho\frac{\partial^2 u_i}{\partial t^2}, \\ e_{jkl}\frac{\partial^2 u_i}{\partial x_j \partial x_k} + \varepsilon^S_{ki}\frac{\partial^2 V}{\partial x_i \partial x_k} = 0, \\ T_{ij} = C^E_{ijkl}S_{kl} - e_{kij}E_k, \\ D_i = e_{ikl}S_{kl} + \varepsilon^S_{ki}E_k, \end{cases} \qquad i, j, k, l = 1, 2, 3 \qquad (1)$$

where u_i is the components of the mechanical displacement vector, V is the electric potential, C^E is the elastic modulus tensor, e is the tensor of the piezomodules, T_{ij},

S_{ij} are the strain and deformation tensors, ε^S is the permittivity tensor, ρ is the density of the medium, E is the electric field vector ($E_i = -\partial V/\partial x$), and D is the electric displacement vector.

The system of partial differential equations of the second order (1) can be transformed to solve the problem of finding the Eigen frequencies in COMSOL to the following form:

$$ea \cdot \omega^2 \cdot u - \nabla \cdot (c\nabla u) = 0, \tag{2}$$

where $u = (u_1, u_2, u_3, V)^T$, and ea, c are the matrices, depending on the material constants. This solution approach allows to take into account all three spatial components of the mechanical displacements vector, as well as the effect of mechanical loading of the electrodes. The boundary conditions on the two lateral boundaries are given periodically. Finding the resonant and antiresonant frequencies requires fixing the wave number so that the value of the induced deformation of the barium titanate film and the film thickness can be varied.

3 Effect of Lattice Misfit Strain at the Different Film Thicknesses on the Resonant and Antiresonant Frequencies

The properties of ferroelectric films differ greatly from the bulk samples. When films are placed to the substrate, large mechanical stresses may appear at the film–substrate interface. These stresses arise from the discrepancy between the parameters of the film and substrate lattices, the differences in the thermal expansion coefficients, and the formation of spontaneous deformations during phase transitions [17].

Large deformations of a film can result in a specific domain structure and considerable growth of the spontaneous polarization [1]. The misfit strain of the film provides the interface of its crystal lattice with the lattice of the substrate. The deviation from intrinsic crystallographic symmetry with a change in the lattice period reduces the interphase energy of the film–substrate interface, but increases the energy of mechanical stresses due to elastic deformation of the film [24, 25]. The discrepancy between the crystal lattices of the piezoelectric layer and the substrate leads to a change in the dielectric permeability constant and the piezoelectric coefficient. The property that determines the peculiarity of the interaction of the film with the substrate is the mismatch parameter u_m [24, 25], which depends both on the mismatch between the dimensions of the crystal lattices of the film and the substrate and the difference in the coefficients of their thermal expansion, and on the film deposition mode.

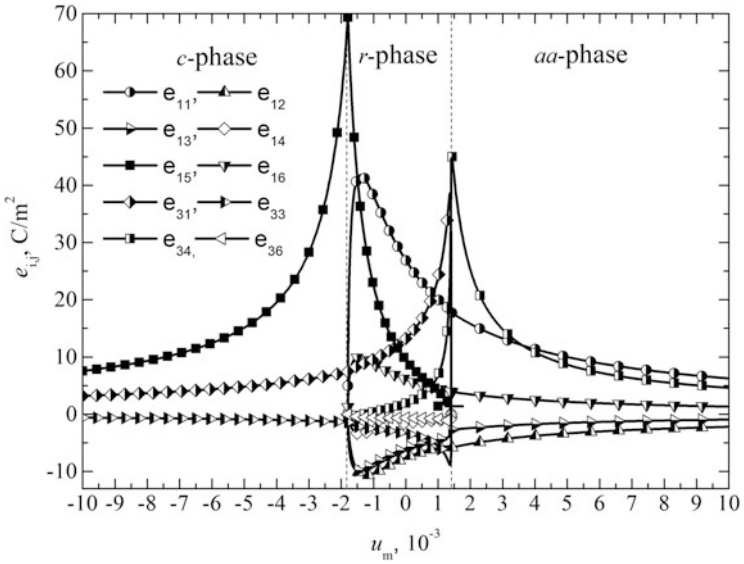

Fig. 2 The dependence of piezoelectric moduli e_{11}, e_{12}, e_{13}, e_{14}, e_{15}, e_{16}, e_{31}, e_{33}, e_{34}, and e_{36} for the BT film on the lattice misfit strain u_m

Figure 2 shows graphs illustrating the influence of the u_m parameter on the piezoelectric constants of a barium titanate film. As the graphs show, there are three phases. In the c- and aa-phases, the constants change slightly, and in r-phase the change in the constants occurs abruptly. It is not difficult to see that the change in material constants is particularly large near phase transitions.

Figure 3a, b shows the graphs of the resonant frequencies fr and the antiresonant frequencies fa of the structure shown in Fig. 1. The calculations were carried out for the first two resonances at value of $u_m = -10^{-2} \ldots 10^{-2}$, and film thicknesses of 20 nm, 200 nm, and 2 µm. As the figure shows, closer to the phase transition ($u_m = -1.85 \cdot 10^{-3}$ and $u_m = 1.85 \cdot 10^{-3}$) at film thickness of 20 and 200 nm, the frequency change is the largest and its abrupt jump takes place. In addition, films of thickness 20 and 200 nm are characterized by the superposition of the resonant and antiresonant frequencies (Fig. 3a) in c- and aa-phase, the r-phase has a slight discrepancy between them. At film thickness of 2 µm, starting with the r-phase, a sharp discontinuity is observed between the resonant and antiresonant frequencies (Fig. 3b). It is also observed in a-phase. In addition, films with thickness of 20 and 200 nm have higher frequency—from 635 to 660 MHz and from 1175 to 1250 MHz, than film with thickness of 2 µm—from 250 to 500 MHz and from 400 to 602 MHz.

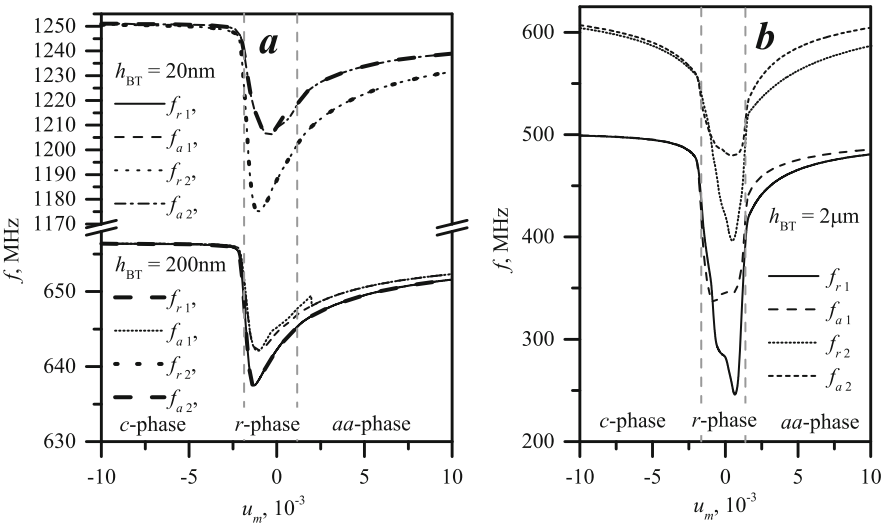

Fig. 3 The effect of the lattice misfit strain u_m on the resonance (f_r) and antiresonance (f_a) frequencies of the IDT at film thicknesses 20 nm (**a**), 200 nm (**a**), and 2 μm (**b**)

4 Scattering Parameters at Various Values of the Lattice Misfit Strain

For the calculation of the scattering parameters we will consider a model different from the one used for the calculation of the resonant and antiresonant frequencies. The model is a 300 nm thick BT film placed on a 0.25 μm MgO substrate, on which 100 nm thick and 2 μm wide aluminum electrodes are applied. The distance between the electrodes is 2 μm. The radiating and absorbing IDT has 40 pairs of electrodes. The geometric period of the IDT is 8 μm. The distance between the IDTs is 1.81 mm. The model is surrounded on all sides by the absorption region with thickness 10 μm.

The calculations were carried out for the values $u_m = -2 \cdot 10^{-3}$, $-4 \cdot 10^{-3}$, and 10^{-2}. The first resonance is observed at about of 640 MHz.

Figures 4 and 5 shows graphs of the reflection (S_{11}) and transmission (S_{21}) coefficients. As the graphs show, the frequencies of peaks at the dependence of the reflection and transmission coefficients on the *um* parameter change slightly. This could be expected, since the calculation was carried out in the c-phase and there are no significant changes in the constants.

Figures 4 and 5 also make it possible to draw a conclusion that the maximum values of the transmission and reflection coefficients are achieved at $u_m = -10^{-2}$.

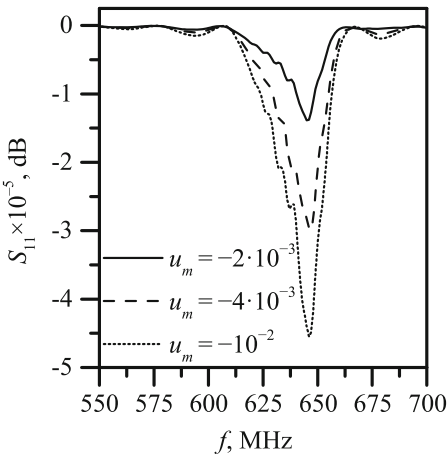

Fig. 4 The effect of the lattice misfit strain u_m on the parameter S_{11}

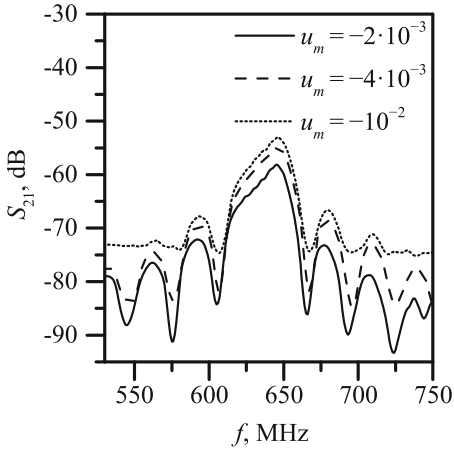

Fig. 5 The effect of the lattice misfit strain u_m on the parameter S_{21}

5 Conclusion

The calculation results of two models are presented. The first model is "periodic" and allows calculating the resonant and antiresonant frequencies. This model made it possible to determine the features of the behavior of resonant and antiresonant frequencies, depending on the film thickness and the value of the parameter u_m.

The second one is a real device (SAW filter) with real parameters. It allows finding out how the transmission and reflection coefficients behave for different u_m values and making a conclusion that the characteristics can be changed significantly close to the phase boundaries.

Acknowledgements This study was supported by the Russian Science Foundation under Project No. 14-19-01676.

References

1. Mukhortov, V.M., Yuzyuk, Y.I.: Heterostructures Based on Nanoscale Ferroelectric Films. Southern Scientific Centre of the Russian Academy of Sciences Publishers, Rostov-on-Don (2008)
2. Sigov, A.S., Mishina, E.D., Mukhortov, V.M.: Thin ferroelectric films: preparation and prospects of integration. Phys. Solid State **52**(4), 762–770 (2010)
3. Biryukov, S.V., Mukhortov, V.M., Mukhortov, V.M.: A new sensor for dynamic strain based on thin piezoelectric films obtained with ion plasma deposition. Mir izmereniy **7**, 45–52 (2007)
4. Esipov, Y.V., Mukhortov, V.M.: Thin-film ferroelectric integral sensors of dynamic deformation for monitoring sophisticated mechanical systems. Tech. Phys. **54**(1), 78–81 (2009)
5. Esipov, Y.V., Mukhortov, V.M., Kalinchuk, V.V.: Test equipment for analyzing the deformation of models of three-dimensional structures. Meas. Tech. **51**(10), 1104–1109 (2008)
6. Esipov, Y.V., Mukhortov, V.M., Kalinchuk, V.V., Andjikovich, I.E.: Early diagnosis technology of rod constructions diagnosis with use of deformation ferroelectric sensors. Ecol. Bull. Sci. Cent. Black Sea Econ. Cooper. **4**, 29–35 (2018)
7. Matthews, H.: Surface Wave Filters Design, Construction, and Use. Wiley, New York (1977)
8. Emanetoglu, N., Gorla, C., Liu, Y., Liang, S., Lu, Y.: Epitaxial ZnO piezoelectric thin films for saw filters. Mater. Sci. Semicond. Process. **2**(3), 247–252 (1999)
9. Omori, T., Hashimoto, K., Yamaguchi, M.: PZT thin films for SAW and BAW devices. In: International Symposium on Acoustic Wave Devices for Future Mobile Communication Systems Chiba, p. 6. Chiba University, Chiba (2001)
10. Kirby, P., Komuro, E., Imura, M., Zhang, Q., Su, Q.-X., Whatmore, R.: High frequency thin film ferroelectric acoustic resonators and filters. Integr. Ferroelectr. **41**(1–4), 91–100 (2001)
11. Salut, R., Daniau, W., Ballandras, S., Gariglio, S., Triscone, G., Triscone, J.M.: P1H-3 epitaxial Pb(Zr0.2Ti0.8)O3 thin layers for the fabrication of radio-frequency elastic wave transducers. In: 2007 IEEE Ultrasonics Symposium Proceedings, pp. 1421–1424. IEEE, New York (2007)
12. Khassaf, H., Khakpash, N., Sun, F., Sbrockey N.M., Tompa, G.S., Kalkur, T.S., Alpay, S.P.: Strain engineered barium strontium titanate for tunable thin film resonators. Appl. Phys. Lett. **104**(20), 202902 (2014)
13. Mukhortov, V.M., Biryukov, S.V., Golovko, Y.I., Karapet'yan, G.Y., Masychev, S.I., Mukhortov, V.M.: Surface acoustic waves in thin films of barium strontium titanate on magnesium oxide substrates. Tech. Phys. Lett. **37**(3), 207–209 (2011)
14. Biryukov, S.V., Golovko, Y.I., Masychev, S.I., Mukhortov, V.M.: Surface acoustic wave converters with electrically adjustable sensitivity. Nauka Yuga Rossii **12**, 11–15 (2016)
15. Nye, J.F.: Physical Properties of Crystals. Their Representation by Tensors and Matrices. Clarendon Press, Oxford (1954)
16. Blistanov, A.A., Bondarenko, V.S., Perelomova, N.V.: Acoustic Crystals. Nauka, Moscow (1982)
17. Shirokov, V.B., Golovko, Y.I., Mukhortov, V.M., Yuzyuk, Y.I., Janolin, P.E., Dkhil, B.: Thickness dependence of the properties of epitaxial barium strontium titanate thin films. Phys. Solid State **57**(8), 1529–1534 (2015)
18. Li, Y.L., Cross, L.E., Chen, L.Q.: A phenomenological thermodynamic potential for BaTiO3 single crystals. J. Appl. Phys. **98**(6), 064101 (2005)
19. Pertsev, N.A., Zembilgotov, A.G., Tagantsev, A.K.: Effect of mechanical boundary conditions on phase diagrams of epitaxial ferroelectric thin films. Phys. Rev. Lett. **80**(9), 1988–1991 (1998)
20. Berlincourt, D., Jaffe, H.: Elastic and piezoelectric coefficients of single-crystal barium titanate. Phys. Rev. **111**(1), 143–148 (1958)
21. Shirokov, V.B., Yuzyuk, Y.I., Kalinchuk, V.V., Lemanov, V.V.: Material constants of (Ba,Sr)TiO3 solid solutions. Phys. Solid State **55**(4), 773–779 (2013)

22. Shirokov, V.B., Kalinchuk, V.V., Yuzyuk, Y.I., Lemanov, V.V., Belyankova, T.I.: Formulation of the phenomenological theory of thin ferroelectric films. Ecol. Bull. Sci. Cent. Black Sea Econ. Cooper. **4**, 68 (2010)
23. Shirokov, V.B., Yuzyuk, Y.I., Dkhil, B., Lemanov, V.V.: Phenomenological description of phase transitions in thin BaTiO3 films. Phys. Solid State **50**(5), 928–936 (2008)
24. Shirokov, V.B., Kalinchuk, V.V., Shakhovoi, R.A., Yuzyuk, Y.I.: Material constants of barium titanate thin films. Phys. Solid State **57**(8), 1535–1540 (2015)
25. Shirokov, V.B., Kalinchuk, V.V., Shakhovoy, R.A., Yuzyuk, Y.I.: The problem of determining elastic constants of thin ferroelectric films. Dokl. Phys. **60**(8), 349–354 (2015)
26. Mason, W.P. (ed.): Physical Acoustics. Principles and Methods. Vol. 1. Methods and Devices. Part A. Academic, New York/London (1964)

Control of Nanosensors Forming on Base of Aluminum Template

A. Vakhrushev, R. Valeev, A. Fedotov, and A. Severyukhin

Abstract The results of the investigation of deposition processes of nanofilms formation on amorphous porous anodic aluminum oxide substrates, based on which it is possible to create various optic highly sensitive nanosensors, are presented in this research. The study was carried out by molecular dynamics simulation. The modified embedded atom method was used for calculation, temperature and pressure were maintained by Nose–Hoover thermostat and barostat. The different types of atoms were deposited on aluminum oxide substrates. The aims of investigation were understanding of process mechanisms of nanofilms forming and of process of filling nanopores with atoms of various substances and establishing the basic parameters governing these processes. The results of modeling the processes of precipitation of pure molecular sulfide of zinc and with the addition of additives in the form of copper atoms and manganese sulfide molecules are presented.

1 Statement of the Problem

Porous anodic aluminum oxide (AAO) is quite often used as a template to synthesize different nanostructures: nanowires, nanopoints, nanorings, nanotubes, etc., due to its hexagonal-ordered arrangement of pores vertically aligned to the film surface (Fig. 1). AAO can be successfully used as a carrier of catalytically active nanoparticles as well as nanostructures of [1, 3, 4, 10]. This gives the possibility to form the ordered aggregates of nanostructures of semiconductor fluorescent material of the same size and shape that allows representing each nanostructure as a separate light emitter. The coherent addition of radiation from each light source results in significant light intensity increase [2, 9]. The lighting properties of electroluminescent light sources (ELS) depend on the fluorescent material layer thickness and its structure. So, the problems of studying electrochemical and

A. Vakhrushev (✉) · R. Valeev · A. Fedotov · A. Severyukhin
Federal State Budgetary Institution of Science "Udmurt Federal Research Center of the Ural Branch of the Russian Academy of Sciences", Izhevsk, Russia

V. P. Matveenko et al. (eds.), *Dynamics and Control of Advanced Structures and Machines*, https://doi.org/10.1007/978-3-319-90884-7_20

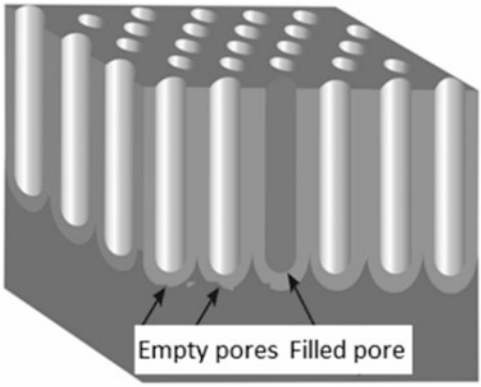

Fig. 1 Porous anodic aluminum oxide

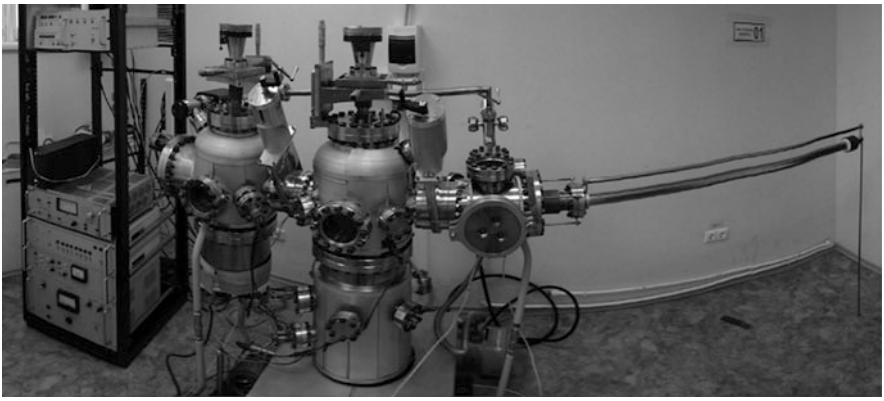

Fig. 2 Experimental device for filling processes of nanopores into templates of aluminum oxide by atoms of various materials

magnetic effects in porous AAO and application of similar templates as optic sensors are topical.

Despite the wide application of nanosystems on base of aluminum template, the questions of detailed investigation of their composition, structure, and processes in them still arise. The understanding of mechanisms and investigation of nanofilms forming and functioning, interaction of nanostructures and nanoparticles they contain, as well as the development of engineering ideas and approaches to managing and using these processes, will give the possibility to control properly the design nanocomposites and find perspective areas of their application. That is why it is very important to investigate the processes of such nanostructure growth which we carried out for several years. Experimental studies are performed on the installation shown in Fig. 2. The methods of theoretical investigation of these processes by

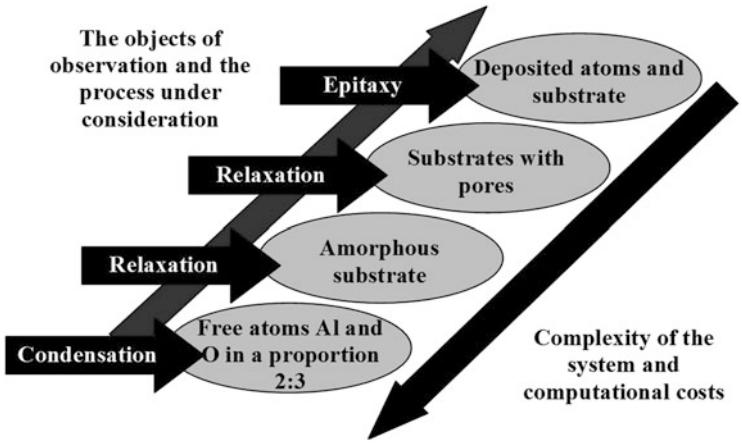

Fig. 3 Steps of solving the problem of forming nanofilm coatings based on porous aluminum oxide

the molecular dynamics method in Fig. 3 are shown. The interested reader can get acquainted with the experimental and modeling technique in detail in [5–8].

In the work, we investigated the influence of dimensional parameters of the pores in aluminum oxide matrix on the processes formation of nanofilm coatings. Gold, silver, chromium, copper, iron, gallium, germanium, titanium, platinum, and vanadium were used as precipitated materials in the experiments and while modeling. In this paper, we present the simulation results of nanofilm formation on porous templates at the deposition of molecular zinc sulfide (ZnS).

Nanofilms based on ZnS are actively used in optical systems of IR band. For industrial purposes zinc sulfide is produced by chemical deposition from zinc gases and vapors onto the template. ZnS is not always applied in the pure state, the material is frequently added to admixtures and additives. The introduction of silver admixture into the composition results in the luminescence in the blue light region. The addition of copper as an alloying metal allows using the luminescence of green color, which is applied in display boards, panels, luminophors, oscillograph tubes.

When investigating luminophor properties, the luminescence brightness is usually the determining parameter. However, to find out main physical mechanisms underlying luminescence, it is necessary to investigate both spectral and kinetic characteristics of electroluminophor that confirms the importance of theoretical studies of processes of nanofilm deposition onto porous templates.

2 Results of Simulation and Discussions

In multiparticle potentials, such as Abel–Tersoff, Stillinger–Weber, embedded atom method, the bond formation and breakage occur due to the principles of force field performance. Nevertheless, for multiparticle potentials rather large amount of

empirical parameters is required. Especially for alloys and complex compounds it is necessary to obtain additional characteristics of force fields, adapting the action of energy fields for multimolecular nanostructures.

In order to obtain realistic results maximally fitting the experimental data, the sizes of the modeling region were significantly increased. The amorphous aluminum oxide templates with the following dimensions: length—19.1 nm, width—19.1 nm, height—11.6 nm were used in the modeling process. The total number of atoms in the template after the pore formation was about 122,000. Before the precipitation process the template was at rest, at the beginning its temperature was 293 K and it was further maintained at the same level. The pore with the radius of 5 and 10 nm deep was cut in aluminum oxide template. The lower template layer was fixed to avoid its vertical movement at the precipitation stage. The rest of the atoms were not fixed and could freely move in any direction.

The number of precipitated ZnS molecules was 200,000. The proportion of alloying elements increased in proportion to its composition increased the percentage of epitaxial atoms. The precipitation was uniform along the whole template surface and with the same intensity in time. The atom velocity at epitaxy was 0.05 nm/ps.

The evaporation process of nanofilms from pure zinc sulfide is demonstrated in Fig. 4. The duration of the complete deposition stage was 0.6 ns. Analysis of the graphical results indicates that a pore is gradually buried with nanofilm. Initially, the neck starts forming on the sides above the hole (Fig. 4a), which is gradually covered later on. Zinc sulfide molecules partially get into the pore, but its complete dense filling does not occur (Fig. 4b and c). Nevertheless, practically all internal surface of the porous hole appears to be covered with ZnS molecules by the deposition stage completion. The gradual pore filling results in the emergence of rounded overgrowths above the pore region.

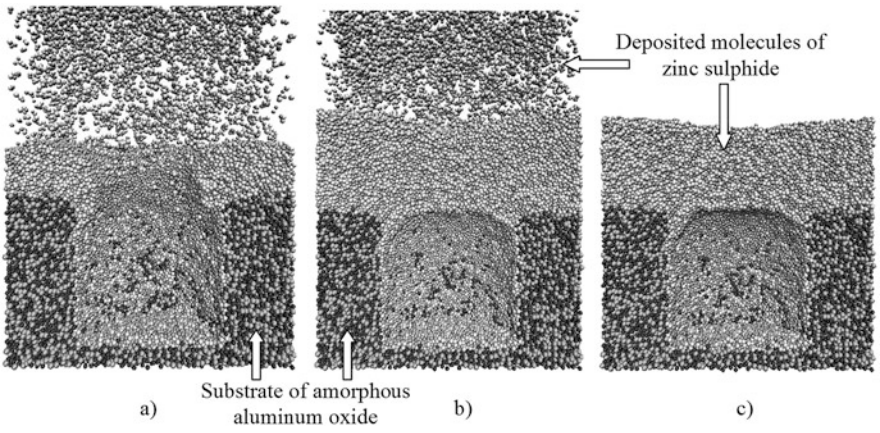

Fig. 4 Result of burying the porous template of aluminum oxide with zinc sulfide for the deposition time: (**a**) 0.2 ns, (**b**) 0.4 ns, and (**c**) 0.6 ns

In general, the surface of ZnS nanofilm formed is rather even with slight flash above the pore region. The formation of molecular agglomerates above the template during epitaxy is not registered, therefore, the resultant film does not have considerable relief changes in the surface. The nanofilm intensity growth was even. The resultant thickness of the nanofilm formed for pure zinc sulfide was 6.6–6.8 nm.

To investigate the possibility of controlling the processes of deposition and formation of nanofilms and burying of porous templates, the angle to the normal line of the porous template in which the epitaxial atoms and molecules move to the deposition surface was selected as one of the modeling control parameters.

The percentage of atoms in the pore relative to the total number of particles being deposited for different time moments of the condensation stage and nanofilm growth and different angles relative to the normal line of epitaxy direction is given in Fig. 5.

The graph analysis demonstrates that the deposition process only slightly depends on the angle, at which the atoms are evaporated, and it is practically identical in time. Slight deviations of the atom share in the pore are observed at the time moments of 200–400 ps, when the active rearrangement of the internal structure of nanofilms and nanoformations in the pore takes place. Afterwards, the dependencies under consideration are stabilized and reach the stationary regime. The stationary behavior of the atom percentage in the pore relative to the total amount of the particles being deposited (time moments of 450–600 ps) still has a slight difference for different deposition angles. The deviation from the normal line to the template surface results in slight increase in the area onto which the atoms are deposited that is explicitly confirmed in the graph considered. The deposition angles for all graphs are given in degrees.

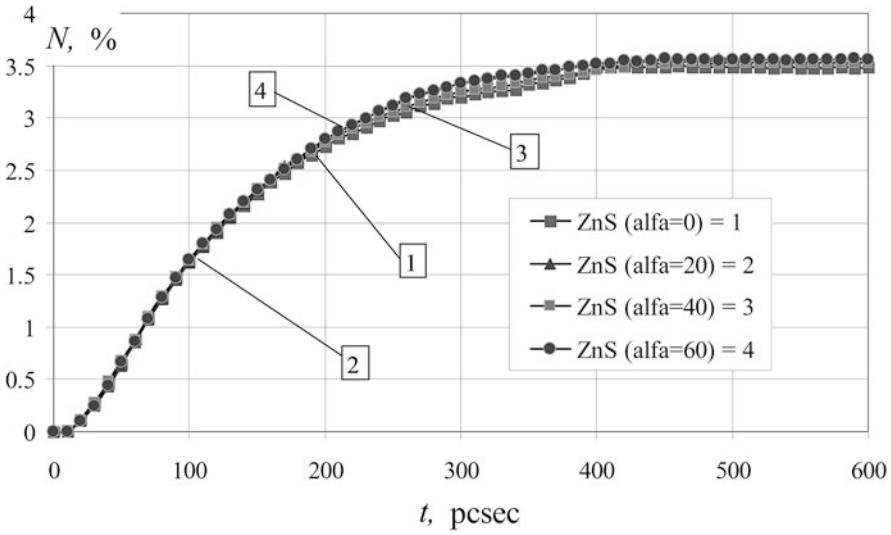

Fig. 5 Percentage of atoms in the pore relative to the total number of particles being deposited for different deposition angle

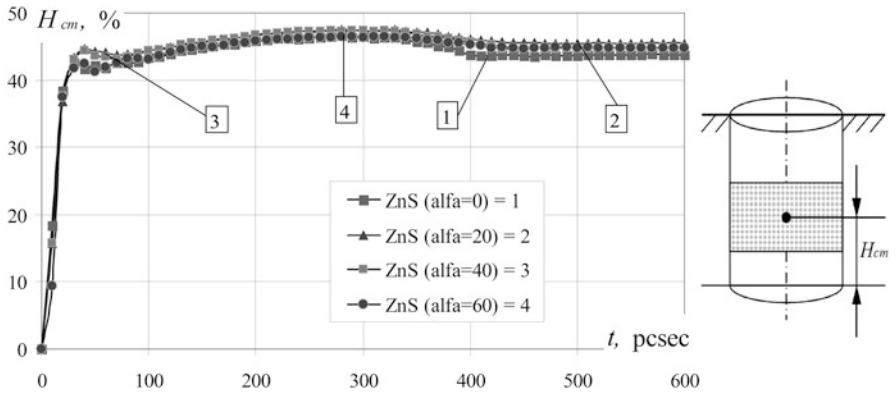

Fig. 6 Relative depth of the mass center of nanoformations in the pore for different deposition angle

Similar behavior is observed for the position of mass center of nanostructure being formed inside the pore shown in Fig. 6. As we can see from the behavior of the graphs in Fig. 5, the change in the height of mass center of the deposited atoms and molecules inside the pore also only slightly depends on the deposition angle. Slight deviations in the behavior of dependencies occur for the time moment of 30 ps of the condensation stage. The height of nanostructures for the deposition angles of 20° and 40° is a bit lower. After the time moment of 400 ps the situation changes and the mass center for the epitaxy angle of 0° has the least height. Thus, for the case of deposition along the normal line to the template surface the mass center of atoms and molecules inside the pore is the lowest. Nevertheless, the deviations between the graphs in Fig. 6 are slight and do not exceed 5%.

To continue with the analysis, the thickness of the nanofilm being formed above the template surface was considered. The computational algorithm of the nanofilm thickness considers its layer-by-layer structure at each time moment. The numeration of layers starts from the template surface and increases at the distance from it. The thickness of layers in the algorithm can vary, but it should depend on the crystalline structure type of the material being formed and lattice parameters, in particular, distances to the nearest neighbors. In the prevailing majority of cases, the thickness of the nanofilm intermediary layers of 0.2–0.3 nm provides the satisfactory accuracy of calculations. For each layer, starting from the first, the number of particles in the layer and atomic density are calculated. These values are compared with similar values on the previous layer. If the spatial layers become much rarer, the computational process stops. The nanofilm final thickness will comprise all layers previously considered. The level of atomic density is a variable algorithmic value, the value of 50% was used in this work.

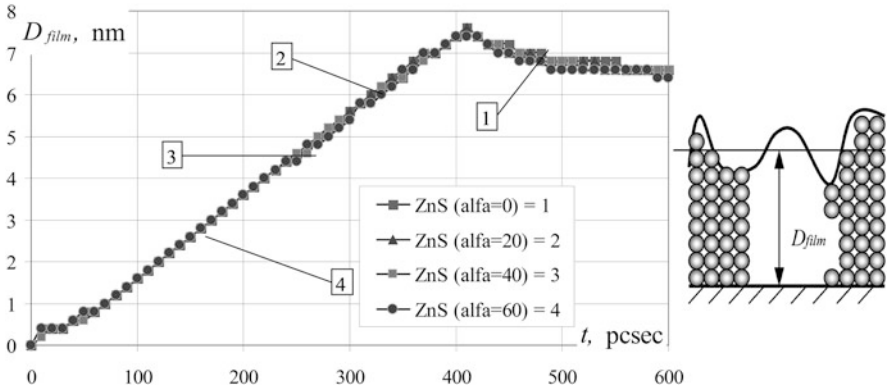

Fig. 7 Nanofilm average thickness on the template surface for different deposition angles

The nanofilm thickness growth on the template surface for different deposition angles is presented in Fig. 7. For the initial time moments (0–400 ps) linear growth of the nanofilm thickness is observed. At the time moments of 400–600 ps the deposited atoms and molecules are compacted and the internal structure is rearranged, so the film average thickness slightly decreases.

3 Conclusion

The results of modeling the processes of precipitation of pure molecular sulfide of zinc and with the addition of additives in the form of copper atoms and manganese sulfide molecules have shown that the addition of uniformly distributed alloying elements to the nanofilms does not significantly affect the process of pore contraction. The process of incubation proceeds with partial filling of the cavity in the substrate. The growth of the nanofilm proceeds evenly, without sudden jumps and shifts.

When adding alloying elements, there are no visual changes in the growth processes, there is an insignificant deviation of functional dependencies within the limits of not more than 0.3%. The introduction of additives leads to an increase in the number of deposited atoms and a regular increase in the thickness of nanostructured coatings of substrates. The highest nanofilms were detected in the cases of 10% alloying additives, which led to the appearance of an additional 0.2–0.6 nm layer-by-layer deposition.

Investigations into the possibility of controlling the growth processes of nanofilms, overgrowing porous substrates, and the formation of nanostructured coatings have shown that the epitaxial deposition angles and heating of the nanosystem to temperatures of 293–593 K do not lead to a significant change

in the formation of nanoformations. At the same time, there is a slight restructuring of the structure and internal organization of nanoelements, but there is no certain filling of the pores and changes in the properties of the nanofilms.

Acknowledgements The investigation was carried out in the frameworks of support by the Ural Branch of the Russian Academy of Sciences (projects No 18-10-1-29) and financial support of Russian Science Foundation (project No 15-19-10002).

References

1. Li, A.P., Muller, F., Birner, A., Nielsch, K., Gosele, U.: Hexagonal pore Ar-rays with a 50–420 nm interpore distance formed by self-organization in anodic alumina. J. Appl. Phys. **84**(11), 6023–6026 (1998)
2. Masuda, H.: Highly ordered nanohole arrays in anodic porous alumina. In: Ordered Porous Nanostructures and Applications. Nanostructure Science and Technology, pp. 37–55. Springer, New York (2005)
3. Mu, C., Yu, Y., Liao, W., Zhao, X., Xu, D., Chen, X., Yu, D.: Controlling growth and field emission properties of silicon nanotube arrays by multistep template replication and chemical vapour deposition. Appl. Phys. Lett. **87**(11), 1–3 (2005)
4. Nikolaev, A.E., Melnik, Yu.V., Kuznetsov, N.I., Strelchuk, A.M., Kovarsky, A.P., Vassilevski, K.V., Dmitriev, V.A.: GaN pn-structures grown by hydride vapor phase epitaxy. Mat. Res. Soc. Symp. Proc. **482**, 251–256 (1998)
5. Vakhrushev, A.V.: Computational Multiscale Modeling of Multiphase Nanosystems. Theory and Applications. Apple Academic Press, Waretown (2018)
6. Vakhrushev, A.V., Severyukhin, A.V., Fedotov, A.Yu., Valeev, R.G.: Research nanofilms deposition processes on a substrate of porous aluminum oxide by means of mathematical simulation. Comput. Contin. Mech. **9**(1), 59–72 (2016)
7. Vakhrushev, A.V., Fedotov, A.Yu., Severyukhin, A.V., Valeev, R.G.: On the structure and properties of nanofilms deposited on porous aluminum oxide substrates. Nanosci. Technol. Int. J. **8**(3), 167–192 (2017)
8. Vakhrushev, A.V., Fedotov, A.Yu., Severyukhin, A.V., Valeev, R.G.: Influence of pore size parameters on the mechanisms of formation of nano-films coatings on porous alumina substrates. Bull. South Ural State Univ. Ser. Math. Model. Programm. **10**(2), 83–97 (2017)
9. Xu, H.J., Li, X.J.: Structure and photoluminescent properties of a ZnS/Si nanoheterostructure based on a silicon nanoporous pillar array. Semicond. Sci. Technol. **24**(7), 075008 (2009)
10. Ying, J.Y.: Nanoporous systems and templates the unique self-assembly and synthesis of nanostructures. Sci. Spectra **18**, 56–63 (1999)

Dynamic Coupling Characteristics of Slender Suspension Footbridges with Wind-Resistant Ropes

Y. B. Yang and J. D. Yau

Abstract An analytical study is presented for the slender suspension bridge with inclined wind-resistant ropes (i.e., wind-guys) susceptible to coupled flexural and torsional vibrations. Based on the linearized deflection theory of classical suspension bridges, the modal coupling mechanism of a single-span footbridge is studied analytically. The free vibration analysis is conducted to obtain the closed-form solutions of modal frequencies and modal shapes of the suspended beam with horizontal wing guys, from which the key parameters and coupling factors dominating the flexural–torsional coupled vibrations are identified. To evaluate the coupling nature of flexural–torsional vibrations for the suspended beam, the modal-based coupling contribution factor is presented in this study.

1 Introduction

Paralleling the advances in constructional materials and technology, a modern suspension footbridge is designed toward the features of a lighter and more slender form. Such a slender suspension footbridge with low stiffness, mass, and damping ratio is more susceptible to coupled flexural and torsional vibrations due to the existence of dense modal frequencies.

In the design of traditional suspension bridges, wind or seismic resistance are crucial factors to be considered in determining the main geometric shape of the bridge. In the past several decades, numerous researchers and engineering scientists have devoted themselves to the theoretical analyses, experimental tests,

Y. B. Yang (✉)
School of Civil Engineering, Chongqing University, Chongqing, China

Department of Civil Engineering, National Taiwan University, Taipei, Taiwan
e-mail: ybyang@ntu.edu.tw

J. D. Yau
Department of Architecture, Tamkang University, Taipei, Taiwan
e-mail: jdyau@mail.tku.edu.tw

V. P. Matveenko et al. (eds.), *Dynamics and Control of Advanced Structures and Machines*, https://doi.org/10.1007/978-3-319-90884-7_21

and structural health monitoring for long-span suspension bridges under various traffic conditions [1, 2]. In comparison, rather little works were carried out for the pedestrian suspension bridges that are getting more popular in the world.

The structural characteristics of a slender suspension footbridge investigated herein include the following components: (1) two vertical strong suspension cables to hang a narrow bridge deck; (2) a flexible bridge deck with no stiffening girders; and (3) two symmetrical pre-tensioned wind-guys via inclined wind-ties to stabilize the additional torsion induced by pedestrians or wind loads. The inclined wind-guys play a key role in coupling the lateral and torsional vibrations of a suspension footbridge. In this paper, an analytical approach based on the linearized deflection theory of suspension bridges [3, 4] is presented to extract the key parameters dominating the dynamic coupling characteristics of the flexural and torsional modes of the slender suspension footbridge. To carry out the free vibration analysis analytically, closed-form solutions for the characteristic equations and modal shapes are derived from the decoupled equations of the suspension footbridges with horizontal wind-guys, from which approximate shape functions used for coupled flexure and torsion of the suspension beam are obtained. Then the dynamic coupling characteristics of a slender suspension footbridge with inclined wind-guys are investigated and the modal mass-based coupling contribution factor is presented to assess the dynamic coupling characteristics in the flexural and torsional vibrations of the suspended beam.

2 Formulation of the Problem and Governing Equations

Figure 1 depicts a schematic diagram of a single-span suspension footbridge in static equilibrium under the gravity loads and pre-tensioned wind-guys. With reference to Fig. 1a and b, the suspension footbridge with pre-tensioned wind-guys (or wind-resistant ropes) is simulated as a *single-span suspended beam* with hinge supports. The following symbols are defined: B = width of the bridge deck, B_c = width of the walkway below the two suspended cables, (E_cA_c, E_rA_r) = axial rigidities of the suspension cables and wind-guys, (H, h) = total horizontal forces in the cables and wind-guys, L = span length of the beam, w = self-weight per unit length, $Y_0 f(x)$ = sag function of the suspension cables, Y_0 = cable sag, $y_0 f(x)$ = arching function of the wind-guys, y_0 = rising height in the inclined wind-guys, and α = angle of inclination of the wind-guys.

For analytical formulation, the linearized deflection theory of suspension bridges [4] is adopted to describe the spatial motion of the suspended beam. The following are the basic assumptions adopted:

1. The beam is prismatic, rigid in cross section, and of the Bernoulli–Euler type;
2. The suspension cables and wind-guys are *parabolic* and *symmetrical* with respect to the beam axis (see Fig. 1a and b);

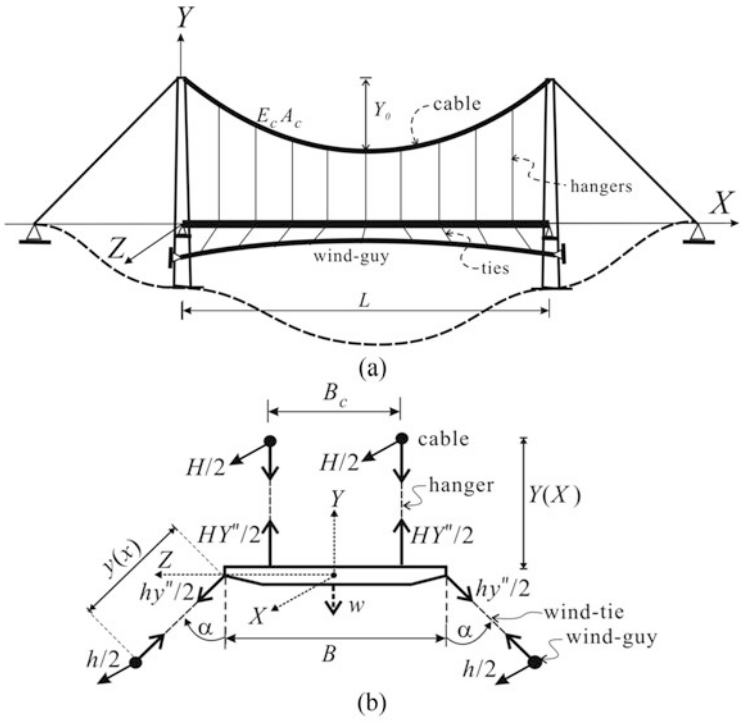

Fig. 1 Schematic of a suspension footbridge in static equilibrium: (**a**) elevation; (**b**) free body diagram of the cross section

3. The angles (α) of inclination of the wind-guys are the same at the two sides of both ends of the beam (see Fig. 1b);
4. The tensile cables along with vertical hangers are assumed to carry all the dead loads (w) of the beam and the vertical force components of the wind-guys via the wind-ties (see Fig. 1b);
5. Both the hangers and wind-ties are inextensible and weightless; and
6. The mass of the beam, including those of the cables and wind-guys, is uniformly distributed along the length.

As shown in Fig. 2, we regard the tensile forces induced by the suspension cables and the inclined wind-guys as the external forces acting on the suspended beam. Based on the classical suspension beam theory [3] and considering the equations of equilibrium for the translations along the (Y, Z) axes and for the torsional rotation about the X axis, one can write the following differential equations of motion for the suspended beam:

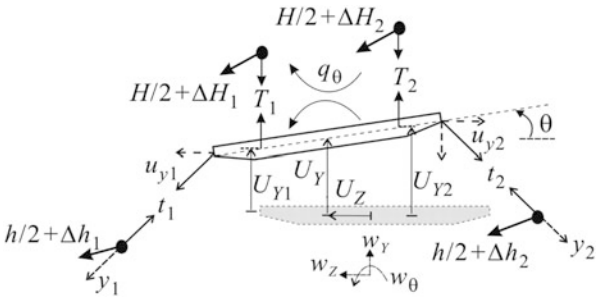

Fig. 2 Kinematics of cross section in deformed position

Vertical equation (Y):

$$m\ddot{U}_Y + EI_Z U_Y'''' - \left(H + h(\cos\alpha)^2\right) U_Y'' + \left(S + s(\cos\alpha)^2\right) \int_0^L 2U_Y dx = w_Y \tag{1}$$

Coupled equations in flexure (Z) *and torsion* (X):

$$\begin{Bmatrix} m\ddot{U}_Z + EI_Y U_Z'''' \\ I_\theta \ddot{\theta} + \frac{4y_0(hB\sin\alpha)}{L^2}\theta \end{Bmatrix} - \begin{bmatrix} h(\sin\alpha)^2 & \frac{hB\sin 2\alpha}{4} \\ \frac{hB\sin 2\alpha}{4} & GJ + \frac{HB_c^2 + h(B\cos\alpha)^2}{4} \end{bmatrix} \begin{Bmatrix} U_Z'' \\ \theta'' \end{Bmatrix} + \begin{bmatrix} 2s(\sin\alpha)^2 & \frac{sB\sin 2\alpha}{2} \\ \frac{sB\sin 2\alpha}{2} & \frac{SB_c^2 + s(B\cos\alpha)^2}{2} \end{bmatrix} \begin{Bmatrix} \int_0^L U_Z dx \\ \int_0^L \theta dx \end{Bmatrix} = \begin{Bmatrix} w_Z \\ w_\theta \end{Bmatrix} \tag{2}$$

$$S = \left(\frac{8Y_0}{L^2}\right)^2 \frac{E_c A_c}{L_c}, \quad s = \left(\frac{8y_0}{L^2}\right)^2 \frac{E_r A_r}{L_r},$$
$$L_c = \int_0^L \left(\sqrt{1 + Y'^2}\right)^3 dx, \quad L_r = \int_0^L \left(\sqrt{1 + y'^2}\right)^3 dx \tag{3}$$

Here, (EI_Y, EI_Z) = flexural rigidities about the Y and Z-axes, respectively, GJ = torsional rigidity, (m, I_θ) = mass and torsional mass inertia per unit length, respectively, (U_Y, U_Z) = vertical (Y) and lateral (Z) displacements, respectively, and (w_Y, w_Z, w_θ) = external loads acting on the beam.

3 Free Vibration Analysis

In the following, two cases will be conducted for the free vibration of a slender suspension bridge with pre-tensioned wind-guys. In Sect. 3.1 the shape functions of the suspended beam with horizontal wind-guys will be derived analytically. With these, the coupling characteristics of the free vibration of the suspended beam with inclined wind-guys will be explored in the sections to follow.

3.1 Decoupled Case

For the uncoupled case of a suspended beam with horizontal wind-guys, that is, with $\alpha = \pi/2$, the integro-differential equations in Eqs. (1) and (2) become

$$m\ddot{U}_Y + EI_Z U_Y'''' - HU_Y'' + 2S\int_0^L U_Y dx = 0, \tag{4}$$

$$m\ddot{U}_Z + EI_Y U_Z'''' - hU_Z'' + 2s\int_0^L U_Z dx = 0, \tag{5}$$

$$I_\theta\ddot{\theta} - \left(GJ + \frac{HB_c^2}{4}\right)\theta'' + \frac{4y_0hB}{L^2}\theta + \frac{SB_c^2}{2}\int_0^L \theta dx = 0 \tag{6}$$

The suspended beam is stiffened by the suspension cables in both the vertical flexural and torsional directions and by the pre-tensioned wind-guys in the horizontal plane. For the purpose of analytical investigation, the lateral-flexural (U_z) and torsional (θ) vibrations will be considered in the following free vibration analysis. By solving Eqs. (5) and (6) for the beam with hinged supports, the characteristic equations and the corresponding n-th natural modes in flexure and torsion are listed as Tables 1 and 2, respectively. In Tables 1 and 2, the following parameters are used: $k = h/EI_Y$ and

$$k_{1n}^2 = w_n^2\left(\sqrt{\left(\frac{k}{2w_n^2}\right)^2 + 1} - \frac{k}{2w_n^2}\right), \quad k_{2n}^2 = w_n^2\left(\sqrt{\left(\frac{k}{2w_n^2}\right)^2 + 1} + \frac{k}{2w_n^2}\right),$$

$$\beta_n = \omega_n\sqrt{\frac{I_\theta - 4y_0hB/(\omega_n L)^2}{GJ + HB_c^2/4}}, \quad w_n^4 = \frac{m\omega_n^2}{EI_Y} \tag{7}$$

From the closed-form solutions of natural frequencies and modal shapes in flexure and torsion derived for the suspended beam, a set of approximate shape functions can be selected for the coupled flexural and torsional modes of the suspended beam with inclined wind-guys in the following section.

Table 1 Dynamic properties of the suspended beam in flexural vibration (U_{Zn})

	Odd modes ($n = 1, 3, 5, \ldots$)	Even modes ($n = 1, 2, 3, \ldots$)
Characteristic equation	$\frac{(k_{2n}L)^3 \tan(k_{1n}L/2) + (k_{1n}L)^3 \tanh(k_{2n}L/2)}{(k_{1n}L)^2 + (k_{2n}L)^2}$ $+(w_nL)^6 \left(\frac{EI_Y}{4sL^5}\right) - \frac{(w_nL)^2}{2} = 0$	$\omega_{2n}^2 = \frac{EI_Y}{m}\left(\frac{2n\pi}{L}\right)^4$ $+ \frac{h}{m}\left(\frac{2n\pi}{L}\right)^2$
Modal shapes	$1 - \frac{\cos k_{1n}x + \tan(k_{1n}L/2)\sin k_{1n}x}{1 + (k_{1n}/k_{2n})^2}$ $+\left(\frac{k_{1n}}{k_{2n}}\right)^2 \frac{(\tanh(k_{2n}L/2)\sinh k_{2n}x - \cosh k_{2n}x)}{1 + (k_{1n}/k_{2n})^2}$	$\sin\left(\frac{2n\pi x}{L}\right)$

Table 2 Dynamic properties of the suspended beam in torsional vibration (θ_n)

	Odd modes ($n = 1, 3, 5, \ldots$)	Even modes ($n = 1, 2, 3, \ldots$)
Characteristic equation	$\tan\frac{\beta_n L}{2} = \frac{\beta_n L}{2} - (\beta_n L)^3 \left(\frac{GJ + \frac{HB_c^2}{4}}{SB_c^2 L^3}\right)$	$\omega_{2n}^2 = \frac{GJ + B_c^2 H/4}{I_\theta}\left(\frac{2n\pi}{L}\right)^2$ $+ \frac{8y_0 hB}{I_\theta L^3}$
Modal shapes	$1 - \tan\left(\frac{\beta_n L}{2}\right)\sin\beta_n x - \cos\beta_n x$	$\sin\left(\frac{2n\pi x}{L}\right)$

Table 3 Properties of the suspension footbridge

L m	Y_0 m	y_0 m	B_c m	B m	EI_Y kNm^2	GJ kNm^2	h kN	m t/m	I_θ tm^2/m	E_cA_c kN	E_rA_r kN
250	20	10	2	3.5	7×10^7	4×10^4	3000	0.75	0.6	5.4×10^6	1.7×10^6

Table 4 Distribution of natural frequencies for symmetrical modes

Natural frequency/mode (n)	$n = 1, 3, 5, 7, 9, 11, 13, 15$
Flexure $\omega_{Zn} = \left(\frac{\eta_{Zn}\pi}{L}\right)^2 \sqrt{\frac{EI_Y}{m}}$	$\eta_{Zn} =$ **1.4**, 3.0, 5.0, 7.0, 9.0, 11.0, 13.0, 15.0
Torsion $\omega_{\theta n} = \frac{\eta_{\theta n}\pi}{L}\sqrt{\frac{GJ + HB_c^2/4}{I_\theta}}$	$\eta_{\theta n} =$ **2.9**[a], **3.9**, **5.2**, **7.1**, **9.1**, **11.1**, **13.1**, 15.0

[a]Strengthened by suspension cables and pre-tensioned wind-guys

3.2 *Determination of Shape Functions*

With the properties given in Table 3 for the suspension footbridge with horizontal wind-guys, the distribution of natural frequencies obtained from the exact solutions of Table 1 is listed in Table 4. Here, the bold values in Table 4 represent the strengthening natural frequencies in flexural and torsional induced by suspension cables and pre-tensioned wind-guys.

As indicated for the symmetrical modes, the higher frequencies of odd flexural modes are mostly dominated by the corresponding modal shape of a simple beam, that is, $\sin(n\pi x/L)|_{n=3,5,7,\ldots}$. Thus, the lateral displacement of the suspended beam can be represented by

$$U_Z(x,t) = \sum_{n=1,2,3,\ldots} q_{Zn}(t) \sin\frac{n\pi x}{L} \tag{8}$$

In contrast, the torsional frequencies of the symmetrical modes do not have such a regular distribution as the flexural modes. Inspired by the torsional shape functions of symmetrical modes shown in Table 1, we can represent the torsional shape of the suspended beam as

$$\theta(x,t) = \sum_{n=1,3,5,\ldots} q_{\theta n}(t)\left(1 - \sin\frac{n\pi x}{L} - \cos\frac{2n\pi x}{L}\right) + \sum_{n=2,4,6,\ldots} q_{\theta n}(t)\sin\frac{n\pi x}{L} \tag{9}$$

Here, the shape functions of odd modes with multi curvatures are selected to simulate the symmetrical modes for better convergence to account for the cable-induced additional stiffness than the sinusoidal functions.

3.3 Generalized Coupled Equations of the Suspended Beam

For illustration, the first two shape functions shown in Eqs. (8) and (9) are selected. By Galerkin's method, one can derive the following coupled equations of free motion for the first (symmetrical) and second (anti-symmetrical) modes, respectively, of the suspended beam as

Symmetrical mode:

$$\begin{bmatrix} m/2 & 0 \\ 0 & (2-16/3\pi)\, I_\theta \end{bmatrix} \begin{Bmatrix} \ddot{q}_{Z1} \\ \ddot{q}_{\theta 1} \end{Bmatrix} + \begin{bmatrix} k_{Z1}/2 & C_1 \\ C_1 & k_{\theta 1} \end{bmatrix} \begin{Bmatrix} q_{Z1} \\ q_{\theta 1} \end{Bmatrix} = \begin{Bmatrix} 0 \\ 0 \end{Bmatrix} \tag{10}$$

Anti-symmetrical mode:

$$\begin{bmatrix} m & 0 \\ 0 & I_\theta \end{bmatrix} \begin{Bmatrix} \ddot{q}_{Z2} \\ \ddot{q}_{\theta 2} \end{Bmatrix} + \begin{bmatrix} k_{Z2} & C_2 \\ C_2 & k_{\theta 2} \end{bmatrix} \begin{Bmatrix} q_{Z2} \\ q_{\theta 2} \end{Bmatrix} = \begin{Bmatrix} 0 \\ 0 \end{Bmatrix} \tag{11}$$

Here, the generalized torsional stiffness coefficients are given as follows:

$$C_1 = \left(\frac{8}{3\pi} - \frac{1}{2}\right)\frac{hB\sin 2\alpha}{4}\left(\frac{\pi}{L}\right)^2, \quad C_2 = \frac{hB(\sin 2\alpha)}{4}\left(\frac{2\pi}{L}\right)^2,$$

$$k_{Z1} = EI_Y\left(\frac{\pi}{L}\right)^4 + h\left(\frac{\pi\sin\alpha}{L}\right)^2 + \frac{8sL(\sin\alpha)^2}{\pi^2},$$

$$k_{Z2} = EI_Y\left(\frac{2\pi}{L}\right)^4 + h\left(\frac{2\pi\sin\alpha}{L}\right)^2,$$

$$k_{\theta 1} = \left(\frac{5}{2} - \frac{16}{3\pi}\right)\left(GJ + \frac{HB_c^2 + h(B\cos\alpha)^2}{4}\right)\left(\frac{\pi}{L}\right)^2 + \frac{8hBy_0}{L^2}\left(1 - \frac{8}{3\pi}\right) + \frac{SB_c^2 + s(B\cos\alpha)^2}{2}L\left(1 - \frac{2}{\pi}\right)^2,$$

$$k_{\theta 2} = \left(GJ + \frac{B_c^2H + h(B\cos\alpha)^2}{4}\right)\left(\frac{2\pi}{L}\right)^2 + 4\frac{hBy_0}{L^2}\sin\alpha \tag{12}$$

The coupled terms (C_1, C_2) in Eqs. (10) and (11) are related to the pretension force (h) in the inclined wind-guys. Solving the eigenvalue problem for the free vibration analysis in Eqs. (10) and (11) yields the approximate natural frequencies of the suspended beam.

3.4 Natural Frequencies

To analytically demonstrate the additional torsional stiffness induced by the suspension cables and inclined wind-guys, the decoupled case of unstressed wind-guys with inclined angle of $\alpha = \pi/4$ is considered. With the condition of $h = 0$ or $C_1 = C_2 = 0$, the generalized equations in Eqs. (10) and (11) of the suspended beam become decoupled and the frequencies obtained have been listed in Table 5. Thus the frequency ratio of the first symmetrical mode $(j = 1)$ to the first anti-symmetrical mode $(j = 2)$ in torsion of the suspension bridge is

$$\frac{\Omega_{Z1}^2}{\Omega_{Z2}^2} = \frac{1}{4} + \frac{4sL}{\pi^2 EI_Y(2\pi/L)^4} = \frac{1}{4} + \left(\frac{4y_0}{\pi^3 L}\right)^2\frac{E_rA_r/L_r}{EI_Y/L^3} < 1, \tag{13}$$

$$\frac{\Omega_{\theta 1}^2}{\Omega_{\theta 2}^2} = \frac{(5/2 - 16/3\pi)}{8\,(1 - 8/3\pi)} + \frac{(SB_c^2 + sB^2/2)L(1 - 2/\pi)^2}{16\,(1 - 8/3\pi)\left(GJ + B_c^2H/4\right)(\pi/L)^2} > 1 \tag{14}$$

Table 5 Natural frequencies of the suspended beam with unstressed wind-guys

	Lateral flexure	Torsion
Symmetrical frequencies	$\Omega_{Z1} = \sqrt{\frac{EI_Y}{m}\left(\frac{\pi}{L}\right)^4 + \frac{4sL}{m\pi^2}}$	$\Omega_{\theta 1} = \sqrt{\left(\frac{5}{2} - \frac{16}{3\pi}\right)\frac{GJ+B_c^2H/4}{I_\theta(2-16/3\pi)}\left(\frac{\pi}{L}\right)^2 + \frac{(SB_c^2+sB^2/2)L}{2I_\theta(2-16/3\pi)}\left(1-\frac{2}{\pi}\right)^2}$
Anti-symmetrical frequencies	$\Omega_{Z2} = \left(\frac{2\pi}{L}\right)^2\sqrt{\frac{EI_Y}{m}}$	$\Omega_{\theta 2} = \left(\frac{2\pi}{L}\right)\sqrt{\frac{GJ+B_c^2H/4}{I_\theta}}$

As indicated in Eq. (14), the torsional stiffness factors of (SB_c^2, sB^2), which are related to the aspect ratios of $(B/L, B_c/L, Y_0/L, y_0/L)$ and the axial stiffness of $(E_cA_c/L_c, E_rA_r/L_r)$ of the suspension cables and wind-guys, play a key role in increasing the torsional stiffness of the first symmetrical mode of a suspension footbridge. Clearly, the additional torsional stiffness factors explain why the frequency of the first symmetrical mode is higher than that of the first anti-symmetrical one.

3.5 *Coupled Modes*

As revealed in Sect. 3.4, the first torsional frequency of the anti-symmetrical mode is smaller than the one of the symmetrical modes induced by strengthening of the suspension cables and wind-guys. To evaluate the coupling between the lateral-flexural and torsional modes, only the first anti-symmetrical modes are studied in this section. Solving the eigenvalue problem for the first anti-symmetrical modes of Eq. (11) yields the following frequencies and modal shapes:

$$\Omega_{j2}^2 = \frac{\Omega_{Z2}^2}{2}\left[1 + f_2^2 \mp \sqrt{(1-f_2^2)^2 + (2c_2)^2}\right], \quad j = Z, \theta \tag{15}$$

$$[\Psi]_2 = \left[\{\phi_{Z2}\}\ \{\phi_{\theta 2}\}\right] = \begin{bmatrix} 1 & \psi_2 \\ -\psi_2/r^2 & 1 \end{bmatrix},$$

$$\psi_2 = r\left[\frac{1-f_2^2}{2c_2} + \sqrt{\left(\frac{1-f_2^2}{2c_2}\right)^2 + 1}\right], \tag{16}$$

where $c_2 = C_2/(k_{z2}r)$, $f_2 = \Omega_{\theta 2}/\Omega_{Z2} = \sqrt{k_{\theta 2}/k_{Z2}}/r$, and $I_\theta = mr^2$. With the eigenvectors shown in Eq. (16), the 2nd generalized modal mass matrix is given by

$$\begin{bmatrix} 1 & \psi_2 \\ -\psi_2/r^2 & 1 \end{bmatrix}^T \begin{bmatrix} m & 0 \\ 0 & I_\theta \end{bmatrix} \begin{bmatrix} 1 & \psi_2 \\ -\psi_2/r^2 & 1 \end{bmatrix} = \left(1 + \frac{\psi_2^2}{r^2}\right)\begin{bmatrix} m & 0 \\ 0 & I_\theta \end{bmatrix} \tag{17}$$

As indicated above, the skew-diagonal terms with (ψ_2, ψ_2/r^2) play a role to couple the flexure with torsion of the suspended beam in vibration. For example, if the pretension force (h) disappears in the wind-resistant ropes, then the coupling factor ψ_2 becomes zero and the coupled equations in Eq. (11) will become decoupled, as indicated in Sect. 3.4. In the following examples, such coupling factors are used to estimate the coupling degree of the vibration modes in both flexure and torsion.

4 Numerical Investigation of Coupled Modes

Let us represent the n-th mode $\{\phi_n\}$ of the suspended beam as $\{\phi_n\} = \{\varphi_f\}_n + \{\varphi_t\}_n$, where $\{\varphi_f\}_n$ = sub-vector of the flexural component in $\{\phi_n\}$, and $\{\varphi_t\}_n$ = sub-vector of the torsional component in $\{\phi_n\}$. Thus the n-th modal mass contributed by the flexural or torsional components can be respectively expressed as

$$m_{f,n} = \{\varphi_f\}_n{}^T \mathbf{m} \{\varphi_f\}_n \ , \quad m_{t,n} = \{\varphi_t\}_n{}^T \mathbf{m} \{\varphi_t\}_n, \tag{18}$$

where $\mathbf{m}$ represents the mass matrix of the suspended beam. With the components of the n-th modal mass given in Eq. (18), the coupling contribution factors (CCF) of flexure ($\chi_{f,n}$) or torsion ($\chi_{t,n}$) to the corresponding torsional or flexural mode are respectively defined as

$$\chi_{f,n} = \frac{m_{f,n}}{m_{f,n} + m_{t,n}} \ , \quad \chi_{t,n} = \frac{m_{t,n}}{m_{f,n} + m_{t,n}}. \tag{19}$$

Adopting the properties of the suspended beam with inclined wind-guys in Table 3, one can obtain the numerical results of natural frequencies and torsional–flexural coupled modes as listed in Tables 6 and 7, respectively. Let us examine the torsional and flexural modes plotted in Table 7. The first symmetric torsional mode (T1) appears to have multi-curvatures due to the additional stiffness of tensile cables and pre-tensioned wind-guys. Such additional torsional stiffness may enable the first symmetric torsional frequency (T1) to be higher than the first anti-symmetric torsional one (T2), that is, $\Omega_{\theta 2} < \Omega_{\theta 1}$ (see the frequencies in Table 6). On the other hand, the coupling contribution factors of the vibration modes in torsion and flexure have been shown in Table 7 as well. As can be seen, the larger the ratio of $\chi_{t,n}/\chi_{f,n}$,

Table 6 Natural frequencies for the suspended beam

α	Modal type	1st symm. ($n = 1$)	1st anti-symm. ($n = 2$)	2nd symm. ($n = 3$)	2nd anti-symm. ($n = 4$)
$\pi/4$	Flexural $\Omega_{b,n}$ (Hz)	0.36 (L1)	0.38 (L2)	2.21 (L3)	3.90[a] (L4)
	Torsional $\Omega_{\theta,n}$ (Hz)	1.54 (T1)	1.23 (T2)	2.01 (T3)	2.32 (T4)

[a]*The* 4th *lateral frequency of a simple beam:* $f_4 = \left[(4\pi/L)^2\sqrt{EI_Y/m}\right]/2\pi = 3.90$ Hz

Table 7 Coupled vibration modes of the suspended beam

$\alpha = \pi / 4$	Coupled modes	CCF ($\chi_{t,n} / \chi_{f,n}$) (%)
Torsional-flexural mode Solid = torsional • = flexural	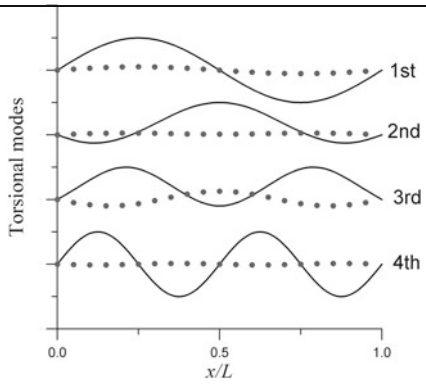	**0.29** / 99.71 **1.39** / 98.61 **3.46** / 96.54 **0.06** / 99.94
Flexural-torsional mode Solid =lateral • = torsional	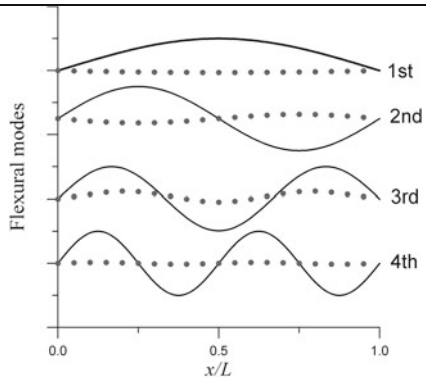	99.71 / **0.29** 98.61 / **1.39** 96.54 / **3.46** 99.94 / **0.06**

the more contribution of torsion to couple the flexural mode will be. Thus there exists a significant coupling phenomenon in torsion and flexure on the 3rd coupled modes, as plotted in Table 7.

5 Concluding Remarks

Based on the linearized deflection theory of classical suspension bridges, the coupled equations of motion for a slender suspension footbridge with pre-tensioned wind-guys are solved analytically. To assess the coupling nature of torsion/flexure on the flexural/torsional modes, this study presented a modal mass-based coupling contribution factor. From the free vibration analysis, the key parameters such as torsional stiffness factors (SB_c^2, $s(B\cos\alpha)^2$), aspect ratios (Y_0/L, y_0/L, B/L, B_c/L), and axial stiffness (E_cA_c/L_c, E_rA_r/L_r) dominating the flexural–torsional coupled vibrations are identified. The added stiffness of the tensile cables and pre-tensioned

wind-guys can significantly raise the first symmetric frequencies in the lateral and torsional directions, such that the first symmetric frequency in torsion becomes higher than the first anti-symmetric one.

Acknowledgements The research reported herein is sponsored partially by the grant from the Ministry of Science and Technology, Taiwan through the serial Nos. (MOST 102-2923-E-032-002-MY3, 106-2923-E-002-007-MY3, 106-2221-E-032-022) and by Chongqing Science and Technology Commission via Grant No. cstc2015jcyjys30003. Such financial aids are gratefully acknowledged.

References

1. Alampalli, S., Moreau, W.J.: Review of Inspection, Evaluation and Maintenance of Suspension Bridge, and Inspection, Evaluation and Maintenance of Suspension Bridges - Case Studies. CRC Press, Boca Raton (2015)
2. Gimsing, N.J.: Cable-Supported Bridges - Concept and Design, 2nd ed. Wiley, Chichester (1997)
3. Rocard, Y.: Dynamic Instability. Frederick Ungar Publishing Company, New York (1957)
4. Yau, J.D., Yang, Y.B.: Vibration of a suspension bridge installed with a water pipeline and subjected to moving trains. Eng. Struct. **30**, 632–642 (2008)